Gold Nanorod-based Assemblies and Composites

Cancer Therapeutics, Sensors and Tissue Engineering Materials

by

Huang-Chiao Huang

A Dissertation Presented in Partial Fulfillment
of the Requirements for the Degree
Doctor of Philosophy

Approved April 2012 by the
Graduate Supervisory Committee:

Kaushal Rege, Chair
Michael Sierks
Lenore Dai
B Ramakrishna
Bryan Vogt

ARIZONA STATE UNIVERSITY

May 2012

ABSTRACT

Gold nanoparticles as potential diagnostic, therapeutic and sensing systems have a long history of use in medicine, and have expanded to a variety of applications. Gold nanoparticles are attractive in biological applications due to their unique optical, chemical and biological properties. Particularly, gold nanorods (GNRs) are increasingly used due to superior optical property in the near infrared (NIR) window. Light absorbed by the nanorod can be dissipated as heat efficiently or re-emitted by the particle. However, the limitations for clinical translation of gold nanorods include low yields, poor stability, depth-restricted imaging, and resistance of cancer cells to hyperthermia, are severe. A novel high-throughput synthesis method was employed to significantly increase in yields of solid and porous gold nanorods/wires. Stable functional nanoassemblies and nanomaterials were generated by interfacing gold nanorods with a variety of polymeric and polypeptide-based coatings, resulting in unique properties of polymer-gold nanorod assemblies and composites. Here the use of these modified gold nanorods in a variety of applications including optical sensors, cancer therapeutics, and nanobiomaterials were described.

ACKNOWLEDGMENTS

First and foremost I gratefully thank my advisor Dr. Kaushal Rege, his for absolute support and guidance during the past five years of my professional journey. I acknowledge Dr. Nathan Newman, Director of LE-CEEE, Karl Weiss and Dr. Zhenquan Liu for access to John M. Cowley Center for high resolution electron microscopy used on several research studies. I am gratefully to Dr. Su Lin of the Center for Center for Single Molecule Biophysics, Biodesign Institute, ASU for training and invaluable assistance to the laser facility; and Dr. Sergei Sarovsky at the Center for Innovations in Medicine, Biodesign Institute, ASU for access to the DLS instrument. Many thanks to Dr. Christine Pauken at the Harrington Department of Bioengineering, ASU for tissue culture training, access to lyophilizer. I thank to Dr. Bret Judson and Dr. Page Baluch at the W. M. Keck Bioimaging Laboratory, ASU for their training and access to confocal microscopy. Great thanks to Dr. Joseph Wang at Jacobs School of Engineering, University California San Diego (UCSD) for training on nanoparticles synthesis. I appreciate Dr. Michel Sadelain and Gertrude Gunset at the Memorial Sloan Kettering Cancer Center, New York, NY for their generous donation of the PC3-PSMA cells employed in this research. Thanks to Fred Pena for all technical support. I am thankful to my colleagues, in Dr. Rege's group and Dr. Sierks's laboratory for their assistant and help. I gratefully thank the financing agency: start-up funds from the state of Arizona, Defense Threat Reduction Agency (DTRA), National Institutes of Health (NIH) and National Science Foundation (NSF). Moreover, I am obliged to my parents and my entire family for providing unconditional and unlimited support throughout my life.

TABLE OF CONTENTS

Page

CHAPTER Page

LIST OF TABLES

TABLE Page

LIST OF FIGURES

FIGURE Page

FIGURE Page

FIGURE Page

FIGURE Page

FIGURE Page

FIGURE Page

FIGURE Page

CHAPTER

1. Introduction

1.1 Gold Nanoparticles

Plasmonic gold nanoparticles are being increasingly investigated as potential therapeutics, drug delivery vehicles, imaging agents and diagnostics due to their unique properties which include enhance biocompatibility over many other metals, ease of chemical conjugation and most importantly, their optical and photothermal properties. Localized surface plasmon resonance (LSPR), involves the collective oscillation of free electrons in metallic nanoparticles upon light excitation. The scattering and absorption properties of gold nanoparticles are greatly enhanced upon LSPR excitation, and are dependent on size and shape of the nanoparticle as well as the dielectric constant of the surrounding medium[1]. The intensity of absorption and scattering efficacies of gold nanoparticles are orders of magnitude higher than most absorbing molecular dyes and scattering organic dyes[2], which makes them excellent candidates for contrast agents and sensors. On the other hand, the photothermal property of gold nanoparticles has been employed to generate heat for therapeutic applications. Briefly, free electrons on the gold surface oscillate upon laser irradiation, generating 'hot' electrons due electron-electron repulsion. Hot electrons then collide with Au lattice ions resulting in heating of the gold nanocrystal lattice in 1 pico(10^{-12}) second, know as electron-phonon interaction. Finally, heat transfer from the Au lattice to the surrounding medium through phonon-phonon relaxation in 100 pico(10^{-12}) second[3]. Light in the near infrared (NIR) (700-1100 nm) wavelength

region penetrates superficial tissue the most (~ 0.5 mm up to several centimeters) due to minimal light absorption by water, blood and melanin, and so is best suit for photon-based noninvasive *in vivo* applications[4]. In particular, gold nanoshells, nanorods and nanocages[5-7], which absorb light in the NIR region resulting in dissipation of heat to the surrounding tissue, have been widely explored.

1.2 Synthesis of Gold NanoparitIces

1.2.1 Gold Nanospheres

Gold nanospheres (gold colloids) are commonly prepared via citrate reduction of gold salt ($HAuCl_4$) in water, based on methods first introduced by Turkevitch et al. in1951[8]. Controlling gold/citrate ratio and temperature during synthesis steps determines the size of the gold nanospheres; the size of the gold nanospheres typically ranges from between 2-100 nm with a corresponding single surface plasmon resonance (SPR) band between 510-570 nm. Many other strategies, including the use of various reductants, ligands[9,10], dendrimers[11,12], and block copolymers[13], have been reported for the generation of gold nanospheres.

1.2.2 Gold Nanorods

Gold nanorods have been synthesized through different methods; the following three methods are presented in chronological order. Gold nanorods were synthesized using a *template method* introduced by Martin et al.[14] Template-based methods involve deposition of gold within the nanopores of porous polycarbonate or alumina template membranes. The diameter and the length of

the gold are tunable and can be controlled by pore diameter of template membranes and the amount of gold deposited within the membrane pores. After deposition, gold nanorods can be collected by dissolution of membrane followed by polymer stabilization. A new high through put method has been developed to overcome the yield limitations associated with traditional template methods; this is described in Chapter 2.

Electrochemical synthesis of gold nanorods was introduced by Yu et al.[15] and Chang et al.[16]. The process starts with the consumption of gold metal anode and formation of anions in a cetyl trimethylammonium bromide (CTAB) surfactant rich electrolytic solution; the anions were then reduced on the cathode surface or within the rod-shaped micelles with sonication. The aspect ratio (length divided by width) of the rods can be controlled with presence of silver ions at different concentration and introduction rate.

Seed-mediated growth method is among the most popular methods for the generation of gold nanorods. Developed by Murphy and co-workers[17-19], the multistep seed-mediated growth method involves: (1) formation of gold seeds by reducing of gold salt with strong reducing agent (sodium borohydride, $NaBH_4$) in the presence of citrate, (2) growth, using gold seeds as nucleation sites introduced into a growth solution of gold salt along with a weak reducing agent (ascorbic acid) and CTAB surfactant. In this method, the aspect ratio of rods can be controlled based on gold seed concentration; presence of silver ions in the growth solution can increase yield of rods. Subsequently, El-Sayed et al.[20]

introduced several modifications to seed-mediated growth method developed by Murphy et al., and further improved the yield of rods with an accompanying reduction in the formation of byproducts. El-Sayed et al. replaced citrate with CTAB surfactant during gold seed synthesis, and adjusted silver ion concentration to control the aspect ratio of nanorods between 1.5 and 5. CTAB forms a bilayer[21] on the surface of the nanorods; repulsion between the cationic head groups of the surfactant is known to result in stable aqueous dispersions of the gold nanorods. The surface plasmon resonance (SPR) band of gold nanorods falls in two regions: (1) A weak band in the visible region around 520 nm is similar to that of gold nanospheres, which is due the electron oscillations along the diameter, known as the transverse band; (2) A strong longitudinal band in the NIR region is due to the electron oscillations along the length of the rods. This strong longitudinal band is tunable based on the aspect ratio of the gold nanorods; the higher the aspect ratio the more red shift of the band will occur (Figure 1).

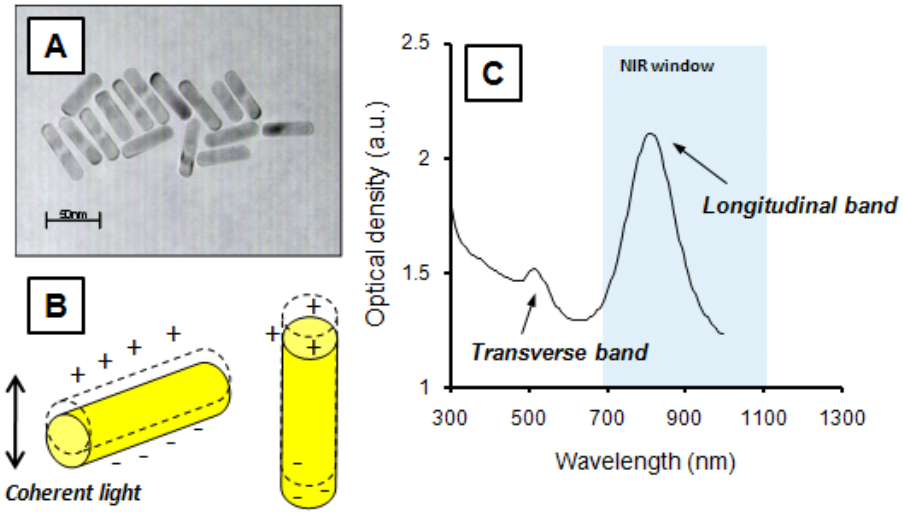

Figure 1.SEM, surface plasmon resonance, and absorption spectrum of GNR.

1.2.3 Gold Nanoshells and Gold Nanocages

Nanoshells are a unique class of nanoparticles with a composite metallic shell (e.g. gold) / dielectric core (e.g. silica) structure. The most well known method for preparing gold nanoshells (few nanometers thick) with silica core (around 100nm) was introduced by Oldenburg and Halas et al.[22-24]. The mono-dispersed silica cores were prepared via basic reduction (Na_4OH) of tetraethyl orthosilicate (TEOS) in ethanol, known as Stober method, and then followed by surface amination to provide positively charged of silica cores. The negatively charged gold colloid (2-4 nm in diameter) can be adsorbed on the silica surface to provide nucleation sites and allow additional gold to be reduced into a complete shell with a controlled thickness. Typically, gold nanoshells posses a single SPR band in NIR region (700-1100 nm) and can be controlled based on gold shell thickness; reducing shell thickness from 20 nm to 5 nm results in absorption peak red shift from 700 nm to 1000 nm and is due to increased coupling between plasmons. The ratio between scattering and absorbing events of gold nanoshells depends on the size of the silica core; smaller silica cores show higher absorption of energy, while larger silica cores are more effective at scattering incident light energy. Introduced by Xia et al., hollow and porous gold nanocages are formed via galvanic replacement reaction between silver nanocubes and $HAuCl_4$ solution[25-27]. Deposition of gold atoms and removal of silver atoms on silver nanocubes results in formation of Au/Ag alloy shell around partially hollow silver nanocubes; followed by different degree of dealloying will result in formation of corner-reconstructed Au/Ag nanoboxes and then to Au nanocages with pores in

the wall. Hollow and porous gold nanocages posses' single SRP band around 800nm was reported by their group.

1.3 Gold-based Sensors

Localized surface plasmon resonance (LSPR) property of noble metal nanoparticles has been employed for numerous biosensing applications. LSPR spectrum of the nanoparticle is dependent on the size and shape as well as the dielectric constant of surrounding media, and can easily be measured using a spectrophotometer. The first type of biosensing is based on colloid aggregation of gold. Upon biomolecular interactions, affected spacing between biomolecular conjugated gold nanoparticles can result in colloidal color changes; the color shifts from blue to red as the interparticle distance increases. This gold *colloid* colorimetric assay was introduced to detect DNA hybridization by Martin et al.[28]. Briefly, a mixture two groups of single stranded DNA-modified gold nanoparticles was first prepared; upon introduction of the third single stranded DNA, complementary DNA hybridization lead to aggregation of the gold colloid accompany abrupt color change from red to purplish. Increased temperature or change in ionic strength resulted in a reverse process. Biosensing based on colloidal aggregation has been reported to detect specific targets (e.g. amino acids sequences, metal ions) using DNA, protein or antibodies modified gold nanoparticles[29-34]. The second type of gold biosensing is based on change in the dielectric constant of gold nanoparticle surrounding medium, leading to a dateable LSPR spectrum red shift. It has been demonstrate for detection of antigen-antibody recognition events and protein-enzyme interactions using gold

nanospheres or gold nanorods[35-37]. Most importantly, gold nanorods were reported to posses higher sensitivity than nanospheres is LSPR-based sensing[37]. Gold nanoparticle-based biosensing have been demonstrate successful and promising; however, improve sensitivity to single-molecule detection, integrate LSPR spectroscopy with proper molecular identification and multi-fictionalization of the system are required for a wide variety of needs. Detection limit can be improved by implementation of advance LSPR equipment. Dahlin et al.[38] reported using high-resolution LSPR spectroscopy with a minimum noise level (< 5×10^{-4} nm, < 5×10^{-6} extinction units); and successfully detected neutravidin (deglycosylated version of avidin protein) binding at less than 0.1 ng/cm^2 using biotin(Vitamin H)-functionalized arrays. LSPR-shift assays can only detect binding of molecules; however the identification of unknown molecules cannot be achieved with LSPR spectroscopy. Coupling molecular identification techniques to LSPR spectroscopy thus is critical. Surface Enhanced Raman Scattering (SERS) is a surface-sensitive technique, in which the local electromagnetic fields enhance Raman scattering (inelastic scattering) as much as 10^{14} to 10^{15} times when molecules adsorb on plasmonic nanoparticles[39]. Since the nanoparticle LSPR can be easily tuned (based on shape and size) to maximized SERS; LSPR spectral-shift assays have been reported in combination with SERS to demonstrate for both molecular quantification and identification[40]. Complementary mass spectrometry (MS) molecular identification with LSPR sensors has been proposed and still is in its beginning stages.

Large-scale study of proteins is considered the next step in the study of biological systems. Multiplex chip based LSPR detector have been demonstrate to provide high through put, label-free immobilization of immunoglobulin A (IgA) to a series of six antibodies at different concentrations[41]. In which, a limit of detection of 100 pg/mL was reported.

1.4 *In vivo Imaging*

Several groups have investigated gold nanoparticles as useful contrast agents for *in vitro* darkfield imaging based on their light resonant scattering property. Darkfield microscopy works by illuminating the sample with light at an angle and collect only the scattered light from the target. Loo et al. demonstrated *in vitro* targeting, imaging as well as ablation of human epidermal growth factor receptor 2 (HER2) positive cancer cells using antibody-targeted gold nanoshells[7,42]. El-Sayed et al. successfully showed *in vitro* darkfield imaging of cancer cells using antibody-conjugated gold nanospheres[43] and nanorods[5]. Even though the extinction cross-section of gold nanorods is dominated by absorption the amount of scattering is sensitive enough for several imaging techniques. These *in vitro* darkfield microscopy studies indicated that light scattering properties of gold nanoparticles can facilitate their use as contrast agents for imaging, while their light absorption properties allow for cancer cell ablation due to hyperthermia. However, for *in vivo* imaging applications of gold nanoparticles, the use of appropriate scattering-based imaging technologies is necessary. Several biomedical imaging modalities, including optical coherence tomography (OCT)[42,44-48], two photon luminescence (TPL)[49-53], photoacoustic tomography

(PAT)[54-65], surface enhanced Raman scattering (SERS)[66-70] and diffuse optical spectroscopy (DOS)[71]have been demonstrated successful for tissue/tumors imaging using either passive or active targeting gold nanoparticles as contrast agents. Although successful, these optical or acoustic scattering-based imaging techniques listed above have limited tissue penetration depths and are therefore challenging in cases of deep tissue imaging. Common hospital diagnostic tools, such as X-ray computed tomography (CT) and magnetic resonance (MR) imaging are better suited for deep tissue *in vivo* diagnostic with the presence of appropriate contrast agents, and have also been investigated for *in vivo* tumor/tissue imaging using gold nanoparticles and Au_3Cu_1 nanocapsules (Copper core with gold shell) as contrast agents[72-74].

1.5 Cancer Therapy

1.5.1 Photothermal Ablation

Properties such as high conversion of strongly absorbed light to heat, photostability, and biocompatibility make gold nanoparticles attractive candidates for photothermal therapy as a potential adjunctive therapeutic modality in addition to conventional treatments (e.g. surgery, chemotherapy, and radiation therapy). The ability to generate moderate to highly elevated temperatures (40-50°C) at a desired site with externally tunable control possesses significant promise for cancer therapy compared to whole-body hyperthermia. In the last few years, *in vitro* studies of photothermal treatments using immunotargeted gold nanoparticles, including gold nanospheres[43,75], gold nanorods[5], gold nanoshells[7], gold nanoclusters[76] and gold nanocages[77], have demonstrated the ability to

selectively induce cancer cell damage via hyperthermia, while leaving the non-targeted cells unaffected. The use of polypeptide-gold nanorod nanocomposites for synergistic administration of hyperthermia and chemotherapeutic drugs for enhanced ablation of cancer cells have been demonstrated in Chapter 6. The following sections focus on *in vivo* cancer photothermal therapies using gold nanoparticles.

1.5.1.1 Gold nanospheres / clusters

The surface plasmon resonance (SPR) absorption of gold nanospheres is in the visible region (~520 nm) and is therefore suitable mainly for superficial cancers due to strong absorption of light in this wavelength region by blood. Both pulsed and continuous visible-wavelength lasers have been employed for cancer cell ablation *in vitro*[43,78]. Clustering of antibody-conjugated gold nanoparticles results in red-shifting of absorption and formation of microbubble around clusters upon pulsed near-IR lasers irradiation, which resulted in effective *in vitro* and [76,79]and *in vivo* cell damage[80].

1.5.1.2 Gold nanoshells

Gold nanoshells consist an ultrathin gold shell surrounding a dielectric core (e.g. silica[81]) and demonstrate a tunable photothermal response to near infrared (NIR) light between 650-900 nm. Hirsch et al.[82] demonstrated successful irreversible thermal destruction of xenograft canine transmissible venereal tumor in female non-obese diabetic mice due to significant temperature increase ($\Delta T = 35°C$) upon exposure of interstitially injected PEG-conjugated (PEGylated) gold

nanoshells to low dose (820 nm, 4 W/cm^2) NIR laser. O'Neal et al.[83] demonstrated that xenograft murine colon carcinoma tumor bearing female albino mice when intravenously injected with PEGylated gold nanoshells followed by laser irradiation (820 nm, 4 W/cm^2) for 3 minutes appeared tumor free up to few month, while laser treatment alone control animals showed growth in tumor size. Stern et al.[84] demonstrated high degree (93%) regression of tumor at high dose nanoshells (8.5 µl/g) usage using prostate cancer cell (PC-3) bearing male athymic (nu/nu) mice; while a slightly lower nanoshells dose (7.0 µL/g) did not result cancer cell ablation. Recently, Schwartz et al.[85] successfully demonstrated passive delivery of PEGylated gold nanoshells to brain tumors in orthotopic canine model, and selectively elevate tumor tissue temperature to around 66°C. In all cases discussed above, gold nanoshell surfaces were coated with poly (ethylene glycol) (or PEG)[86,87] by combining thiol group functionalized PEG with nanoshells to improve biocompatibility and longer circulation times. PEGylated gold nanoshells, preferentially accumulated at the tumor site due to the highly permeable and poorly organized vascular networks (enhanced permeability and retention or EPR effect)[88]. In order to further increase the efficiency of in vivo photothermal ablation using gold nanoshells, specific molecular targeting strategies have also been investigated[7]. Melancon et al.[89]employed epidermal growth factor receptor (EGFR) targeted hollow gold nanoshells (30 nm average diameter) for in vitro photothermal ablation. In addition, the in vivo biodistribution of antibody conjugated gold nanoshells was investigated. Targeted gold nanoshells showed higher delivery efficacy to tumors than non-targeted nanoshells (6.8% ID/g vs 4.6% ID/g) (ID/g: Injected Dose per Gram of Tissue).

However a majority of gold nanoshells were found in spleen, liver, and kidney (~65% ID/g).

1.5.1.3 Gold nanorods

Cylindrical gold nanorods also demonstrate a tunable photothermal response to near infrared (NIR) light as a function of nanoparticle aspect ratio (length/diameter). Different modification strategies have been investigated for replacing cetyltrimethyl ammonium bromide (CTAB) on nanorods for use in biological applications, due to cytotoxicity of the surfactant.

Huang et al.[5] demonstrated in vitro study of anti-epidermal growth factor antibodies modified gold nanorods, targeted to malignant oral epithelial cell cancer cells, and subjected to laser irradiation from an external source leading to the selective localization of hyperthermic treatment. Niidome et al.[90] modified gold nanorods with polyethylene glycol (PEG), which led to reduced gold nanorod (GNR) cytotoxicity while maintaining the stability of gold nanorods in mice. Thirty minutes after intravenous injection, half (~54%) of the injected PEGylated gold nanorods remained in the blood vessels of mice, while unmodified CTAB gold nanorods were seen to accumulate in the liver. El-Sayed et al.[91] demonstrated photothermal therapy of subcutaneous squamous cell carcinoma xenografts grown in nude mice using non-targeted PEGylated gold nanorods irradiated by near-infrared (NIR) laser (1.7-1.9 W/cm^2, 10 min). Two weeks after nanorod injection, greater than 96% decrease in average tumor growth (ΔV= ~900 mm^3) was observed when tumors were directly-injected with

PEGylated gold nanorods (45 µL, OD_{800}= 40); while >74% decrease in average tumor growth was seen in the case where PEGylated gold nanorods (100 ul, OD_{800}= 120) were injected intravenously. Importantly, heating efficiencies in the case of direct injection was similar to that observed with gold nanoshells (3.59±0.5 vs. 3.74±0.7).[82]Kawano et al.[92] demonstrated the site specific accumulation of poly (N-isopropylacrylamide) (PNIPAM) encapsulated gold nanorods can be induced by laser due to rapid photothermal phase transition of the nanoparticles, allowing light controlled targeted delivery. In which, nanoparticles were accumulated at tumor site due to hydrophobic interaction induced by the photothermal effect. Their results showed ~10% of injected PNIPAM coated gold nanorods accumulated at the irradiated site after laser irradiation and ~46% of injected PNIPAM coated gold nanorods accumulated in lungs after 30 min. PEGylated gold nanorods were used as a control to show dispersion in blood. The worrying problem will be the non-specific accumulation of PNIPAM coated gold nanorods.

Studies on biodistribution and stability of intravenously injected PEGylated gold nanorods in mice indicated that higher PEG grafting levels helped avoid the reticuloendothelial system (RES) circulation. A PEG to gold molar ratio of 1.5 was reported as optimum for circulation as well as the enhanced permeability and retention (EPR) effect. The uptake in the liver was saturated at 19.5 µg of nanorod injection dose, in addition to non-specific accumulation in the spleen and tumor[93,94]. Subsequent studies demonstrated that gold nanorods grafted with 5 kilo Dalton (kDa) or 10kDa PEG showed higher circulation stability in mice than

those conjugated with 2kDa or 20kDa.[94] Suppression of tumor growth following near-infrared pulsed laser irradiation was more effective in the case of direct intratumoral injection of nanorods compared to when nanorods were administered intravenously. This result correlates well with the biodistribution study of PEGylated nanospheres in tumor bearing mice model by Zhang et al[59], which reported that 20 nm gold nanospheres coated with PEG (5kDa) exhibited the lowest uptake by reticuloendothelial cells and the slowest clearance from the body.

Goodrich et al.[95] demonstrated photothermal therapy using PEGylated gold nanorods in murine colon cancer model. Tumor-containing animals were intravenously (tail vein) injected with PEGylated gold nanorods followed by photothermal treatment; approximately 44% of the photothermally treated mice (nanorod and laser treated) survived after 60 days of treatment, while the mean survival time for the “nanorod alone” and “ laser irradiation alone” groups were 9.5 and 9.7 days respectively. Substantial accumulation of gold nanorods was found in the liver, spleen and lymph nodes 30 days post injection. These results are not only important for the development of gold nanorods-based photothermal therapies, but also emphasize the importance of specific targeting strategies in order to increase efficacy and decrease in non-specific accumulation in different organ sites.

1.5.2 Drug Delivery

Surface-modified gold nanospheres[96-98], gold nanoshells[99-101], and gold nanorods[51,102] have been successfully employed for delivering various therapeutics, including plasmid DNA, small interfering RNA (siRNA), and chemotherapeutic drugs to cancer cells. Various controlled delivery mechanisms including, pulsed laser induced cleavage of gold-thiol bonds[99,103], drug release under acidic pH environment[97], controllable bond strength (covalent vs. hydrophobic/electrostatic) based diffusion[96], photothermal modulation and NIR-induced surface coating shrinkage[104] have been investigated for delivery using gold nanoparticles. PEG-grafted gold nanospheres were covalently linked with tumor necrosis factor alpha (TNF-α), which is a cytokine with anticancer efficacy known to enhance hyperthermic injury[105-107]. TNF-α loaded nanoparticles were intravenously injected in murine fibrosarcoma-bearing mice via the tail vein, and the combination of TNF-α and hyperthermia led to increased tumor recession compared to the individual treatments acting alone. In the study, hyperthermia was carried out through immersion of tumor and its surrounding tissue in hyperthermic temperature water bath instead of selective activation of photothermal effect of gold nanospheres by laser, presumably since the SPR band of gold nanospheres is in the visible wavelength region. Chen et al.[108] reported that delivery of methotrexate (MTX), a dihydrofolate reductase inhibitor, by gold nanospheres suppressed Lewis lung carcinoma tumor growth in mouse while direct delivery of MTX at the same drug dose showed no effect. Recently, Lu et al.[103] successfully demonstrated in vivo and in vitro NIR-induced silencing of NF-kB p65 via receptor targeted hollow gold nanospheres carrying siRNA recognizing NF-kB p65 subnits. HeLa cervical cancer xenograft-bearing mice

were injected intravenously with folate receptor-targeted PEGylated hollow gold nanospheres carrying p65 siRNA. Following circulation for 6 hours, tumors were treated with moderate NIR irradiation (50 mW/cm^2) for 1 minute. Down-regulation of NF-kB was observed only in tumors irradiated with NIR light which induced a shape transformation of gold nanoparticles leading to siRNA release to the cytosol, in a process called photothermal transfection. In addition, it was demonstrated that photothermal transfection of NF-kB p65 siRNA can successfully sensitize tumors to irinotecan, a chemotherapeutic drug, leading to inhibition of tumor growth.

1.6 Summary

NIR absorbing gold nanoparticles can be used as therapeutic agents either through photothermal ablation (efficient conversion of light energy into heat) or as drug delivery devices; also they have been successfully demonstrate as contrast agents for numerous of imaging modalities as well as for sensing applications. However, beside for drug delivery application, the use of NIR absorbing gold nanoparticles can be restricted by the limited tissue penetration depths of NIR light, and are therefore challenging for *in vivo* deep tissue light based-therapy or imaging. Numerous surface functionalized gold nanoparticles have been demonstrated to improve theranostic and sensing systems. The following studies and proposed work focus on the surface modification of gold nanorods, which is critical to advancing the use of gold nanoparticles in medical and sensing nanotechnology.

CHAPTER

2. Multisegment High Throughput Synthesis of Gold Nanorods and Nanowires via Templated Method

2.1 Introduction

The field of nanotechnology has revolutionized numerous research fields including material science, electronics, optics, energy systems, and medicine[109]. Metallic nanowires/rods in particular had significant applications in sensing/detection[110-115], catalysis[116], electrical devices[117,118], and fuel cells[119,120]. Numerous techniques for synthesizing metallic nanowires have been reported[121-127]. However, most methods are only suitable for laboratory small-scale research applications, but are not practical for larger-scale, low-cost generation of nanomaterials. Martin et al. have mentioned "if practical applications (for nanomaterials) are to be realized, methods for mass-producing template-synthesized nanostructures will be required[122]."

This chapter describes a high-throughput method for generation of gold nanorods and nanowires using multisegment template-assisted synthesis with an eye towards the increasing the yield of nanorods and nanowires. The study was carried out in collaboration with Jason Burdick (graduate student), and Professor Joseph Wang[128]. Template-directed electrodeposition within cylindrical nanopores of a porous membrane represents an attractive and reproducible approach for preparing metal nanowires and nanorods of different aspect ratios (with diameters of 10-300 nm and lengths of 50-1000 nm)[124]. In this method, a

thin conductive layer (e.g. Ag, Au, Cu) is sputtered onto one end of the porous alumina templates. From which desired metallic nanoparticles can be electrodeposited within the pores of alumina. The final stage involves the selective dissolution of both the alumina membrane and the conductive layer, in the presence of polymeric stabilizer (e.g. polyvinyl pyrrole). While the above method is useful for preparing nanorods and nanowires, it suffers from certain disadvantages. First, only a very small portion of the porous template is commonly used for generating nanowires; for example, commercial alumina templates (Whatman Anodisc) use < 5% of the membrane for nanowire growth, while most of the membrane is used for mechanical support or left unused.[129] Second, the fragility of the alumina templates further limits the throughput of this method and necessitates the development of alternative methods for increasing the yield from a single membrane. Finally, the high cost of metals such as gold and silver make current approaches unfeasible for the scale-up of nanowire production. As a result, novel methods are required for short processing times, and low processing costs involved with the generation of large batches of nanowires that are associated with existing methods.

A new multisegment templated synthetic process, described in this chapter, was developed for preparing gold nanorods and nanowires in order to improve the throughput and lower the cost by using most of the cylindrical pores of the membrane. This simple method, illustrated in Figure 2, involves the sequential electrodeposition of segments of a desirable metal that resists chemical etching (e.g. gold) and very short segments (‘gaps’) of a non-desirable “sacrificial” metal

susceptible to chemical etching (e.g. silver) into the template membrane. Following this alternate multisegment deposition, the template first is dissolved then followed by selective dissolution of the sacrificial metallic gaps, leading to the generation of multiple nanowires of the desirable metal from each pore. The final step involves the introduction of surface coating (e.g. polyvinylpyrrolidone PVP, polystyrene sulfonate PSS) to prevent nanowires aggregation. The simplicity and cost-effectiveness of the new multisegment template method was evaluated for the generation of both, solid and porous gold nanowires. This approach results in considerable savings in material requirements, processing times and costs, and is a generic method that can be applied for scaling up the generation of other metal nanowires (which resist chemical etching) in concert with short segments of other 'non-desirable' metals which are susceptible to such etching.

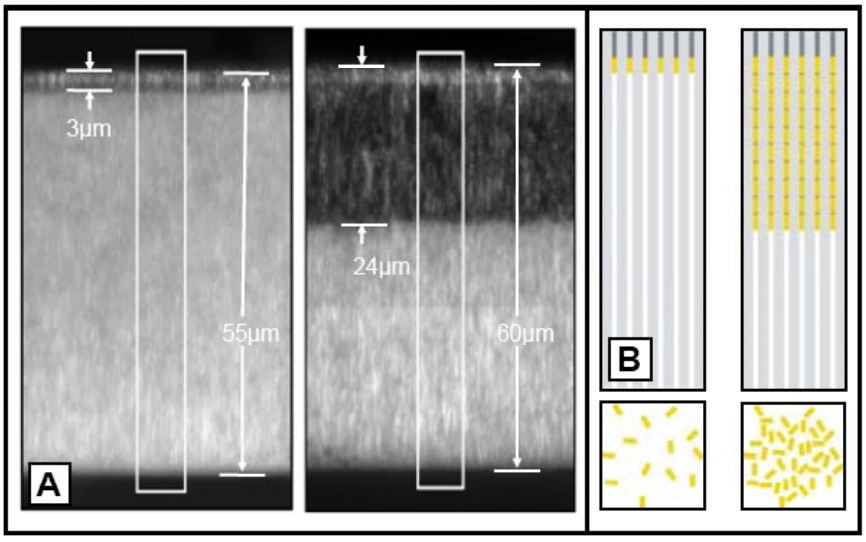

Figure 2.SEM images and schematic of membrane template with single and multisegment approach.

2.2 Materials and Methods

2.2.1 Materials

Alumina membranes (pore size, 200 nm; thickness,60 μm) were purchased from Anodisc Whatman (Cat. No. 6809-6022; Maidstone, UK); Table 1 describes the details of the membrane specifications. Gold targets for membrane sputtering were purchased from Denton Vacuum (Moorestown, NJ). Gold and silver plating solutions (Orotemp 24 RTU RACK and 1025 RTU @ 4.5 Troy/Gallon, respectively) were obtained from Technic Inc. (Anaheim, CA). All chemicals were used as received. Nanopure water was employed for all solution preparation and rinsing steps (18 MΩ, ELGA purelab-ultra model Ultra Scientific, Marlow, Buckinghamshire, UK).

Table 1.Details of anodisc alumina membranes with a specified pore size of 200 nm and thickness of 60 μm.

Pore size	200 nm
Pore density	10^9 /cm^2
Membrane diameter	25 mm
Initial cost of individual membranes	2.5
Number of pores per membrane	$5*10^9$
Membrane thickness	60 μm

2.2.2 Instrumentation

Gold sputtering machine, Denton Vacuum Desk III TSC (Moorestown, NJ, USA) was used for membranes sputtering. Potentiostatic electrodeposition of metals

was carried out with a CHI 621A potentiostat (CH Instruments, Austin, TX). Platinum wire and Ag/AgCl (3M KCl, CH Instruments) served as the counter and reference electrodes, respectively. All working electrode potentials are with respect to Ag/AgCl reference electrodes. Optical images were acquired with a Nikon Eclipse 80i microscope (Nikon Corp., Tokyo, Japan) outfitted with a Photometrics CoolSnap CF camera (Roper Scientific, Duluth, GA). Scanning electron microscopy (SEM) images were obtained with an FEI XL30 SEM instrument (FEI Co., Hillsboro, OR), under an accelerating potential of 30 kV.

2.2.3 Preparation of Nanoporous Alumina Membrane

In addition to those purchased alumina membranes (pore size, 200 nm; thickness, 60 μm), alumina membranes with a pore size of ~30 nm were self-prepared by anodizing pure (99.99%) aluminum in an acidic electrolyte at varying potentials and below ambient temperatures to prevent dissolution of oxidized structures in acidic electrolytes and local heating. Briefly, prior to anodization, pure (99.99%) aluminum foil was washed with (1M, 1mL) NaOH sodium hydroxide to remove surface grease. Nanoporous alumina templates were prepared using a dc power supply. Al foil was anodized in a 1.8M H_2SO_4 solution at 18°C at a constant applied voltage 15 V for 15 minutes, then followed by 20 V for 2 hr 20 min. Alumina removal was carried out in an aqueous mixture of 0.1M copper chloride ($CuCl_2$) and 20% vol Hydrogen Chloride (HCl) at 25°C for about 2 minutes. Removal of the barrier oxide layer was carried out by chemical etching in 5 vol% phosphoric acid (H_3PO_4) for 30 minutes.

2.2.4 Layered Template Synthesis

A thin layer of gold film was first sputtered on the branched side of the alumina membranes providing an electrical contact for the subsequent electrochemical deposition steps. Sputtered membranes were then transferred to a three-electrode electrochemical growth cell where a sacrificial layer silver was first deposited at 2 coulombs charge throughout the branched area and into the body of the membrane at a working electrode potential of -0.9 V. Alternating layers of gold and silver were then deposited on top of the sacrificial silver layer; each gold-silver layer comprised of 0.7 coulombs of gold and 0.1 coulombs of silver, both deposited at -0.9 V. Gold and silver solutions were removed and added in repeats without disassembling the growth cell which is a significant time-saving advantage of the current nanowire synthesis method. During the solution replacement, the membrane, the growth cell, and the reference and counter electrodes were rinsed with nanopure deionized water again without disassembly of the growth cell. Upon completion of multisegment growth, a final rinse was performed and the membrane was removed from the growth cell. Membranes were then divided such that 25 % of the membrane area was saved for imaging and 75 % was dissolved for analysis of nanowire yields. The alumina membranes were first dissolved with 3 M NaOH for 15 minutes and rinsed, following which, the silver segments were dissolved with 35 v/v% concentrated HNO_3 for another 15 minutes with agitation and sonication. Free gold nanowires were then precipitated via centrifugation and rinsed in nanopure water repeatedly until a neutral pH was achieved. Scanning electron microscopy (SEM) images used to

determine membrane yield were from 1:10 dilutions of the final 1 mL nanowire suspension volume.

2.3 Results and Discussion

The current high-throughput method relies on the alternate deposition of two types of metals, one that is resistant to chemical etching (the target nanowires) and one that is susceptible to such etching (the short removable gap segment). This is similar to on-wire fabrication of nanogap structures[130,131]. This concept has been demonstrated for the generation of both, solid and porous gold nanorods / nanowires using intermediate silver segments that can be selectively removed using nitric acid. Figure 2 shows SEM images and a schematic of the single layer and multisegment methods employed for the generation of solid gold nanowires. Nanorods, 700 nm in length and 200 nm in diameter, were generated using alumina templates with a 3 μm sacrificial silver layer and approximately 100 nm silver layer(s) between gold layers. As seen in the figure 4, the sequential electrodeposition of gold and silver segments results a significant usage of the available volume of the cylindrical pores in the alumina membrane. While the traditional single-layer method uses only 3 μm of the pore height, the multisegment method exploits 24 μm of the pore height (seen as dark grey in Figure 3), resulting in an eight-fold increase in the yield of gold nanowires for a single membrane. The SEM image of the cross-section multicomponent nanowires containing alternating layers of gold/silver generated upon dissolution of the alumina membrane (prior to the dissolution of the silver ‘gaps’) is shown in Figure 3. The shorter silver sections (dark grey color) are separated by the longer

gold nanowire segments (lighter grey). The length of the gold and silver segments can be controlled based on the charge used in the electrodeposition of these metals.

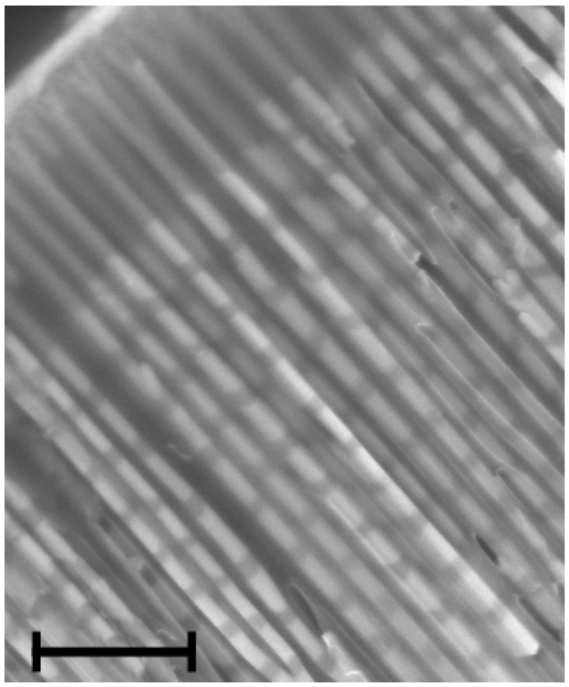

Figure 3.SEM image of 10 gold segments with silver gaps. (Scale bar, 2 μm)

Figure 4 demonstrates a comparison of the yield of gold nanowires obtained by the single- and multisegment methods. These SEM images compare nanowires generated using a single layer (left) and 25 layers (right), respectively. The top images (A) are concentrated nanowire samples at a high magnification while the bottom ones (B) are for a 10-fold diluted sample at a 25-fold lower magnification. Comparison of the left and right images clearly demonstrates the high yield obtained by the multilayer approach in a single experimental run. The center plot demonstrates the estimated yield from nanowire samples obtained using different

numbers of alternating gold-silver layers grown in one AAO template. This plot indicates that the yield scales linearly with the number of layers employed over the entire 1-25 layers range. The yield was estimated by feeding SEM micrographs (with the same acquisition parameters) of the freestanding nanowires from different samples (number of layers= 1, 10, 15, 25) into a Matlab program. The program applied thresholding to the images, then counted the number of white pixels in the image and with proper calibration correlated the number of white pixels to the number of nanowires in the sample. A 25-fold improvement in throughput is thus obtained for a single AAO template.

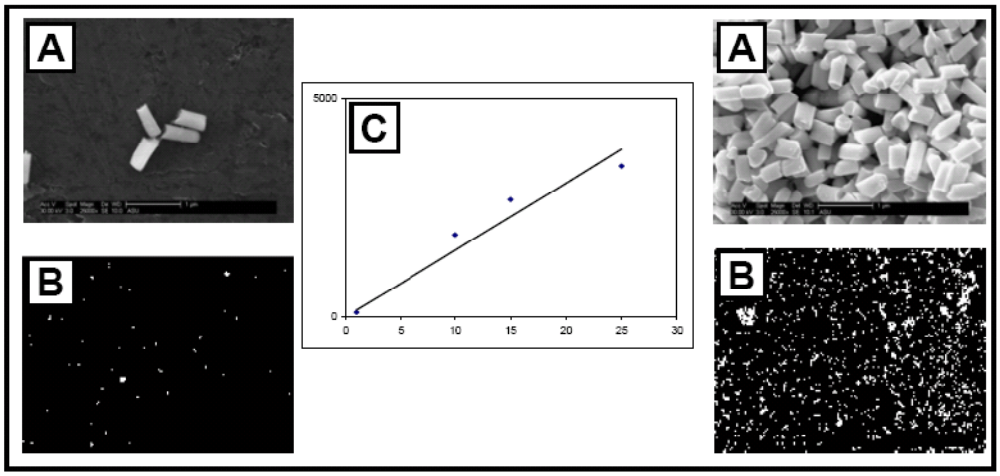

Figure 4.Estimation of the number of nanorods from different multilayer samples.

In addition to the generation of solid gold nanorods/nanowires, high-yield synthesis of porous gold nanorods/nanowires, highlights the versatility of the templated multisegment method. High surface areas of porous, metallic nanowires can be exploited for drug delivery, catalysis, sensing, and energy storage applications. In this method, a single Au-Ag mixture plating solution was

used in connection to different deposition potentials for depositing alternate alloy and silver segments. Following sodium hydroxide-based dissolution of the membrane template, a single nitric-acid treatment was used for dissolving the intermediate silver layers as well as for etching the silver from the alloy segment. Such selective dealloying of the silver resulted in the high-yield generation of porous gold nanorods/nanowires. Figure 5 A and B are grown from a single Au-Ag (85-15%) plating solution by varying the deposition potential between -1.2 V and -0.6 V, respectively. The porosity of such nanowires can also be tailored by controlling the composition of the plating solution[132]. The new high-throughput method therefore allows for the preparation of mixture of nanowires of different porosities, by simply adding gold to the plating solution after deposition of each alloy-silver bisegment.

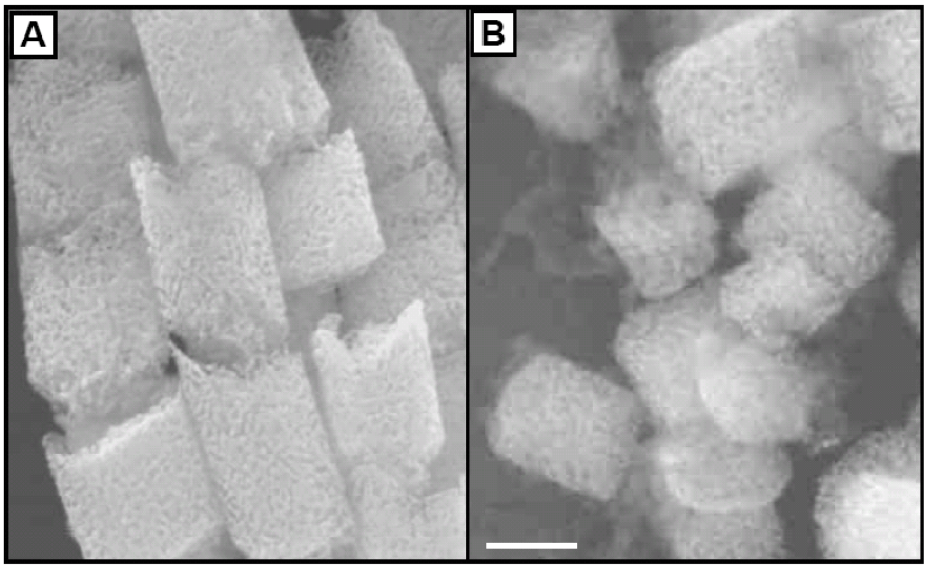

Figure 5.Porous gold nanorods. (Scale bar, 200 nm)

The cost of production of nanorods/nanowires is an important consideration in all practical applications. In order to investigate the cost-effectiveness of the multisegment templated approach, an analysis that compares the material requirements, cost, and time required for generating 25 batches of gold nanowires using the single layer method was carried out, and compared to twenty five gold nanowire segments generated using the multisegmented deposition method. Table 2 compares the materials savings associated with the multisegment templated approach compared to the traditional single-layer method; the gold requirements are the same in both cases since this is the basis of comparison between the two methods. However, approximately 14-fold less silver is required using the multisegment method. The use of a new template membrane for every batch of the single-layer method necessitates the deposition of a sacrificial silver layer for each step; both these add significantly to the material requirements of the traditional method. The multisegment method, on the other hand, uses only one membrane and requires only one sacrificial silver layer. Taken together, the multilayer method results in significant material savings for the number of alumina templates used, the amount of silver plating solution used, and the amount of post growth solution used (not shown).

Table 2. Comparison of materials used in single layer and multisegment method.

		Single Layer Method	Multilayer Method
Volume of Gold per Pore		0.022 μm^3	0.55 μm^3
Volume of Gold per Membrane		0.11 mm^3	2.75 mm^3
Volume of Silver per Pore	(Sacrificial Silver)	0.094 μm^3	0.094 μm^3
	(Silver "gaps")		0.075 μm^3
Volume of Silver per Membrane		0.471 mm^3	0.85 mm^3
Material required toprepare 25 segments of gold nanorods	(Gold)	2.75 mm^3	2.75 mm^3
	(Silver)	**11.78 mm^3**	**0.88 mm**

Table 3 compares the cost requirements for the synthesis of nanowires using the single and multisegment methods. As expected, the cost-effectiveness of the multisegment method scales according to the number of layers employed. In other words, the multisegment method becomes more attractive as the number of layers is increased. For the current process (25 nanowire batches), the multisegment process is cheaper than the single-layer method by a factor of 25 saving up to $155. Finally, the high-throughput nature of the multisegment method results in considerable savings in processing times (Table 4). While the single layer method requires over one day for generating 25 batches of gold nanowires, the multisegment method is capable of accomplishing this task in a matter of 5 hours, resulting in a significant (> 5-fold) saving in processing times (22.5 h).

Table 3.Cost analysis comparing single layer and multisegment methods.

	Single Layer Method	**Multilayer Method**
Membrane cost	$2.5 * 25	$2.5
Gold electrical cost	$4* 25	$4
Gold solution	$0.06	$0.06
Silver solution	$0.25	$0.02
Total	$162.8	$6.6

Table 4.Comparison of processing time using single and multisegment method.

	Single Layer Method	**Multilayer Method**
Gold electrical contact	8 min	8 min
Sacrificial silver layer	20 min	20 min
Gold layer	9 min	9 min
Silver layer		1 min
Gold layer		9 min
Remove alumina	15 min	15 min
Remove silver	15 min	15 min
	*repeat above steps 25 times	*repeat silver and gold layer 24 times
Total	27.9 hr	5.1 hr

Using commercially available alumina membranes, solid and porous nanorod/wires, with a diameter ~200 nm had been successfully synthesized using a high throughput technique. However, smaller sized particles are required for effective endocytosis by epithelial cells and reticuloendothelial clearance[133,134]. As a result, alumina membranes with a pore size of ~30 nm (Figure 6) were generated by anodizing pure (99.99%) aluminum in an acidic electrolyte for preparation of NIR absorbing gold nanorods and bi-segmented gold/polymer nanorods. Porous membranes had been created in slightly soluble electrolytes (e.g. sulfuric, phosphoric, chromic and oxalic acid)[135]. In our case, sulfuric acid

was employed. Upon electrochemical anodization of aluminum, hydrogen evolves at the cathode; oxidization occurs at the anode electrode.

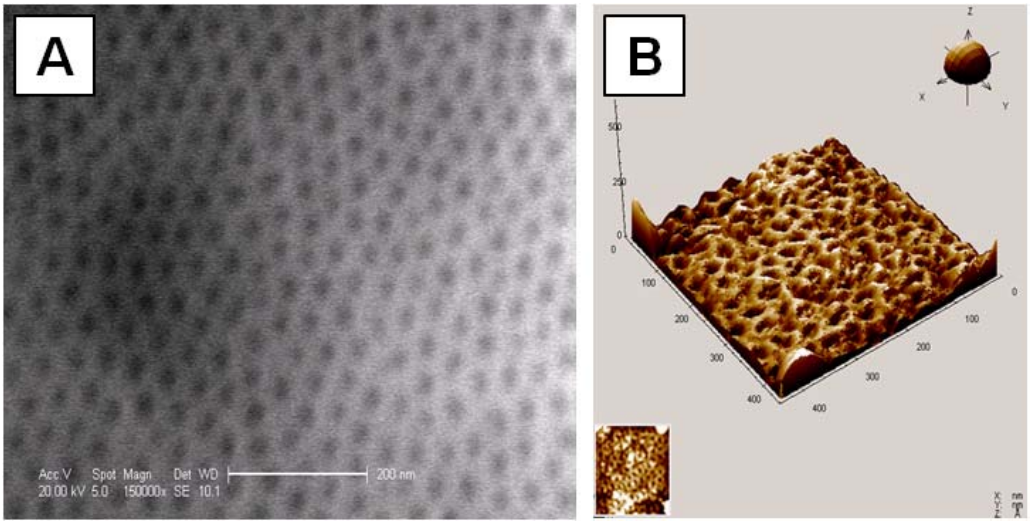

Figure 6.SEM (A) and AFM (B) characterization of alumina membrane template for preparing GNRs. Represented Scale bar 200 nm. Image courtesy of Professor Joseph Wang.

Electrodeposition was carried out to generate smaller sized nanoparticles using these self-prepared porous alumina membranes. Figure 7A shows the SEM image of gold nanorods prepared at a deposit charge at 0.03 Coulombs; Figure 7B shows the spectra of NIR-absorbing gold nanorods at various deposition charges-0.025, 0.03 and 0.07 Coulombs. The relatively poor homogeneity of the nanorod colloid (formed at 0.03 C) in Figure 7A resulted in a broad longitudinal band falling between 650-950 nm (Figure 7B) which can possible limit the efficacy of photothermal effect. However, slight increases in deposition charge resulted in a significant shift of the gold nanorod LSPR spectrum from near to far infra-red as seen in Figure 7B.

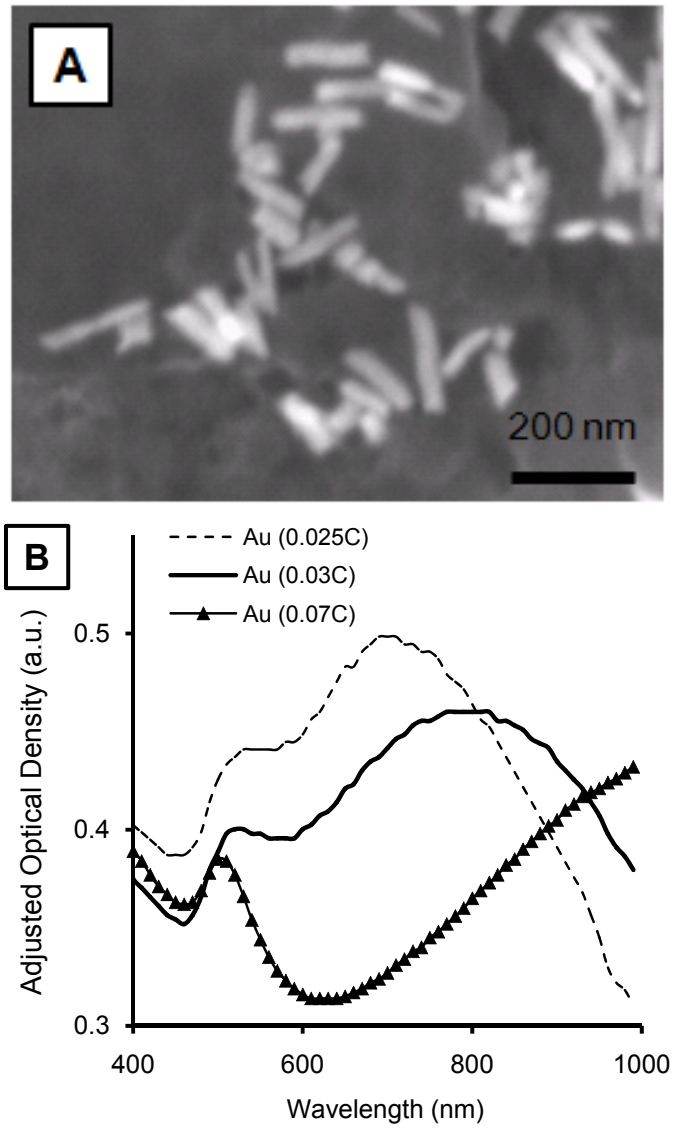

Figure 7.(A) SEM image of GNRs prepared via electrodeposition of gold in alumina template at a deposition charge of 0.03C. (B) Spectra of NIR absorbing gold nanorods at various deposition charges.

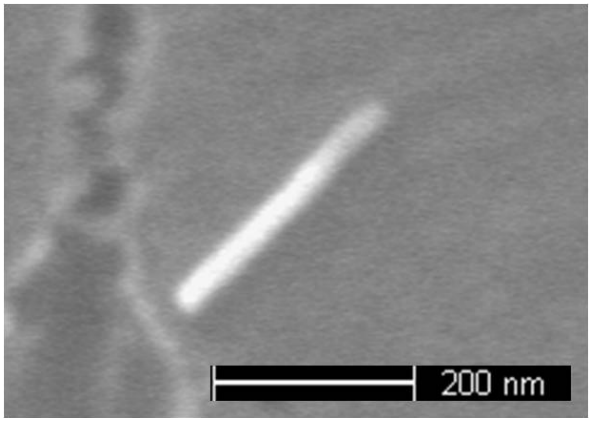

Figure 8.Possible generation of bi-segmented gold (white segment) and polypyrrole-COOH (grey segment) nanorod.

Figure 8 demonstrates the possible generation of bi-segmented gold with polypyrrole-COOH nanorod (further elemental analysis needs to be carried out to verify polypyrrole segment). Moreover, it was found that insufficient stabilization leads to aggregation of gold nanorods, presumably due to high van der Waals interactions between these similar nanoparticles. Taken together, these challenges associated with generation of nanoscale gold rods using template method will require development of more sophisticated synthesis techniques. As a consequence, chemically synthesized GNRs were used for our studies on photothermal ablation of cancer cells. The simplicity of this technique, in concert with reliable optical properties and relative homogeneity of the nanorod population, made it appropriate for our applications.

2.4 Conclusion

In summary, A multisegment template approach for the high-throughput, cost-effective generation of solid and porous gold nanorods/nanowires have been developed. The method results in significant savings in material and processing

costs and overall processing times. While the method has been presented for the generation of gold nanorods/nanowires, the approach can be readily extended to other metals via a judicious selection of the non-desirable gap metals. Additional segments (e.g., nickel) could be added to the gold segment to facilitate magnetic manipulation (for drug delivery and/or imaging applications). It is anticipated that this approach can facilitate larger-scale synthesis of metallic nanorods/nanowires for a variety of biomedical or energy related applications.

CHAPTER

3. Cationic Polymer Coated Nanorods for Photothermal Ablation and Non-viral Gene Delivery

3.1 Introduction

Nanoparticles have the potential to transform medicine by impacting therapeutics, drug delivery platforms, imaging agents, and diagnostics[136-140]. Unique optical and photothermal properties of gold nanoparticles make them attractive candidates drug delivery and near infrared (NIR) bio-imaging applications. As described previously, gold nanorods posses a tunable photothermal response in the near infrared (NIR) region based on nanoparticle aspect ratio[141,142]. In addition, gold nanorods have been employed in diagnostics[143,144], therapeutic systems[145-148], imaging[149], sensing[150-152], and responsive materials / assemblies[153,154].

In Chapter 2, high throughput template technique was implemented to generate rod-shaped nanoparticles leading to increased throughput and decreased cost. However, the heterogeneity and instability of the smaller sized gold nanorods synthesized via template electrodeposition could limit their applications. Therefore, this chapter focuses on the investigation of the stabilization of chemically (seed growth method) synthesized gold nanorods using polymers for photothermal ablation and gene delivery.

The seed growth method, also known as cetyltrimethyl ammonium bromide (CTAB)-templated growth, is one of the most widely used technique for making homogeneous gold nanorods (GNRs) colloids[155]. GNRs with peak longitudinal wavelengths in the visual and near-infrared region of the absorption spectrum can be reproducibly synthesized using this method. The stability of gold nanorods is maintained via CTAB molecules that form a bilayer 'shell' around the gold nanorod 'core'. The electrostatic repulsion between the cationic quaternary ammonium head groups of the CTAB surfactant results in stable gold nanorod dispersions in aqueous media. However, due to the high toxicity of CTAB molecules, various modification strategies[156-162], have been demonstrated to replace CTAB on nanorods in order to improve biocompatibility and reduce toxicity of gold nanorods for biological applications[156,163].

This chapter describes that cetyltrimethyl ammonium bromide (CTAB)-based gold nanorods, prepared by the commonly used seed-mediated method, demonstrate poor stability in phosphate buffered saline (PBS), serum-free media (SFM) and serum-containing media (SCM), depending on the number of centrifugation steps carried out to remove excess CTAB from the dispersion. Layer-by-layer deposition[164] of cationic polymers (polyelectrolytes) generated in our laboratory[165] was used in order to increase the short-term and long-term stability of gold nanorods in biological media. Polyelectrolyte-coated gold nanorods exhibit excellent long-term optical stability in all three biologically media even after four weeks of storage. In addition, stabilization of the optical response resulted in a reliable, photothermal response of the well-dispersed gold nanorods

over the period of investigation. Cytotoxicity evaluation indicated that gold nanorods coated with these polymers were less cytotoxic to mammalian cells than those covered with 25kDa polyethyleneimine (pEI25). Stable and biocompatible polyelectrolyte-coated nanorods were investigated for the photothermal ablation of PC3-PSMA cells using NIR laser irradiation. Sub-toxic concentrations of these nanorods were also employed for delivering plasmid DNA to these cells. Coating with cationic polyelectrolytes can lead to stable, biocompatible gold nanorod assemblies that can be useful for a variety of applications including non-viral gene delivery and photothermal ablation of cancer cells.

3.2 Materials and Methods

3.2.1 Materials

Sodium borohydride, powder, reagent grade, ≥98.5%, cetyl trimethylammonium bromide (CTAB), 95%, gold (III) chloride trihydrate ($HAuCl_4 \cdot 3H_2O$), 99.9+%, L-ascorbic acid, reagent grade, ethyleneglycol diglycidyl ether (EDGE) and 3,3'-diamino-N-methyl dipropylamine (3,3'), and branched poly(ethyleneimine) (M_W = 25,000, M_N = 10,000; henceforth called pEI25) were purchased from Sigma-Aldrich. Crystalline silver nitrate was purchased from Spectrum and poly(styrene sulfonate, sodium salt; henceforth called PSS) (MW14,900) was purchased from Polysciences, Inc. All chemicals were used as received without further purification.

3.2.2 Generation of Gold Nanorods (GNRs)

Gold nanorods were synthesized using the seed-mediated method as reported by El-Sayed et al.[155] First, a seed solution was prepared by adding 0.6 mL iced water-cooled sodium borohydride (0.01 M) in order to reduce a solution of 5 mL CTAB (0.2 M) (cetyl trimethylammonium bromide) in 5mL auric acid (0.0005 M) ($HAuCl_4.3H_2O$). Secondly, the growth solution was prepared by 70 µL L-ascorbic acid (0.0788 M) reduction of 5 mL CTAB (0.2 M) in 5mL auric acid (0.001 M) ($HAuCl_4.3H_2O$) containing 250 µL silver nitrate (0.004 M). Seed solution (12 µl) was introduced to a 10 mL growth solution which resulted in the generation of gold nanorods after four hours of continuous stirring (250 rpm) at 29°C. Gold nanorods that possessed absorbance maxima (λ_{max}) at different wavelengths (750-900 nm) in the near infrared (NIR) region of the absorption spectrum were generated by slightly tuning silver nitrate amount (250-290 µL) in this method.

3.2.3 Polymer Synthesis and Characterization

Polymerizations were carried out as described previously in collaboration with Sutapa Barua[165]. Briefly, ethyleneglycol diglycidylether (EGDE; 2.3 mmol) was reacted with equimolar quantities of 3,3'-diamino-N-methyl dipropylamine (3,3') resulting in the formation of the EGDE-3,3' cationic polymer[165]. Neat, as-purchased solutions were employed in the polymerization reaction, which was carried out in 7 mL glass scintillation vials for 16h. Following completion of the reaction, the resulting polymer was diluted to a concentration of 2 mg/mL in phosphate-buffered saline (0.01 X PBS, 1X PBS diluted 100 fold; pH=7.4, final salt concentration 1.5 mM). The solution pH was adjusted to 7.4 using 30 vol% hydrochloric acid in deionized (DI) water in order to compensate for the basicity

of the cationic polymer. Polymer formation was confirmed using Fourier Transform Infrared (FT-IR) spectroscopy and the molecular weight was determined using gel-permeation chromatography as described previously[165].

3.2.4 Generation of Polyelectrolyte (PE) Gold Nanorods (PE-GNRs) Dispersion

Gold nanorods were coated with polyelectrolytes (PEs) using a layer-by-layer deposition approach. Briefly, gold nanorods ($OD_{\lambda max}$= 0.5), in 1.5 mL microcentrifuge tubes, were first centrifuged at 6000 rcf for 10 min using a Microfuge 18 Centrifuge (Beckman Coulter) in order to remove excess CTAB. Following removal of the supernatant, nanorods were resuspended in 0.5 mL of poly(styrene sulfonate) or PSS solution (2 mg/mL PSS in 0.01X PBS; ~1.5mM salt concentration) and were immediately sonicated for 25 min leading to the formation of PSS-CTAB-GNRs. Excess PSS was removed by centrifugation at 6000 rcf for 10 min, and different amounts of cationic polyelectrolytes, either pEI25 or EGDE-3,3' polymer, were added and sonicated for 25 minutes, leading to the formation of pEI25-PSS-CTAB-GNRs or EGDE3,3'-PSS-CTAB-GNRs. Finally, cationic polyelectrolyte coated gold nanorods (PE-GNRs) were centrifuged and re-suspended in different aqueous media (DI Water, PBS, serum-free media, or serum-containing media) to monitor their stability. The conditions for generating these different PE-GNRs are summarized in Table 5.

Table 5.Composition of the PE-GNR assemblies employed for study.

First Layer Polyelectrolyte	Polyelectrolyte Concentration (mg / mL)	Second Layer Polyelectrolyte	Polyelectrolyte Concentration (mg / mL)					
PSS	2	EGDE-3,3'	0	0.2	0.4	1	2	3
PSS	2	25kDa pEI	0.2	0.4	1	2	3	4

3.2.5 Determination of Short- and Long-Term Optical Stability

CTAB-gold nanorods with optical density 0.5 at 800 nm were first prepared and dispersed in deionized (DI) water using the seed-mediated method. Aliquots (0.5 mL) of CTAB gold nanorods, placed in 1.5 mL centrifuge tubes, were centrifuged and resuspended in the same volume of DI water, 1X PBS, serum-free medium (SFM) or serum-containing medium (SCM). Absorption spectra were determined at different times using a temperature-controlled plate reader (Biotek Synergy 2) for up to 48 h; spectra were typically measured between 400-999 nm. Absorbance spectra were monitored every week for a period of four weeks as described above for long -term optical stability studies.

3.2.6 Determination of Photothermal Response

Dispersions of CTAB- (1 h) or PE-coated (1 h and 4 weeks) gold nanorods in serum free media (RPMI-1640 medium plus 1% penicillin / streptomycin) were employed for determining the temperature response of gold nanorods following exposure to near-infrared (NIR) laser treatment. Stable, EGDE3,3'-PSS-CTAB-gold nanorods were prepared and diluted to form a stock solution with a maximum optical density of 0.22 at 770 nm (maximal absorbance wavelength). A titanium CW sapphire (Ti:S) laser (Spectra-Physics, Tsunami) pumped by a solid

state laser (Spectra-Physics, Millennia) was used for determining the photothermal response. Samples were diluted and placed in a 96 well plate (diameter ~6.4 mm, height ~10.7 mm) in the path of the laser (diameter of the laser spot was 2 mm). The laser was turned on for 15 min and the temperature of the dispersion was monitored using a k-type thermocouple; laser output was fixed at 600 mW (20 W/cm^2).

3.2.7 Cell Culture

RPMI 1640 with L-Glutamine and HEPES (RPMI-1640 medium), Pen-Strep Solution: 10,000 units /mL Penicillin and 10,000 µg/mL Streptomycin in 0.85% NaCl, and fetal bovine serum (FBS) were purchased from Hyclone. Serum-free medium (SFM) is RPMI-1640 medium plus 1% antibiotics. Serum-containing medium is SFM plus 10% FBS. The PC3-PSMA human prostate cancer cell line[166] was a generous gift from Dr. Michel Sadelain of the Memorial Sloan Cancer Center, New York, NY. Cells were cultured in a 5% CO2 incubator at 37^{o}C using RPMI-1640 medium containing 10% heat-inactivated fetal bovine serum (FBS) and 1% antibiotics (10,000 units /mL penicillin G and 10,000 µg/mL streptomycin).

3.2.8 Cytotoxicity of Polyelectrolyte (PE)-Coated Gold Nanorods

Stable polyelectrolyte (EGDE3,3'-PSS-CTAB and pEI25-PSS-CTAB) gold nanorods with absorbance maximum at 770 nm were prepared as described above. PC3-PSMA human prostate cancer cells were seeded in a 24 well plate with a density of 50,000 cells per well and allowed to attach overnight at 37°C, in

a 5% CO_2 incubator. Different amounts of polyelectrolyte-coated gold nanorods (PE-GNRs, dispersed in serum-free media) were added into each well and the final volume in each well was brought up to 500 µL with serum-free media. Cells were incubated for 5 h to determine the cytotoxicity of PE-GNR assemblies. Following incubation, cells were treated with 100µL of 4µM ethidium homodimer-1 (EthD-1; Invitrogen) and 2µM Calcein AM (Invitrogen) for 30 min and imaged immediately using Zeiss AxioObserver D1 inverted microscope (10 × X/0.3 numerical aperture (NA) objective; Carl Zeiss MicroImaging Inc., Germany). Fluorescence using excitation at 530 nm and emission at 645 nm were used for the microscopy; dead/dying cells with compromised nuclei stained positive (red) for EthD-1. Quantitative analyses of PE-GNR induced cell death were carried out by manually counting the number of dead cells in all cases using the Cell Counter plug-in in ImageJ software (Rasband, W. S., ImageJ, U.S. National Institutes of Health, Bethesda, MD, http://rsb.info.nih.gov/ij/, 1997-2005). The number of dead cells in both live and dead controls was determined for at least two independent experiments, and their average values were calculated. The number and percentage of red fluorescent cells was determined for each concentration of PE-GNR assemblies as a function of dose.

3.2.9 Photothermal Ablation of PC3-PSMA Cells using EGDE3,3'-PSS-CTAB-GNRs

Stable polyelectrolyte gold nanorods (EGDE3,3'-PSS-CTAB-GNR) with an optical density 0.2 at 800 nm were prepared as described above. PC3-PSMA human prostate cancer cells were seeded in a 96 well plate with a density of

30,000 cells/well and allowed to attach overnight at 37°C, in a 5% CO_2 incubator. PE-GNRs (EGDE3,3'-PSS-CTAB-GNR) were diluted to an optical density of 0.1 with serum-free media. The laser excitation source was tuned to 800 nm in order to coincide with the longitudinal absorption maximum of the EGDE3,3'-PSS-CTAB-GNR. First, cell culture media was replaced by 200 µl of EGDE3,3'-PSS-CTAB-GNR solution (OD_{800}= 0.1) followed by exposure to laser irradiation for 7 min at different power densities (7.5 - 25 W/cm^2). The temperature of the dispersion was measured using a K-type thermocouple immediately after removal of the laser treatment. Following treatment, EGDE3,3'-PSS-CTAB-GNR containing media was removed and immediately replaced with fresh serum-containing cell culture media and the cells were returned to the 37°C incubator. After 24 h, cells were treated with 4 µM ethidium homodimer-1 (EthD-1; Invitrogen) for 30 min and imaged using Zeiss AxioObserver D1 inverted microscope (10 × X/0.3 numerical aperture (NA) objective; Carl Zeiss MicroImaging Inc., Germany). Fluorescence using excitation at 530 nm and emission at 645 nm were used for the microscopy; dead/dying cells with compromised nuclei stained positive (red) for EthD-1. Quantitative analysis of PE-GNR induced cell death was carried out by manually counting the number of dead cells in all cases using the Cell Counter plug-in in ImageJ software (Rasband, W. S., ImageJ, U.S. National Institutes of Health, Bethesda, MD, http://rsb.info.nih.gov/ij/, 1997-2005). The number of dead cells in both live and dead controls was determined for at least two independent experiments, and their average values were calculated.

3.2.10 Transfection of PC3-PSMA Cells using PE-GNRs

3.2.10.1 Plasmid DNA Loading on PE-GNRs

The pGL3 control vector (Promega Corp., Madison, WI), which encodes for the modified firefly luciferase protein under the control of an SV40 promoter, was used in transfection experiments. E.coli (XL1 Blue) cells containing the pGL3 plasmid DNA were cultured overnight (16 h, 37 °C, 150 rpm) in 15 mL tubes (Fisher) in 5 mL Terrific Broth (MP Biomedicals, LLC) containing 1 mg/mL ampicillin (Research Products International, Corp.). The cultures were then centrifuged at 5400 g and 4°C for 10 min. Plasmid DNA was purified according to the QIAprep Miniprep Kit (Qiagen®) protocol and DNA concentration and purity were determined based on absorbance at 260 and 280 nm determined using NanoDrop Spectrophotometer (ND-1000; NanoDrop Technologies). Plasmid DNA concentrations of 100-130 ng/µl were used in all experiments and the volume was adjusted in order to load 350 ng of plasmid on PE-GNRs prior to transfection. PE-GNRs (optical density 0.25 * 10-2) were mixed with 350 ng pGL3 plasmid DNA in the presence of serum-free media for 30 min. The PE-GNR-pGL3 plasmid assemblies were then centrifuged at 6,000 rcf for 10 min. The plasmid amount of DNA remaining in the supernatant after centrifugation was determined using calibration of fluorescence intensity vs. plasmid DNA concentration (not shown); ethidium bromide was used for calibrating DNA amounts.

3.2.10.2 Transfections

Cellular transfection was carried out in collaboration with Sutapa Barua. PC3-PSMA cells were seeded in 24-well plates (Costar) at a density of50,000cells/well and allowed to attach overnight. PE-GNR-pGL3 plasmid assemblies were added to each well in the presence of serum-free media for 6 h; CTAB-GNRs with equivalent amounts of plasmid DNA were used as controls. The media was then replaced with serum-containing media for 48 h following which cells were permeabilized with 100 µL of cell lysis buffer (Promega, Madison, WI). The luciferase activity in cell lysates was measured using a luciferase assay kit (Promega, Madison, WI) using a plate reader (Bio-Tek Synergy 2). The relative light units (RLU) determined from the assay were normalized with respect to protein concentration in the cell lysates, measured using the Pierce® BCA Protein Assay Kit (Pierce Biotechnology, Rockford, IL). Luciferase activity in cell lysates was expressed as relative light units (RLU) per milligram (mg) of protein. Transfection experiments were performed at least in triplicate.

3.3 Results and Discussion

3.3.1 Polyelectrolytes Enhanced Short-Term and Long-Term Stability of Gold Nanorods Dispersed in Biologically Relevant Media

The short-term stability of as-prepared CTAB gold nanorods (CTAB-GNRs) was investigated in four different aqueous biologically relevant media: de-ionized (DI) water, phosphate-buffered saline (PBS), serum-free media (RPMI-1640) and serum-containing media (RPMI-1640 + 10% fetal bovine serum or FBS). The nanorods were centrifuged once as part of the synthesis protocol and

resuspended in equivalent volumes of the respective media in order to remove excess CTAB and prevent CTAB crystallization in the aqueous dispersion at ambient temperature. The short-term optical stability was determined by monitoring the longitudinal peak in the near infrared region of the absorbance spectrum as a function of time for 48 h. Gold nanorods dispersions demonstrated excellent stability in DI water (Figure 9A) and in serum-containing media (SCM; Figure 9D); the longitudinal peak was maintained over the period of the investigation (48h). It is possible that interactions with serum proteins (e.g. albumin) resulted in enhanced stability of gold nanorods in serum-containing media[167,168]. However, the absorbance of CTAB-GNRs decreased rapidly in PBS (Figure 9B) and serum-free media (SFM; Figure 9C). A 30-40% decrease of the absorbance values of the initial values was observed two hours of dispersion in the two media, indicating rapid nanorod aggregation in PBS and SFM. The aggregation is induced presumably due to the higher salt concentration (~150 mM) of these solutions, which screened repulsive interactions between individual CTAB-covered nanorods.

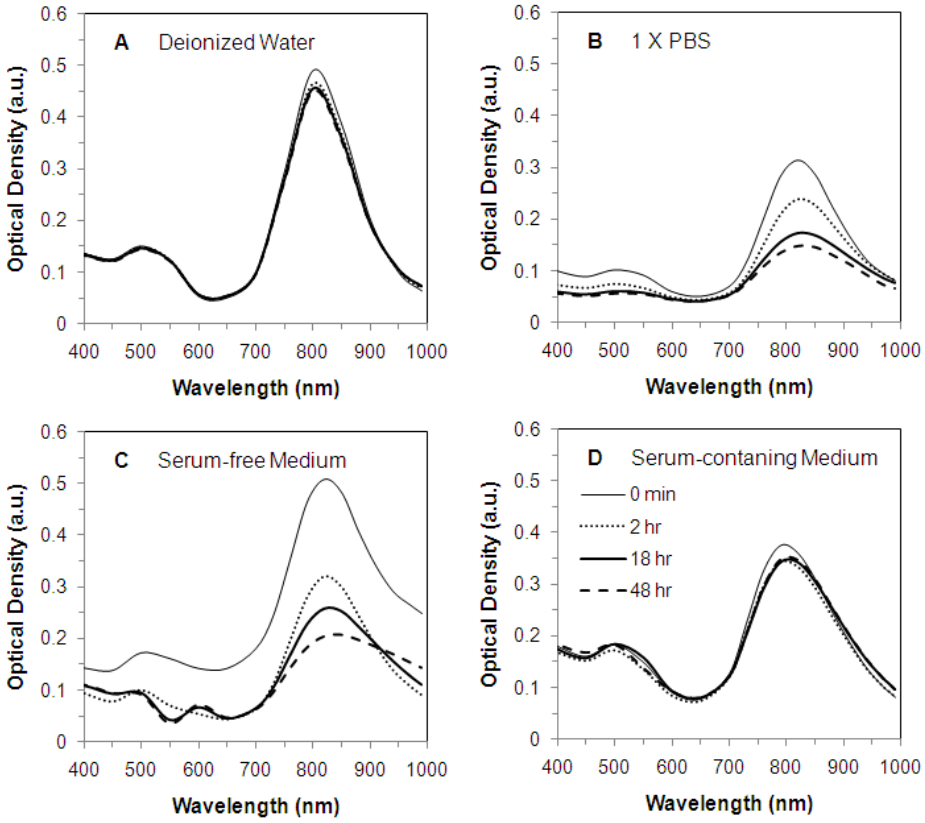

Figure 9.Short-term optical stability of CTAB-gold nanorods (CTAB-GNRs) dispersed in different biologically relevant media.
CTAB-GNRs, optical density 0.5 at 800 nm, were centrifuged once and resuspended in same volume of (A) deionized or DI water, (B), phosphate-buffered saline (PBS) (C) serum-free medium, and (D) serum-containing medium. Absorbance spectra were monitored from 400 nm to 999 nm for up to 48 h in respective media.

Multiple centrifugation rounds are thought to be necessary to successfully remove excess CTAB from gold nanorod dispersions[5]. However, removal of CTAB molecules self-assembled on the surface of the gold nanorods results in aggregation and loss of stability of the nanoparticles. I investigated the role of subsequent centrifugation rounds on the stability of CTAB-GNRs in aqueous media. In this case, long-term (up to four weeks; Figure 10) stability of CTAB-GNRs following two additional rounds of centrifugation was monitored. While

CTAB-GNRs maintained stable in DI water, aggregation occurred in PBS, SFM, and SCM after a total of three times centrifugation (including the one round necessary in the preparation of gold nanorods), leading to a complete loss of their light absorption properties in the near infrared region (Figure 10). While the stability of CTAB-GNRs is excellent in DI water, their poor stability in biological media can limit their utility in biological applications.

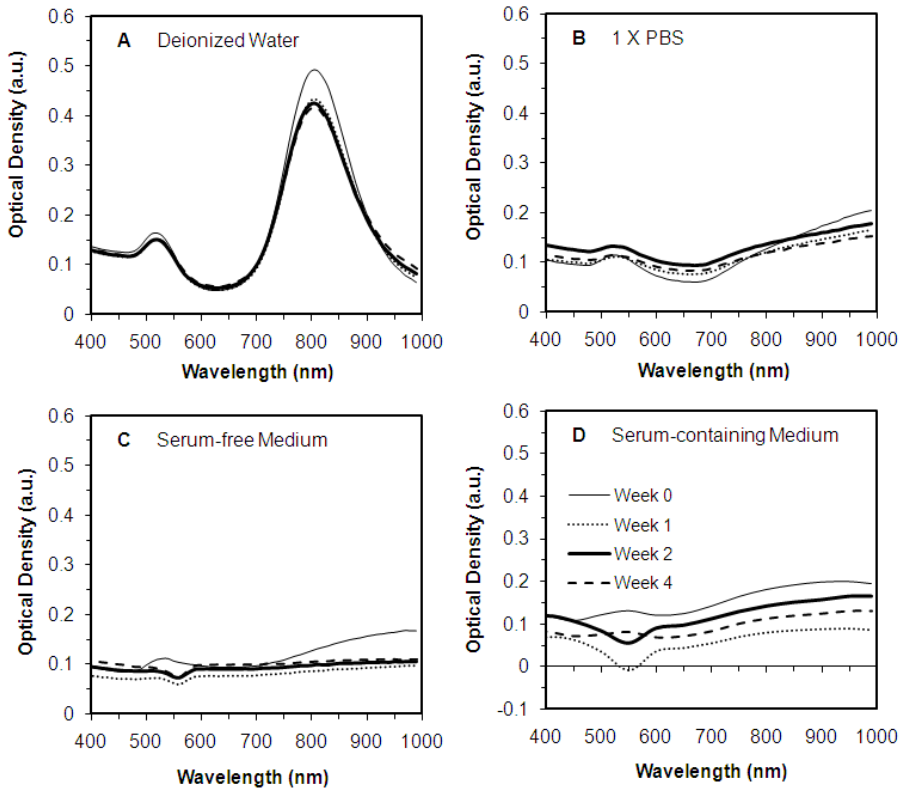

Figure 10.Long-term UV-visible spectrums of CTAB-GNRs dispersed in different biologically relevant media.
CTAB-GNRs, optical density 0.5 at 800 nm were centrifuged three times and resuspended in same volume of (A) deionized water, (B) PBS and (C) serum-free medium, and (D) serum-containing medium. Spectra were measured immediately following preparation ("Week 0"), 1, 2, and 4 weeks after preparation. Similar results were seen with GNRs with a maximal absorption peak at 750 nm.

Various strategies have been reported for enhancing the stability of nanoparticles in aqueous media. For example, self-assembly / conjugation with polyethylene glycol (PEGylation) is a widely used method for enhancing nanoparticle stability and increasing biocompatibility[169]. Unfortunately, the presence of PEG on nanoparticle surface results in reduced interactions with proteins and uptake by cells[169]. This is not desirable in cases where the nanorods might be employed for applications which require cellular binding and uptake (e.g. gene delivery). It was hypothesized that coating CTAB-GNRs with cationic polyelectrolyte layers could result in stable dispersions of gold nanorods that also demonstrate high gene delivery and photothermal ablation efficacies. Cationic polymers developed in our laboratory were employed for this purpose.

CTAB-GNRs were first coated with the anionic polymer poly(styrene sulfonate) (PSS); free PSS was removed by centrifugation of the resulting PSS-CTAB-GNRs followed by removal of supernatant. The PSS-CTAB-GNRs were then resuspended in solutions containing different concentrations of the cationic polymers pEI25 or EGDE-3,3' (prepared in our laboratory) in 0.01 X PBS (PBS diluted 100 fold; pH=7.4, final salt concentration 1.5 mM) leading to the formation of pEI25-PSS-CTAB-GNRs or EGDE3,3'-PSS-CTAB-GNRs. The EGDE-3,3' cationic polyelectrolyte was generated using the ring opening polymerization of ethyleneglycol diglycidylether and 3,3'-diamino-N-methyl dipropylamine as described previously[165]. Following equilibration with PSS-CTAB-GNRs, excess cationic polymer was removed by centrifugation and the polyelectrolyte-nanorod assemblies were dispersed in serum-free medium in order to investigate their

optical stability. The use of low concentrations of the EGDE-3,3'polymer did not enhance the stability of the gold nanorods (Figures 11A and 11B), which aggregated presumably due to bridging between the PSS layer and EGDE-3,3'polymer layer between different nanorods leading to loss of the longitudinal peak in the NIR region. However, 'recovery' of the NIR peak was made possible by increasing the concentration of the EGDE-3,3' polymer (Figures 11C and 11D). Increasing EGDE-3,3' polymer adsorption on PSS-CTAB-GNRs leads to inter-particle repulsion due to an increase in cationic charges on the surface, and therefore, results in enhanced stability of the GNR dispersion. The short-term stability of these dispersions was significantly enhanced at EGDE-3,3' polymer concentration at 3 mg/mL compared to CTAB-GNRs (Figure 11D).

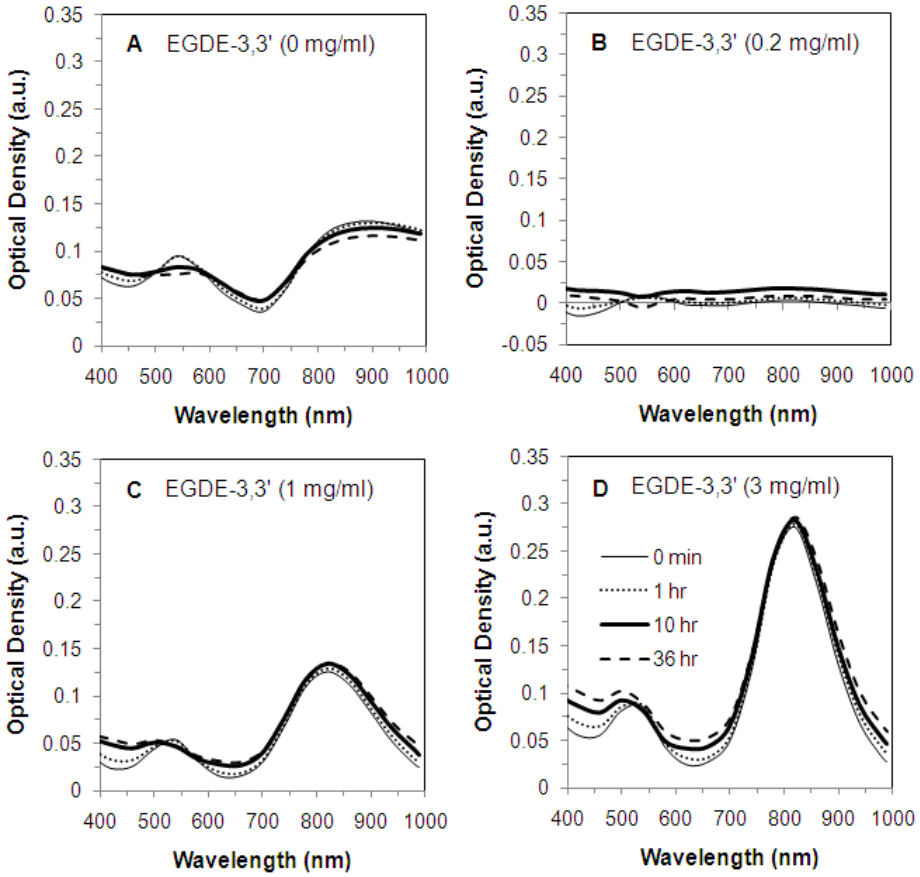

Figure 11.Stability of EGDE3,3'-PSS-CTAB-GNRs, in serum free media (SFM) as monitored by the transverse and longitudinal absorption peaks.
CTAB nanorods were coated with the anionic polyelectrolyte PSS (2mg/mL), followed by coating with different concentrations of EGDE-3,3' cationic polyelectrolytes, (A) 0 mg/mL, (B) 0.2 mg/mL, (C) 1 mg/mL, and (D) 3 mg/mLEGDE-3,3' polymer. The absorption spectra of polyelectrolyte-coated GNRs were monitored for up to 36 h using a temperature-controlled plate reader. See Experimental section for details.

Similar trend was found with using another cationic polymer, 25 kDa polyethyleneimine (pEI25), for stabilizing GNRs (Figures 12A-D). Low concentrations of pEI25 resulted in aggregation and loss of the NIR absorption peak due to bridging with the anionic PSS layers, while stable pEI25-PSS-CTAB-GNRs dispersions were formed in the media with an increase in pEI25

concentration. The amount of cationic polyelectrolyte required for NIR peak recovery was similar in cases of both, the EGDE-3,3' polymer and pEI25.

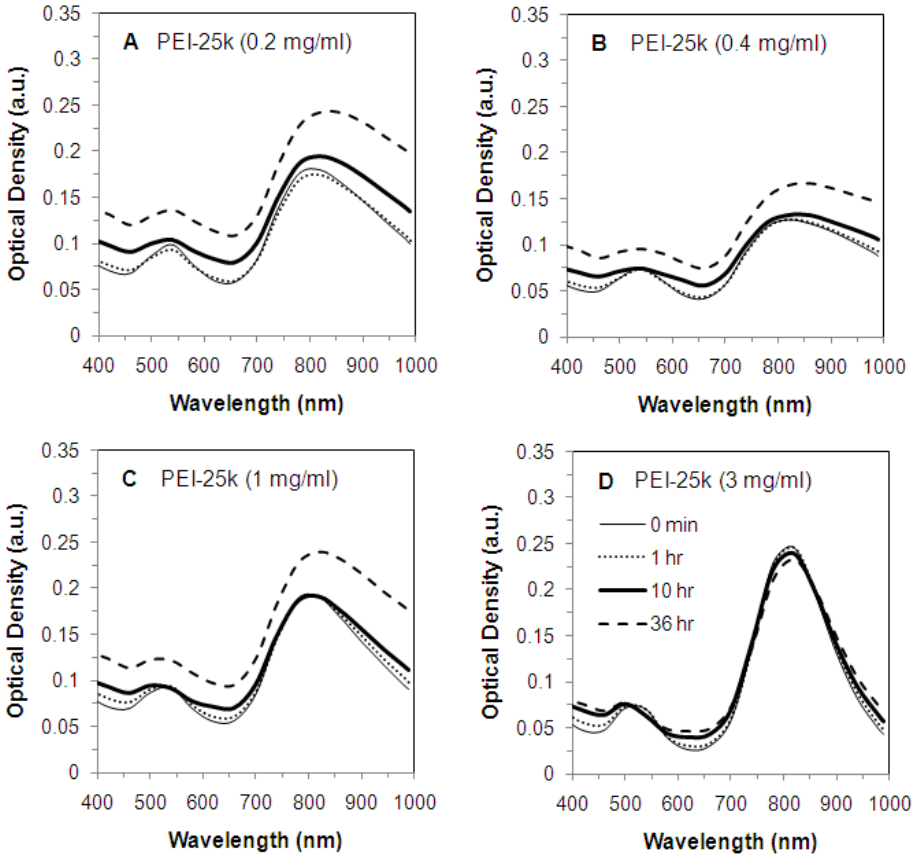

Figure 12.Stability of pEI25-PSS-CTAB-GNRs in serum free media as monitored by the transverse and longitudinal absorption peaks.
CTAB-gold nanorods were coated with the anionic polyelectrolyte PSS (2mg/mL), followed by coating with different concentrations of pEI25cationic polyelectrolytes, (A) 0.2 mg/mL, (B) 0.4 mg/mL, (C) 1 mg/mL, and (D) 3 mg/mL, pEI-25k polymer. The absorption spectra of polyelectrolyte-coated GNRs were monitored for up to 36 h using a temperature-controlled plate reader. See Experimental section for details.

In addition to the study of short-term stability with PE-GNR assemblies, polyelectrolytes were investigated for maintaining the longer-term stability of nanorod dispersions. The NIR light absorption properties of EGDE-3,3' and

pEI25-based gold nanorods remained invariant over a period of four weeks in serum-free media (Figure 13A and13B). The near-infrared (NIR) absorption peak (~770 nm) was maximal following immediate preparation of the nanorods (0 day) in serum-containing media. However, the peak absorbance value settled to a lower maximum in one week and was found to be stable thereafter. It is possible that serum-polyelectrolyte interactions result in the precipitation of a portion of the nanorods dispersed in serum-containing media over the period of one week, leading to a reduction in the NIR peak absorbance. Taken together, it can be seen that polyelectrolytes stabilize gold nanorod dispersions in both serum-free and serum-containing media over extended periods of time, making this a viable strategy for their use in biological applications.

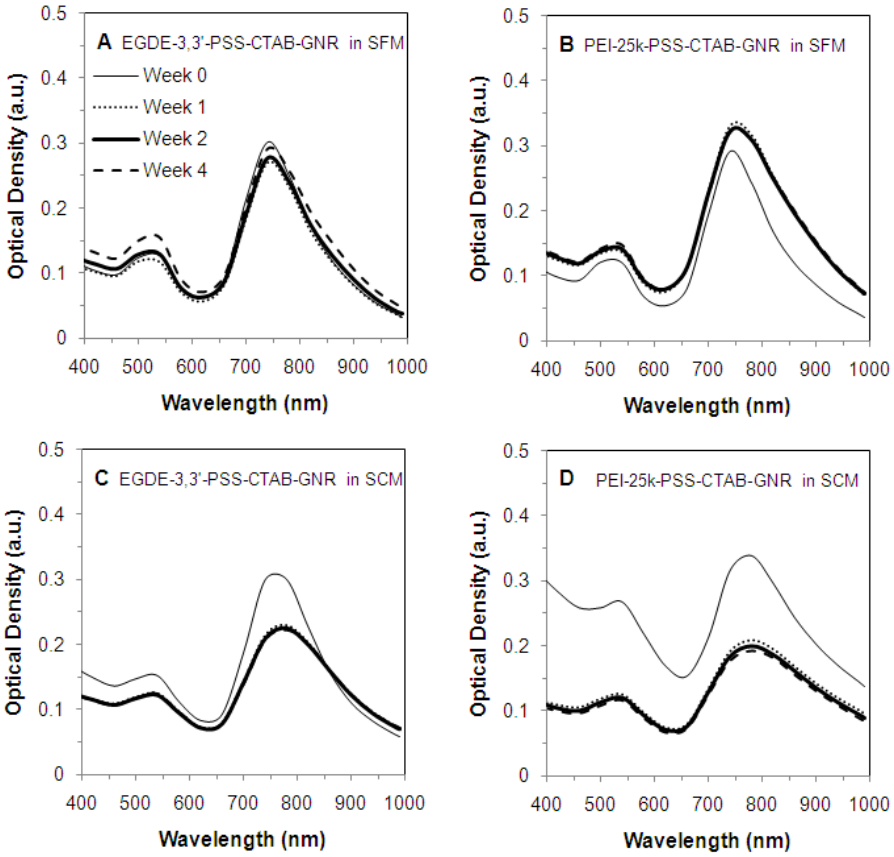

Figure 13.Long term UV-visible spectra of polyelectrolyte–coated gold nanorods dispersed in serum-free media and serum-containing media
EGDE3.3'-PSS-CTAB-GNRs (λ_{max} = 770 nm) dispersed in serum-free media (A) and serum-containing media (C); pEI25k-PSS-CTAB-GNRs dispersed in serum-free media (B) and serum-containing media (D).

3.3.2 EGDE3,3'-PSS-CTAB-GNRs Demonstrate Lower Cytotoxicities that pEI25-PSS-CTAB-GNRs

The cytotoxicity of pEI25-PSS-CTAB-GNRs compared to that of EGDE3,3'-PSS-CTAB-GNRs with PC3-PSMA human prostate cancer cells was evaluated. Following treatment with different PE-GNR concentrations (Figure 14 (i)), cells were treated with ethidium homodimer which fluoresces red in dead/dying cells; and the phase contrast and fluorescence microscopy images of cells were collected (Figures 14 (ii) and 14 (iii)). In figures 14 (ii) – 14 (iv), EGDE3,3'-coated

GNRs demonstrated less toxicity than pEI25-coated GNRs, indicating that the candidate from a recently generated polymer library in our laboratory[165] is less cytotoxic than pEI25, which is a standard for polymer-mediated gene delivery. Moreover, it was observed that EGDE3,3'-coated GNRs were more toxic than as-prepared CTAB-GNRs (centrifuged once) at comparable optical densities (not shown). It is possible that the aggregation of CTAB-GNRs reduces the interaction of surface CTAB molecules with cells and also reduces uptake due to increased size, which lower overall cytotoxicities.

(i)

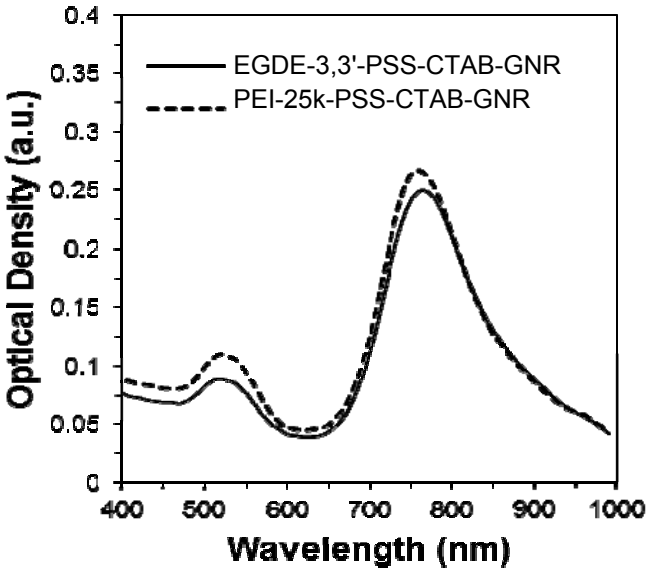

(ii)

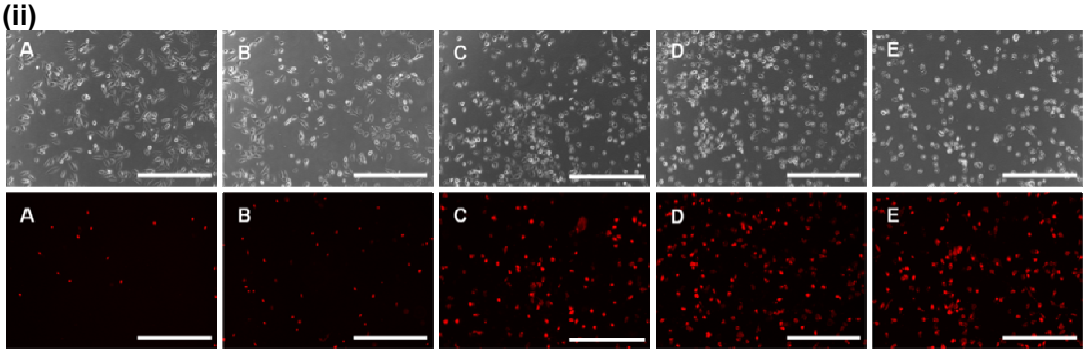

(iii)

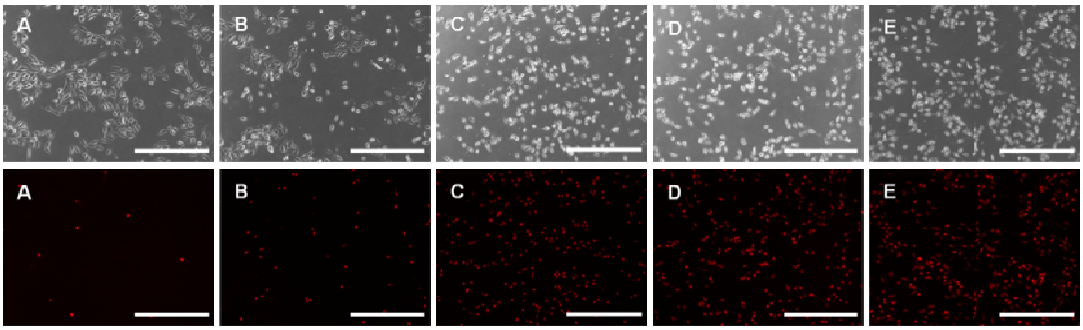

(iv)

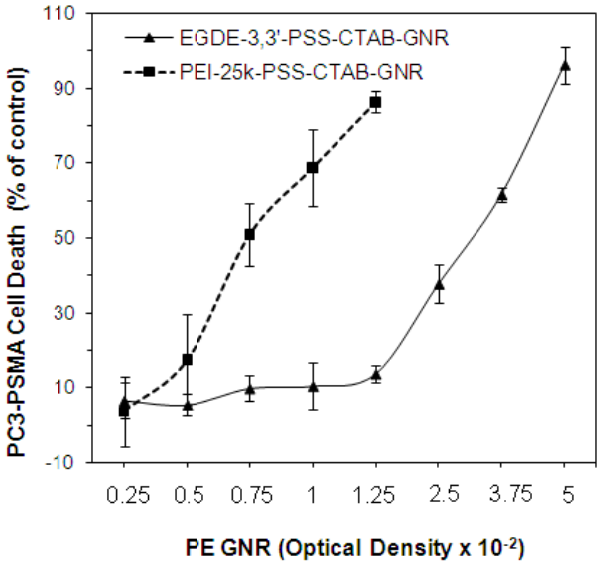

Figure 14.Cytotoxicity of polyelectrolyte-coated gold nanorods (PE-GNRs). (i) Absorption spectra of PE-coated nanorods employed in the cytotoxicity analysis.(ii) Phase contrast and fluorescence microscopy images that show the cytotoxicity of EGDE-3,3'-PSS-GNRs, toward PC3-PSMA cells. Red fluorescent ethidium homodimer-1, which stains DNA in compromised (dead) nuclei, was used to determine cytotoxicity following 6 h treatment. A total of 10, 25, 50, 75 and 100 µL of EGDE-3,3'-PSS-CTAB-GNRs (optical density = 0.25), were added to cells. The final volume in each well was brought up to 500 µL, resulting in final optical densities of A: 0.005, B: 0.0125, C: 0.025, D: 0.0375, and E: 0.05. Scale bar: 500 µm.(iii) Phase-contrast and fluorescence microscopy images that show the cytotoxicity of pEI25-PSS GNRs. A: 5 µL (O.D.=0.0025), B: 10 µL (O.D.=0.005), C: 15 µL (O.D.=0.0075), D: 20 µL (O.D.=0.01), and E 25 µL (O.D.=0.0125), of pEI25-PSS-GNRs. Other conditions are similar to those described above. Scale bar: 500 µm. (iv) Comparison of cytotoxicity of pEI25-PSS-CTAB-GNRs and EGDE3,3'-PSS-CTAB-GNRs as a function of PE-GNR optical density.

3.3.3 Polyelectrolytes Maintain Long-Term Photothermal Activity of GNRs

In order to determine if increased stability resulted in stable photothermal properties over a period of time, the photothermal response of PE-GNRs were determined both, one hour after preparation as well as after four weeks of storage in serum-free media. PE-stabilized gold nanorods demonstrated a reproducible photothermal response as a function of the nanorod concentration in the dispersion (Figure 15). The temperature of the media rose rapidly in the first five minutes of laser exposure after which, the temperature either rose gradually as in the case of higher nanorod concentrations or remained invariant as in the case of lower nanorod concentrations. Interestingly, the steady-state temperature of the dispersion increased by approximately 10°C following a doubling of the gold nanorod concentration (as determined by the nanorod optical density), indicating that the photothermal response of PE-GNR dispersion followed Arrhenius-like behavior. Importantly, the photothermal response of EGDE3,3'-coated gold nanorods after four weeks of storage closely followed the same trend observed for freshly prepared nanorods for all concentrations employed in the investigation (Figure 15). However, CTAB-GNRs demonstrated a lower photothermal response compared to EGDE3,3-PSS-CTAB-GNRs at similar concentrations only one hour after preparation; while the temperature increase with EGDE3,3-PSS-CTAB-GNRS (OD = 0.22) was approximately 53°Cafter 15 min of exposure to the laser, the temperature of a dispersion containing a higher concentration of CTAB-GNRs (i.e. OD = 0.5) rose only to 32°C after an equivalent laser exposure time. Expectedly, these results correlate well with optical stability in that, gold nanorods that demonstrate stable optical behavior also demonstrate effective photothermal behavior. Conversely,

aggregation leads to a loss in the photothermal efficacy of CTAB gold nanorods. Taken together, polyelectrolyte-mediated stabilization helps maintain the optical as well as photothermal properties of gold nanorods for extended periods of time.

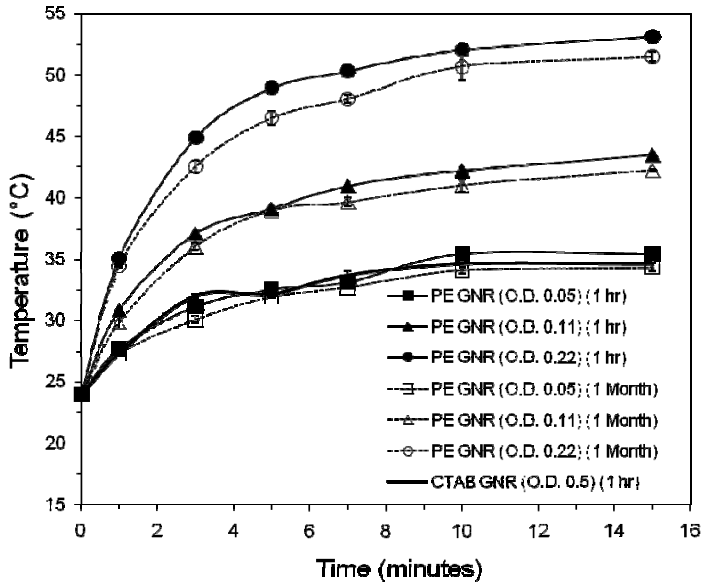

Figure 15.Photothermal response of EGDE3,3'-PSS-CTAB-GNRsin serum-free media.
Different concentrations (as determined by their optical densities) of nanorods were irradiated with continuous wavelength (CW) laser at 770nm (20 W/cm^2) for a maximum of fifteen minutes. The temperature of the dispersion was monitored using a k-thermocouple. Steady-state temperatures showed an increase of approximately 10°C with a doubling of nanorod concentration indicating Arrhenius-like behavior.

3.3.4 EGDE3,3'-PSS-CTAB-GNRs Induce Photothermal Ablation of PC3-PSMA Human Prostate Cancer Cells

Following the demonstration of stable photothermal properties above, the ability of EGDE3,3'-PSS-CTAB-GNRs to induce hyperthermic death in PC3-PSMA human prostate cancer cells following NIR laser irradiation was investigated. Cells were treated with a final concentration of 0.1 OD of EGDE3,3'-PSS-CTAB-GNRs (absorbance spectrum in Figure 16 (i)) which resulted in a final

temperature of approximately 42°C following 7 min of laser irradiation (Figure 15). Laser irradiation induced significant cell death in PC3-PSMA human prostate cancer cells after 24 h of PE-GNR treatments (Figure 16 (ii) A and B). Although cell morphology remained invariant immediately after PE-GNR/laser treatment, extensive changes in cell morphology and high ethidium homodimer staining of compromised nuclei were seen after 24 h, indicating that cell death occurred presumably due to apoptosis of these cells. Negligible loss of cell viability was observed in PC3-PSMA cells treated with EGDE3,3'-PSS-CTAB-GNRs but not exposed to NIR laser irradiation (Figure 16 (ii) C, D), laser alone (Figure 16 (ii) E and F); the viability of these cells was similar to untreated PC3-PSMA cells (Figure 16 (ii) G and H).

(i)

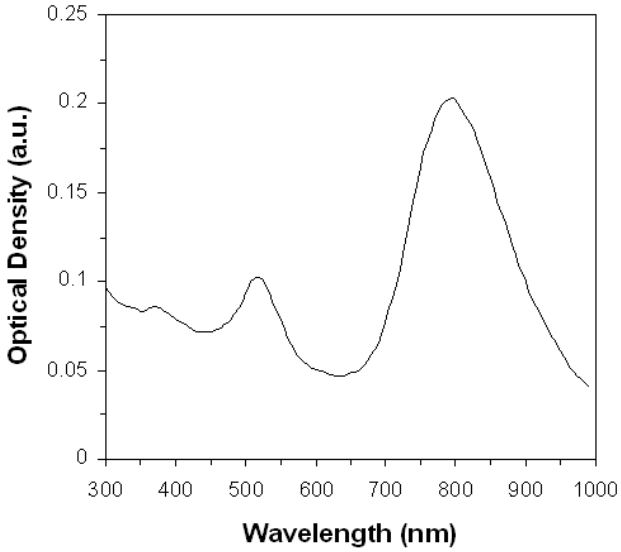

(ii)

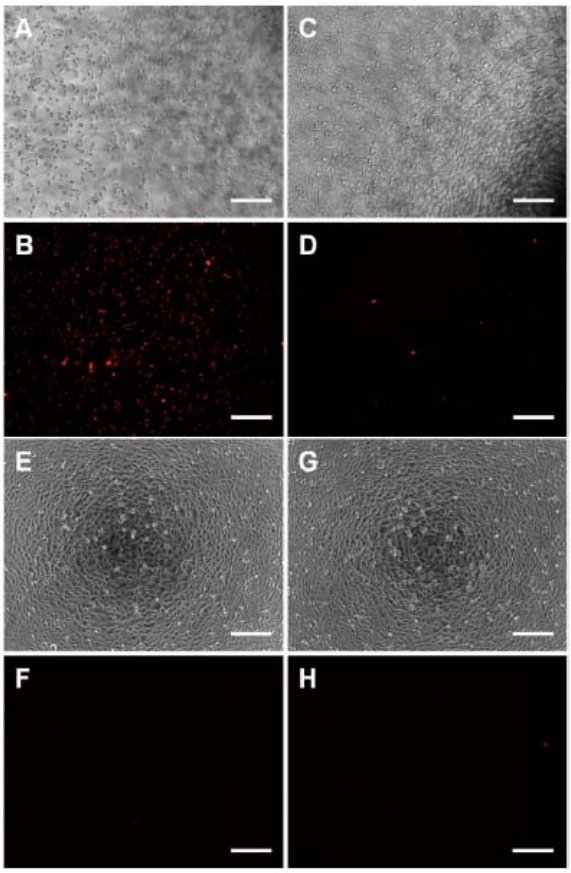
A
C
B
D
E
G
F
H

(iii)

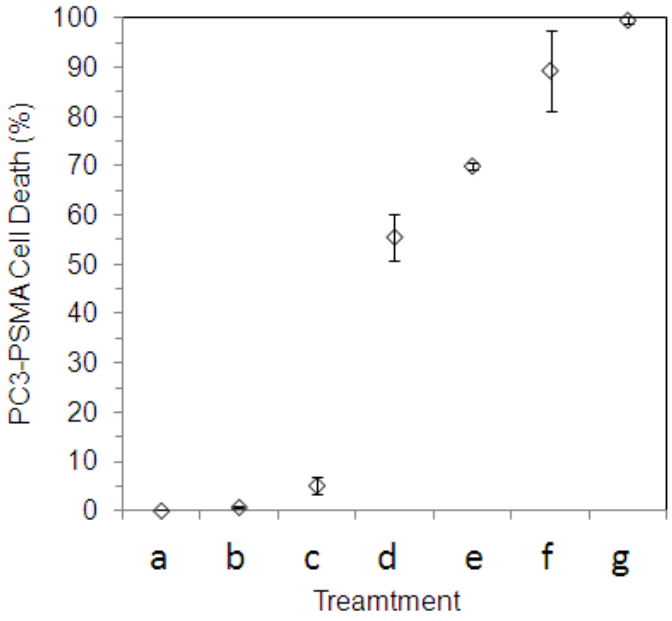
PC3-PSMA Cell Death (%)
100
90
80
70
60
50
40
30
20
10
0
a
b
c
d
e
f
g
Treamtment

(iv)

Treatments	Details	Media Temp. (°C)
a	Live Control: No treatment.	22±0.5
b	Laser Control: Laser 25 W/cm^2 for 7 min	25±0.7
c	PE-GNR Control: Laser 0 W/cm^2 for 7 min	22±0.5
d	Laser treatment: PE-GNR + 7.5 W/cm^2 laser for 7 min	30±0.3
e	Laser treatment: PE-GNR + 15 W/cm^2 laser for 7 min	35±0.6
f	Laser treatment: PE-GNR + 20 W/cm^2 laser for 7 min	41±1.0
g	Laser treatment: PE-GNR + 25 W/cm^2 laser for 7 min	43±0.6

Figure 16.Photothermal Ablation of PC3-PSMA human prostate cancer cells using EGDE3,3'-PSS-CTAB-GNRs.
(i) Absorbance spectrum of EGDE3,3'-PSS-CTAB-GNRs used in the photothermal ablation studies.(ii)Phase contrast images (A, C, E, G) and fluorescence microscopy images (B, D, F, H) of PC3-PSMA cells treated as described below; red fluorescence is due to ethidium homodimer staining of compromised nuclei. Scale bar: 200 μm. A, B: EGDE3,3'-PSS-CTAB-GNRs + laser (7 minutes; power density: 20 W/cm^2). C, D: EGDE3,3'-PSS-CTAB-GNRs (without laser treatment). E, F: laser alone (no nanorods). G, H: No treatment. (iii) Photothermal ablation of PC3-PSMA cells using EGDE3,3'-PSS-CTAB-GNR (PE-GNR) assemblies (OD= 0.1) as a function of laser power density. (iv) corresponded temperature at different treatment conditions.

PC3-PSMA cells were treated with EGDE3,3'-PSS-CTAB-GNR assemblies (OD = 0.1) and subjected to different power densities ranging from 7.5 - 25 W/cm^2 in order to investigate if tuning laser power densities resulted in differential cell death. As seen in Figure 16 (iii), increasing laser power density resulted in an increase in media temperature in correlation with the extent of PC3-PSMA cell death. Interestingly, PC3-PSMA cell death was as high as 55% and 70%, following laser treatment at power densities 7.5 W/cm^2 and 15 W/cm^2, even though the media temperature was only 30^{o}C and 35^{o}C, respectively. This

apparent discrepancy can be explained due to two reasons. First, the temperature measurements were carried out immediately after the laser was turned off. It is possible that these recordings were somewhat lower than those during the photothermal treatment, especially in the case of cells directly in the path of the laser spot which was 2 mm in diameter (well diameter ~6.5 mm). Second, it is important to note that negligible cell death was seen immediately after the seven-minute laser treatment and that the cell viability was determined 24 h after the photothermal treatment. It is possible that a significant number cells die due to the bystander effect[170] over the 24 h period following signals from those cells directly in the path of the laser. While these two factors can explain the high levels of PC3-PSMA cell death observed in these experiments, the role of the bystander effect on PE-GNR induced hyperthermic ablation of cancer cells have not been directly determined as part of this investigation. As may be expected, higher laser power densities resulted in higher PC3-PSMA cell death(> 85%). Cells treated with the laser alone (without PE-GNRs) and PE-GNRs alone (without laser irradiation) did not induce PC3-PSMA cell death.

It is important to point out that a balance exists between polyelectrolyte cytotoxicity and PE-GNR-induced hyperthermic ablation of cancer cells. While low concentrations of polyelectrolytes are not sufficient for either stabilizing GNRs or for inducing hyperthermic temperatures, higher concentrations are cytotoxic and are therefore, not useful in hyperthermic ablation of cancer cells. As a result, concentrations of EGDE3,3'-PSS-CTAB-GNRs that were not toxic to PC3-PSMA cells but demonstrated photothermal activity were chosen for the

ablation of these cells. In contrast, pEI25-coated GNRs were highly toxic to the cells at concentrations that would result in hyperthermic temperatures (> 40°C) and therefore, were not included in this study. The use of such untargeted PE-GNRs can be useful in the hyperthermic ablation of relatively accessible tumors such as bladder or prostate tumors.

3.3.5 EGDE3,3'-PSS-CTAB-GNRs Successfully Deliver Exogenous DNA to Prostate Cancer Cells In Vitro.

Cationic polymers have emerged as promising candidates for delivering exogenous nucleic acids, including plasmid DNA, to a variety of mammalian cells[171-173].The efficacy of stable PE-GNR assemblies to bind and deliver plasmid DNA to PC3-PSMA cells *in vitro* was investigated. Greater than 95% of the original plasmid DNA amount (350 ng) was loaded on PE-GNRs, while only 50-55% was loaded on equivalent amounts of CTAB-GNRs (Table 6).

Table 6 Loading of pGL3 plasmid DNA on CTAB-GNR and PE-GNRs.
Plasmid DNA (350 ng) was loaded on gold nanorods (optical density, OD = 0.25 $*10^{-2}$) for 30 min following which, the nanorods were centrifuged and supernatant was assayed for DNA content using ethidium bromide. The amount of plasmid DNA loaded on gold nanorods was determined by mass balance and the DNA-loaded assemblies were used in the transfection experiments. Representative loading experiments are shown in the table.

	Optical Density (a.u.) $* 10^{-2}$	Initial pDNA (ng)	pDNA (ng) in the supernatant	pDNA (ng) loaded on the GNRs	% pDNA loaded on the GNRs
CTAB-GNR	0.25	350	170.6	179.4	51.25
EGDE3,3'-PSS-CTAB-GNR	0.25	350	10.6	339.4	96.97
pEI25k-PSS-CTAB-GNR	0.25	350	15	335	95.71

Different sub-toxic concentrations of PE-GNRs loaded with pGL3 plasmid DNA were delivered to PC3-PSMA cells; luciferase protein expression was used as a reporter for transgene expression. GNR concentrations were kept below OD $0.25*10^{-2}$ in order to compare the transfection activity of EGDE-3,3' polymer with that of pEI25 which was toxic to cells beyond this concentration (Figure 14). EGDE3,3'-based PE-GNRs resulted in up to ten-fold higher transgene expression in PC3-PSMA cells compared to pEI25-based PE-GNRs (Figure 17) after 48 h following transfection. CTAB-GNRs did not demonstrate any transfection activity under these conditions (not shown), presumably due to a combination of low DNA loading, nanoparticle aggregation which can lead to reduced cellular uptake, and inherently poor transfection efficacy[174,175]. The use of polyelectrolytes not only overcomes the poor GNR stability associated with CTAB, but also facilitates higher plasmid DNA binding and enhanced transfection activity of the resulting assemblies. The lower cytotoxicity of EGDE3,3'-PSS-CTAB-GNRs makes it an attractive vector for non-viral gene delivery, compared to assemblies based on pEI25. Taken together, these results indicate that interfacing engineered polyelectrolytes with gold nanorods results in stable multifunctional assemblies that possess photothermal ablation, gene delivery, and optical imaging capabilities[145,149,176-178] all on a single platform.

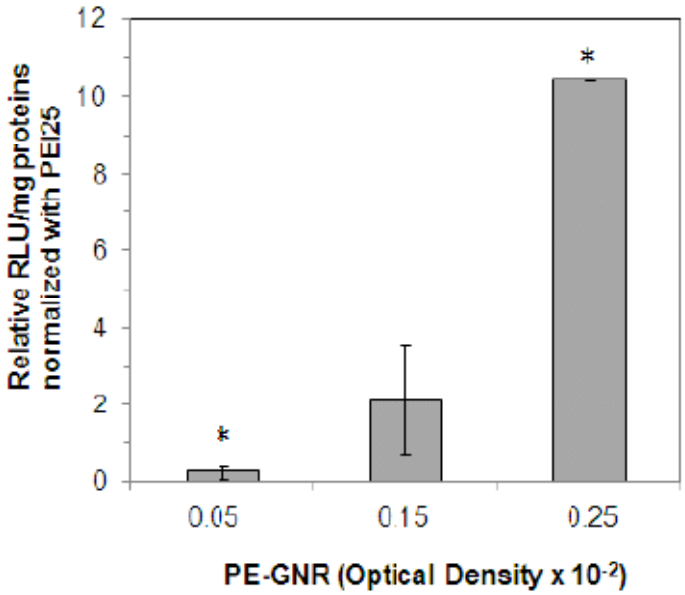

Figure 17. Transfection of PC3-PSMA human prostate cancer cells using EGDE3,3'-PSS-CTAB-GNRs and pEI25-PSS-CTAB-GNRs.
PC3-PSMA cells were treated with different concentrations of PE-GNRs containing 350 ng of pGL3 plasmid for 6 h. Luciferase expression, in relative luminescence units or RLU was analyzed 48 h following transfection and normalized to protein content in each case (RLU /mg). The normalized luciferase expression for EGDE3,3'-PSS-CTAB-GNRs is reported relative to that for pEI25-PSS-CTAB-GNRs. CTAB-GNRs did not demonstrate any transgene expression activity at similar optical densities. Asterisks indicate p values < 0.02 determined using two-tailed Student's t-test for a minimum of three independent experiments.

3.4 Conclusions

Gold nanorods prepared using the widely used CTAB-based seed-mediated method demonstrate poor stability in phosphate buffered saline (PBS), serum-free media (SFM) and serum-containing media (SCM) following centrifugation. A layer-by-layer deposition of polyelectrolytes was employed in order to enhance the short-term and long-term stability of gold nanorods in these media. Polyelectrolyte-coated gold nanorods (PE-GNRs) demonstrate excellent long-term optical stability in all three media as determined by their optical properties even after four weeks of storage. Stabilization of the optical response, in turn,

resulted in a reliable photothermal response of the well-dispersed gold nanorods over the period investigated, which facilitated their successful use in the photothermal ablation of PC3-PSMA human prostate cancer cells using near infrared laser irradiation. Gold nanorods coated with the recently developed EGDE-3,3' polymer in our laboratory demonstrated lower cytotoxicities and higher transfection efficacies than 25kDa poly(ethyleneimine) or pEI25, which is a current standard for polymer-mediated gene delivery. While EGDE-3,3'-coated GNRs demonstrated higher toxicities than CTAB-GNRs at similar optical densities, PE-GNRs possess greater advantages including stable photothermal properties, higher transfection efficacies, and the ability to further derivative residual reactive amines[165]. These results indicate that cationic polyelectrolytes can lead to stable, biocompatible and multifunctional gold nanorod assemblies, which can be useful for a variety of simultaneous applications including biological sensing, optical imaging, non-viral gene delivery, and localized hyperthermia. Further discovery and engineering of polyelectrolytes that optimize toxicity, stability, and gene delivery efficacy will be required in case of polyelectrolyte-coated assemblies. While the current *in vitro* results are indeed encouraging, future studies on therapeutic efficacy, biocompatibility, and biodistribution in appropriate animal models will be needed in order to fully realize the potential of these assemblies.

CHAPTER

4. Gold Nanorods Induced Extracellular Hyperthermic Ablation of Cancer Cells and Spatiotemporal Distribution

4.1 Introduction

Most previous studies have focused on nanoparticle-mediated 'intracellular' hyperthermia in which, gold nanoparticles are first internalized by cells followed by laser irradiation to induce temperature elevation leading to cell damage. In this approach, hyperthermic temperatures are generated inside cancer cells by the internalized nanoparticles. An alternate approach is to use plasmonic nanoparticles in the extracellular space of the cancer cells, mimicking their extravasation from the leaky tumor vasculature into this region, particularly in cases of poor or sluggish flow *in vivo*. Laser irradiation of nanoparticles in the extracellular space leads to generation of heat outside the cell (extracellular hyperthermia) which can be employed for cancer cell ablation.

Various mathematical models have been developed to study the different physical and transport mechanisms that play a role in using nanoparticles for hyperthermic cancer treatment. Heat transport in tissues has been studied for a number of decades and is now largely based on the use of on the Pennes' bio-heat equation[179]. The heat transport equation has been used by a number of researchers for the specific problem of laser induced heat generation/transport from gold nanoparticles[180-183]. The spatial transport of nanoparticles, which is governed by nanoparticle diffusion and binding, has also been modeled

previously[184]. Finally, hyperthermal cell injury/death has been modeled using the Arrhenius rate model, isoeffective dose model, and other models[185].

While the use of intracellular hyperthermia has been extensively explored, the objective of the work is to present a mathematical model and experimental results for heat generation, heat transport, and cellular injury/death for the laser induced heating of nanorods dispersion outside prostate cancer cells. Spatiotemporal profiles of temperature increase following laser irradiation of gold nanorods were determined experimentally and were used to evaluate the mathematical model. The validated temperature model was then used to predict cell death following gold nanorod induced extracellular hyperthermia and the model predictions were quantitatively compared to experimental results. Last, the model was used to predict how selective binding of gold nanorods to cancer cells might influence the efficacy of extracellular hyperthermia.

The experimental work described in this Chapter was carried out by me, Huang-Chiao Huang, under Dr. Kaushal Rege's (PI's) guidance; the theoretical modeling was done by Professor Jeffrey J. Heys, Department of Chemical and Biological Engineering, Montana State University.

4.2 Materials and Methods

4.2.1 Experimental

4.2.1.1 Generation of gold nanorods

Gold nanorods were synthesized using the seed-mediated method[155] following the same procedure in Chapter 3.2.2, this method was employed to generate gold nanorod population that possessed absorbance maxima at λ_{max}= 800 nm. Gold nanorods dispersion was further diluted with deionized (DI) to obtain specific optical density (OD_{800}) (Figure 18).

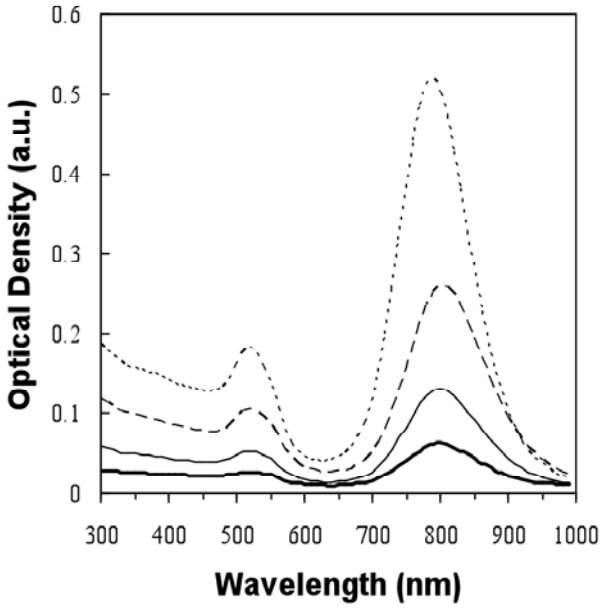

Figure 18.Absorbance spectrum of gold nanorods employed in the current study indicated different concentrations as determined using optical densities.

4.2.1.2 Preparation of PEGylated nanorods

Thiolated poly(ethylene glycol) (mPEG-SH, MW5000) was obtained from Creative PEGworks. The polymer (3 mg/mL) was added to GNR (optical density 0.5 at λ_{max}= 800 nm) and the dispersion was sonicated for thirty minutes. After sonication, the mPEG-SH-GNR mixture were centrifuged at 6,000 rcf for ten minutes in order to remove excess mPEG-SH molecules, followed by

resuspension in serum-free media, resulting in stock mPEG-GNR dispersions with final optical densities (OD_{800}) of 0.15 and 0.2.

4.2.1.3 Photothermal response of GNR and determination of spatiotemporal temperature profiles

The photothermal response of gold nanorods (CTAB-GNRs) to laser irradiation was determined using a titanium CW sapphire (Ti:S) laser (Spectra-Physics, Tsunami) pumped by a solid state laser (Spectra-Physics, Millennia). The experiment was carried out in a 24 well plate (15.6 mm internal diameter of the well). The laser excitation source was tuned to 800 nm (2 mm diameter) in order to coincide with the longitudinal absorption maximum of the CTAB-GNR dispersions (1 mL) with various optical densities (OD_{800}= 0.065, 0.148, 0.285, and 0.50) . A fixed laser power density of 20 W/cm^2 was employed for fifteen minutes. The dispersion temperature was monitored using a FLUKE 54 II (Type J) thermocouple immediately after laser irradiation at three different locations, (1) center, (2) 4 mm from center, (3) at the edge of the well (Figure 19).

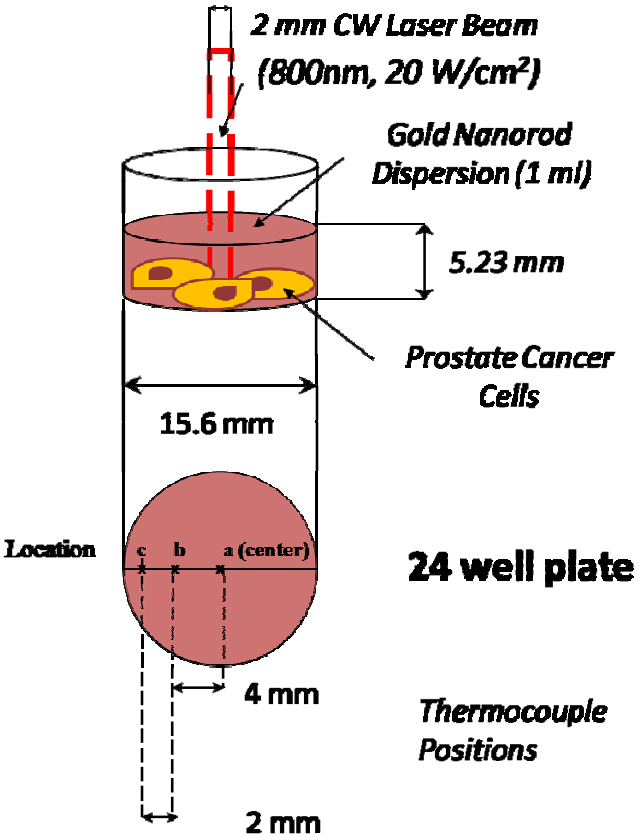

Figure 19. Schematic of the laser experiment which shows approximate positions (a,b,c) of the thermocouple used for determining spatiotemporal temperature distribution. (Cells not to scale)

4.2.1.4 Cell culture

The PC3-PSMA human prostate cancer cell line[166] was a generous gift from Dr. Michel Sadelain of the Memorial Sloan Cancer Center, New York, NY. Cells culture condition was same as mentioned in Chapter 3.2.7.

4.2.1.5 Photothermal cell ablation

The laser irradiation experiment was carried out with a titanium CW sapphire (Ti:S) laser (Spectra-Physics, Tsunami) pumped by a solid state laser (Spectra-Physics, Millennia). Prior to laser irradiation, serum-containing media in PC3-

PSMA cell cultured 96 well plates were replaced by 200 µl of mPEG-GNR (OD_{800}= 0.15 and 0.2, in serum free media). PEGylated nanorods were used in cell ablation studies in order to minimize adhesion to the cell surface and maintain them in dispersion in the extracellular space. As before, the laser excitation source was tuned to 800 nm (2 mm diameter) in order to coincide with the longitudinal absorption maximum of the mPEG-GNR; a fixed laser power density of 20 W/cm^2 was used for different exposure times (4, 8, 12, and 20 min), while monitoring the dispersion temperature using a FLUKE 54 II (Type J) thermocouple immediately after laser exposure. The mPEG-GNR dispersion was immediately removed and replaced by fresh serum containing media after laser exposure.

4.2.1.6 Cell viability assay (MTT)

Cell viability was assayed 24 h after laser irradiation, using MTT cell proliferation assay kit (ATCC CA#30-1010k). Following addition of the MTT reagent (6 h at 37^oC), cells were treated with a lysis buffer from the kit and kept at room temperature in the dark for 4 h in order to carry out complete lysis and solubilization of the MTT product. The absorbance of each well was measured using a plate reader (Bio-Tek Synergy 2) at 570 nm. For data analysis, absorbance readouts were normalized to the live (untreated) and dead (5 µl of 30 % hydrogen peroxide-treated) controls.

4.2.2 Theoretical Model

The modeling of GNR use in hyperthermal cancer treatment requires a three part model, and is provided by Dr. Jeffery Heys: (4.2.2.1) a heat transport (or energy balance) equation, (4.2.2.2) a cell death model, and (4.2.2.3) a GNR spatial distribution model. Each of the three parts is described below.

4.2.2.1 Heat transport model

The temperature distribution model for either a fluid or tissue containing GNRs is based on the Pennes' bio-heat equation [179,183] with an additional term to account for energy released by the GNRs:

$$\frac{\partial T}{\partial t} = \alpha \nabla^2 T + \frac{Q}{\rho C_p}\left(1 - 10^{-OD}\right) + \frac{w C_{pb}}{\rho C_p}(T - T_b) \qquad (1)$$

Where the first term on the right side is heat conduction (diffusion), the second is plasmonic heating by the GNRs from laser irradiation, and the third term is heat transfer due to blood flow. The parameters used in the model are defined in Table 7.

Table 7. Heat transport model parameters based on [182,186]

parameter	description	value
ρ	tissue or fluid density	1000 kg/m^3
Q	laser energy	0.008 − 0.038 W/mm^3
C_p	tissue or fluid heat capacity	3.4 kJ/(kg K)
OD	optical density	0 to 0.5
$\alpha = k/(\rho C_p)$	tissue or fluid thermal diffusivity with GNRs	3.0×10^{-7} m^2/s

The incident laser power (5 to 20 W/cm^2) was divided by the sample depth to obtain Q, the laser power per volume required in equation 1. The value used for each parameter is consistent with values used previously by others except for the

thermal diffusivity, which is approximately twice the value for pure water. The thermal diffusivity value utilized in the model was chosen because it gave the best agreement with the experimental data as described later in the results section. It is also reasonable to assume that the presence of a high concentration of GNR in the solution would significantly increase the thermal diffusivity of the solution[187].

Three types of boundary conditions are commonly used during the solving of the heat transfer model (Figure 20). First, if the surrounding fluid or tissue is held at a fixed temperature, a Dirichlet condition can be applied, which specifies the temperature along the boundary. Second, a heat flux or Neumann boundary condition can be used in conjunction with Newton's law of cooling to give:

$$k\frac{\partial T}{\partial n} = U(T - T_0) \qquad (2)$$

Here, U is the overall heat transfer coefficient for the region adjacent to the model boundary, and $T_0$is the bulk temperature of the surroundings. The final type of boundary condition is a symmetry condition, which is equivalent, in practice, to a zero temperature gradient boundary condition. The model domain and boundary conditions are shown in Figure 4.3. For the *in vitro* cell culture based system described here, U_{air}= 0.08 (W/m^{2}°C),U_{wall}= 1X10^{-5} (W/m^{2}°C), and k= 1 (W/m°C) were used in the model, and T_{air} and T_{wall} were measured to be 23°C.

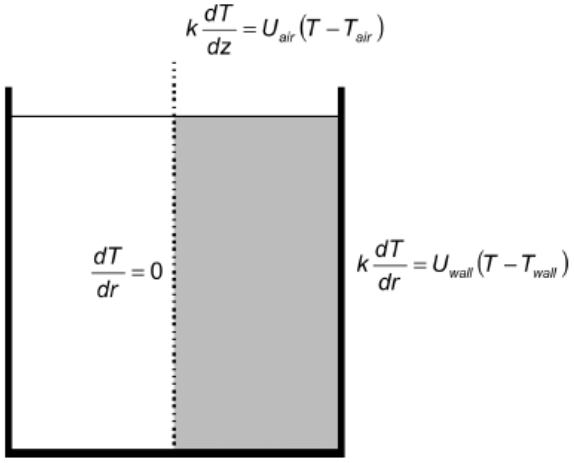

Figure 20.The model domain (grey) represents a symmetrical cross-section of a well in a plate.
The top boundary is the air-solution interface, the right and bottom boundaries are plate-solution interfaces, and the left boundary (dotted line) is the symmetry axis

4.2.2.2 Cell death model

Cell injury and death is predicted using the Arrhenius injury model[182,188]. The cell injury rate is calculated by

$$\mathrm{k} = \mathrm{A}\mathrm{e}^{\frac{-\mathrm{E_a}}{\mathrm{RT}}} \qquad (3)$$

Where $E_a$is the activation energy, R is the gas constant, T is the temperature, and A is a scaling factor. The values for E_a and A were determined for the experimental cell line studied here using isothermal cell viability tests, and the values used in the model are A= $6X10^{29}s^{-1}$, and E_a= 200 kJ/mol. These values are consistent with the values measured for similar cell lines and tissues[189,190]. Finally, the cell injury rate is integrated over time to account for injury accumulation, and the fraction of tissue that is injured over time is given by

$$\mathrm{F_D} = 1 - \mathrm{e}^{-\int_0^t \mathrm{k}\,\mathrm{dt}} \qquad (4)$$

Thus healthy tissue has F_D= 0 and dead tissue has F_D= 1.

4.2.2.3 GNR spatial distribution

The distribution of GNRs in the extracellular dispersion is governed by diffusion, binding, unbinding, and cell internalization events. Initial studies on tumor spheroids have established the potential for mathematical models to accurately model the spatial distribution of nanoparticles[184], but the general applicability of these models to other tissues and nanoparticle systems is still unknown. It is, in general, difficult to estimate the diffusivity of the nanoparticles in the tissues, and the rate of particle binding, unbinding, and internalization within the cell are challenging to measure.

It is possible to obtain a simplified model for the problems of interest here using scaling analysis. The diffusivity of nanoparticles in water is very small (< 10-8 cm^2/s), and the diffusivity within a tissue is even smaller[184]. The result of the small diffusivity is that diffusion through only a 100 μm of tissue requires a number of hours depending on the concentration and temperature[184]. The internalization of particles into cells is also relatively small for the time scales of interest here because the internalization rate is typically an order of magnitude less than the unbinding rate. This means that a GNR attached to a cell surface is 10 times more likely to go back into solution than to be internalized. Of course, internalization is largely irreversible, so given sufficient time many particles will be internalized, but this can take a few hours.

For the systems of interest here, it is valid to assume that most GNRs do not diffuse into tissue and are not internalized by the cells, but they remain in the extracellular dispersion or bound to the surface of the tissue. The concentration of bound particles is governed by the equation

$$\frac{\partial C_b}{\partial t} = k_a C_{bs} C - k_d C_b \quad (5)$$

Where C_b is the concentration of bound particles, C_{bs} is the concentration of open binding sites, C is the concentration of free particles in solution, and k_b and k_d are the association (binding) and disassociation (unbinding) rates, respectively. If sufficient time has elapsed before turning on the laser, equilibrium is achieved so the binding model can be simplified using a pseudo-steady-state assumption. The concentration of bound particles then becomes

$C_b = k_{eq} C_{bs}$ (6)

Where $k_{eq} = /k_a'/k_d$ and $K_a' = k_a C$. The particle contrast (i.e., the ratio in bound particles between health and cancerous tissues) is determined by the ratio of binding site concentration between healthy and cancerous tissues.

4.3 Results and Discussion

The first set of model validation results focuses on the comparison of the heat transfer model with experimental temperature measurements with different ODs (i.e., different GNR concentrations) and different laser irradiation levels. The first experimental conditions used a 24-well plate and 4 different OD_{800} (0.065, 0.148, 0.285, and 0.50). The temperature was measured at 4 different locations within a well, and two different samples at each OD_{800} were employed. The

experimental measurements and simulation predictions at three radially spaced points in the domain are shown in Figure 21.

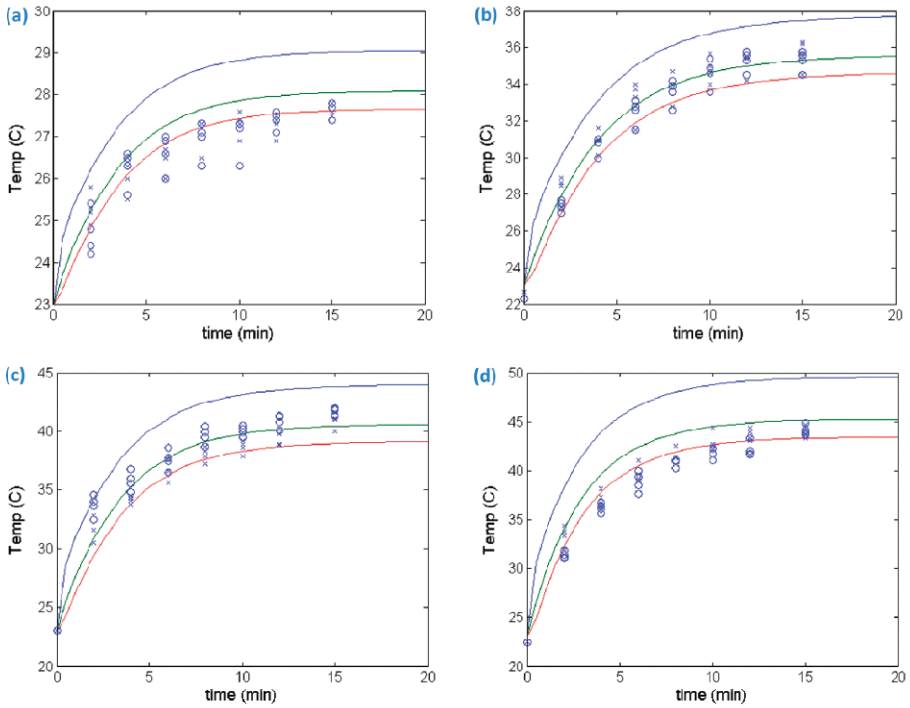

Figure 21.Experimental temperature measurementsand heat transfer model predictions.
Experimental temperature measurements (2 samples, circles and crosses) and heat transfer model predictions (solid lines for three radial points in the domain) for 4 different OD_{800}s - (a) 0.065, (b) 0.148, (c) 0.285, and (d) 0.50.

Significant spatial differences were not seen in the current set up indicating that even though the laser diameter was only 2 mm in a well of approximately 16 mm diameter, the heat transfer was rapid throughout the gold nanorod dispersion. The model predictions are in good agreement with the experimental measurements for all optical densities, and the largest errors occur at the lowest optical density. However, even at the lowest optical density, the experimental measurement and model prediction agree once steady-state is achieved. The

model simply predicts a slightly faster heating rate than is measured experimentally. The model predicts the temperature distribution throughout the well being irradiated with the laser. Figure 22 shows the temperature contours within the well, and as expected, the highest temperatures occur along the well axis where the laser is focused, and the coolest temperatures occur near the wall at the surface of the fluid.

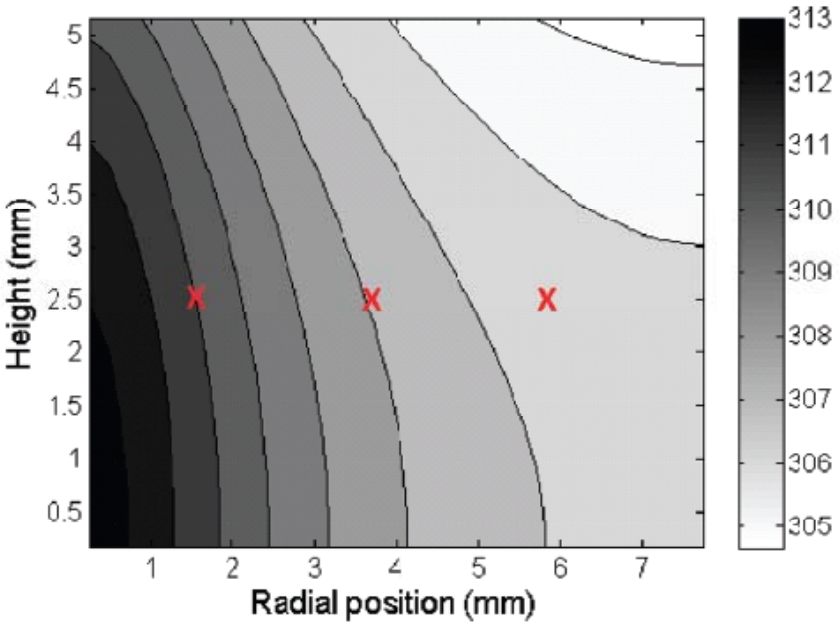

Figure 22.Temperature distribution within the well for an OD=0.45.
The temperature is reported in K, and approximate locations of the thermocouples are shown by 'X'.

The second set of comparisons between experimental measurements and the heat transfer model uses GNR dispersions in a 96-well plate and different laser energy levels. The results are summarized in Figure 23 and show good agreement at the lower two laser energy levels. At the highest laser energy level, the model predicts a higher temperature than is measured experimentally,

especially at steady-state. The most likely cause for this difference is the assumptions behind Newton's law of cooling for the upper boundary. This boundary condition lumps radiative cooling, evaporative cooling, and convective cooling into a single parameter that is independent of temperature. In other words, it assumes that all these energy loss mechanisms are (linearly) proportional to the temperature. In reality, none of these energy loss mechanisms are linear with temperature changes, and these nonlinear effects become important at temperatures above 50°C or 60°C[191].

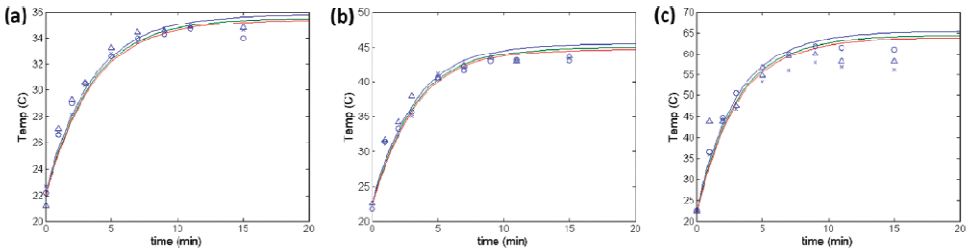

Figure 23.Heat transfer model prediction at different radial locations (solid lines) and experimental temperature measurements (open circles and crosses) at three different laser energy levels.
(a) 0.008 W/mm^3, (b) 0.016 W/mm^3, and (c) 0.032 W/mm^3.

Once acceptable agreement between the heat transfer model and experimental measurements was achieved, the next set of validation experiments focused on the cell death model. The GNR dispersion with cells attached to the bottom of the well was then irradiated for 0, 4, 8, 12, or 20 minutes, and the temperature was also monitored immediately after switching the laser off. A cell viability assay was conducted after irradiation, and the viability measurements were compared to model predictions. Figure 24 shows the temperature and cell viability results for a GNR solution with an $OD_{800}$of 0.15.

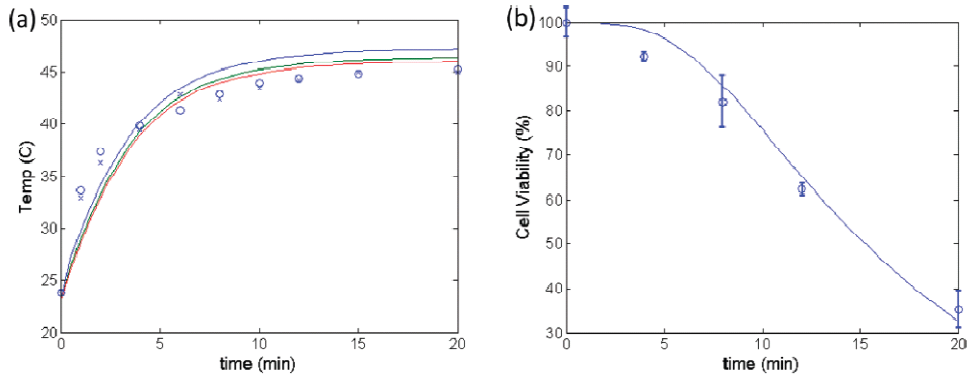

Figure 24. (a) Temperature measurements and model predictions for a GNR dispersion with OD_{800}= 0.15. (b) Cell Viability measurements and predictions for different laser irradiation times.

The model predictions of the temperature are slightly lower than the experimental measurements for lower laser exposure times, and are slightly higher for exposure times greater than five minutes. The cell death predictions deviate slightly from experimental measurements, but these differences can be expected from the temperature predictions. Lower values of temperature at the initial laser exposure times (< 5 minutes) result in predictions of high cancer cell viability. Conversely, higher temperature predictions lead to modest over-estimatation of cell death predictions (or lower predictions of cell viability values). The model and experimental results for a GNR solution with an OD_{800}= 0.2, shown in Figure 25, are similar to the OD_{800}= 0.15 results. Here, the temperature agreement and cell viability agreement are improved, with the largest errors being in the early cell viability results. The temperature within the well varies both temporally and spatially.

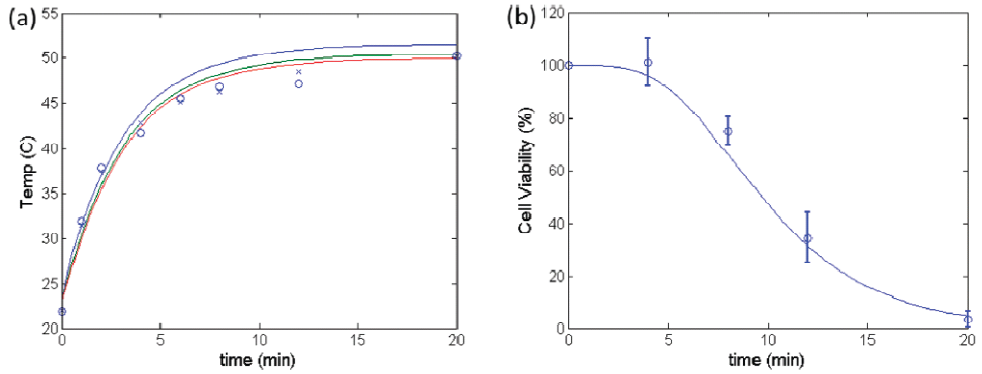

Figure 25.(a) Temperature measurements and model predictions for a GNR dispersion with OD_{800}=0.20. (b) Cell Viability measurements and predictions for different laser irradiation times.

To help visualize the impact of the spatial temperature variation on cell viability, the well bottom in the model was covered with a monolayer consisting of approximately 13,000 cells. Each cell was assigned a random number between 0 and 1, and when the cell viability dropped below that random number, the cell was removed from the model. Figure 26 shows the viable cells after 10 minutes and after 18 minutes of laser irradiation. The solution in the well above the cells contained GNR with an OD_{800}= 0.2. Despite the small spatial temperature differences, there is a lower loss of cell viability for the outer regions of the well. The higher temperatures at the center result in a higher rate of cell death.

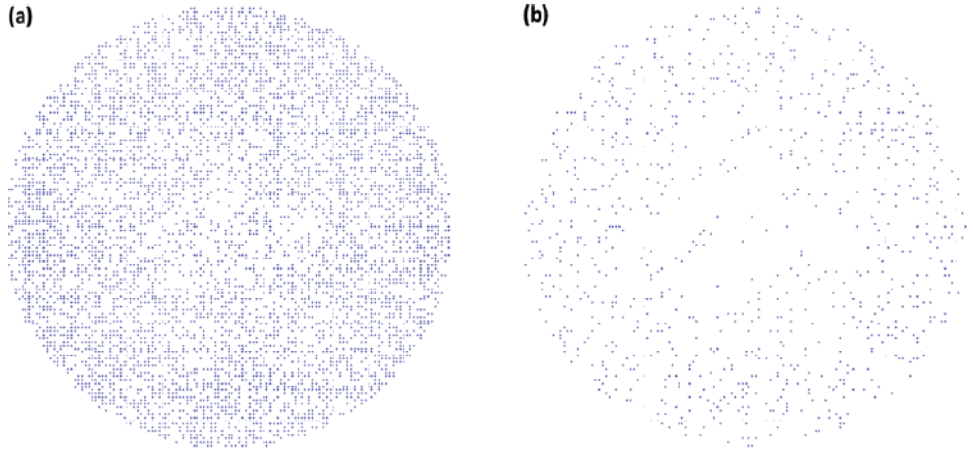

Figure 26.Cell viability predictions.
Viability predictions for approximately 13,000 cells along the bottom of the well after laser irradiation for (a) 10 minutes and (b) 18 minutes with GNR solution at OD_{800}= 0.20. The cells disappear when their cell viability level falls below a randomly assigned threshold.

The final model prediction is speculative in nature, and was carried out to elucidate the role of nanoparticle binding to cell surface on hyperthermia. Some evidence has shown that cancer cells are more susceptible to damage from elevated temperatures than healthy cells due to the hypoxic environment[192]. To model this impact, it was assumed in the model that the inner 1.2 mm (in diameter) of a 6mm well was cancerous cells, and for these cells, E_a= 198 kJ/mol was used instead of E_a= 200 kJ/mol to simulate the increased heat sensitivity. Further, GNRs can be conjugated with cancer cell targeting antibodies that will increase their potential for binding to malignant cells versus healthy cells. To model the impact of this change, the GNR concentration was increased by 20% near the cancer cells versus the healthy cells, which represents an assumed increase of 20% in the number of binding sites for cancerous versus healthy cells. It is important to remind the reader that the targeted nanorods in this case are still external to the cell and have not been internalized. The predicted living

cell populations at the bottom of the well are once again shown for ten and eighteen minutes of laser irradiation in Figure 27. At the ten-minute point, 31% of the healthy cells have been killed, and 65% of the cancer cells have died. At the eighteen-minute point, 71% and 96% of the healthy and cancer cells, respectively, have died.

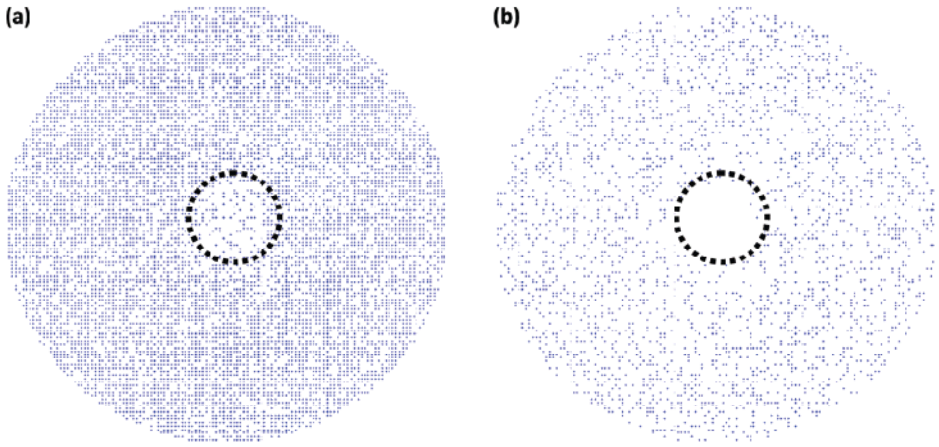

Figure 27.Cell viability predictions for approximately 13,000 cells along the bottom of the well after laser irradiation.
(a) 10 minutes and (b) 18 minutes with GNR solution at OD_{800}=0.17. The inner 1.2 mm has cancerous cells with lower activation energy for cell injury and an increased number of GNR binding site (simulating targeting delivery of GNRs to cancer cells). The cells disappear when their cell viability level falls below a randomly assigned threshold.

The model parameters were changed only a small amount between the results shown in Figures 26 and 27. However, the impact on cell death over the tumor region in the model was far greater, overall, than the small individual changes to cell injury activation energy and GNR concentration. This dramatic change is simply a result of the impact of these two parameters being multiplicative (or geometric) instead of additive (or arithmetic). Multiplicative interactions can

cause multiple small changes to result in a large change overall, much larger than simply adding up the small changes.

4.4 Conclusions

In this Chapter, the nanorod dispersion was irradiated with near infrared (NIR) laser and the spatiotemporal distribution of temperature was determined experimentally. This information was employed to develop and validate theoretical models of spatiotemporal temperature profiles for gold nanorod dispersions undergoing laser irradiation, and the impact of the resulting heat generation on the viability of human prostate cancer cells. A cell injury/death model was then coupled to the heat transfer model to predict spatial and temporal variations in cell death and injury. The model predictions agreed well with experimental measurements of both, temperature and cell death profiles. Finally, the model was extended to examine the impact of selective binding of gold nanorods to cancer cells compared to non-malignant cells, coupled with a small change in cell injury activation energy. The impact of these relatively minor changes results in a dramatic change in the overall cell death rate. Taken together, extracellular hyperthermia using gold nanorods is a promising therapeutic strategy and tailoring the cellular binding efficacy of nanorods can result in varying therapeutic efficacies using this approach.

CHAPTER

5.Optically / Photothermally Responsive Polypeptide Conjugated Gold Nanorod Assemblies

5.1 Introduction

Chapter 3 demonstrated that polyelectrolyte coated gold nanorods absorb near infrared (NIR) light converting this energy to heat for photothermal ablation, in which PE-GNRs can be used as a potential drug delivery device. This chapter describes an investigation into interfacing proteins/polypeptides with nanoparticles to generate novel functional nanomaterials for sensing, tissue engineering, and/or drug delivery applications. Optically responsive nanoassemblies have demonstrated promise as molecular-scale switching devices[193,194], sensors[195-197], drug delivery systems[198-202], and for biomedical imaging[145,203].The ability to convert incident light energy to heat energy due to surface plasmon resonance activity makes gold nanorods attractive candidates for modulating polypeptide (or protein) structure / phase transition using optical methods (i.e. near infrared light). While the ability to induce irreversible structural change in proteins can play a role in therapeutic applications, the ability to reversibly control protein structure lends flexibility for a variety of applications including site-specific drug delivery, biosensors, and switching.

Elastin-like polypeptides (ELPs) are derived from a portion of mammalian elastin characterized by the sequence, VPGXG, where V=valine, P=proline, G=glycine, and X=any amino acid except proline. ELPs exhibit a thermally induced phase

transition at the inverse transition temperature (T_t), characterized by reversible intramolecular contraction and intermolecular coacervation[204]. The transition temperature (T_t) is the temperature at which hydrophobic folding and assembly transition occurs. Below T_t, ELP dissolved in aqueous solution; upon heating, ELPs undergo a phase separation, commonly known as coacervation. Further heating of ELP leads to coalescence of coacervate into larger droplets[205]. The phase transition of ELP is reversible and can be easily characterized based on turbidity measurement vs temperature plot; T_t is defined as the temperature at 50% the maximum turbidity of solution. The thermal transition behavior of ELPs is reversible and has been exploited in a number of applications including, bioseparations[206-208], drug delivery[209-213], sensors[214-216], and tissue engineering[217,218]. These reports have traditionally employed thermal activation as means of inducing phase transitions in ELPs. However, the ability to remotely and reversibly control the thermal response may be critical in applications such as targeted hyperthermia to tumors that may require precise spatial control in deep-seated tissues.

The formation of gold nanorod (GNR)-elastin-like polypeptide (ELP) nanoassemblies whose optical response can be remotely controlled based on near-infrared (NIR) light exposure has been demonstrated. In this study, cysteine-containing ELPs (denoted C_2ELP due to the presence of two cysteines in the ELP repeat sequence) were self-assembled on gold nanorods (GNRs) leading to GNR-C_2ELP nanoassemblies. Exposure of GNR-C_2ELP assemblies to NIR laser resulted in the heating of GNRs due to surface plasmon

resonance[219,220]. Heat transfer from the GNRs resulted in a temperature increase of the self-assembled C_2ELP above its transition temperature (T_t)[204,206,221], leading to a detectable phase transition and aggregation of the GNR-C_2ELP assemblies. This phase transition was quantified using an optical readout, based on an increase in the optical density of the GNR-C_2ELP dispersion. This optical response was seen only in the case of GNR-C_2ELP nanoassemblies. While a photothermal response was observed in the case of a dispersion consisting of GNRs alone, no optical response could be seen due to the absence of the C_2ELP. As expected, C_2ELP solutions demonstrated neither a photothermal nor an optical response. The reproducibility and reversibility of optical response of GNR-C_2ELP nanoassemblies was demonstrated across multiple cycles following exposure and removal of the laser irradiation. Studies described in this chapter demonstrate that polypeptides can be interfaced with GNRs resulting in optically responsive nanoassemblies, with potential applications in (bio)sensing, tissue engineering, and drug delivery.

5.2 Materials and Methods

5.2.1 Design, Expression, and Purification of C_2ELP

This portion of the work was carried out in collaboration with Dr. Zaki Megeed and Dr. Piyush Koria at the Center for Engineering in Medicine, Massachusetts General Hospital and Harvard Medical School in Boston, MA.

5.2.1.1 C_2ELP gene synthesis

Cysteine-containing ELPs were formed via recursive directional ligation[221], yielding the following amino acid sequence, where cysteine residues are shown in bold and underlined font; the name C_2ELP denotes the two cysteines that are part of the ELP repeat sequence:

MVSA**C**RGPG-(VG VPGVG VPGVG VPGVG VPGVG VPG)$_8$–(VG VPGVG VPGVG VPG**C**G VPGVG VPG)$_2$-WP

Briefly, oligonucleotides encoding the ELP were cloned into pUC19, followed by cloning into a modified version of the pET25b+ expression vector at the sfiI site[221]. E. coli BLR (DE3) (Novagen) was used as a bacterial host.

5.2.1.2 C_2ELP expression and purification

Expression vector pET25b+, containing C_2ELP cassette was transformed into BLR cells. A starter culture of 50 mL was then inoculated overnight in terrific broth. The next day the 50 mL culture was added to a 1 L culture. The 1 L flasks were then inoculated overnight in an incubator shaker at 250 rpm and 37°C. Bacterial cells were harvested by centrifugation at 4°C the next day. The bacterial pellet was resuspended in 1X phosphate buffered saline (PBS) and the cells were disrupted by sonication on ice. The lysate was cleared by centrifugation followed by a polyethyleneimine treatment (final concentration: 0.5% w/v) in order to precipitate soluble nucleic acids. After another round of centrifugation to pellet nucleic acids, the cleared supernatant containing C_2ELP was transferred to a clean centrifuge tube. The tube was heated to 45°C in presence of 1M NaCl to precipitate C_2ELP. A warm centrifugation at 45°C was carried out to pellet C_2ELP. The supernatant was then discarded and the pellet

was re-solublized in PBS in the presence of 10 mM DTT. Another cold spin at 4°C was performed to remove insoluble contaminants. This cycle was repeated two more times. For the final resuspension step, C_2ELPwas resuspended in purified water and then lyophilized and stored at 4°C.

5.2.1.3 C_2ELP characterization

The lyophilized C_2ELP was resuspended in 1X phosphate buffer saline (PBS). The resuspended material was then subjected to SDS-PAGE under denaturing conditions in order to determine the purity of the polypeptide. The gel was then stained with simply blue safe stain (Invitrogen, Carlsbad, CA) to visualize the proteins. As seen in Figure 28, C_2ELP corresponds to a molecular weight of ~22kDa.

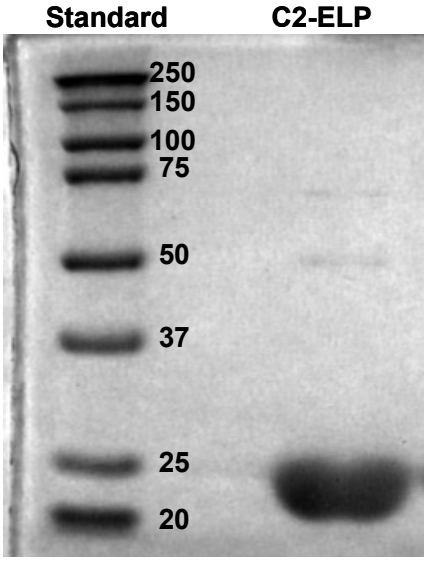

Figure 28.Denaturing SDS-PAGE analysis of C_2ELP employed in the current study.
The molecular weight of the polypeptide was 22kDa.

5.2.2 Determination of T_t of C_2ELP

The inverse transition temperature (T_t) of C_2ELP was characterized by monitoring the absorbance of C_2ELP solution at 610 nm as a function of temperature with a UV-visible spectrophotometer (Beckman DU530) in 0.5X PBS. Briefly, 1 mL of C_2ELP was placed in a disposal cuvette. The temperature of C_2ELP was tuned by placing the C_2ELP-containted cuvette into a Precision 288 Digital Water Bath (Thermo Scientific) and was recalibrated by Digi-Sense Type J Thermocouple before absorbance measurement. The absorbance of C_2ELP was monitored at 610 nm with a UV-visible spectrophotometer (Beckman DU530) immediately after withdrawing the cuvette out of the water bath. The T_t is defined as the temperature at half the maximum absorbance value of C_2ELP solution. The temperature response of the C_2ELP indicated a T_t value of 33.4°C (Figure 29). The absorbance at 610 nm was selected for determining the T_t value since gold nanorods show the lowest absorbance at this wavelength (Figure 30) as a result of which, the absorbance of the solution is indicative of turbidity increase due to C_2ELP alone.

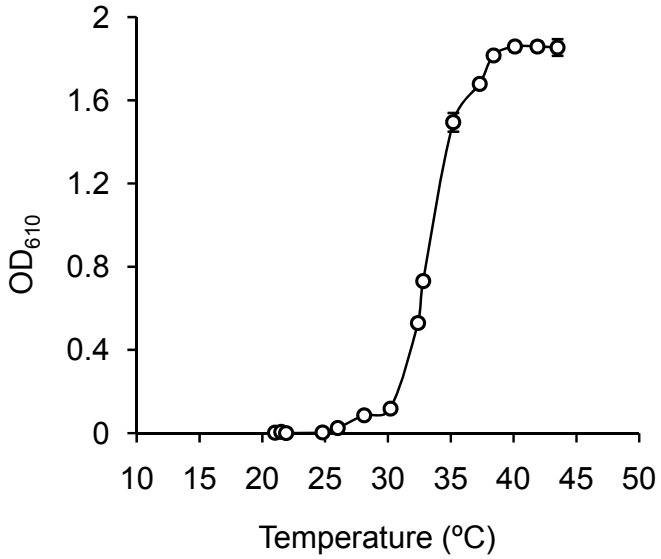

Figure 29.Temperature-dependent phase transition of C_2ELPas measured by change in optical density at 610 nm (OD_{610}) indicates a transition temperature (T_t) of 33.4ºC.

5.2.3 Generation of Gold Nanorods

Gold nanorods were synthesized using the seed-mediated method as described by El-Sayed et al.[155] Following the same procedure in Chapter 3.2.2, this method was employed to generate two different gold nanorod populations that possessed absorbance maxima at (λ_{max}) at 710nm and 810nm, respectively. Each nanorod population was diluted with DI water to an optical density ~0.5 (Figure 30).

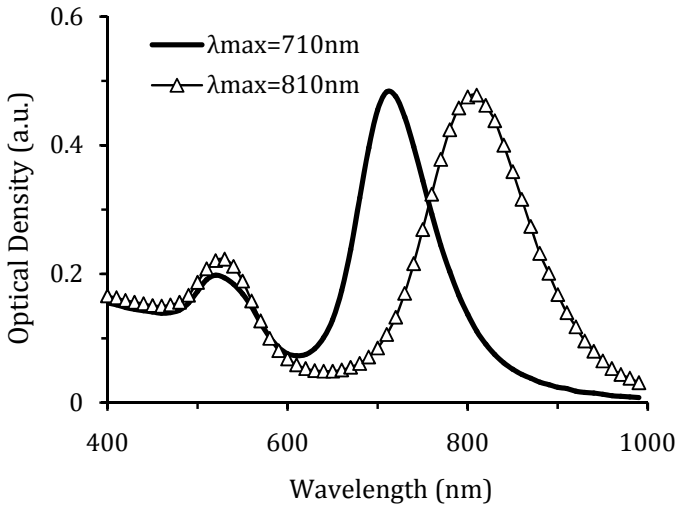

Figure 30.Absorption spectra of gold nanorods generated using the seed-mediated method.
The nanorods demonstrated peak absorbances at 710 nm and 810 nm and are denoted as GNR (710 nm) and GNR (810 nm), respectively.

5.2.4 Generation of Gold Nanorod / C_2ELP Nanoassemblies

C_2ELP (2 mg/mL in 1X PBS) was added into deionized (DI) water at a 1:1 volume ratio, to form C_2ELP solution (1 mg/mL in 0.5X PBS; "C_2ELP alone"). Gold nanorods (1mL; λ_{max}=710 nm or 810 nm) in DI water having an absorbance of ~0.5 were added to an equal volume (1 mL) of 1X PBS in order to bring the final concentration to 0.5X PBS ("GNR alone"). The absorbance of the resulting solution was verified to be similar for all cases following mixing. C_2ELP (T_t= 33.4°C) was self-assembled on gold nanorods overnight leading to formation of the nanoassemblies via gold-thiol bonds ("GNR- C_2ELP assemblies"). Briefly, 1mL of C_2ELP (2 mg/mL in 1X PBS) was mixed with 1 mL of GNR dispersion in DI Water to form a 2 mL GNR-C_2ELP dispersion (1 mg/mL in 0.5X PBS). Prior to self-assembly, 20 mg of Reductacryl® resin (EMD Biosciences Inc.) were added to C_2ELP (1 mL) for 15 min in order to reduce the cysteines in the polypeptide.

Reduced C_2ELP was separated from the Reductacryl® resin by centrifugation at 13,000 rpm for 10 minutes and immediately added to gold nanorods at a volumetric ratio of 1:1 and stirred overnight at room temperature. Equivalent concentrations of gold nanorods (without self-assembled C_2ELP) and C_2ELP (without gold nanorods) were used as controls in the subsequent experiments.

5.2.5 Optical Response of GNR-C_2ELP Nanoassemblies

A titanium CW sapphire (Ti:S) laser (Spectra-Physics, Tsunami) pumped by a solid state laser (Spectra-Physics, Millennia) was used for the laser irradiation experiment. The excitation source was tuned to 720 nm or 810 nm in order to coincide with the longitudinal absorption maximum of the GNR-C_2ELP nanoassemblies and GNRs in the two cases, respectively. In case of GNR (λ_{max}= 710 nm), self assembly with C_2ELP resulted in a slight red shift of the absorbance peak to 720 nm resulting in GNR-C_2ELP (λ_{max}= 720 nm) (Figure 31). As a result, the laser was tuned to the absorption maximum of the nanoassemblies. In the second case, GNR (λ_{max}= 810 nm), laser wavelength that corresponded with the absorption maximum of the nanorods was used. The wavelength of the laser was tuned to the same wavelength as the maximal absorbance of the GNR-C_2ELP nanoassemblies to maximize photothermal effect efficacy of the nanorods.

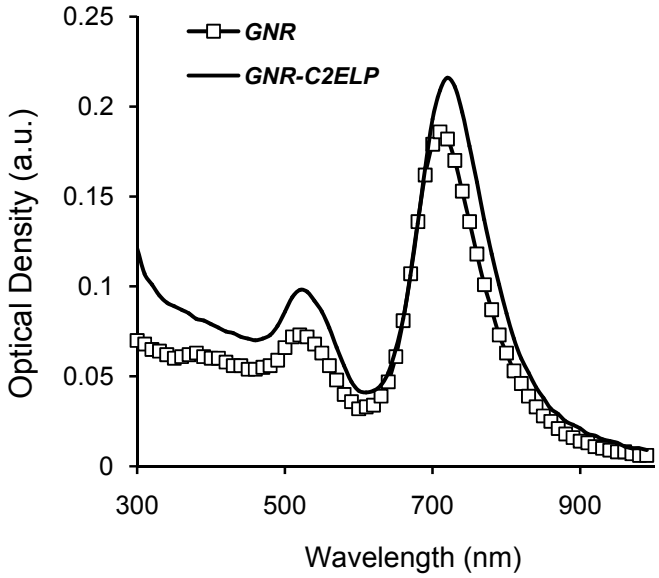

Figure 31.Absorbance spectrum of GNR (λ_{max}= 710 nm) and GNR (λ_{max}= 710 nm)-C_2ELP nanoassemblies at 25^{o}C (<T_t).
A red-shift can be observed in the longitudinal peak in case of the nanorod polypeptide assemblies resulting in peak absorbance at 720 nm of the GNR-C_2ELP (λ_{max}= 720 nm) nanoassemblies.

As with the T_t measurements before, absorbance at 610 nm was employed for evaluating the optical response of the GNR-C_2ELP nanoassemblies. The optical response of 1 mL GNR-C_2ELP assemblies in response to laser exposure in 0.5X PBS was first characterized by monitoring the absorbance at 610 nm using with a UV-visible spectrophotometer (Beckman DU530) as a function of the employed laser power. Briefly, GNR, C_2ELP, and GNR-C_2ELP dispersion (1 mL in disposal cuvettes) were exposed to laser light at different power densities (0-510 mW) for 5 minutes. The laser, tuned to 720 nm or 810 nm (~2 mm diameter beam) was focused through the center of the cuvette in a vertical fashion. The temperature of the all solutions and dispersions were monitored as a function of the laser power using a Digi-Sense Type J Thermocouple.

In order to obtain the kinetics of the optical response and the corresponding temperature response, cuvettes containing 1 mL of GNR-C_2ELP dispersion, GNR dispersion or C_2ELP solution were exposed to a maximum laser power (460 mW for GNR (λ_{max}=720 nm); 510 mW for GNR (λ_{max}=810 nm) for different periods of time (0-10 min) beginning at room temperature. The optical response was characterized by monitoring the absorbance at 610 nm (OD_{600}) as a function of time with a UV-visible spectrophotometer (Beckman DU530); as before, the kinetics of the temperature response were monitored using a Digi-Sense Type J Thermocouple.

5.3 Results and Discussion

Environmentally responsive biomolecules and nanoparticle-biomolecule systems are being actively pursued with an eye towards enhancing sensing, therapeutic, and device capabilities[222]. Temperature-based control is a powerful strategy for generating robust environmentally responsive systems. However, localized control of temperature can be of importance in biological applications including tumor-targeted hyperthermia[223], functional devices[224], and cell patterning[225]. The temperature-responsive properties of elastin-like polypeptides (ELPs) were interfaced with the ability to remotely tune the thermal response of gold nanorods using near infrared irradiation, in order to generate optically responsive nanoparticle-polypeptide assemblies.

A 22 kilo Dalton (kDa), cysteine-containing elastin-like polypeptide (C_2ELP; Figure 28 and 29), was expressed in E. Coli and purified as described in the

methods section previously[221]. The inverse transition temperature (T_t) of C_2ELP was experimentally determined to be 33.4^{o}C (Figure 29). Gold nanorods (GNRs) (710 nm and 820 nm; Figure 30)were generated using the seed-mediated chemical synthesis method[155]. C_2ELP (T_t=33.4^{o}C) was first reduced using Reductacryl® (in order to reduce cysteines) and then self-assembled on GNR (λ_{max}= 710 nm). Upon incubation with C_2ELP, the maximal absorbance peak showed a slight red-shift to 10 nm due to the self assembly of the polypeptide on the nanorods[226] (Figure 31) indicating the formation of GNR-C_2ELP (λ_{max}= 720 nm) nanoassemblies.

The optical response of the GNR-C_2ELP (λ_{max}= 720 nm) nanoassemblies was investigated using near infrared (NIR) laser-irradiation. Figure 32a shows the change in absorbance as a function of laser power following exposure of the GNR-C_2ELP (λ_{max}= 720 nm) nanoassemblies to a 720 nm NIR laser for 5 minutes. While no change in dispersion optical density was observed for laser powers below 300 mW, a sharp transition and strong optical response were observed for laser powers in excess of 350 mW, indicating that energy from the laser was converted into heat due to the plasmonic properties of gold nanorods. This, in turn, resulted in an increase in temperature of the self-assembled elastin, leading to the aggregation of GNR-C_2ELP (λ_{max}= 720 nm) and the observed optical response. I measured the solution temperature using a J-thermocouple (Figure 32b) and correlated it with the profile with laser power employed in order to investigate the observed photothermal response. The observed temperature at a laser power of 300 mW was 32.8°C, which is below the T_t (33.4°C) of the self-

assembled C_2ELP. However, when the laser power was increased to 400 mW, the temperature of the GNR- C_2ELP dispersion reached 35.3°C (>T_t) following the five minute NIR exposure. This resulted in a sharp increase in the optical density, indicating that laser powers higher than 350 mW were required for inducing the optical response. The range of laser power (350-650 mW) and / or power densities (5-7 W/cm^2) that induce the optical response described in the above experiments is either significantly lower[227,228] or comparable[229,230] to those used in other reports in the literature on NIR-mediated photothermal activation of gold nanoparticle-based systems. These results are consistent with expected behavior in that, the optical response due to ELP self-assembly was seen beyond a threshold laser power which was necessary to raise the ELP temperature beyond its corresponding T_t.

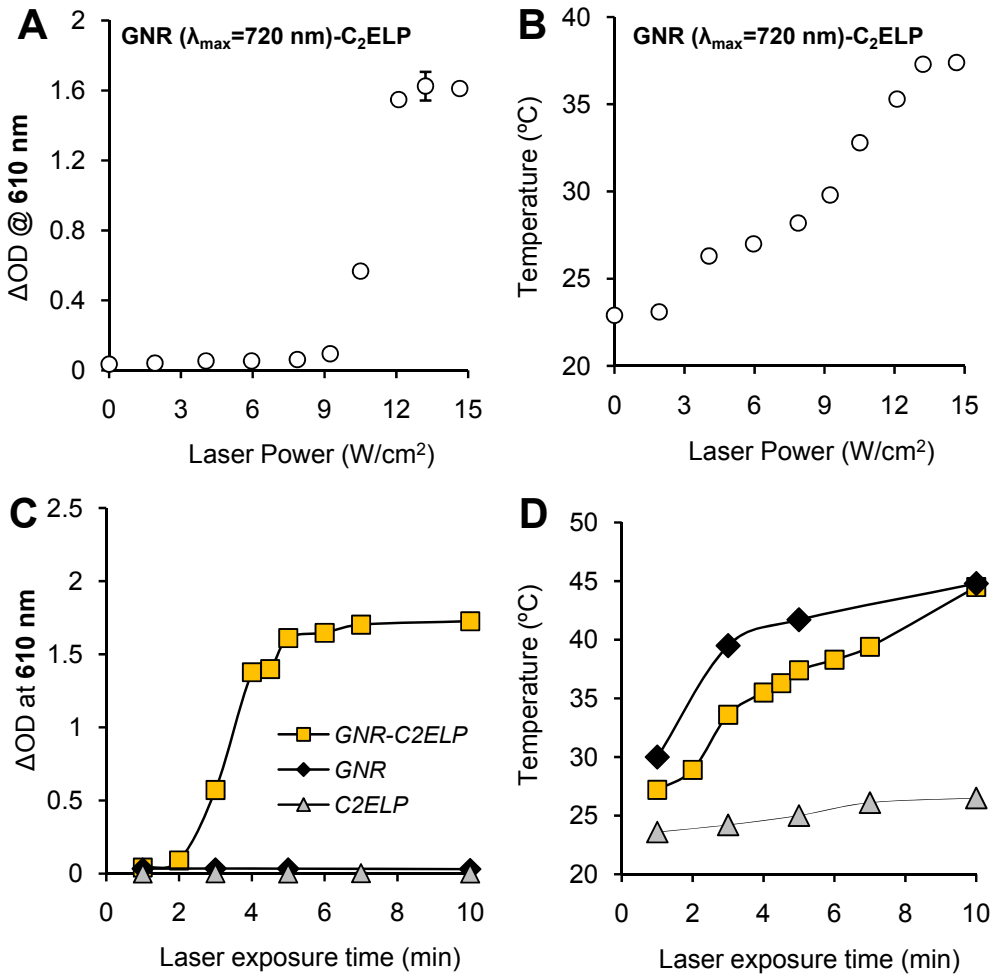

Figure 32.Optical response (in optical density at 610 nm) of gold nanorod (GNR; λ_{max}= 720 nm)-C_2ELP assemblies.
(a) Optical response and (b) temperature response as a function of laser power following 5 minute exposure to 720 nm laser. Kinetics of (c) optical and (d) temperature response of GNR-C_2ELP assemblies following excitation with 720 nm laser. Lines connecting data points are for visualization only.

The kinetics of the optical response were then investigated by measuring the absorbance of GNR-C_2ELP (λ_{max}= 720 nm) as a function of time(Figure 32c); in addition the kinetics of the optical response were correlated with the kinetics of temperature increase (Figure 32d) in order to explain the photothermal effect. Figure 32c shows the optical response of GNR-C_2ELP (λ_{max}= 720 nm), GNR, and

C_2ELP as a function of laser exposure time. The laser power was fixed at the maximum power (460 mW) in order to reliably generate the maximal optical response. The optical density of the GNR-C_2ELP (λ_{max}= 720 nm) nanoassemblies increased sharply after two minutes of laser exposure and reached a plateau after five minutes. Although the maximal optical response was observed five minutes following laser exposure, a detectable response was observed after only two-and-a half minutes of laser exposure time. In contrast, no change in optical density was seen either in the case of nanorods alone or C_2ELP alone, indicating that the optical response was specific to nanorod-polypeptide assemblies. Figure 33 shows digital snapshots of the time-dependent phase transition and optical response of GNR-C_2ELP (λ_{max}= 720 nm) nanoassemblies as a function of time following laser exposure (laser power= 460 mW); the respective laser exposure times (in minutes) are shown by the timer in the background. As seen in the figure, the GNR-C_2ELP (λ_{max}= 720 nm) dispersion continued to be optically clear after one minute of laser exposure time. However, the solution turbidity increased after three minutes of laser exposure and reached a maximum in five minutes. The optical density remained invariant following five minutes of laser exposure consistent with the absorbance measurements in Figure 32c.

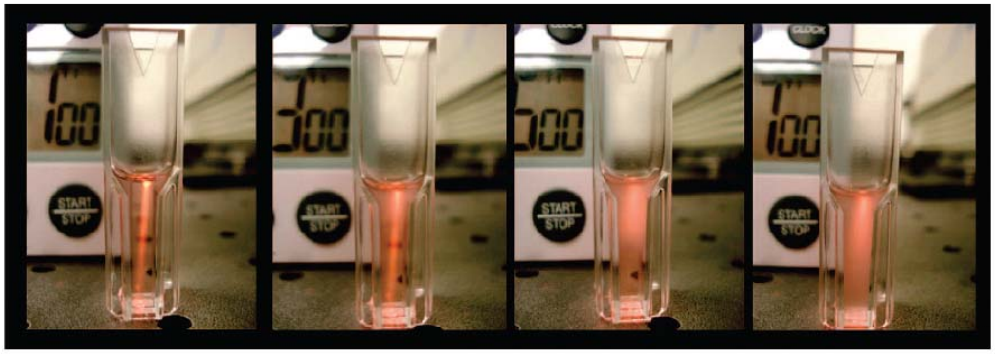

Figure 33.Digital images of the optical response of GNR (λ_{max}= 720 nm)-C_2ELP nanoassemblies as a function of laser exposure time.
Change in optical density remained invariant after 5 minutes following laser exposure. The corresponding laser exposure times can be seen in the timer in the background.

The temperature response of the GNR-C_2ELP (λ_{max}= 720 nm) was determined as a function of time and compared with the response of solution containing C_2ELP alone and nanorods dispersion alone. The observed temperatures of the GNR-C_2ELP dispersion were 33.6°C, 35.5°C, and 37.4°C following 3, 4, and 5 minutes of exposure with 720 nm laser, respectively (Figure 32d). The time required for the solution temperature to increase beyond the transition temperature of C_2ELP following NIR irradiation was well correlated with the observed change in solution optical density (Figure 32c). In addition, the kinetics of temperature increase of GNR-C_2ELP nanoassemblies closely followed the rise in temperature of GNR alone. Thus, although the temperature of GNRs alone rose faster than GNR-C_2ELP nanoassemblies (as may be expected), no change in optical response was observed in the former case (Figures 32c and 32d). No change in solution temperature was observed with C_2ELP alone upon exposure to the laser, which explains the lack of optical response in this case. In order to examine if the observed optical response was reversible, GNR-C_2ELP (λ_{max}= 720 nm)

assemblies were subjected to five alternating cycles in which the laser exposure was turned on for 5 minutes and then turned off for 5 minutes. Following laser exposure (laser power = 460 mW) for five minutes, the absorbance of the dispersion increased up to 1.2 absorbance units indicating formation of the aggregated nanoassemblies (Figure 34). The optical density of the dispersion returned to baseline values in approximately two minutes following removal of the laser excitation. This behavior was reproducible over the five cycles tested, indicating that the optical response of the GNR-C_2ELP assemblies was indeed reversible and reproducible across multiple cycles.

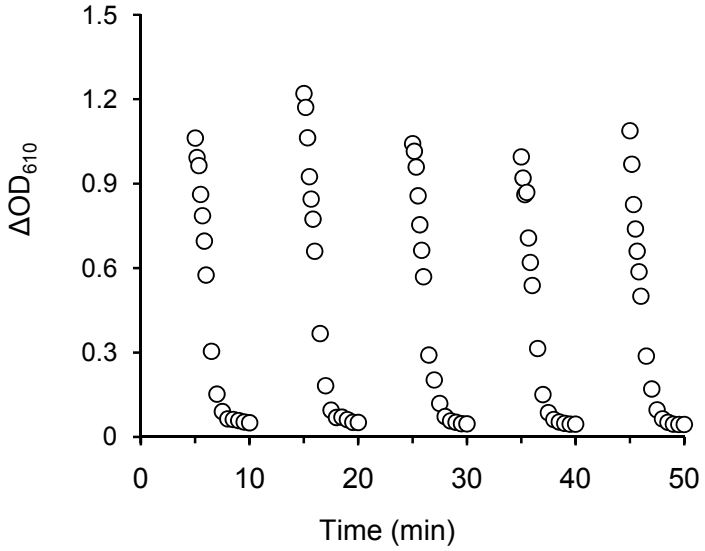

Figure 34. Reversibility of optical response of GNR-C_2ELP (λ_{max} = 720 nm) assemblies.
GNR-C_2ELP assemblies were subjected to alternating cycles laser exposure in which the laser was turned on and off for five minutes each. The absorbance of the suspension was noted as a function of time.

The optical response was also evaluated with another set of gold nanorods that demonstrated peak absorbance at 810 nm. In the case of these nanorods, i.e.

GNR (λ_{max}= 810 nm), the laser wavelength was tuned to the maximal peak absorbance of the nanorods (i.e. 810 nm) and not to the peak absorbance of the nanoassemblies. ELP self-assembly was shown to result only in a minor red-shift of the peak absorbance peak (Figure 31) of the nanorods. As a result, the laser was tuned to the peak absorbance of the nanorods in this case. As with the GNR-C_2ELPλ_{max}= 720 nm) assemblies, the temperature profile (Figure 35b) of these nanoassemblies closely followed the laser power employed (Figure 35a). The optical response was specific to the GNR-C_2ELP nanoassemblies; no change in absorbance was seen with solutions containing C_2ELP alone and nanorods alone (Figure 35c). Finally, the optical response of the GNR-C_2ELP nanoassemblies closely followed the kinetics of temperature increase (Figure 35d). The increase in temperature in case of GNR (λ_{max}= 810 nm)-C_2ELP closely followed that of GNR (λ_{max}= 810 nm) alone. However, the optical response was seen only in case of the former due to the presence of the self-assembled C_2ELP. These results are consistent with those observed with the GNR-C_2ELP (λ_{max}= 720 nm) assemblies indicating that the optical response can be obtained with nanorods that absorb at different wavelengths of the near-infrared region of the absorption spectrum, which further expands the application range of these nanoassemblies.

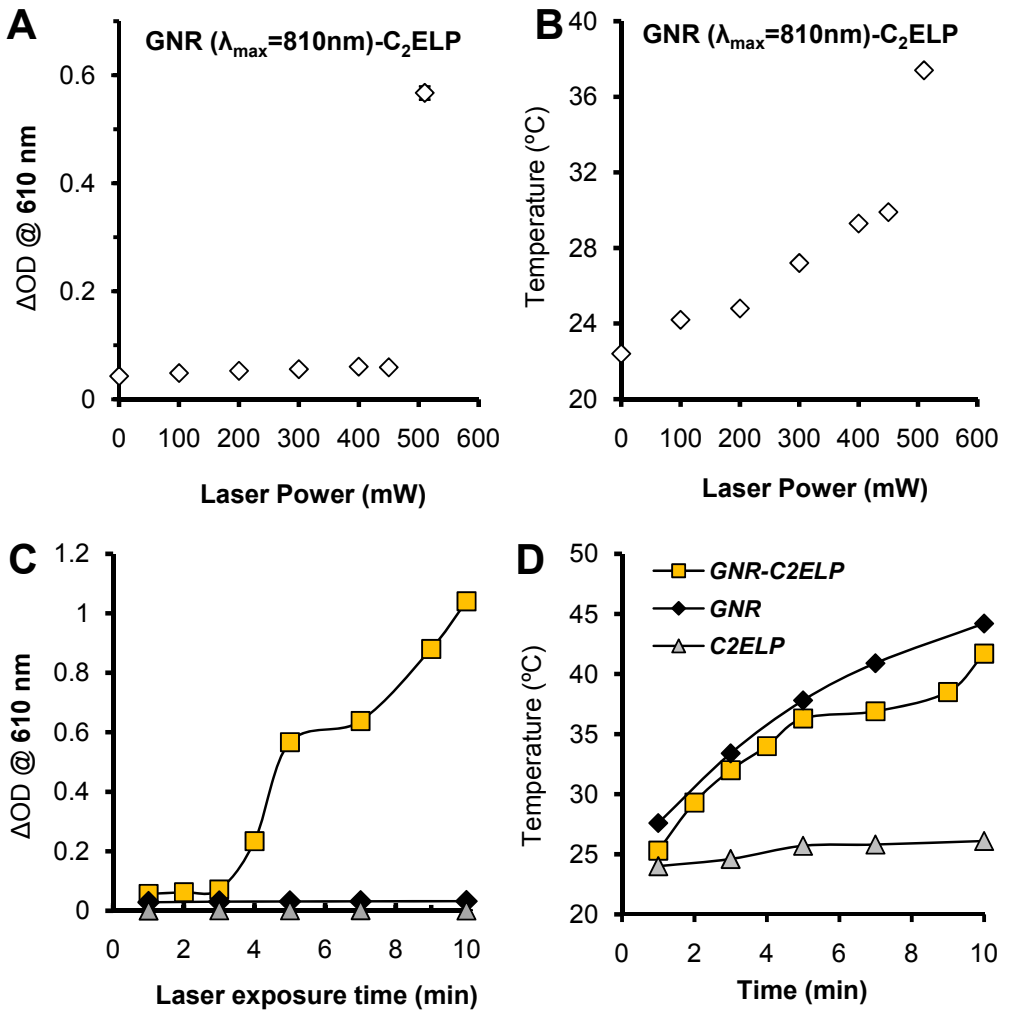

Figure 35.Optical response (in absorbance units at 610nnm) of gold nanorod (GNR; λ_{max}= 810 nm)-C_2ELP assemblies.
(a) Optical response and (b) temperature response as a function of laser power following 5 minute exposure to 810 nm laser. Kinetics of(c) optical and (d) temperature response of GNR-C_2ELP nanoassemblies following excitation with 810 nm laser. Lines connecting the data points are for visualization only.

5.4 Conclusions

In this Chapter, I have investigated novel optically responsive polypeptide-based nanoassemblies in which, heat transfer from NIR-absorbing gold nanorods resulted in a conformational change in the self-assembled elastin-like polypeptide (ELP) leading to a detectable optical response. In addition to GNRs, carbon

nanotubes[231,232] and magnetic nanoparticles[233-235], which have been reported to generate heat upon exposure to laser or RF field, may be interfaced with ELP for thermal, photothermal, and magnetothermal applications (e.g. sensing). Such ability to control nanoscale assembly and nanomaterial properties by optical manipulation can be exploited in the development of novel sensors, drug delivery systems, functional molecular and nanoscale devices, and imaging agents.

CHAPTER

6. Investigation of Phase Separation Behavior and Formation of Plasmonic Nanocomposites from Polypeptide-Gold Nanorod Nanoassemblies

6.1 Introduction

Chapter 5 demonstrated the remote and reversible control of the photothermal response of GNR-C_2ELP nanoassemblies. This chapter investigates the use of multiple cysteines within the polypeptide sequence in order to facilitate irreversible cross-linking with GNRs leading to GNR-ELP nanocomposites. It was hypothesized that increasing the number the thiol-containing amino acid, cysteine, within the ELP sequence, from C_2ELP to C_{12}ELP (or C_8ELP), will facilitate inter-polypeptide and polypeptide-gold nanorod (GNR) cross-linking, resulting in the formation of GNR-C_nELP nanocomposites. Specifically, the effects of CTAB (used for templating the synthesis of gold nanorods), and GNR concentrations on modulating the C_{12}ELP transition temperature and GNR-C_{12}ELP nanocomposite formation were investigated. Moreover, the phase separation behavior and kinetics of GNR-C_{12}ELP nanocomposite formation were followed using a mathematical model. These nanocomposites have potential applications in drug delivery materials, wound healing and related topical skin diseases, scaffolds for tissue engineering and antibacterial films.

6.2 Materials and Methods

6.2.1 Materials

Cetyltrimethyl ammonium bromide (CTAB), gold (III) chloride trihydrate (HAuCl4•3H2O), L-ascorbic acid, sodium borohydride and silver nitrate were obtained from Sigma-Aldrich. Dithiothreitol (DTT) and Reductacryl® resin were purchased from EMD. All chemicals were used as received without further purification.

6.2.2 Gold Nanorod Synthesis

Gold nanorods were synthesized using the seed-mediated method[155] as described in Chapter 3.2.2 previously. This method was employed for generating gold nanorods (GNRs) that possessed absorbance maxima (λ_{max}) in the near infrared (NIR) region of the light absorption spectrum. Specifically for this study, nanorod aliquots, with an initial CTAB concentration of 100 mM, were pelleted by centrifugation (6000 rcf, 10 min), following which, the clear supernatant was removed, and resuspended in nanopure water to various final volumes. Further centrifugation, decantation and dilution steps allowed the generation of a series of nanorod samples(0.1-2.9mM) with various concentrations of CTAB (0.5-8 mM).Note that CTAB concentration (0.0013-0.038 mM)bound to the surface of the gold nanorods(0.1-2.9 mM)is negligible compared to free CTAB molecules (0.5-8 mM) in the dispersion[236]. In all cases, the concentration of gold in GNRs was determined using inductively coupled plasma optical emission spectrometry (ICP-OES, iCAP 6000 Series, Thermo Electron Corporation), and are reported in terms of millimolar units.

6.2.3 Synthesis, Expression, and Purification of Cysteine containing Elastin-like Polypeptides (ELPs)

Elastin-like polypeptides containing eight or twelve cysteines (C_8ELP or C_{12}ELP), were generated using recursive directional ligation method described previously[237]. C_8ELP and C_{12}ELP respectively contain eight and twelve cysteines residues (shown in bold) in the sequence: MVSACRGPG-(VG VPGVG VPGVG VPGVG VPGVG VPG)$_8$-(VG VPGVG VPGVG VPG**C**G VPGVG VPG)$_{8\ or12}$-WP. Both C_8ELP and C_{12}ELP were generated, expressed, purification lyophilized and stored at room temperature as described previously in Chapter 5.2.1[237].

6.2.4 Determination of Transition Temperature (T_t)

The transition temperatures (T_t) of C_8ELP and C_{12}ELP were characterized as described in Chapter 5.2.2 previously. The temperature response of the C_8ELP and C_{12}ELP indicated transition temperature (T_t) values of 31.3°C and 30.5°C.

6.2.5Formation of Elastin-like Polypeptide-Gold Nanorod (GNR-C_{12}ELP) Nanoassemblies

Gold nanorods, in presence of different CTAB concentrations (described previously) were incubated with C_{12}ELPovernight at 4°C, leading to formation of the nanoassemblies mediated by gold-thiol bonds[237,238]. Briefly, prior to self-assembly, C_{12}ELP was treated with Reductacryl® resin for 15 min at a 1:5 weight ratio, in order to reduce the cysteines in the polypeptide chain. Reduced C_{12}ELP (2 mg/mL in 1X phosphate buffered-saline or PBS) was separated from the Reductacryl® resin by centrifugation at 8,000 rcf for 10 min and mixed with GNR

dispersions at a volumetric ratio of 1:1. This resulted in the formation of a series of GNR-C_{12}ELP nanoassemblies in 0.5X PBS and differing CTAB concentrations. It should be noted that the concentration of C_{12}ELP was always kept at 0.023 mM, while the CTAB and GNR concentrations were varied from 0.25 to 4 mM and 0.05 to 1.45 mM, respectively.C_{12}ELP solutions with various concentrations of CTAB (no gold nanorods) were prepared in 0.5X PBS as controls.

6.2.6Preparation of Solid-Phase GNR-C_{12}ELP Nanocomposites from Liquid-Phase Nanoassemblies

Nanocomposites were prepared by incubating 1.5 mL GNR-C_{12}ELP nanoassemblies in a 1 cm diameter home-made acrylic column deviceat37°C (or 60°C) for 4 h. This system resulted in the formation of the nanocomposite film on a circular cover slip originally placed at the bottom of the device. Following nanocomposite formation, the clear supernatant was removed from the column, and the absorption spectra of the GNR-C_{12}ELP nanocomposite were determined using a plate reader (Biotek Synergy 2) at room temperature; absorption spectra were measured between 400-999 nm with 5 nm intervals.

6.2.7Kinetics of Phase Separation of Liquid-Phase Nanoassemblies leading to Formation of Solid-Phase Nanocomposites

Aliquots of 200 µLGNR-C_{12}ELP nanoassemblies and C_{12}ELPsolutions, initially at 4°C, were placed in a plate reader set to 37°C in order to facilitate phase separation and formation of nanocomposites. A spectrophometric assay was employed to monitor the change in sample turbidity as a function of time in order

to investigate the phase separation process. The optical densities of C_{12}ELPsolution and GNR-C_{12}ELP dispersion were monitored at 800 nm and at λ_{max} of GNR, respectively, as a function of time and CTAB concentration. The temperature, which increased from 4 to ~37°Cin a nonlinear fashion, was monitored as a function of time using a FLUKE 54 II (Type K) thermometer throughout the incubation period (Note: the solution temperature, remained steady in the range of 35 ± 2°Cafter 30 minutes).

6.2.8Modeling Phase Transition and Nanocomposite Formation Kinetics

A double-exponential model, described previously in the literature[239], was used to fit the optical density curve of the phase separation process leading to nanocomposite formation in Matlab (The MathWorks, Natick MA). The model was used mainly to compare nanocomposite formation under the different conditions employed.

$$y = y_0 - ae^{-k_c t} + be^{-k_m t} \quad (7)$$

In this model, y and y_0 represent the optical densities at t and t close to ∞, respectively. Coacervation and maturation constants were indicated by k_c and k_m, respectively, while *a* and bare proportionality factors. In this model, the velocity of coacervation, V_c is defined as a*k_c and the velocity of maturation, V_m, is defined as b*k_m.

6.2.9Photothermal Properties of Nanocomposites

A titanium CW sapphire (Ti:S) laser (Spectra-Physics, Tsunami) pumped by a solid-state laser (Spectra-Physics, Millennia) was used in order to investigate the

photothermal properties of the nanocomposites prepared under different conditions. The excitation source was tuned to overlap with the longitudinal maxima of the nanocomposites. A GNR-C_{12}ELP nanocomposite film was placed at the bottom of a 24-well plate (Corning) and covered with 500 µl of 1X PBS as the supernatant. Laser light (20 W/cm^2) was focused at the center of the nanocomposite for 15 min. The supernatant temperature was monitored by FLUKE 54 II (Type K) thermocouple as a function of time during laser exposure. Laser irradiation of 1X PBS solution in a 24-well plate in the absence of the nanocomposite film was used as control; temperature remained invariant at 24± 0.5°C after 15 min laser exposure.

6.2.9 Dissolution of GNR-C_{12}ELP Nanocomposite

For dissolution experiments, the PBS supernatants were removed from individual GNR-C_{12}ELP nanocomposites and replaced with equivalent volumes of 10 mM dithiothreitol (DTT) solution for 30 minutes at 4°C, following which, absorbance spectra were determined as a function of time in order to investigate dissolution kinetics. Detailed dissolution kinetics of GNR-C_{12}ELP nanocomposites were investigated using three different DTT concentrations (1, 5, 10 mM). In this experiment, the PBS supernatants were removed from individual GNR-C_{12}ELP nanocomposites and replaced with equivalent volumes a reducing agent, dithiothreitol (DTT); the supernatant optical density was monitor using plate reader at a fixed wavelength (in this case, the λ_{max} of the GNR spectrum) for 2 hours at 4°C. The dissolution percentage was calculated based on the initial, final and real-time measurement values of OD.

6.2.10Fourier Transform Infrared (FT-IR) Spectroscopy

Gold nanorods and C_8ELP and C_{12}ELP-based nanocomposites were loaded on a germanium attenuated total reflectance (GATR) crystal such that they covered the central area of the crystal. The sample chamber was equilibrated to approximately 4 mbar pressure in order to minimize the interference of atmospheric moisture and CO_2. The absorption spectrum was measured between 650 and 4,000 cm-1 using a Bruker IFS 66 v/S FT-IR spectrometer and the background spectrum was subtracted from all sample spectra as described previously.[165]

6.2.10 Field-Emission Scanning Electron microscopy (SEM)

SEM samples were prepared by placing GNR-C_{12}ELP nanocomposites on a flat alumina substrate. The nanocomposite on the substrate was allowed to dry out in open laboratory atmosphere. SEM images were obtained with an environmental field-emission SEM (PHILIPS FEI XL-30 SEM) operating an accelerating voltage of 25 kV, and several magnifications between 2500 and 20,000 X.

(NOTE: Nanocomposite formation kinetics study was carried out usingGNR-C_{12}ELP nanoassemblies; dissolution study and material characterization was investigated using both GNR-C_8ELP and GNR-C_{12}ELP)

6.3 Results and Discussion

In this study, I investigated factors that influenced the formation of GNR-C_{12}ELP nanocomposites, with an eye towards gaining a better understanding and control of the formation of these novel environmentally responsive materials. Schematics depicting the individual components (GNR and CTAB), GNR-ELP nanoassemblies in dispersion and solid-phase nanocomposites are shown in Figure 36. The presence of CTAB is critical for GNR formation and for maintaining GNR stability in aqueous media, although appropriate surface modification strategies can be employed instead of CTAB in order to maintain the stability of GNRs once formed[51,240,241]. Due to this key role, the effects of CTAB on the transition temperature of C_{12}ELP and formation of GNR-C_{12}ELP nanocomposites were first investigated. The role of GNR concentration on the formation of the nanocomposites was also studied.

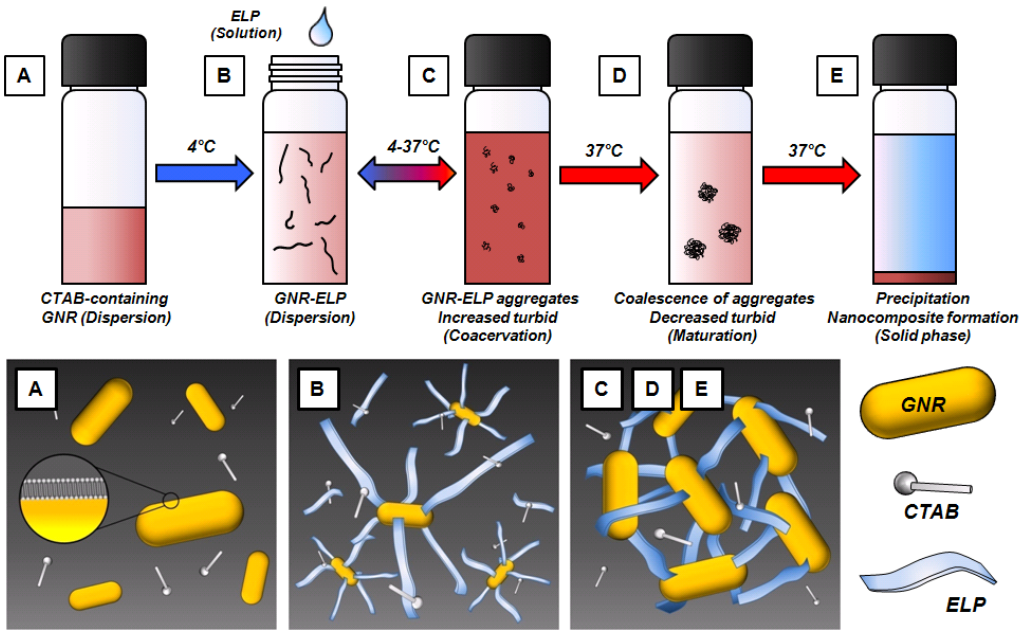

Figure 36.Schematic of the different processes involved in formation of solid-phase ELP-GNR nanocomposites.

The concentration of free CTAB molecules was controlled as described in the experimental section. (B) Cysteine-containing elastin-like polypeptides (C_nELPs; n=12 in the polypeptide repeat sequence) were self-assembled on GNRs via gold-thiol bonds, leading to the formation of GNR-ELP nanoassemblies as liquid-phase dispersions. Presence of high concentration of free CTAB molecules (> 2mM) can inhibit the self-assembly of ELPs onto GNRs. (C) Increasing the dispersion temperature of ELP-GNR nanoassemblies above its characteristic Tt resulted in the formation of ELP-GNR aggregates due to coacervation, leading to increase in turbidity. (D) Coalescence of the GNR-ELP aggregates resulted in decreased turbidity and leading to formation of solid-phase nanocomposite in a process termed maturation. (E) Precipitation of these coalesced aggregates led to the formation of solid-phase nanocomposites.

6.3.1 Effect of CTAB on Transition Temperature of C_{12}ELP Solutions

C_{12}ELP,in the absence of CTAB, demonstrated a transition temperature (T_t) at30.4±0.3°C (Figure 37), which was similar to our previous observations[238].The transition temperature (T_t) of the free C_{12}ELPunderwent a slight decrease (2.64±0.3°C; p-value <0.001) as the CTAB concentration in solution increased from 0 to 0.5 mM, but began to increase significantly at higher CTAB concentrations (≥2 mM)(Figure 38 A). In our hands, the critical micelle concentration (CMC) of CTAB at room temperature in 0.5XPBS solution (salt concentration ~75 mM)was determined to be 0.1 mM (Figure 39). This is close to previously observed values[242,243] and indicates that all CTAB concentrations in the current study were above the CMC of the surfactant.

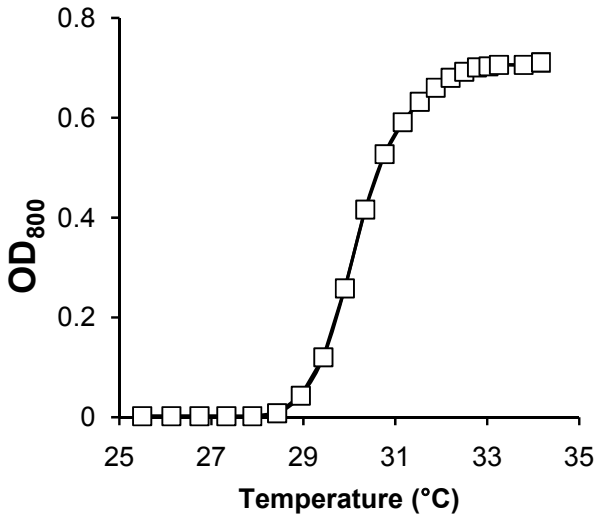

Figure 37.Temperature-dependent phase transition of C_{12}ELP
C_{12}ELP phase transition measured by the change in optical density at 800 nm (OD_{800}) indicates a transition temperature (T_t) of 30.4°C (representative plot from n=4) in the absence of CTAB. The T_t is defined as the temperature where the turbidity (optical density) reaches 50% of the maximum value. The line connecting the data points is included only to aid visualization of data.

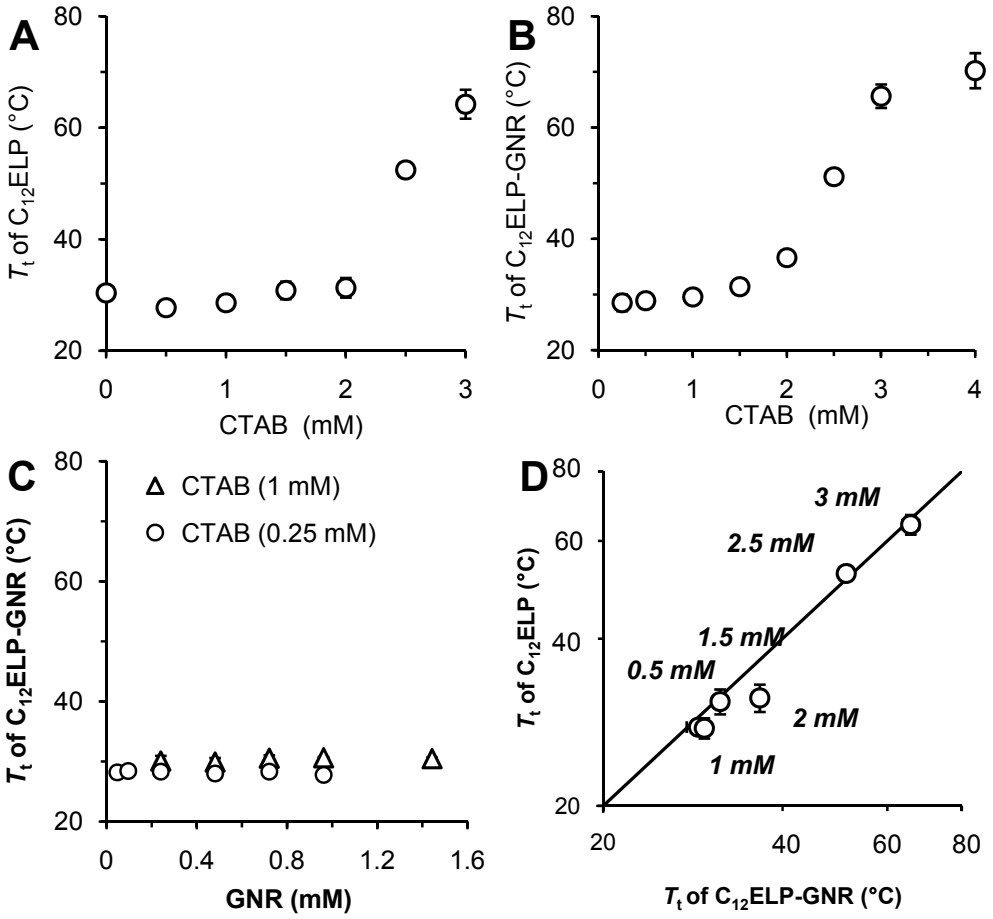

Figure 38.Transition temperatures of C12ELP and GNR-C12ELP nanoassemblies.

(A) Transition temperatures (T_t) of C_{12}ELP as a function of CTAB concentration. The T_t of C_{12}ELP increased significantly for CTAB concentrations>2 mM. (B) Transition temperature (T_t) of GNR-C_{12}ELP nanoassemblies (dispersions) as a function of CTAB concentration. Increase in T_t of nanoassemblies is significant for higher concentration of CTAB (> 2mM). (C)T_t of GNR-C_{12}ELP dispersion plotted as a function of GNR concentration suggest that the nanorods have minimal influence on the T_t of GNR-C_{12}ELP nanoassemblies.(D) Comparison of transition temperatures of GNR-C_{12}ELP andC_{12}ELPat different CTAB concentrations. The data points fall along the solid y = x diagonal line (for visualization), indicating that transition temperatures of GNR-C_{12}ELP nanoassemblies followed similar trends to those observed in case of free C_{12}ELP solutions (i.e. in the absence of GNRs).

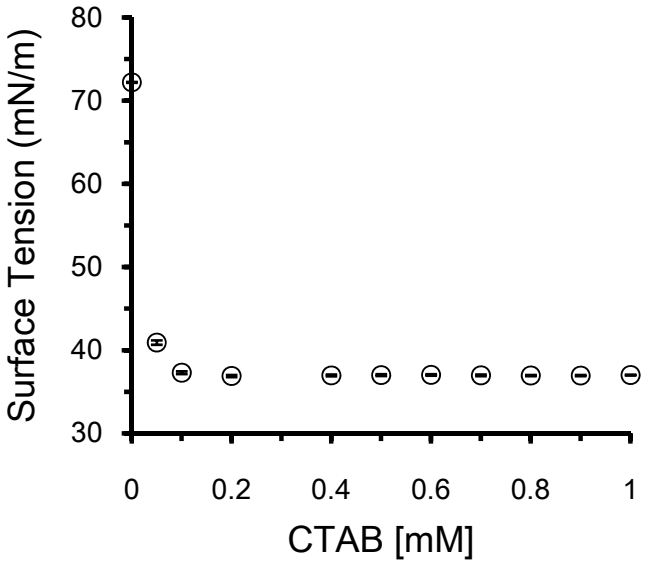

Figure 39.Critical micelle concentration (CMC) of CTAB in 0.5 X PBS (~ 75 mM salt concentration).
CMC was determined to be approximately 0.1 mM using a tensiometer (BiolinScientific, Sigma/701).

The initial modest depression of the T_t at low CTAB concentrations is presumably due to the hydrophobic interaction between CTAB and C_{12}ELP leading to salting out of the polypeptide, which is similar to previous observations[205].The increase in transition temperature at higher CTAB concentrations is presumably due to surfactant-polypeptide interactions, which, in concert with the electrostatic repulsion between the CTAB cationic head groups from the C_{12}ELP-bound micelles, reduce the propensity of ELP molecules to aggregate and coacervate[205,244].

6.3.2.Effect of CTAB and GNR concentration on Transition Temperature of GNR-C_{12}ELP Dispersions (Nanoassemblies)

C_{12}ELPs were first self-assembled on GNRs at 4°C (<T_t of C_{12}ELP) by means of gold-thiol bonds (Figure 36 A and 36B). A red-shift of approximately 10 nm was observed in the maximal absorbance peak, which indicated the formation of GNR-C_{12}ELP nanoassemblies (colloidal dispersions)[237,245](Figure 40). Up to 90% of the initial C_{12}ELP was bound to GNRs under low CTAB concentrations (e.g. 0.25 mM). However, high CTAB concentrations inhibited the binding of C_{12}ELP to GNRs (Figure 41).Thus, in presence of higher CTAB concentrations; the transition temperature of GNR-C_{12}ELP nanoassemblies is an ensemble property of both, bound and unbound C_{12}ELP.

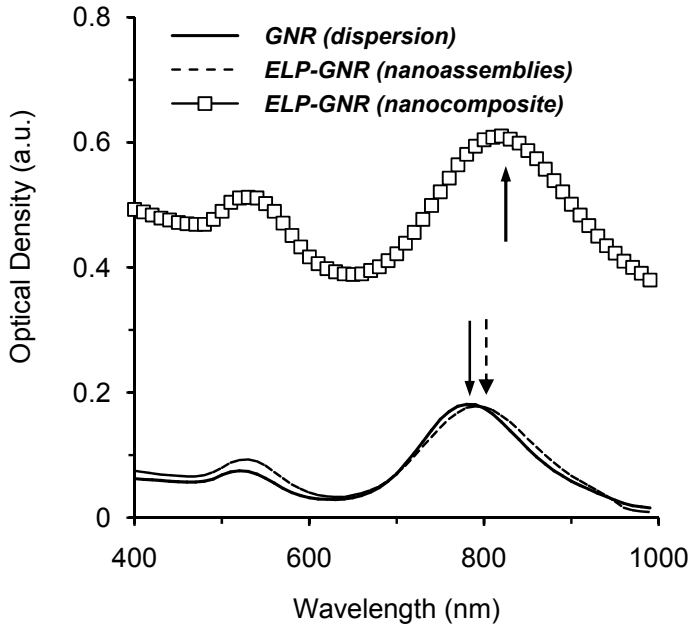

Figure 40.Absorbance spectra of GNR dispersion, GNR-C_{12}ELP nanoassemblies and GNR-C_{12}ELP nanocomposite.
Arrows indicated the maximal absorbance peak. GNR (19 µg/mL) dispersion was mixed with C_{12}ELP (1 mg/mL) overnight at 4°C (CTAB at 0.25 mM), then subjected to 37°C incubation for 4 h to allow GNR-C_{12}ELP nanocomposite formation. A 10 nm red-shift in the maximal absorbance peak, is an indicator of the self-assembly of C_{12}ELP on GNR dispersion.

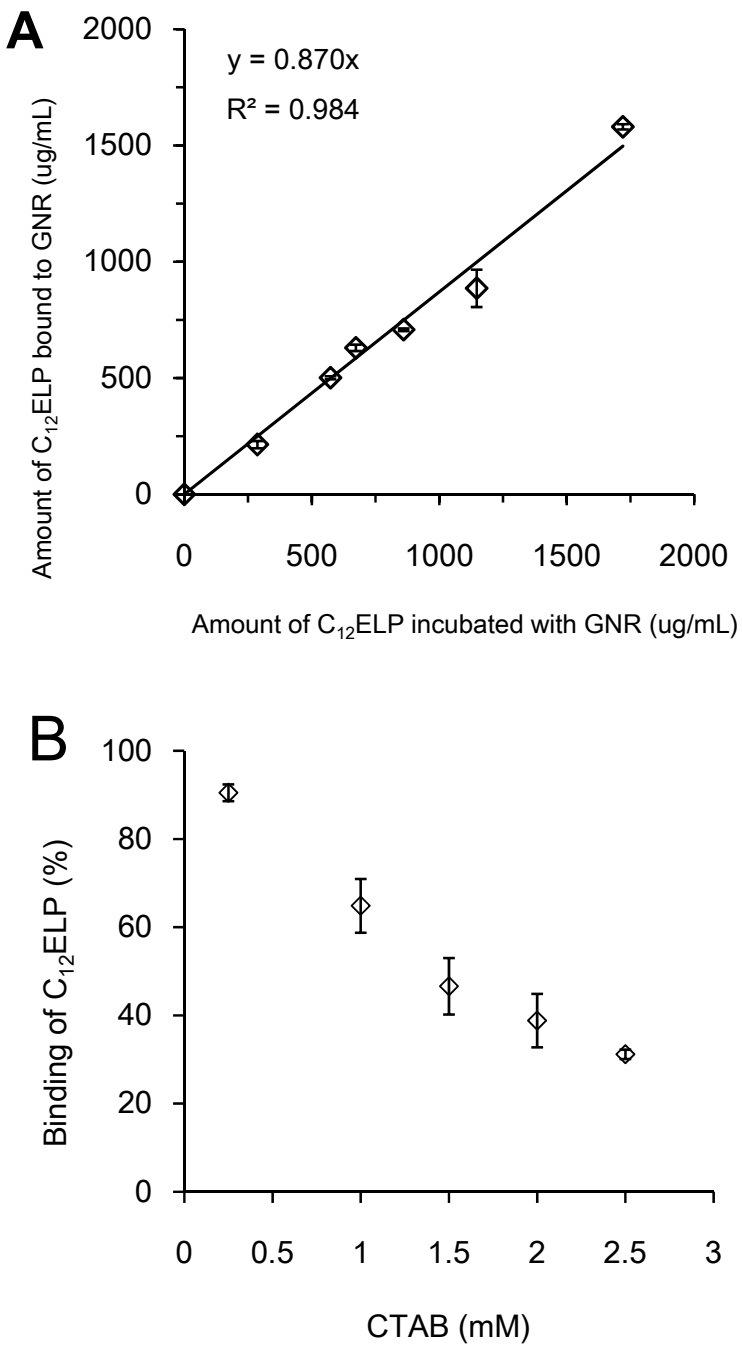

Figure 41.Binding of C_{12}ELP to GNRs.
(A) Loading of C_{12}ELP on GNRs. Aliquots of GNR (19μg/mL) samples were mixed with different amount of C_{12}ELP (0-1700 μg/mL) overnight (CTAB at 0.25 mM), the amounts of C_{12}ELP conjugated on GNR were determined using BCA protein assay. (B) Loading of C_{12}ELPas a function of CTAB concentration. Aliquots of GNR (19μg/mL) samples with various CTAB concentrations (0-2.5

mM) were mixed with C_{12}ELP (~700 µg/mL) overnight, the percentages of C_{12}ELP conjugated on GNR were determined using BCA protein assay.

Two sets of experiments were performed to investigate the influence of CTAB and GNR concentrations on the transition temperature ofGNR-C_{12}ELPdispersions. First, the transition temperature of GNR-C_{12}ELPnanoassemblieswas determined as a function of CTAB concentration at a fixed concentration of C_{12}ELP (0.023 mM) and GNRs (0.24 mM) (Figure 38B).Higher concentrations of CTAB (>2mM) resulted in significant increase in the transition temperature of the nanoassemblies. This is presumably since higher CTAB concentrations impeded the temperature-induced aggregation and collapse of C_{12}ELP.

Secondly, the effect of GNR concentration on the transition temperature of the GNR-C_{12}ELPnanoassemblieswas also studied. In this study, both CTAB (0.25 mM or 1 mM) and C_{12}ELP (0.023 mM) concentrations were held constant, while GNR concentrations were varied from0.05-1.45 mM. Changes in GNR concentration did not influence the transition temperature of GNR-C_{12}ELPdispersions (Figure 38C), indicating minimal effect of GNRs under these conditions.

These studies demonstrated that CTAB-dependent transition temperatures of GNR-C_{12}ELPnanoassemblies followed similar trends to those observed in case of free C_{12}ELPsolutions (i.e. not immobilized on GNRs), as shown by the data in

Figure 38D, most of which lie close to the y=x line. This may be expected since the transition temperature is a property of the polypeptide and not that of GNRs.

6.3.3.Phase Separation of GNR-C_{12}ELPNanoassemblies Leading to Nanocomposite Formation: Effect of CTAB Concentration

Incubating CTAB-containing gold nanorods and cysteine-containing ELPs below the transition temperature of the polypeptide resulted in the formation of well-dispersed nanoassemblies. However, incubation at temperatures above T_t results in temperature-triggered, entropy-dominated phase transition of C_{12}ELP[204,221], which, in concert with GNR-thiol and intra-and inter-molecular cysteine-cysteine cross-linking, resulted in the formation of maroon-colored plasmonic nanocomposites(Figure 42A-E).The colored appearance is due to surface plasmon resonance of gold nanorods as described previously[238].An average red-shift of 36±11 nm was observed in the maximal absorbance peak indicating further change in local refractive index environment upon nanocomposite formation(Figure 40).

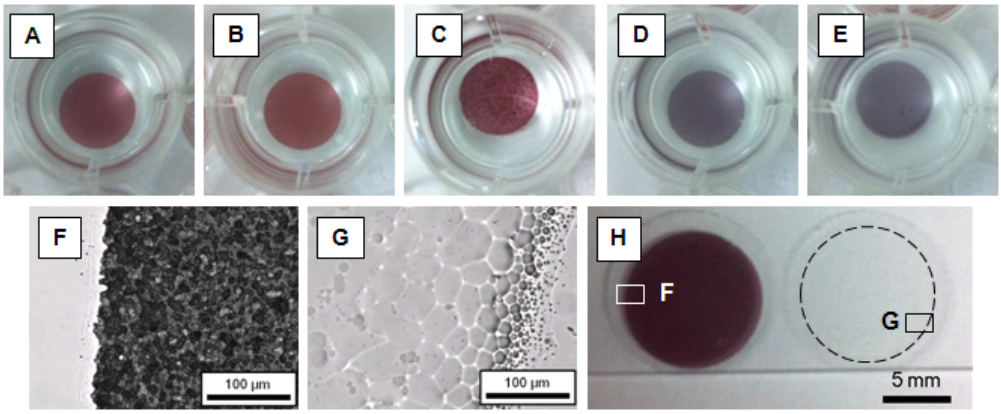

Figure 42.Optical images of solid-phase nanocomposites formed by the phase separation of GNR-C_{12}ELP dispersions at different CTAB concentrations and temperatures.
(A) 0.25 mM (37°C), (B) 1 mM (37°C), (C) 1.5 mM (37°C), (D) 2 mM (60°C) and (E) 2.5 mM (60°C) with fixed C_{12}ELP (0.023 mM) and GNR (0.24 mM) concentrations. Image (F) and (G) are phase contrast microscopy images of GNR-C_{12}ELP nanocomposite (0.25 mM CTAB concentration) and C_{12}ELP coacervates, corresponding to the digital snapshots in image (H).Incubation of GNR-C_{12}ELP nanoassemblies above their characteristic T_t results in the formation of crosslinked, stable maroon-colored nanocomposites. Incubation of C_{12}ELP alone above its characteristic T_t resulted in coacervate formation.

The effect of CTAB concentration on formation of nanocomposites was studied using optical methods. In these studies, the concentrations of both, GNR (0.24 mM) and C_{12}ELP (0.023 mM), were held constant, while CTAB concentration in the system varied from 0.25 to 3 mM. Reproducible formation of maroon-colored nanocomposites was observed in cases where the CTAB concentration was less than 1.5 mM (Figures 42A, 42B and 42C).

The optical density of the GNR-C_{12}ELP dispersion (nanoassemblies) was monitored at λ_{max} (780 nm) of GNRs (different shaped markers in Figure 4) in order to investigate the kinetics of nanocomposite formation. The red dotted line in Figure 4indicates the temperature profile of the dispersion. In this system, increase in optical density is typically due to the aggregation and therefore, local

enrichment, of ELP or ELP-GNR nanoassemblies, in a process known as *coacervation*. These coacervates consist of enriched GNR-C_{12}ELP aggregates dispersed throughout the aqueous phase (Figure 36C). Decrease in optical density can be due to (i) coalescence of coacervates into large droplets leading to decreased scattering as part of *maturation* of coacervates, or (ii) loss in GNR colloidal stability[51].

At 4°C (t= 0), all GNR-C_{12}ELP nanoassemblies in dispersions have the same optical density (~0.3), indicating that all dispersions had the same GNR concentration (0.24 mM). No phase changes occurred at this temperature ($<T_t$).Upon increase in temperature with time, GNR-C_{12}ELP nanoassemblies underwent a slight decrease in optical density (~0.04±0.02) in the first ten minutes for CTAB concentrations between 0.25 and 1.5 mM (Figure 43A). This minimal decrease in optical density may be explained by loss of colloidal stability of a portion of GNRs following structural changes in C_{12}ELP upon temperature change. ELPs can help stabilize GNR dispersions at 4^{o}C, but as the temperature is increased, aggregation of ELPs can lead to loss of stability of a portion of GNRs. However, further aggregation of ELPs results in formation of coacervates, a process characterized by increase in O.D. Increasing the CTAB concentration results in delay in the increase of the O.D. (or onset of coacervation). This is consistent with the propensity of CTAB to inhibit the formation of GNR-C_{12}ELP assemblies and increase the T_t, all of which contribute to delayed coacervation.

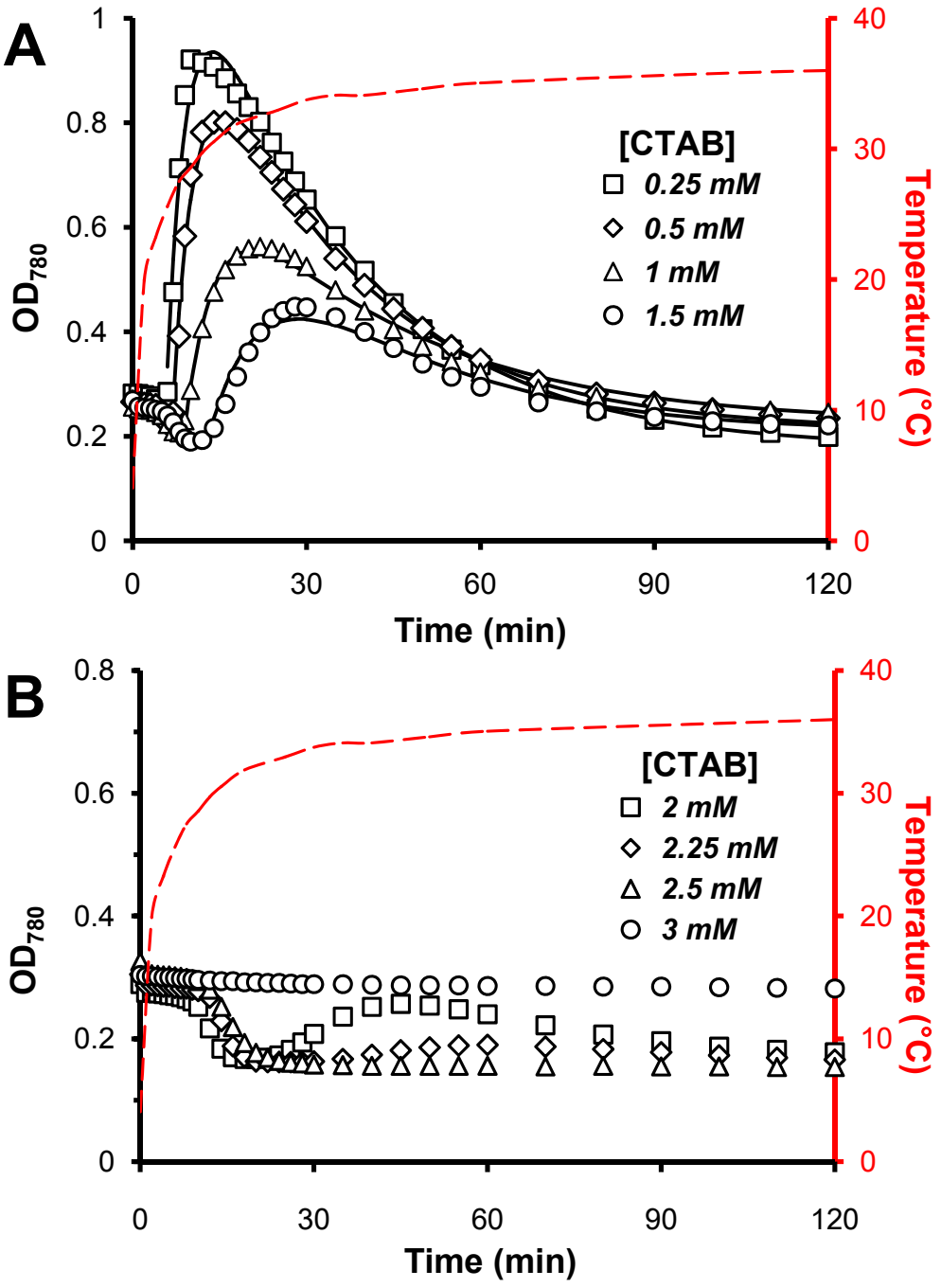

Figure 43.Kinetics of formation of GNR-C_{12}ELP solid-phase nanocomposites from liquid-phase nanoassemblies as a function of CTAB concentration.
(A) 0.25 - 1.5 mM CTAB, (B) 2-3 mM CTAB. GNR (0.24 mM) and C_{12}ELP (0.023 mM) concentrations were kept constant in all cases. Open markers indicate measured optical densities at 780 nm (OD_{780}). Solid lines represent the mathematical fit (equation 7) of experimental optical density data, while the red

dotted line represents the dispersion temperature profile. Nanoassemblies with CTAB concentration between 0.25 and 1.5 mM underwent an initial rapid rise (coacervation) followed by a gradual decrease (maturation) in turbidity. The temperature varied during the coacervation stage, and optical density increases were observed between ~28-37^{o}C. The temperature was largely invariant during the maturation and precipitation stage. Negligible phase separation of nanoassemblies was observed at CTAB concentration between 2 and 3 mM. In the figure legend, (CTAB) indicates concentration of CTAB.

The initial decrease in optical density is followed by the *coacervation* stage, which is characterized by a rapid increase in optical density. As the CTAB concentration in GNR-C_{12}ELP dispersion increased from 0.5 to 1.5 mM, the onset of coacervation was delayed from 5 min to 10 min, and the maximal optical density was lowered from 0.92 to 0.45. This indicated that lower amounts of GNR-C_{12}ELP nanoassemblies underwent phase separation at higher CTAB concentrations. This decrease in the maximal optical density of the curve can, in part, be explained by the inhibition of C_{12}ELP binding to gold nanorods at higher CTAB concentrations(Figure 41).The final *maturation* stage corresponds to a steady decrease in optical density, due to increase in size of the coacervates (Figure 1D). Eventually, precipitation of these leads to the formation of solid-phase nanocomposites (Figure 42A-C).

The formation of extensively cross-linked GNR-C_{12}ELPnanocomposites differs from conventionally observed ELP aggregation (coacervation) and maturation (coalescence of coacervates into droplets), which is typically reversible in the coacervation stage and forms precipitates only upon extended (e.g. overnight) heating[246,247].Optical microscopy (Figure42F) showed uniform and extensive cross-linking of GNR-C_{12}ELPnanocomposites; these materials are stable at 4°C

for more than one year. On the other hand, C_{12}ELP,in the absence of GNRs, formed small precipitate droplets(Figure 42G) held together primarily by hydrophobic interactions. These precipitate droplets were easily dissolved and washed away in aqueous solutions(PBS) at low temperatures (4°C).

In presence of higher CTAB concentrations(2.5 and 3 mM), GNR-C_{12}ELPnanoassembliesdid not form solid-phase nanocomposites at 37°C (data not shown), which is due to the higher transition temperature of the nanoassemblies (≥50°C) (Figure 38B). However, violet-colored nanocomposites were formed at 60°C, which was higher than the transition temperature under these CTAB concentrations (Figure 42D and 42E). The color shift from maroon to violet is presumably due to the surface plasmon coupling of aggregated gold nanorods[34], which resulted in decrease of the maximal absorbance peak due to loss of optical properties[51](Figure 44).These observations support the photothermal responses of these nanocomposites;C_{12}ELP–GNR nanocomposites formed at higher CTAB concentrations(2.5 and 3 mM) demonstrated less pronounced thermal responses upon laser irradiation compared to nanocomposites formed at low CTAB concentrations (0.25, 1, 1.5 mM), even though the GNR concentrations were same in all cases(Figure 45). In presence of CTAB concentrations of 3 mM or more,GNR-C_{12}ELP nanoassemblies showed no change in optical density at 37^{o}C (Figure 43B), indicating that the nanoassemblies remained stable as dispersions due to sufficient amount of the stabilizing surfactant (CTAB).

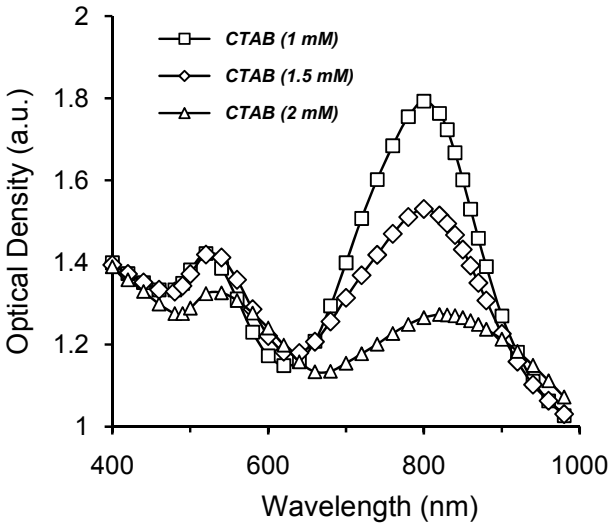

Figure 44.Absorbance spectra of nanocomposites formed using C_{12}ELP -GNR dispersion at various CTAB concentrations.
GNR-C_{12}ELP dispersions containing 1 and 1.5 mM CTAB were incubated at 37°C for 4 h to allow formation of nanocomposites (solid lines). GNR-C_{12}ELP dispersions containing 2 mM CTAB were incubated at 60°C for 4 h to allow formation of nanocomposites (dotted line). Note that a slight difference in thickness of each nanocomposite can result in changes in the intensity of optical density. Thus, the spectra of nanocomposites were normalized to posses same the optical density value at 400 nm for better comparison.

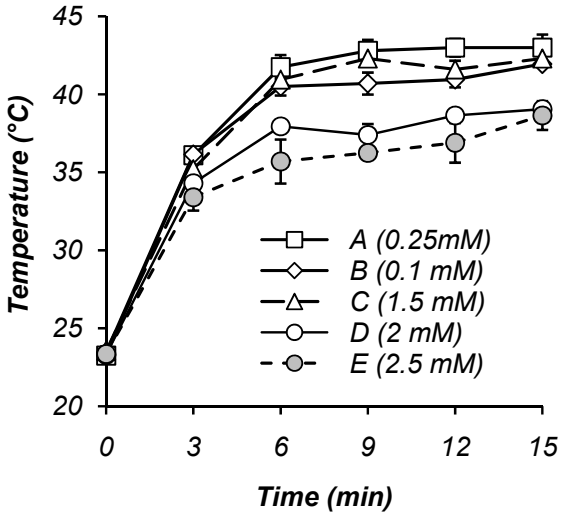

Figure 45.Photothermal responses of C_{12}-ELP GNR nanocomposites.
Nanocomposites formed from dispersions at different CTAB concentrations and temperatures (A) 0.25 mM (37°C), (B) 1 mM (37°C), (C) 1.5 mM (37°C), (D) 2 mM (60°C) and (E) 2.5 mM (60°C). Nanocomposites were exposed to laser at 20

W/cm^2 for 15 min; the supernatant temperature was recorded as a function of time (n=4). Less pronounced photothermal responses were observed in nanocomposites formed at higher CTAB concentrations (2.5 and 3 mM).

The above results indicate that three distinct phenomena could be observed following incubation of GNR-C_{12}ELP nanoassemblies at 37°C (>T_t). First, at CTAB concentrations between 0.25 and 1.5 mM, phase separation of the nanoassemblies led to nanocomposite formation at 37^{o}C. Second, at CTAB concentrations from 2 to 2.5 mM, minimal phase separation of nanoassemblies took place, and no formation of nanocomposites was observed. This CTAB concentration range may be viewed as a 'transition' region in which case, nanocomposite formation was observed at higher temperatures (60^{o}C), which was a direct influence of CTAB on the transition temperatures of both, C_{12}ELP solutions (Figure 38A) and GNR-C_{12}ELP nanoassemblies (Figure 38B). Third, at CTAB concentrations of 3 mM and higher, the nanoassemblies did not undergo phase separation, showed no change in GNR optical density, demonstrated stable dispersions, and no nanocomposite formation was observed.

6.3.4. Mathematical Analyses of GNR-C_{12}ELP Nanocomposite Formation: Effect of CTAB Concentration

The effect of CTAB concentration on the formation of C_{12}ELP-GNR nanocomposites was further studied using a double-exponential kinetic model (equation 7) previously described in the literature for investigating aggregation and coacervation kinetics of ELP[239]. The model was employed to fit the observed optical density data in order to primarily enable a quantitative comparative study between different processing conditions employed (e.g. different CTAB

concentrations). Our data on the kinetics of formation of GNR-ELP nanocomposites qualitatively mirror coacervation and maturation observed previously for ELP alone (i.e. in the absence of GNRs)[239]. As a result, the double-exponential model was considered relevant for investigating GNR-C_{12}ELP nanocomposite formation.

The double-exponential model (equation 7) may be viewed as a solution to first order consecutive reactions consisting of ELP dispersion → ELP aggregates →coalescence of ELP aggregates/nanocomposite formation, in which, optical density is a surrogate for the concentration of aggregates. The first step, ELP dispersion → ELP aggregates, is the coacervation step associated with the coacervation constant (k_c),whereas the second step, ELP aggregates →coalescence of ELP aggregates/nanocomposite formation, is the maturation/precipitation associated with the maturation constant (k_m). Given that the temperature varies from ~28-37°C during the coacervation stage, viewing the double-exponential model purely as a first-order rate model is not strictly valid. However, since the temperature remains largely invariant over the course of the maturation stage, it may be possible to view this portion in terms of a kinetic rate model. Given these limitations, the derived parameters, although similar to first-order rate constants, were used primarily for comparing different processing conditions in the current study.

The double-exponential model, employed to fit the optical density measurements in Figure 38A (solid lines), provided means to follow the overall phase separation

process as an initial *coacervation* (exponential growth in optical density) phase and a subsequent *maturation* phase (exponential decay in optical density). The growth and decay constants, with units of 1/*time*, can represent coacervation and maturation constants, (k_c and k_m) respectively. Constants (k_c *and* k_m), in concert with their concentration proportionality factors (*a and b*),were employed to calculate the coacervation velocity (V_c=ak_c) and maturation velocity (V_m=bk_m), respectively, as defined previously[239]. Based on the maximum optical density and the shape of the curve, the mathematical model allowed derivation of the relative constants of the *coacervation* and *maturation* processes for comparison between different processing conditions. These derived parameters were used to compare the effects of CTAB and GNR during GNR-C_{12}ELP phase separation leading to nanocomposite formation. In all cases, the coefficient of determination (R^2) values were greater than 0.98, with most being higher than 0.99.The coacervation and maturation velocities of nanocomposite formation ranged from ~0.1-3.8 and ~0.02-0.1 (OD/min) respectively. These are similar to those reported in the literature for other ELPs (in the absence of GNRs); while V_c ranged between 0.6-4 (absorbance/min) and V_m ranged between 0.025-0.6 (absorbance/min)[239].

Analyses of the coacervation constant and velocity from the model indicated that the presence of CTAB has a potent effect on the coacervation constant and velocity of coacervation of GNR-C_{12}ELP nanocomposites, but less effect on the maturation stage (Figure 46). This is similar to the effect of CTAB on C_{12}ELP coacervation in the absence of GNRs (Figure 47A). The coacervation constant

(k_c) and velocity (V_c) decreased as the CTAB concentration rose from 0.25 to 1.5 mM. This is similar to the behavior of unbound C_{12}ELP (Figure 47B and 47C), except in case of 0.5 mM CTAB, which showed the highest value of the coacervation constant. Interestingly, presence of 0.5 mM CTAB also resulted in the lowest transition temperature of C_{12}ELP (Figure 38A). As CTAB concentration increased from 0.5 to 2 mM in C_{12}ELP solutions, a decrease in V_c was observed, which corresponded to the slight increase of T_t of GNR-C_{12}ELP (Figure 38B). Overall, in case of both, GNR-C_{12}ELP and C_{12}ELP, the coacervation constant (k_c) and velocity (V_c) values were reduced at higher CTAB concentration.

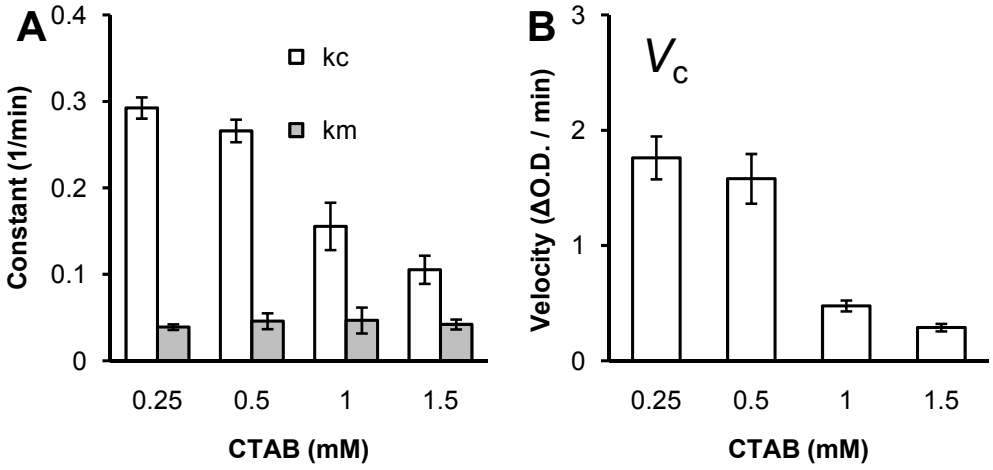

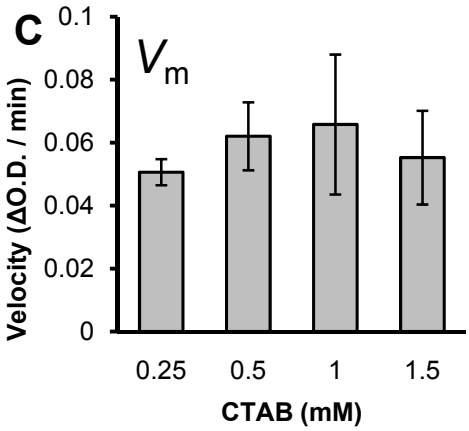

Figure 46.Analyses of GNR-C_{12}ELP coacervation and maturation kinetics as a function of CTAB concentration.
(A) GNR-C_{12}ELP coacervation constant (k_c) and maturation constant (k_m) as a function of CTAB concentration. (B) GNR-C_{12}ELP coacervation velocity (V_c) and (C) GNR-C_{12}ELP maturation velocity (V_m) as a function of CTAB concentration. Coacervation constant (k_c) and velocity (V_c) of GNR-C_{12}ELP were reduced at higher CTAB concentration where the aggregation of GNR-C_{12}ELP was inhibited. On the other hand, CTAB has minimum effect on the maturation constant (k_m) and velocity (V_m).

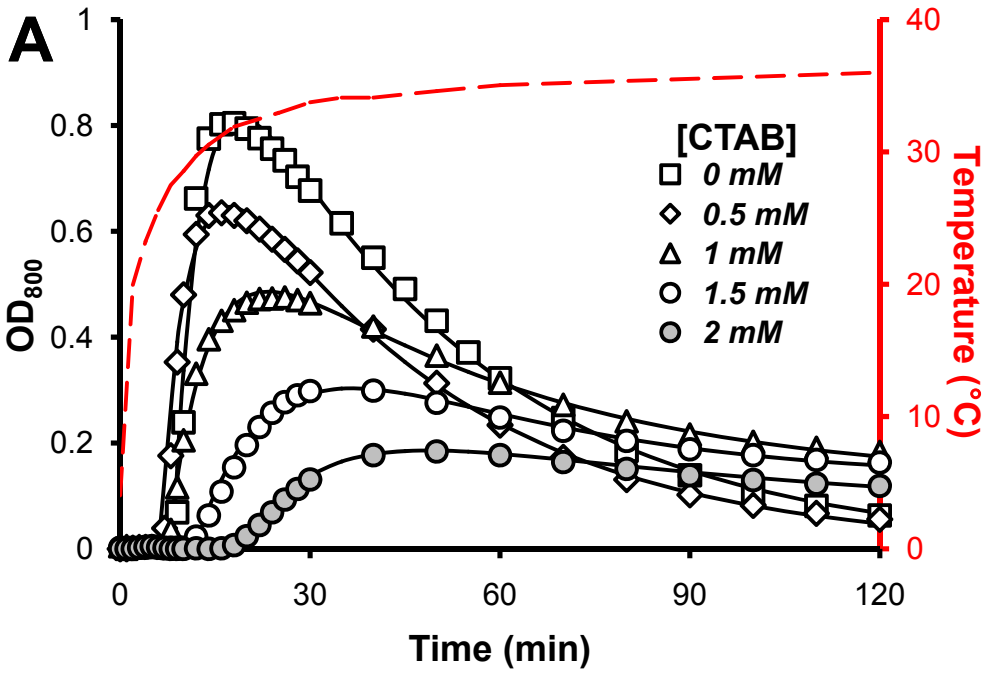

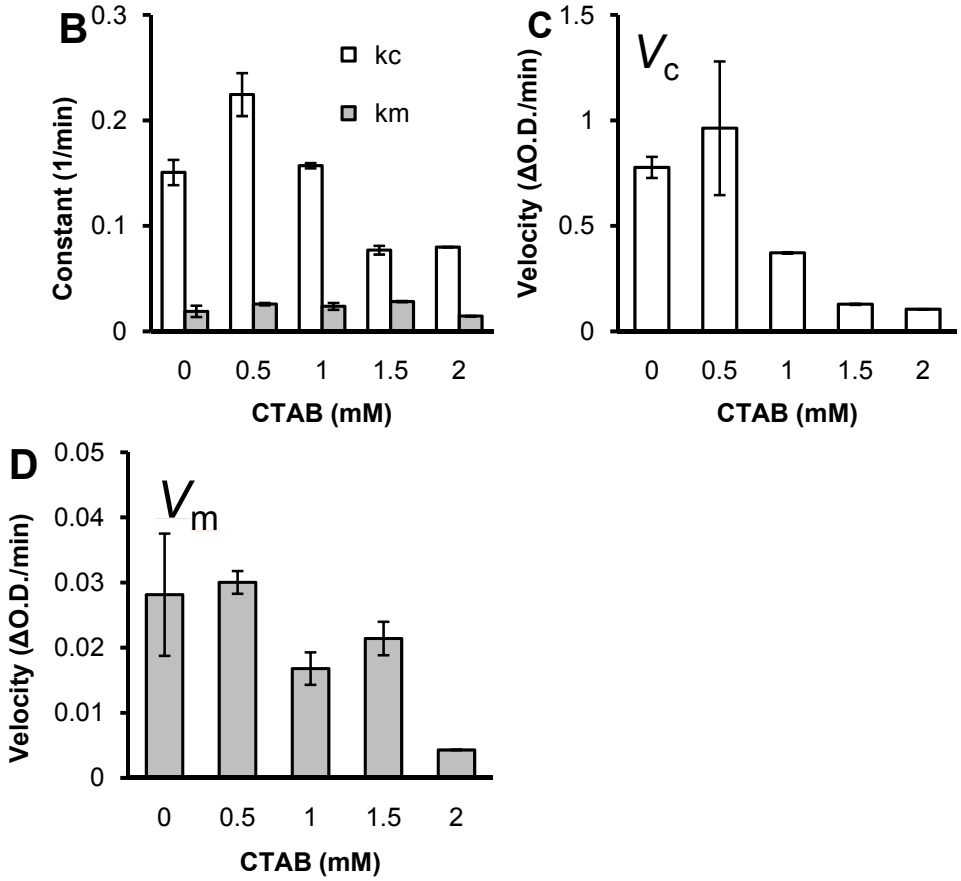

Figure 47.Formation kinetics of C_{12}ELP in presence of various CTAB concentrations.

(A) Coacervation and maturation kinetics of C_{12}ELP in presence of various CTAB concentrations (0-2 mM). Open markers indicated measured optical densities at 800 nm (OD_{800}). Red dotted line represents the temperature profile of the polypeptide solution. Solid lines are mathematical fits of the measured optical density using equation 7. Similar to figure 4A, the initial rise in turbidity, known as coacervation, is followed by the maturation stage, characterized by a steady decrease in turbidity. The OD_{800} data were fit in order to obtain: (B) C_{12}ELP coacervation constant (k_c)and maturation constant (k_m) as a function of CTAB concentration. (C) C_{12}ELP coacervate velocity (V_c) and (D) C_{12}ELP maturation velocity (V_m) as a function of CTAB concentration.

Changing CTAB concentration from 0.25 to 1.5 mM did not affect the maturation constant (k_m) and velocity (V_m) in case of both GNR-C_{12}ELP nanocomposites as well as C_{12}ELP coacervates (Figures 46C and 47D). These data suggest that higher CTAB amounts inhibit the initial coacervation of GNR-C_{12}ELP and C_{12}ELP,

partly by reducing loading of the polypeptide on GNRs, and partly by enhancing the transition temperature. However, once the coacervates are formed, CTAB does not affect their subsequent coalescence and maturation, which ultimately leads to nanocomposite formation. This is consistent with previous observations which indicate that the maturation step is primarily a diffusion-limited process[239].

In addition to obtaining quantitative information on phase separation processes, the model was employed for comparing nanocomposite formation under different conditions. For the same CTAB concentration, it was found that both, the constants and velocity of coacervation and maturation, as determined from the double-exponential model, were higher for GNR-C_{12}ELPs compared to C_{12}ELP (Figure 48). As seen in the figure, GNRs only slightly increased the velocity of coacervation V_c, but significantly enhanced the velocity of maturation V_m. It is possible that the initial coacervation phase is dominated by C_{12}ELP interactions, and that the density and surface area of gold nanorods play a key role in enhancing contact between coacervates, leading to their maturation and precipitation. The presence of gold nanorods therefore facilitates inter- and intra-molecular cross-linking of GNR-C_{12}ELP nanoassemblies, which results in higher coacervation and maturation velocities, albeit the effect on maturation is significantly higher.

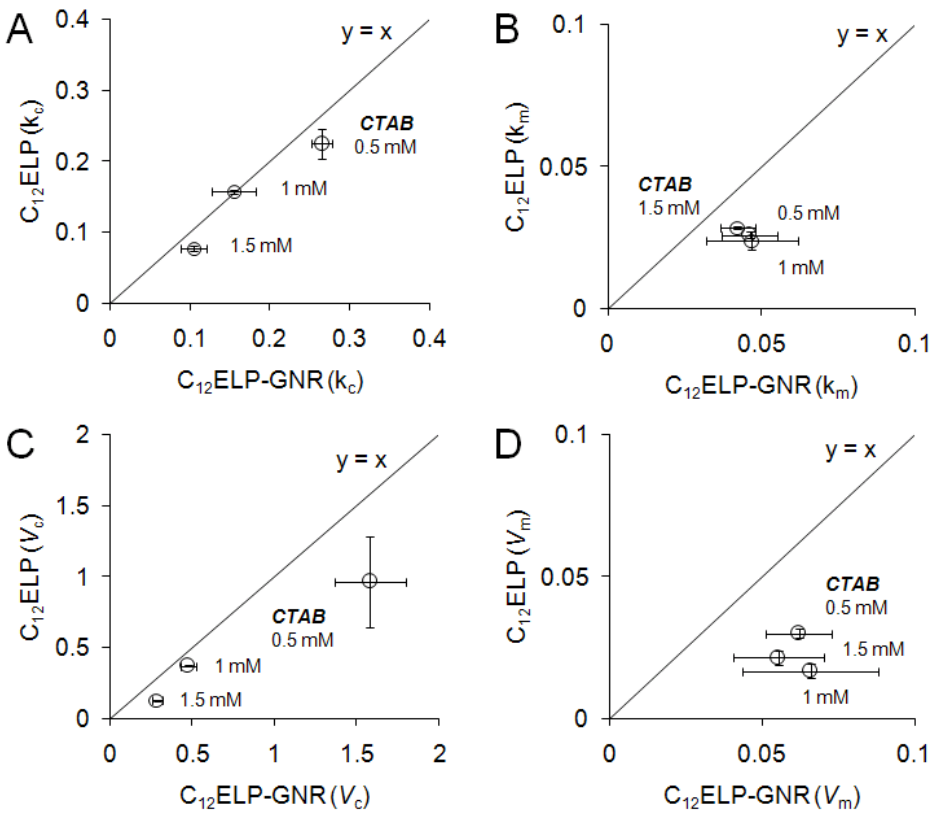

Figure 48. Comparison of model derived parameters.
Comparison of (A) coacervation constant (k_c), (B) maturation constant (k_m), (C) velocity of coacervation (V_c) and (D) velocity of maturation (V_m) for C_{12}ELP solution (y-axis) and GNR-C_{12}ELP dispersion (x-axis) at different CTAB concentrations. In all cases, GNR and C_{12}ELP concentrations were fixed at 0.24 and 0.023mM, respectively, while the CTAB concentration varied from 0.5 to 1 mM. All points fall below the y=x line(except one point which is on the y=x line), indicating that phase separation processes (coacervation and maturation) proceed faster in the case of GNR-C_{12}ELP dispersions compared to the C_{12}ELP system.

Taken together, comparing the model parameters across different conditions indicate that the coacervation process is dominated by ELP and CTAB interactions, while GNRs play a more important role in the maturation and precipitation, leading to nanocomposite formation.

The predictive ability of the model was investigated by determining the coacervation velocity of C_{12}ELP in presence of0.8 mM CTAB. The coacervation velocity (V_c) of C_{12}ELP at CTAB concentrations of 0.5, 1, 1.5 and 2 (Figure 47C) were plotted and the data were fit using a polynomial model as shown in Supplementary Figure 6A. Based on this regression, the ELP coacervation velocity at a CTAB concentration of 0.8 mM was predicted to be 0.56 (O.D./min). The coacervation velocity for C_{12}ELP at 0.8 mM CTAB was also determined experimentally using the spectrophotometric assay in concert with the double-exponential model (Supplementary Figure 46B). The experimentally determined value of V_c was 0.6 OD/min while the predicted value was 0.56 OD/min, indicating a difference of only 7%. These data demonstrate the ability of the model to successfully predict the phase separation under different experimental conditions, leading to formation for C_{12}ELP coacervates as well as GNR-C_{12}ELP nanocomposites.

6.3.5. Phase Separation of GNR-C_{12}ELP Nanoassemblies Leading to Nanocomposite Formation: Effect of GNR Concentration

The effect of GNR concentration on nanocomposite formation of GNR-C_{12}ELP dispersions was also studied. In the study, both CTAB (0.25 mM) and C_{12}ELP (0.023 mM) concentrations were held constant, while GNR concentrations varied from 0.1 to 1 mM. The optical density of GNR-C_{12}ELP dispersions at λ_{max} of nanorod (780 nm) was monitored using a spectrophotometer. The different data points in Figure 9A indicate the GNR-C_{12}ELP dispersion optical density at 780 nm, while the red dotted line is the dispersion temperature profile.

At t= 0 and 4°C, GNR-C_{12}ELP nanoassemblies have different optical densities that corresponded to different GNR concentrations. Prior to coacervation, seven minutes after incubation, a slight decrease in optical density (~0.03) was observed at 0.24 mM GNR concentration, while a more pronounced decrease in optical density (0.26± 0.01) was seen at higher GNR concentrations (0.72 and 1 mM) (Figure 49A). This decrease in optical density was possibly due loss in stability of a portion of GNRs upon increase in temperature, presumably due to initiation of ELP phase change. All samples followed similar coacervation and maturation trend once the characteristic T_t was reached. A maximal optical density was reached at approximately 13±1 minutes for all conditions, and the intensity of the maximal optical density rose as the nanorod concentration increased.

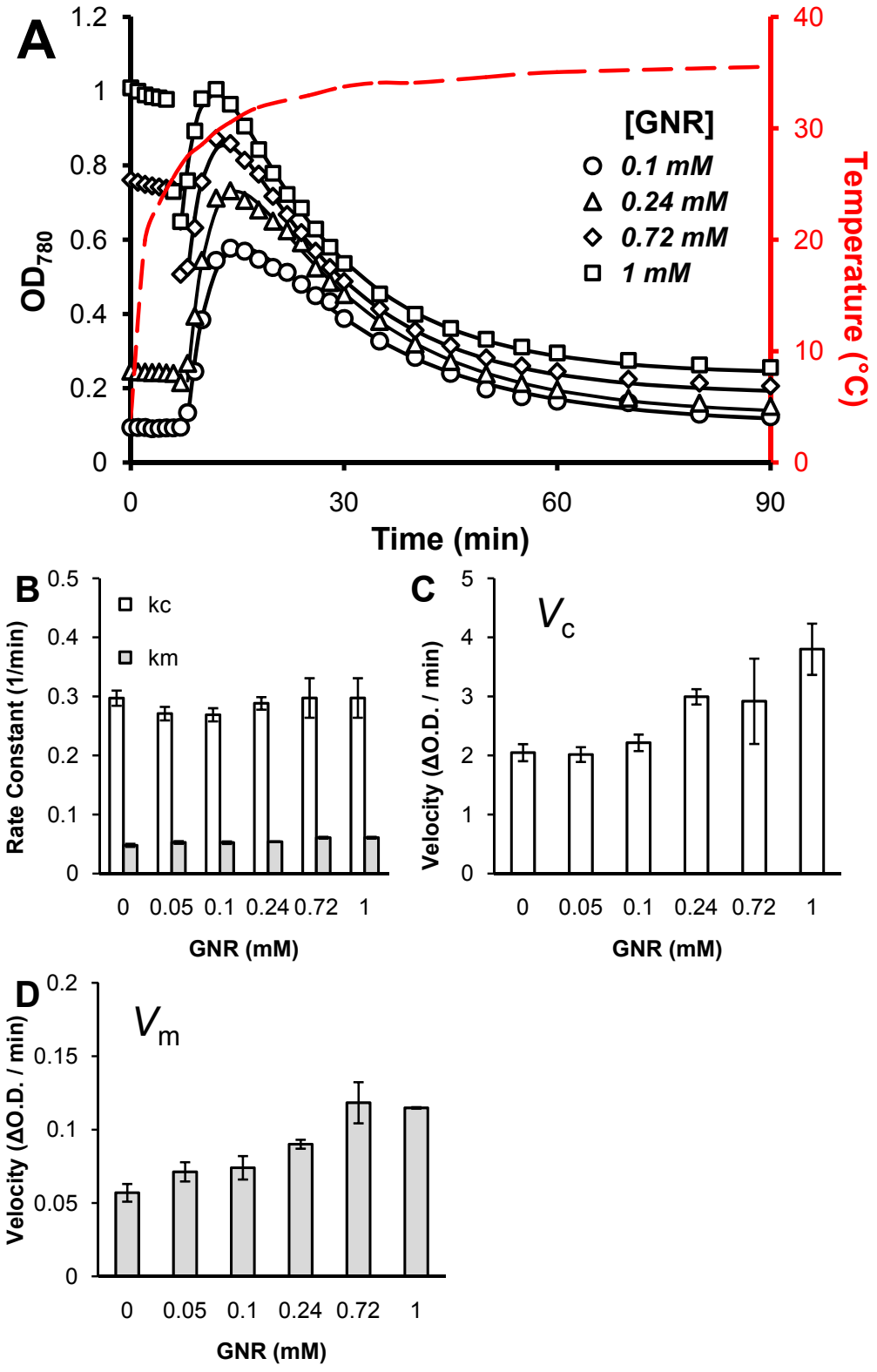
A
1.2
1
0.8
0.6
0.4
0.2
0
OD780
40
30
20
10
0
Temperature (°C)
0
30
60
90
Time (min)
[GNR]
0.1 mM
0.24 mM
0.72 mM
1 mM
B
0.5
0.4
0.3
0.2
0.1
0
Rate Constant (1/min)
kc
km
0
0.05
0.1
0.24
0.72
1
GNR (mM)
C
5
4
3
2
1
0
Vc
Velocity (ΔO.D. / min)
0
0.05
0.1
0.24
0.72
1
GNR (mM)
D
0.2
0.15
0.1
0.05
0
Vm
Velocity (ΔO.D. / min)
0
0.05
0.1
0.24
0.72
1
GNR (mM)

Figure 49.Formation kinetics of GNR-C_{12}ELPas a function of GNR concentration (0.1 to 1 mM).
(A) Coacervation and maturation kinetics of GNR-C_{12}ELP as a function of GNR concentration (0.1 to 1 mM). CTAB (0.25 mM) and C_{12}ELP (0.023 mM) were kept constant. Open markers indicated measured optical densities at 780 nm (OD_{780}) and solid lines are mathematical fits of the data generated using equation 7. The red dotted line represents the dispersion temperature profile. Analyses of GNR-C_{12}ELP coacervation and maturation kinetics as a function of GNR concentration are shown:(B) GNR-C_{12}ELP coacervation constant (k_c)and maturation constant (k_m) as a function of GNR concentration. (C) GNR-C_{12}ELP coacervate velocity (V_c) and (D) GNR-C_{12}ELP maturation velocity (V_m) as a function of GNR concentration. CTAB and C_{12}ELP concentrations were kept constant. Increase of GNR concentration did not alter the coacervation or maturation constants.

Unlike CTAB, increase of gold nanorod concentration did not alter the coacervation constant (k_c= 0.28±0.01) or maturation constant (k_m= 0.055±0.005) of GNR-C_{12}ELP nanocomposites(Figure 49B); in all cases the exponential growth and decay curves followed a similar trend. In Figure 9C and 9D, the coacervation and maturation velocity (V_c and V_m) of GNR-C_{12}ELP dispersions at low nanorod concentrations (0, 0.05 and 0.1mM) were found to be similar (2.1±0.1 /min and 0.067±0.009 /min, respectively). A slight increase in the coacervation and maturation velocity (V_c and V_m) was observed at high nanorod concentrations (0.24, 0.72 and 1 mM), which could be attributed to higher optical densities. These results indicated that gold nanorod content had minimal affect on the phase transition of GNR-C_{12}ELP dispersions under the conditions studied.

6.3.6 Dissolution Kinetics of Nanocomposites

Reduction of disulfide bonds using 10 mM dithiothreitol (DTT) led to the degradation of the nanocomposites within minutes (Figure 50C). While GNE-ELP nanocomposites were stable in the absence of DTT, nanocomposites completely

degraded upon addition of the reducing agent (Figure 50). The absorbance spectra indicated complete recovery of the gold nanorods in the dispersion, as evidenced by the recovery of the transverse and longitudinal peaks at 520 nm and 840 nm, respectively (data not shown). The dissolution kinetics of GNR-C_8ELP and GNR-C_{12}ELP nanocomposites were investigated at three different DTT concentrations (1, 5, 10 mM) as shown in Figure 50C. Nanocomposites were fully dissolved after 15 minutes at a DTT concentration of 10 mM, while it took one hour to fully dissolve nanocomposites with 1 mM DTT.

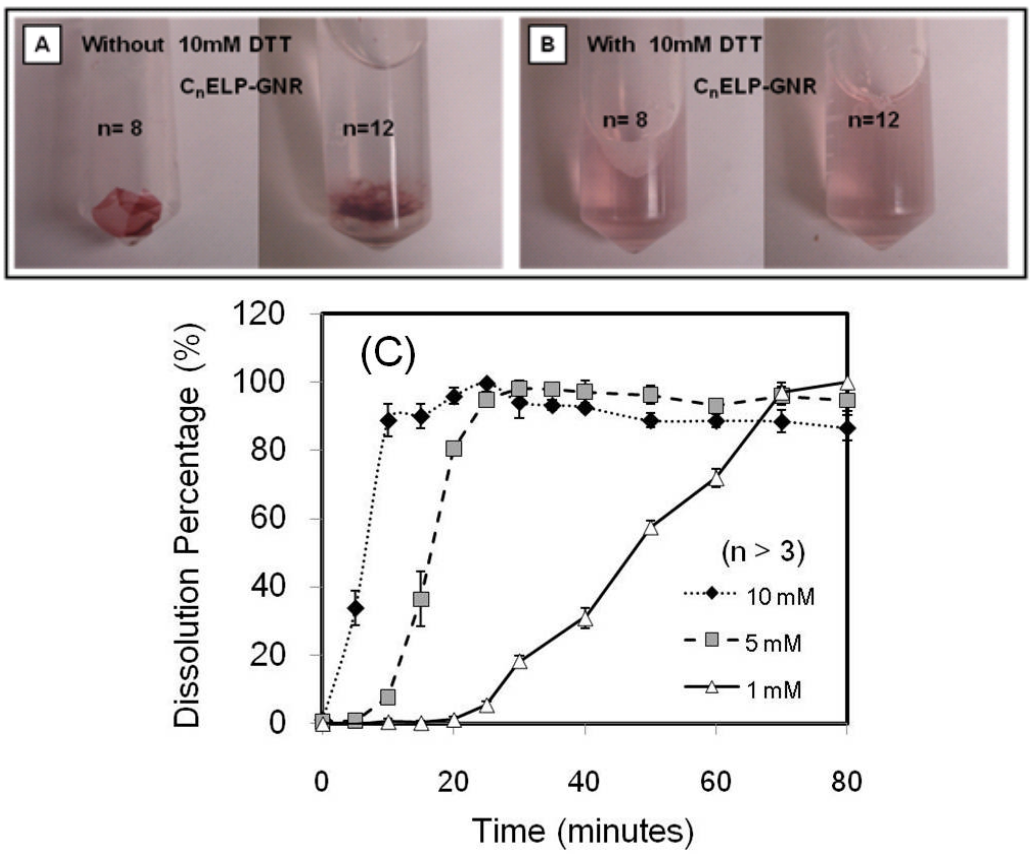

Figure 50.Dissolution of nanocomposites using DTT.
Digital snapshots of C_8ELP-GNR and GNR-C_{12}ELP nanocomposites in presence and absence of DTT.GNR-C_8ELP, GNR-C_{12}ELP nanocomposites were formed by incubation at 37°C for 6 h as described above, followed by cooling and

storage at room temperature (6-24 h). The supernatant was replaced with an equal volume of 10 mM DTT for 30 min at 4°C (24-24.5 h). Images A and B are the GNR-C_8ELP and GNR-C_{12}ELP nanocomposites with and without the presence of DTT. Image C is the dissolution kinetics of GNR-C_{12}ELP nanocomposites was investigated at 3 different DTT concentrations (1, 5, 10 mM). The lines connecting the data points in Figure (c) are for visualization only.

6.3.7NanocompositeCharacterization

Fourier Transform Infrared (FTIR) Spectroscopy for C_8ELP-GNR and GNR-C_{12}ELPnanocomposites indicated a combination of N–H bending and C–N stretching vibrations (amide II peak) at wave number 1550 cm^{-1}, a peak corresponding to the C=O stretches in the amide functionality (amide I peak) at 1645 cm^{-1}, and a band corresponding to the N–H stretching vibrations, at 3200 and 3000 cm^{-1} (Figure 51) which are characteristic of ELP spectra.[217]

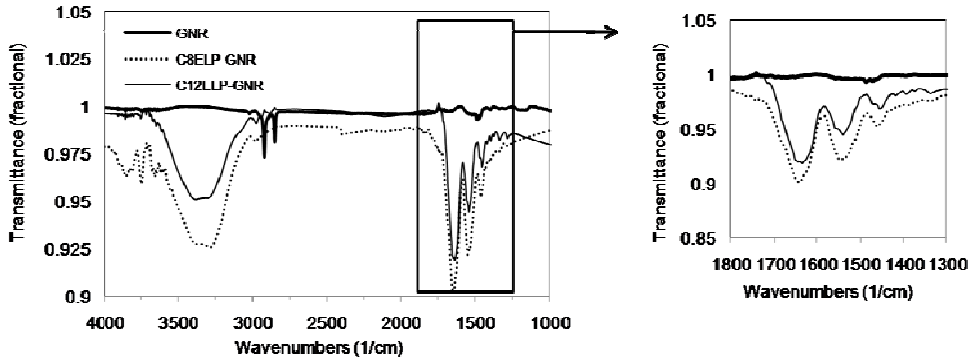

Figure 51.FT-IR spectrum of GNR, GNR-C_8ELP and GNR-C_{12}ELP nanocomposites.

FT-IR (Bruker Vacuum) spectroscopy of GNR-C_8ELP and GNR-C_{12}ELP nanocomposites indicating characteristic peaks at wave numbers of 3500-3000 cm^{-1}, corresponding to the N–H stretching vibrations, 1660 cm^{-1} corresponding to the C=O stretches in the amide functionality (amide I peak), and a peak at 1550 cm^{-1}, which is the combination band of N–H bending and C–N stretching vibrations (amide II peak). CTAB-GNR shows peaks at 2850 and 2917 cm^{-1}, which reflect the symmetric and asymmetric C-H stretching vibrations, respectively. No peaks were observed in the 2550-2600 cm^{-1} region which indicates the absence of the S-H bond.

Field Emission-Scanning Electron Microscopy (FE-SEM) images showed that gold nanorods (~ 50 nm in length) were well dispersed in the nanocomposites (Figure 52), indicating the possibility that the nanocomposites possess stable plasmonic / photothermal properties.

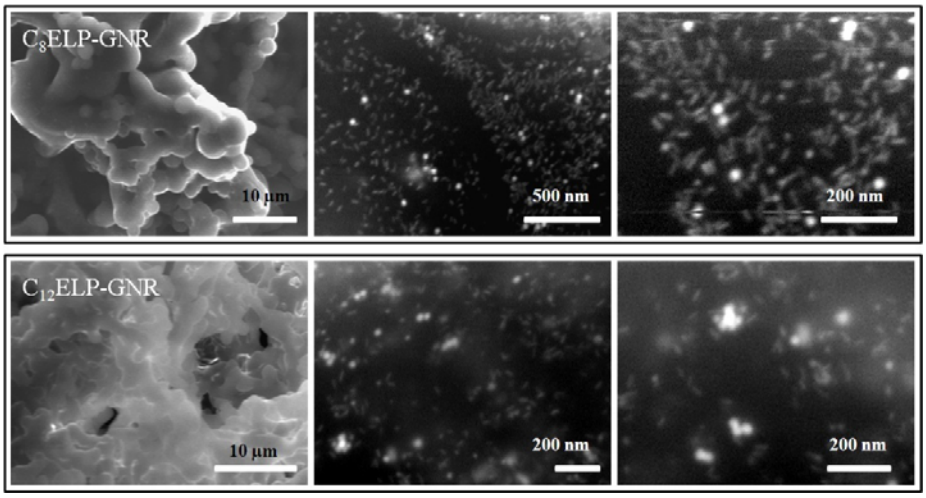

Figure 52.FE-SEM images of GNR-C_8ELP and GNR-C_{12}ELP nanocomposites. Environmental field-emission scanning electron microscopy (PHILIPS FEI XL-30 SEM) operating an accelerating voltage of 25 kV) images indicate a fairly uniform distribution of gold nanorods throughout GNR-C_8ELP and GNR-C_{12}ELP nanocomposites.

6.4. Conclusions

This study describes an investigtion into the phase separation of cysteine-containing elastin-like polypeptdie (C_{12}ELP) self-assembled oncetyltrimethyl ammonium bromide (CTAB)-stabilized gold nanorods (GNRs), leading to nanocomposite formation. The following conclusions can be summarized.(1) Increase in CTAB concentration resulted in a rise of the transition temperature of both,C_{12}ELP solution as well as GNR-C_{12}ELP nanoassemblies. (2) At 37^{o}C and at CTAB concentrations less than 1.5 mM, GNR-C_{12}ELP

nanoassembliesunderwent phase separation resulting in extensively cross-linked nanocomposites, which demonstrated a reliable photothermal response. Higher CTAB concentrations (>2mM) inhibited the formation of these nanocomposites at 37^{o}C. (3) Unlike the concentration-dependent effects of CTAB, GNR content in GNR-C_{12}ELP nanoassemblies has negligible effect on the transition temperature, coacervation and maturation kinetics, and ultimately, on nanocomposite formation. (4) Nanocomposites formed at lower CTAB concentrations and temperatures demonstrated a superior photothermal response compared to those generated using higher CTAB concentrations, which required higher temperatures for formation. These results indicate that it is important to keep the concentration of CTAB to a minimum while forming plasmonic nanocomposites for photothermal delivery of encapsulated drugs. Low CTAB concentrations facilitate straightforward formation of the composites, which also show more robust photothermal responses for simultaneous NIR radiation-triggered delivery of hyperthermia and encapsulated drugs. Taken together, the current study provides a fundamental understanding into factors influencing formation of photothermally active plasmonic nanocomposites, which can have applications in sensors, tissue engineering and regenerative medicine, and drug delivery.

CHAPTER

7. Plasmonic Nanocomposite for Simultaneous Administration of Hyperthermia and Chemotherapeutic Drug to Cancer Cells

7.1 Introduction

Cancer diseases are among the leading causes of death in the United States and account for approximately 1 in every 4 deaths. Hyperthermia involves raising tissue temperature to 43-46^{o}Cto induce tumor ablation[248]and has been investigated as an adjunctive cancer therapy[180]. Cellular injury/death at temperatures above 43^{o}C is attributed to protein denaturation triggered by these elevated temperatures.[249,250] Consequently, microwaves and radio waves,[251,252] magnetic heating,[253] or ultrasound[254] have been employed for hyperthermic ablation of cancer cells.

The ability to generate high temperatures at a desired site with externally tunable control holds significant promise for cancer therapy compared to whole-body hyperthermia. Nanomaterials localized at tumor vicinity can be subjected to laser irradiation from an external source, leading to the selective administration of the hyperthermic treatment.[255] In addition to gold nanoshells[256] and nanocages,[257] gold nanorods[145,258,259] are attractive candidates for ablation of tumors. Recently, photothermolysis, strong NIR absorbance, and magnetic functionality were also demonstrated using 30 nm gold /iron oxide nanoclusters for application in combined imaging and therapy[260].

However, resistance of cancer cells and spatial limitations associated with nanoparticle-induced hyperthermia necessitates the identification of effective combination treatments to enhance therapeutic efficacy. Sub-optimal administration of hyperthermia leads to thermotolerance in cancer cells, which is caused, in part, due to the induction of the heat shock response mediated by heat shock proteins (HSPs)[261]. In particular, HSPs 27, 72, and 90, play a significant role in enabling the survival of cancer cells to hyperthermic conditions[262,263]. In addition, spatial limitations and sub-optimal administration associated with hyperthermia can lead to selection of resistant tumor clones, which further complicates therapy. As a result, therapeutic strategies that can synergistically enhance the efficacy of hyperthermic ablation (e.g. by overcoming HSP resistance) can help advance the potential of this approach in cancer therapy.

In this Chapter, GNR-C_{12}ELP "plasmonic nanocomposites" demonstrate reliable photothermal responses due to the presence of gold nanorods within the polypeptide nanocomposite. Laser irradiation of the nanocomposite led to death of only those cancer cells directly in the path of the laser revealing spatial limitations associated with nanoparticle-induced hyperthermia. In order to simultaneously overcome spatial limitations and cancer cell resistance associated with nanoparticle-induced hyperthermia, the clinically relevant chemotherapeutic drug 17-demethoxy-17-allylaminogeldanamycin (17-AAG), an inhibitor of heat shock protein 90 (HSP90), [264,265], was incorporated in the nanocomposite. Laser irradiation of 17-AAG containing nanocomposites resulted

in hyperthermic temperatures which, in turn, induced the release of 17-AAG from the nanocomposite under these elevated temperatures. This resulted in the synergistic administration of both, hyperthermia and chemotherapy (17-AAG), resulting in death of the entire population of cancer cells, while 'single treatments' (i.e. hyperthermia alone and 17-AAG alone) demonstrated minimal (< 10%) loss of cancer cell viability.

7.2 Material and Methods

7.2.1 Materials

Silver nitrate was purchased from Spectrum and dithiothreitol (DTT) was purchased from EMD. Cetyltrimethylammonium bromide (CTAB), 95 %, Sodium borohydride, powder, reagent grade, ≥ 98.5 %, gold (III) chloride trihydrate ($HAuCl_4 \cdot 3H_2O$), 99.9+ %, L-ascorbic acid, reagent grade were purchased from Sigma. All materials were used as received without further purification.

7.2.2 Gold Nanorod (GNR) Synthesis

Gold nanorods were synthesized using the seed-mediated method as previously described in Chapter 6.2.2 for generating gold nanorods (GNRs) that possessed absorbance maxima (λ_{max}) in the near infrared (NIR) region of the light absorption spectrum.

7.2.3 Synthesis, Expression, and Purification of Cysteine containing Elastin-like Polypeptides (ELPs)

C_{12}ELP were generated, expressed, purification lyophilized and stored at room temperature as described previously in Chapter 6.2.3. The T_t of C_{12}ELP was characterized as described in Chapter 6.2.4.

7.2.4 Generation of C_nELP-GNR Nanoassemblies

GNR- C_{12}ELP nanoassemblies were prepared as following Chapter 6.2.5.

7.2.5 Photothermal Properties of a GNR-C_{12}ELP Nanocomposite Film

GNR-C_{12}ELP dispersion (750 µL of 1 mg/mL in 0.5X PBS; O.D. =0.25; 4°C) in 1 mm diameter acrylic cell (home-made)was immediately incubated in 37°C, 5% CO_2 environment for 3 hours, in order to allow nanocomposite formation on top of a tissue culture treated 1.5 mm diameter cover slip originally placed at the bottom of the acrylic cell. The supernatant was removed from the acrylic cell after incubation and the absorption spectrum of the GNR-C_{12}ELP film was determined using a plate reader (Biotek Synergy 2) at room temperature. The spectrum of nanocomposite was measured between 300-999 nm five individual times.

The photothermal properties of the nanocomposite were determined using irradiation with a titanium CW sapphire (Ti:S) laser (Spectra-Physics, Tsunami) pumped by a solid state laser (Spectra-Physics, Millennia). Briefly, the excitation source was tuned to 850 nm in order to coincide with the longitudinal absorption maximum of the GNR-C_{12}ELP nanocomposite. GNR-C_{12}ELP nanocomposite was placed at the bottom of a 24 well plate (Corning) with 500 µl of 1X PBS as the supernatant over the nanocomposite. The well was irradiated with laser light at

850 nm at power densities of 20 W/cm^2 or 25 W/cm^2 for 15 minutes and the dispersion temperature was monitored by FLUKE 54 II (Type K) thermocouple during laser exposure. Controls with only 500 µl of 1X PBS solution in 24 well plates (i.e. without GNR-C_{12}ELP nanocomposite) were carried out; temperature remained invariant at 24 ± 0.5°C after 15 minutes laser exposure in this case.

7.2.6 Formation of 17-demethoxy-17-allylaminogeldanamycin (17-AAG) Loaded GNR-C_{12}ELP Nanocomposite Film (24 well plate)

GNR-C_{12}ELP dispersion (750 µL of 1 mg/mL, 0.5X PBS, O.D. = 0.25 at 4°C), containing 750 µg of 17-demethoxy-17-allylaminogeldanamycin (17-AAG) (LC Laboratories, MA) was placed in the 1 mm diameter acrylic cell, and immediately transferred to an incubator (37°C, 5 % CO_2) for 3 hours, allowing phase separation and formation of 17-AAG loaded GNR-C_{12}ELP (17AAG-GNR-C_{12}ELP) nanocomposite on top of a tissue culture treated 1.5 mm diameter cover slip. While 6 hours were previously employed for generating C_{12}ELP-GNR nanocomposites (without 17-AAG), analysis of nanocomposite formation kinetics indicated that three hours were sufficient to generate the nanocomposites. As a result, a three-hour incubation period was used for generating 17AAG-GNR-C_{12}ELP nanocomposites in order to reduce processing times. Following incubation, the supernatant, containing free 17-AAG molecules, was removed from the acrylic cell after 3 hours, and assayed for concentration using absorbance analysis. The amount of 17-AAG encapsulated in the nanocomposite was determined from a mass balance on the drug. Briefly, absorbance values of known concentrations of 17-AAG at 335 nm were employed to generate a

standard calibration curve. Following nanocomposite formation, the concentration of 17-AAG in the supernatant was then back-calculated based on the absorbance and the calibration curve. Since the initial amount of 17-AAG is known, the amount encapsulated in the nanocomposite was calculated as the difference of 17-AAG before and after encapsulation. The absorption spectrum of the 17-AAG encapsulated GNR-C_{12}ELP nanocomposite was determined at room temperature using a plate reader (Biotek Synergy 2) with five individual measurements. A peak at 335 nm was used to detect encapsulation of the drug.

7.2.7 Release of 17AAG from 17AAG-GNR-C_{12}ELP Nanocomposites

Drug (17-AAG)-loaded GNR-C_{12}ELP nanocomposites were prepared as described above and placed in a 24 well plate with 500 µl of 1X PBS. The diffusion release of 17-AAG from the nanocomposite was monitored for 24 hours. The laser beam was tuned to 2 mm in diameter for all near infrared (NIR) irradiation-triggered drug release studies. The first laser irradiation lasted for 5 min (850 nm, 25 W/cm^2). Five subsequent laser irradiations (850 nm, 25 W/cm^2) lasted for 10 minutes, followed by a 20 minute period without laser irradiation each. The temperature profile during the 10-minute laser exposure was monitored using a K-type thermocouple.

7.2.8 Cell Culture

The PC3-PSMA human prostate cancer cell line[166] was a generous gift from Dr. Michel Sadelain of the Memorial Sloan Cancer Center, New York, NY. RPMI 1640 with L-Glutamine and HEPES (RPMI-1640 medium), pen-strep solution:

10,000 units /mL penicillin and 10,000 µg/mL streptomycin in 0.85% NaCl, and fetal bovine serum (FBS) were purchased from Hyclone. Serum-free medium (SFM) is RPMI-1640 medium plus 1 % antibiotics. Serum-containing medium is SFM plus 10 % FBS. Cells were cultured in a 5 % CO_2 incubator at 37^oC using RPMI-1640 medium containing 10 % heat-inactivated fetal bovine serum (FBS) and 1 % antibiotics (10,000 units/mL penicillin G and 10,000 µg/mL streptomycin).

7.2.9 Cell Culture and Laser Irradiation on GNR-C_{12}ELP Nanocomposites

GNR-C_{12}ELP and 17AAG-GNR-C_{12}ELP nanocomposites on tissue culture cover slips were prepared as described previously. Prior to cell culture, the nanocomposites were pre-treated with 500 µl serum containing media in a 24 cell culture well plate (Corning) overnight in order to promote cell attachment. The serum-containing media was removed after incubation and the nanocomposite-coated cover slips were washed twice with fresh serum-containing media. PC3-PSMA human prostate cancer cells were seeded on top of the nanocomposites in several wells with a density of 150,000 cells/well and allowed to attach for 24 hours at 37°C, in a 5 % CO_2 incubator. For the laser irradiation experiment, the excitation source was tuned to 850 nm in order to coincide with the longitudinal absorption maximum of the GNR-C_{12}ELP nanocomposite. Nanocomposites with PC3-PSMA cells were exposed to laser irradiation at 850 nm at a power density of 25 W/cm^2 for 7 minutes (no laser exposure for the control samples). The solution temperature was monitored by a FLUKE 54 II (Type K) thermocouple during laser exposure. Fluorescence-based Live/dead® assay was employed to

investigate cancer cell viability 24 hours after laser irradiation. Briefly, cells were treated with 4 μM ethidium homodimer-1 (EthD-1; Invitrogen) and 2 μM calcein AM (Invitrogen) for 30 minutes and imaged using Zeiss AxioObserver D1 inverted microscope (10 × X/0.3 numerical aperture (NA) objective; Carl Zeiss MicroImaging Inc., Germany). Dead/dying cells with compromised nuclei stained positive (red) for EthD-1, viable / live cells stained green for calcein AM.

7.3 Results and Discussion

The absorbance spectrum of the GNR-C_{12}ELP nanocomposite (Figure 53) showed uniform distribution of gold nanorods in the nanocomposite resulted in optical properties similar to that of gold nanorod dispersions; characteristic peaks at 520 nm and in the near infrared (approximately 850 nm) region in the spectrum can be seen, indicating that the nanocomposites indeed demonstrated plasmonic properties due to the uniform distribution of the gold nanorods. Photothermal properties of C_nELP-GNR nanocomposites were investigated by recording the temperature of PBS supernatant (500 μl) above the nanocomposite in 24 well plates. Temperatures in each case reached their respective steady-state values (approximately 46^{o}C) five minutes following laser irradiation, consistent with our previous observations with gold nanorods;[237,266,267] the steady-state temperatures did not change following the relatively minor change in power density from 20 W/cm^2 to 25 W/cm^2.

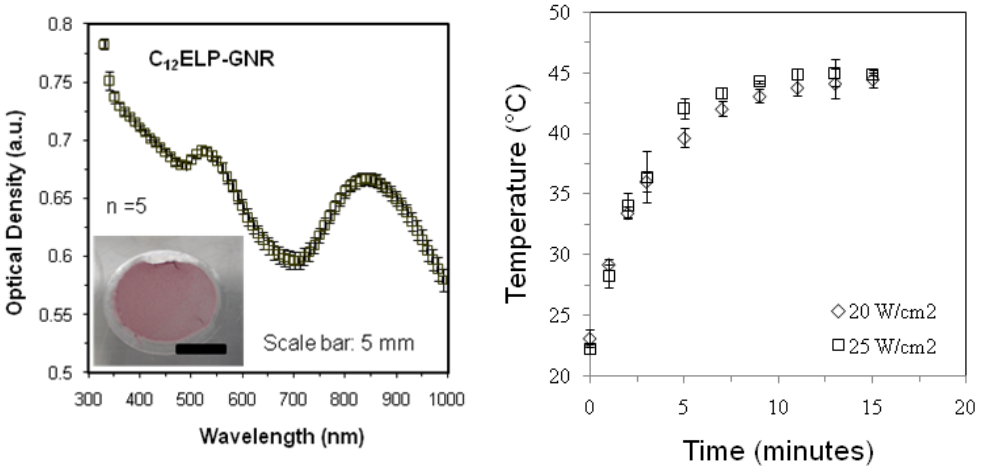

Figure 53.Optical and photothermal response of GNR-C_{12}ELP nanocomposites. GNR-C_{12}ELP nanocomposites were formed on a glass cover slip (inset) and the absorbance (optical density) spectrum of the film was analyzed using a plate reader. The nanocomposite was immersed in PBS was irradiated using an 850 nm laser at two different power densities and the temperature of PBS was measured using a K-type thermocouple.

Sub-optimal administration of hyperthermia can result in the incomplete ablation of tumors and selection of clones that are resistant to treatment. While temperatures above 46^{o}C result in significant loss of cell viability, mild or moderate hyperthermic temperatures (40-46°C) can have differential cytotoxic effects on cells leading to variable efficacies. Constitutive and induced expression of heat shock proteins (HSPs), including HSP90, lead to the refolding of proteins denatured by hyperthermia, and therefore results in overcoming the apoptotic effects of the treatment. In particular, HSP90 is a stress-related protein which interacts with several client proteins and regulates key processes inside cells, including protein degradation, and aids cancer cell survival following hyperthermia. Strategies that combine hyperthermic ablation with chemotherapeutic drugs that can overcome HSP-induced resistance can result in enhancing the efficacy of hyperthermia as an adjuvant treatment. As a

representative example of this approach, the chemotherapeutic HSP90 inhibitor, 17-demethoxy-17-allylaminogeldanamycin (17-AAG) was incorporated in the nanocomposite, with an eye towards generating a multifunctional nanocomposite capable of simultaneously administering both, hyperthermia and chemotherapy, in order to enhance the ablation of cancer cells. The HSP90 inhibitor was incorporated within GNR-C_{12}ELP nanocomposites during their formation leading to 17-AAG-GNR-C_{12}ELP nanocomposites (Figure 54 b inset) The absorbance spectrum of 17-AAG-GNR-C_{12}ELP nanocomposites demonstrated an additional peak at 335 nm (Figure 54 a and b), which was indicative of the incorporation of 17AAG within the polypeptide nanocomposite; approximately 550 ug of the drug were incorporated within a single nanocomposite.

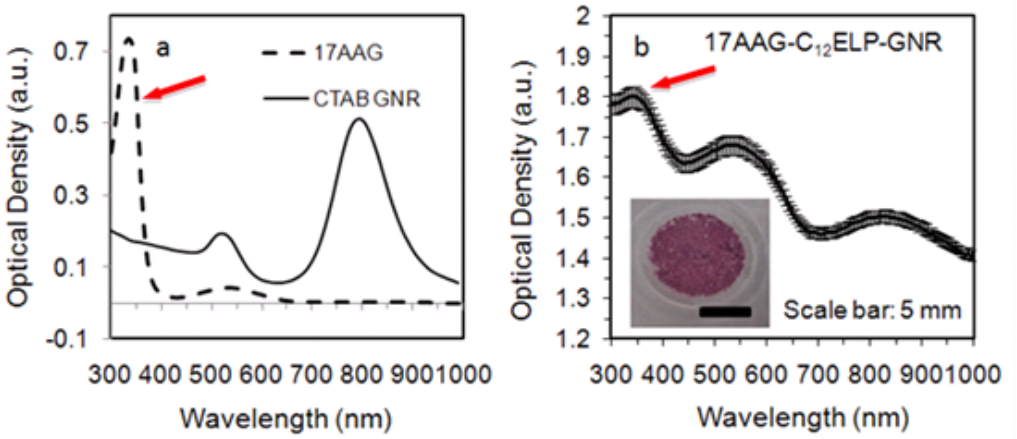

Figure 54.Spectrum of 17-AAG loaded GNR-C_{12}ELP nanocomposites. C_{12}ELP-GNR nanocomposites loaded with heat shock protein 90 (HSP90) inhibitor, 17-AAG, for ablation of cancer cells using a combination treatment of hyperthermia and heat shock protein inhibition. (a). Absorbance spectrum 17-AAG shows a peak at approximately 330 nm which is reflected in the 17-AAG-GNR-C_{12}ELPnanocomposite (b). The inset in (b) shows a digital snapshot of the 17-AAG-GNR-C_{12}ELP nanocomposite loaded with 0.55 mg of the HSP90 inhibitor drug.

Figure 55 shows the diffusion release (leaching) of 17-AAG from the 17-AAG-GNR-C_{12}ELPnanocompositewas monitored for 24 h to a supernatant of 1XPBS (volume 500 ul). Approximately 10 g of the drug were released in the first hour, following which, an additional 7 g of the drug were released over the next 23 hours, indicating that a total of only 3% of the encapsulated drug leached out due to diffusion. This demonstrates that the nanocomposites are able to stably incorporate chemotherapeutic drugs with minimal loss due to leaching. This is significant since unintended drug loss from the nanocomposite can result in undesired side effects. Subjecting the nanocomposite to laser irradiation resulted in an increase in local temperature due to the photothermal effects of gold nanorods, which in turn, led to enhanced release of 17-AAG from the nanocomposite, presumably due to ELP structural changes and aggregation above the transition temperature, which in turn, can result in contraction of the nanocomposite leading to drug efflux. The concomitant temperature increase is shown in Figure 55 b and is similar to that observed with the nanocomposite in the absence of the drug (Figure 53). A five-minute laser irradiation pulse (850 nm laser, 25 W/cm^2) resulted in the release of only 2.5 µg of 17-AAG, indicating longer exposure times were necessary for increased release of the drug. Subsequent laser exposures were therefore carried out for ten minutes each (850 nm, 25 W/cm^2), which resulted in the release of 12.6 µg ± 2.4 µg for each round of laser irradiation. Discolored spots on the GNR-C_{12}ELP nanocomposite(Figure 55a, inset) indicate regions of drug release following exposure to the laser. This is consistent with the temperature profiles in Figure 55 b, which indicated that merely reaching hyperthermic temperatures may not

be enough to trigger drug release and that sustained hyperthermic temperatures may be required.

In order to further investigate the role of laser-induced drug release, nanocomposite for diffusion drug release was first investigated, which is followed by incubation at moderately hyperthermic temperatures (42^{o}C), and finally laser treatments. The total amount of drug originally encapsulated in this nanocomposite was approximately 614 g, which was higher than the amount encapsulated in the nanocomposite shown in Figure 55 a. As seen in Figure 55 c, higher 17-AAG quantities were released following laser irradiation compared to the water bath incubation treatment. It is possible that temperatures directly in the path of the laser are significantly higher than 42-44^{o}C and lead to greater drug release due to more significant changes in the nanocomposite at these locations. This is currently under investigation in our laboratory.

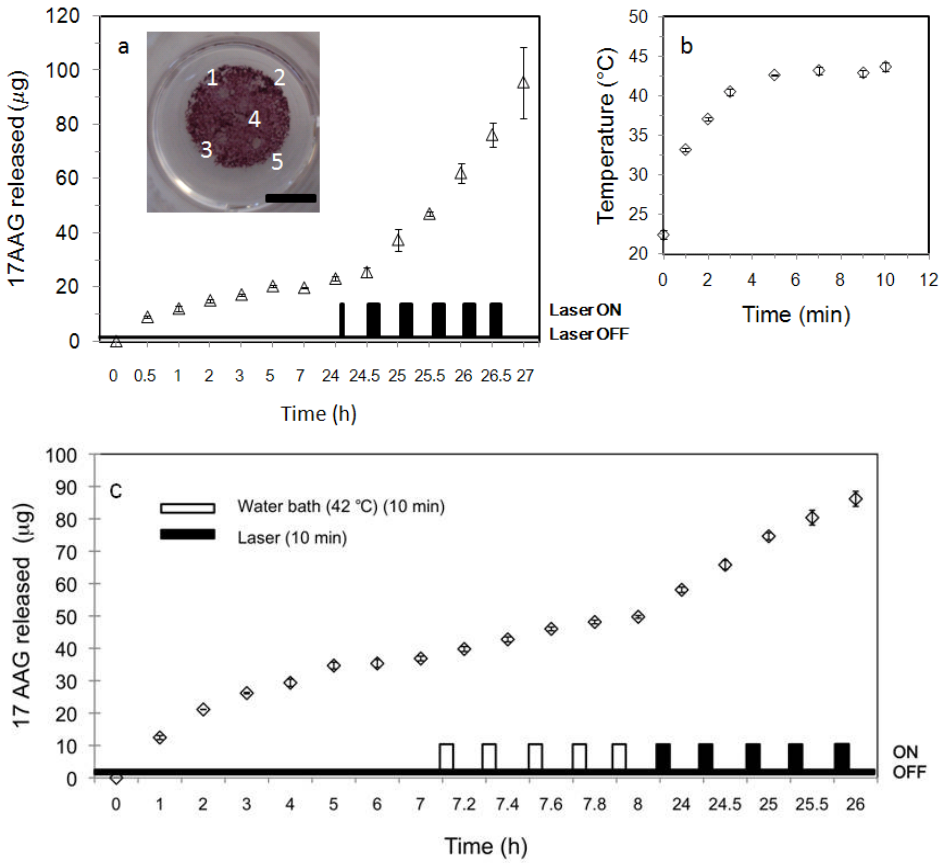

Figure 55.Photothermally activated release of the HSP90 inhibitor drug, 17AAG from 17-AAG-GNR-C_{12}ELPnanocomposites.
(A) Diffusion release (leaching) of 17-AAG from the17-AAG-GNR-C12ELPnanocomposite was monitored for 24 h to a supernatant of PBS (volume 500 ul). The nanocomposite was then subjected to laser irradiation for releasing the drug. The first laser irradiation last for 5 minutes (850 nm, 25 W/cm^2), the second to sixth laser irradiations (850 nm, 25 W/cm^2), were for 10 minutes, with 20 min interval without laser in between each irradiation. Data shown is mean ± one standard deviation from four independent experiments (n= 4)
(B) The temperature profile during 10 minutes laser exposure was monitored with a Type-K thermocouple. The temperature reached 43-44^{o}C (heat shock conditions) following 5 minutes of laser irradiation, and remained invariant thereafter. Laser irradiation resulted in an additional 45-50 µg of 17-AAG released from the 17-AAG-GNR-C_{12}ELP nanocomposites indicating the potential for combined hyperthermia and heat shock inhibition.
(C) Role of laser irradiation on enhancing 17-AAG release from GNR-C_{12}ELP nanocomposites. Nanocomposites were first investigated for diffusion leaching of the drug, followed by incubation a water bath at 42^{o}C, and were finally irradiated with an NIR laser. Higher amounts of drug were released following laser treatment, presumably due to higher localized temperatures in the path of the laser.

Taken together, these results indicate that the photothermal properties of the polypeptide nanocomposite facilitates local increases in temperature following laser irradiation, which in turn, triggers release of the encapsulated drug, presumably due to a combination of increased drug diffusivity and ELP aggregation and contraction at temperatures above the polypeptide transition temperature.

I next evaluated the efficacy of the simultaneous administration of hyperthermia and HSP90 inhibitor for the ablation of prostate cancer cells. In order to account for the efficacy of this combination treatment, two 'single-agent' treatments were first carried out: (1) hyperthermia alone, in which the nanocomposite without the 17-AAG drug was employed for killing cancer cells only due to hyperthermic temperatures in the absence of the drug, and (2) 17-AAG alone, in which loss of cancer cell viability due to constitutive 17-AAG diffusion release from the nanocomposite was evaluated in the absence of laser-induced hyperthermia.

GNR-C_{12}ELP nanocomposites (without 17-AAG) supported the growth of PC3-PSMA human prostate cancer cells, indicating that the plasmonic nanocomposite was not toxic to cells. For the 'hyperthermia alone' treatment, cells were irradiated with an 850 nm laser (25 W/cm^2 laser for 7 minutes) and cell viability was determined using the Live/dead® assay 24 hours after the laser treatment. Phase contrast and fluorescence microscopy images were recorded immediately after staining. As expected, laser irradiation resulted in significant death of PC3-

PSMA cells directly in the path of the laser beam as seen from the red stained cells in Figure 56, consistent with previous observations in literature.[223,268] However, cells outside the path of the laser beam did not undergo any loss of viability as seen from the green-stained living cells in Figure 56. These results highlight spatial limitations associated with nanoparticle-mediated hyperthermic ablation of cancer cells; while nanoparticles and laser irradiation can be employed for localized treatments, effective treatment can be administered only over a limited region leading to ineffective treatment. Importantly, the plasmonic nanocomposite is biocompatible, can be used for the hyperthermic ablation of cancer cells, and in implantable treatments where the spatial limitations of hyperthermia are not a concern.

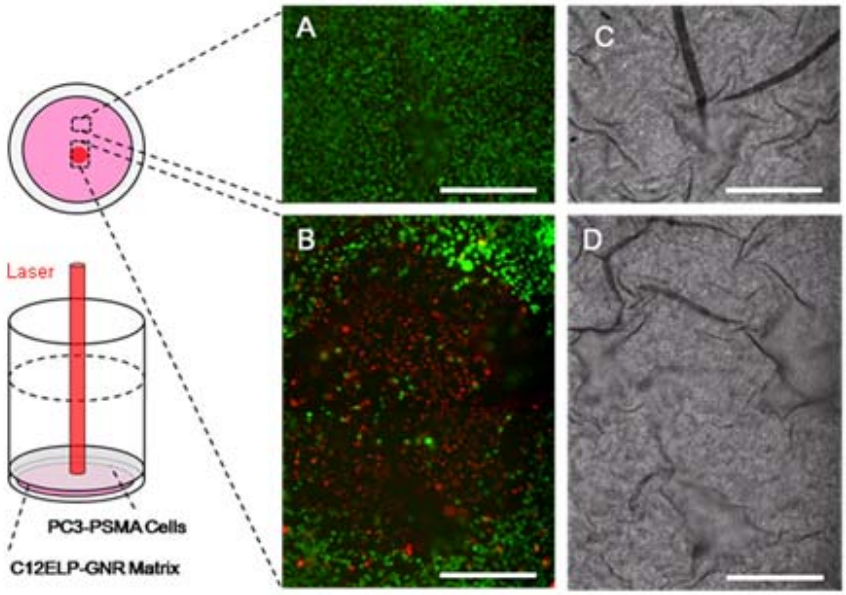

Figure 56.GNR-C_{12}ELP nanocomposites forcell ablation.
GNR-C_{12}ELP nanocomposites cell ablation set up with fluorescence (A, B) and phase (C, D) images. PC3-PSMA human prostate cancer cells were cultured on GNR-C_{12}ELP nanocomposites (without 17-AAG drug) for 24 h, and irradiated with an 850 nm laser (25 W/cm^2) for 7 minutes. Viability of cells directly under the 1mm laser irradiation spot (top; circled area) and outside the laser spot (bottom)

was determined using the Live/dead® assay in which living cells stained green while dead cells stained red. Cells directly under the laser were killed by the hyperthermic treatment while those outside the laser irradiation spot were alive. Approximate locations of the images on the nanocomposite are shown. Representative images from two independent experiments (n = 2). Scale bar: 500 μm.

GNR-C_{12}ELP plasmonic nanocomposites, containing the anti HSP90 drug 17-AAG (17-AAG-GNR-C_{12}ELP), were evaluated in the absence of laser-induced hyperthermia ('drug alone' treatment). The nanocomposites were able to support cell culture for 48 hours, indicating that the constitutive diffusional release of 17-AAG from the nanocomposite was not sufficient to induce cell death in cancer cells (Figure 57). These results also demonstrate that the nanocomposites are able to support mammalian cell culture.

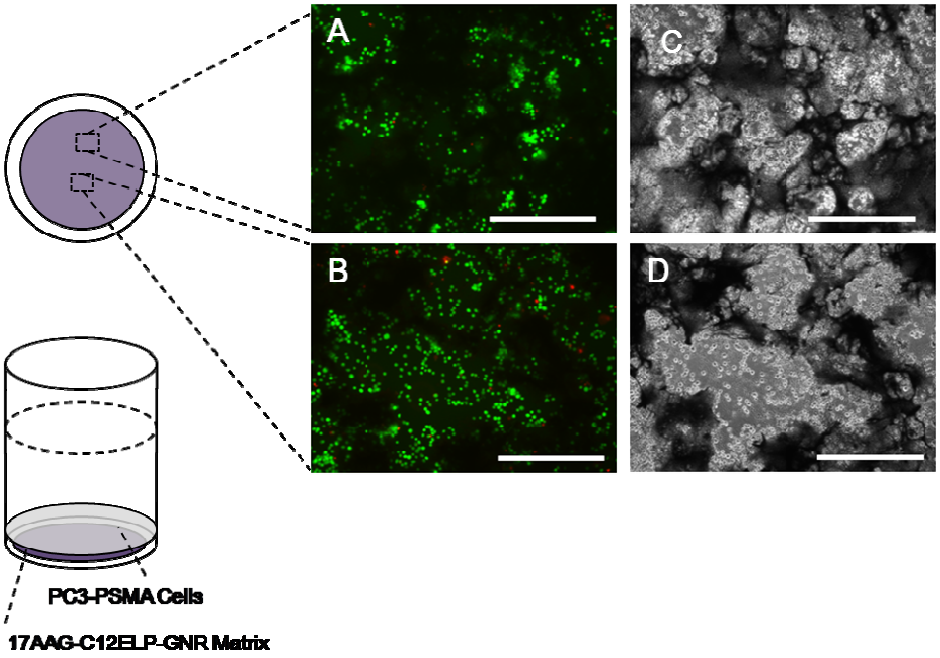

Figure 57.17-AAG-GNR-C_{12}ELPnanocompositefor cell culture.
17-AAG-GNR-C_{12}ELPnanocompositecell culture set up with fluorescence (A, B) and phase (C, D) images. PC3-PSMA human prostate cancer cells were cultured on 17-AAG-GNR-C_{12}ELPnanocomposites for 48 h (no laser treatment) and

viability of cells was determined using the Live/dead® assay. Diffusion release of 17-AAG from the nanocomposite did not alter the viability of the cells. Approximate locations of the images on the nanocomposites are shown. Representative images from three independent experiments (n= 3). Scale bar: 500 μm.

In order to investigate the efficacy of the combination treatment for killing cancer cells, PC3-PSMA cells were exposed to an 850 nm laser (25 W/cm^2 laser for 7 minutes) and as before, cell viability was evaluated 24 hours following the laser treatment. While a single circular shape corresponding to the size of the laser beam could not be located in this case, dead cells could be seen throughout the nanocomposite(Figure 58), indicating that a combination of the hyperthermic temperatures and the triggered release of the anti-HSP90 drug, 17-AAG, was responsible for extensive cancer cell death.

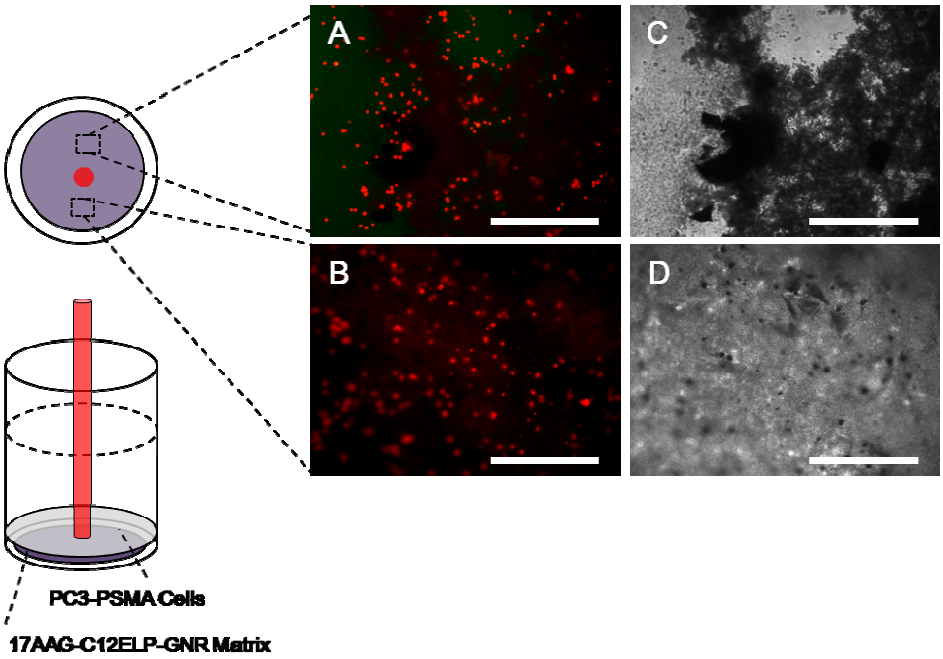

Figure 58.17-AAG-GNR-C_{12}ELPnanocompositesfor combination cell treatment. 17-AAG-GNR-C_{12}ELP nanocomposites cell ablation set up with fluorescence (A, B) and phase (C, D) images. PC3-PSMA human prostate cancer cells were

cultured on 17-AAG-GNR-C_{12}ELP nanocomposites for 24 h and irradiated with an 850 nm laser (25 W/cm^2) for 7 minutes. Cell viability was investigated after 24 h of the laser treatment using the Live/ Dead® assay (total cell culture time = 48 h). Representative images at two different locations away from the laser irradiation spot demonstrate approximately 90 % cell death due to the combination of mild hyperthermia (43^{o}C; Figure 7.6 b) and release of the heat shock inhibitor drug 17AAG (Figure 7.6 a). This pattern of uniform cell death throughout the well is higher than what was seen with the 'single agent (i.e. mild hyperthermia alone and 17-AAG release alone) treatments. Approximate locations of the images on the nanocomposite are shown. Representative images from three independent experiments (n= 3). Scale bar: 500 μm.

The synergistic action between these combination treatments is demonstrated by quantitative analysis of the cell death results (Figure 59). 'Drug-alone' and 'laser-alone' treatments resulted in minimal loss of cell viability (< 10 % of the cell population). However, the combination treatment (laser-induced hyperthermia and release of the HSP90 inhibitor) resulted in over 90% loss in cell viability (Figure 59). These results indicate that drug-loaded nanoparticle-polypeptide nanocomposites can simultaneously overcome (1) cancer cell resistance to nanoparticle induced hyperthermia which is mediated by heat shock protein overexpression and (2) spatial limitations of laser-induced hyperthermia using plasmonic nanoparticles (Table 6.1).

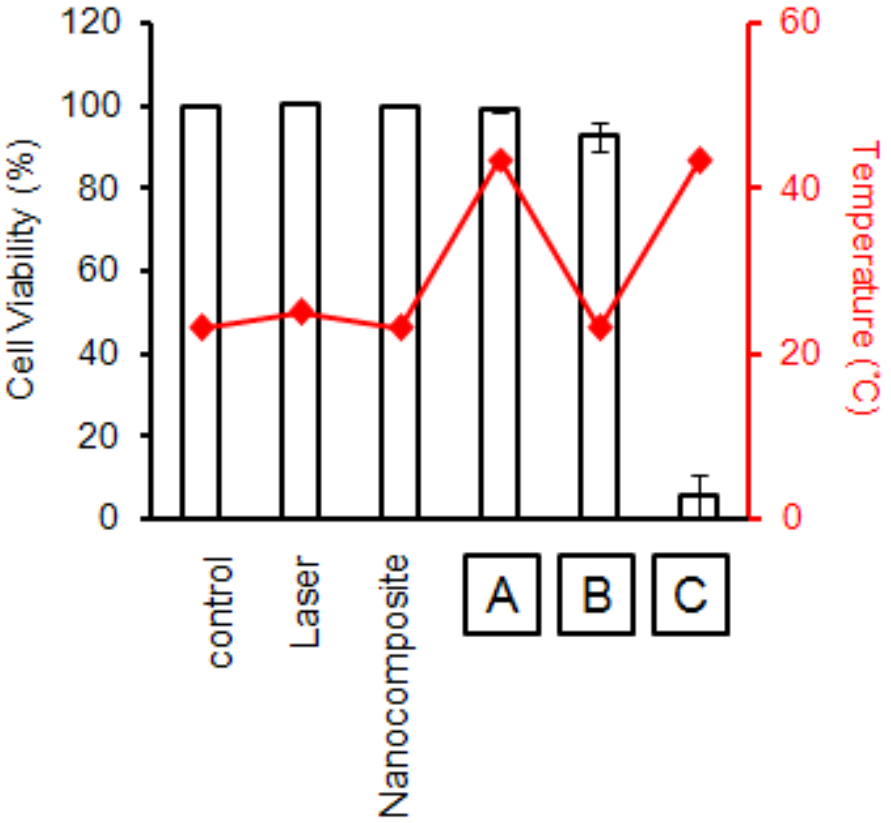

Figure 59.Quantitative analysis of cell death
Analysis of cell death demonstrates the efficacy of the laser-induced combination treatment of hyperthermia and heat shock inhibitor 17-AAG using GNR-C_{12}ELP-17AAG nanocomposites. X-axis legend: Nanocomposite indicates the GNR-C_{12}ELP nanocomposite and 17AAG nanocomposite indicates GNR-C_{12}ELP-17-AAG (i.e. drug-loaded) nanocomposites. (n≧ 3 for all conditions).

Table 8.Summary of Combination Treatments.

Nanocomposite	**Laser Power Density (7 min irradiation)**	**Cell Death**	
		Laser Spot	**Periphery**
GNR-C_{12}ELP	0 W /cm^2	No	No
GNR-C_{12}ELP	25 W /cm^2	**Yes**	No
17-AAG-GNR-C_{12}ELP	0 W /cm^2	No	No
17-AAG-GNR-C_{12}ELP	25 W /cm^2	**Yes**	**Yes**

7.4 Conclusions

In this chapter, it was demonstrated that GNR-C_{12}ELPnanocompositesmaintaining the photothermal properties of the gold nanorods can be employed for the hyperthermic ablation of cancer cells. However, spatial limitations of the administered hyperthermia treatment, in addition to the pro-survival heat shock response associated with cancer cells, led us to incorporate the HSP90 inhibitor, 17-AAG, in the nanocomposite. Laser irradiation of the plasmonic nanocomposite3resulted in simultaneous administration of hyperthermic temperatures and release of 17-AAG. Synergistic action between hyperthermia and HSP90 inhibition led to significant enhancement of cancer cell death. To our knowledge, this is the first report that describes the use of a heat shock protein inhibitor in combination with nanoparticle-induced hyperthermia for the ablation of cancer cells. Our results indicate that such nanocomposites can be used for enhancing the efficacy of hyperthermia as an adjuvant treatment. In addition, this is the first report that describes GNR-ELP nanocomposites as plasmonic nanobiomaterials. The availability of a variety of engineered polypeptides, nanoparticles, and chemotherapeutic drugs, should advance this approach leading to biocompatible plasmonic nanocomposites for different therapeutic modalities and other biomedical applications, including biosensing and regenerative medicine.

CHAPTER

8. Ex vivo Laser Tissue Welding using Polypeptide-Gold Nanorod Nanocomposite Solders

8.1 Introduction

Chapter 6 investigated different physicochemical conditions that influence GNR-C_{12}ELP nanocomposite formation. The effect from both cetyltrimethyl ammonium bromide (surfactant used to template the formation of gold nanorods) and GNR were investigated using optical measurements and model fitting. Chapter 7 employed solid phase nanocomposites, which retained the photothermal properties of nanorods, for simultaneous administration of laser-induced hyperthermia and chemotherapeutic drugs to prostate cancer cells. This chapter involves a detailed investigation into biocompatible, light responsive bioadhesive for laser tissue welding (LTW) of colorectal tissue, using porcine intestinal model, to establish a fluid-tight sealing.

Every year, over 600,000 people in the United States will undergo surgical procedures to treat a number of colorectal diseases such as colorectal cancer, inflammatory bowel disease (IBD), and diverticulitis (*http://www.lapsurg.org/colon.html*). Patients undergo either conventional open surgery or laparoscopic surgeries to remove diseased tissue require end-to-end anastomoses (connection) of the healthy sections. Surgical suturing and stapling are still the most common and important procedures in colorectal anastomoses, however, both techniques rely on piercing healthy tissue and can cause

anastomosis leakage. Leakage of intestinal bacteria from bacteria-rich colorectal system into abdominal lumen can cause serious infection in the potentially deadly form of peritonitis[269-272]. Incidence of anastomotic leakage following standard surgical anastomosis in colorectal surgery are reported from 4% to 17%[269,270,273], and accounts for one-third of the mortality after colorectal surgery[274]. Alternative or supportive anastomosis techniques are urgently required in order to decrease anastomosis leakage rate after colorectal surgery.

Laser tissue welding (LTW) emerged as a "sutureless" surgical method for the anastomosis of ruptured tissues (e.g. vessels, bowel, urinary tract, skin and others[275-283]). Laser tissue welding holds several advantages over conventional suturing and stapling procedures, these include short operation time, immediate fluid-tight sealing, reduced foreign-body reactions (e.g. inflammatory response), scar reduction and accelerated healing[278,284-288]. The mechanism for the LTW involves the tissue absorption of laser light, which converts into heat energy to induce alteration of tissue proteins[282,289]. Interdigitation of the photothermal-altered tissue proteins via covalent and electrostatic interaction[279,290,291] is considered to be the basic effect for the LTW. Laser-assisted colorectal anastomosis have been demonstrated to provide an immediate fluid-tight sealing, and may reduce the frequency of colonic anastomosis leakage[292]. Cilesiz et al. reported *in vivo* Ho:YAG and argon laser welding of rat Intestine resulted in a comparable bursting pressure and healing rate to suture anastomoses[293]. In a canine jejunum study, strong tissue fusion was not possible at or below a surface temperature of 70°C, but was accomplished above 80 °C[284]. Overall, reports

recognized heating tissue above 60 °C is necessary to provide robust closure[294]. The photothermal damaging of tissue is irreversible; possessing the ability to precisely provide, adjust and predict laser dosage based on real-time temperature monitoring systems is critical and has been demonstrated by several groups[284,293,295].

Major concerns associated with LTW include insufficient anastomoses strength, limited light penetration depth and peripheral tissue thermal damage. These problems can be addressed by the introduction of protein-based solders (e.g. albumin-, elastin- and chitosan-based) in concert with near infrared (NIR) light absorbing chromophores (e.g. indocyanine green, fluorescein, and gold nanoparticles)[296,297]. Upon laser irradiation, protein solders denatured and incorporated into welding site to (i) improve the tensile strength of the closure, (ii) minimize peripheral tissue destruction, and (iii) further reduce foreign body responses. Near infrared light (NIR) enabled deeper penetration, while, presence of chromophores can efficiently transfer lower dose light energy into sufficient localized heat energy to reduce unwanted thermal damage[298,299].It has been demonstrated, introduction of protein-based solders in combination with light-absorbing chromophores and growth stimuli is critical for the improvement of anastomoses strength, reduction of tissue thermal damage and acceleration of wound healing process[296-299]. Lauto et al. reported genipin-crosslinked albumin can significantly increased the tensile strength of adhesive-tissue bonds after laser welding[292]. Transforming growth factor-beta (TGF-β), a key component in the fibrogenic process and inflammatory response, has been incorporated into

human albumin solder to accelerate wound healing process after laser welding[300].

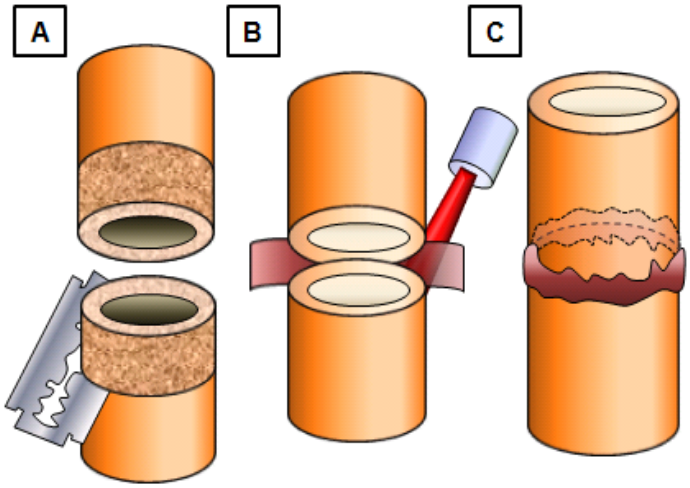

Figure 60.Colorectalsurgery followed by laser tissue welding using nanocomposite solder and laser light.
(A) Removal of diseased tissue. (B) Reconnect of the healthy sections (anastomosis). (C) Achieving a fluid-tight sealing.

In this chapter, It was hypothesized that LTW of colorectal tissues using GNR-C_{12}ELP nanocomposite can result in rapid fluid-tight anastomosis and potentially accelerate wound healing process. Specifically, gold nanorods can maximize the photothermal effect and crosslinked elastin-like polypeptide can improve the anastomoses strength (Figure 60). The GNR-C_{12}ELP nanocomposite advances current solders in several aspects: (i) The light dosage required to induce similar thermal response using gold nanostructures is 10- to 25- fold lower than with photoabsorbing dyes[301]. Among various types of gold nanoparticles, gold nanorods with highest near infrared (NIR) absorption cross-section[302] can convert light into heat most efficiently. Moreover, light in NIR region can provide maximal tissue penetration, due to minimal light absorption by water and blood[4]. In

summary, Presence of NIR light responsive gold nanorods can provide sufficient localized heating with reduced thermal damage of the periphery tissue. (ii) Artificial elastin like polypeptides have been repeatedly reported to be biocompatible and low immunogenicity[303]. Our collaborator successfully demonstrated keratinocyte growth factor modified elastin-like peptides can be used for the *in vivo* treatment of chronic wounds[304]. However, low dynamic shear stiffness associated with hydrogels formed from ELP coacervates can potentially limit their tissue engineering applications where significant load supporting is required[305].

In this study, it first was time reported that crosslinking of elastin-like polypeptide using gold nanorods can provide improved dynamic shear stiffness of nanocomposite. Secondly, unmodified- and surfaced (PEG)modified-nanocomposites were able to support murine fibroblasts (NIH 3T3) growth with minimal cytotoxicity (< 90%). Last, laser tissue welding of porcine intestine using GNR-C_{12}ELP nanocomposites led to a rapid enhancement of tissue mechanical strength (tensile strength, bursting pressure and leaking pressure) of ruptured-tissue. In summary, multifunctional nanocomposite with capabilities of (1) controlled releasing of small molecules (Chapter 7), (2) cell culture supporting with minimum toxicity, and (3) providing robust and stable photothermal responses for laser tissue welding, are promising for tissue regeneration and repair applications.

8.2 Materials and Methods

8.2.1 Materials

Gold (III) chloride trihydrate ($HAuCl_4 \cdot 3H_2O$), cetyltrimethyl ammonium bromide (CTAB), L-ascorbic acid, sodium borohydride and silver nitrate were purchased from Sigma-Aldrich. All chemicals were used as received without further purification. DMEM cell culture medium was purchased from Invitrogen. Pen-Strep solution (10,000 units/mL penicillin and 10,000 µg/mL streptomycin in 0.85% NaCl) and fetal bovine serum (FBS) were purchased from Hyclone. Fresh porcine small intestines were purchased from Animal Technologies Inc., Texas.

8.2.2 Generation of Gold Nanorods

Gold nanorods were synthesized using the seed-mediated method[155] following the same procedure in Chapter 3.2.2, this method was employed to generate gold nanorod population that possessed absorbance maxima (λ_{max}) in the near infrared (NIR) region of the optical spectrum. Nanorod aliquots, with an initial CTAB concentration of 100 mM, were pelleted by centrifugation (6000 rcf, 10 min), following which, the clear supernatant was removed, and resuspended in nanopure water to various final volumes. Further centrifugation, decantation and dilution steps allowed the generation of a series of nanorod samples ($OD_{\lambda max}$= 0.125-2.5; corresponded to 9.5-190 µg/mL) with CTAB concentration less than 0.25 mM. In all cases, the concentration of gold in GNRs was determined using inductively coupled plasma optical emission spectrometry (ICP-OES, iCAP 6000 Series, Thermo Electron Corporation); NIR absorption characteristics of the nanorods were determined using a plate reader (Biotek Synergy 2).

8.2.3 Preparation of Polyethylene Glycol (PEG)-modified Gold Nanorods

Polyethylene glycol (PEG)-modified gold nanorods (PEG-GNRs) were prepared as follows. Aliquots of gold nanorod dispersions (19 μg/mL) were centrifuged at 6,000 rcf for 10 minutes; the supernatants were decanted, and nanorod precipitants were resuspended in thiol-functionalized polyethylene glycol ($mPEG_{5000}$-SH) solutions (Creative PEGWorks) to various concentrations (50-250 μg/mL) for 2 hours at room temperature. The free $mPEG_{5000}$-SH molecules were removed by centrifugation at 6,000 rcf for 10 minutes. The final PEG-GNRs samples were resuspended in nanopure water to their original volume.

8.2.4 Synthesis, Expression, and Purification of Cysteine containing Elastin-like Polypeptides (ELPs)

Elastin-like polypeptides containing twelve cysteines (C_{12}ELP), were generated using recursive directional ligation method described previously[237]. C_{12}ELP contain eight and twelve cysteines residues (shown in bold) in the sequence: MVSACRGPG-(VG VPGVG VPGVG VPGVG VPGVG VPG)$_8$-(VG VPGVG VPGVG VPG**C**G VPGVG VPG)$_{12}$-WP. C_{12}ELP were generated, expressed, purification lyophilized and stored at room temperature as described previously in Chapter 5.2.1[237]. The transition temperature (T_t) of C_{12}ELP was characterized as described in Chapter 5.2.2 previously. The temperature response of the C_{12}ELP indicated transition temperature (T_t) value of 30.5°C.

8.2.5 Preparation of GNR-C_{12}ELP Nanocomposites

Preparation of GNR-C_{12}ELP nanocomposites can be summarized into two steps as described previously in Chapter 6 and 7; the process involves: (i) self-

assemble of C_{12}ELPs on GNRs via gold-thiol bond at 4 °C leading to the formation of nanoassemblies in dispersion form, and (ii) phase separation nanoassemblies leading to the irreversible formation of solid-phase nanocomposites at 37 °C. Briefly, gold nanorod samples (9.5 – 190 µg/ml, nanopure water) at a volume of 1 mL were mixed with 1 mL of C_{12}ELP (2 mg/ml, 1 X PBS) overnight at 4°C. This led to the formation of GNR-C_{12}ELP nanoassemblies at various GNR weight percentages (0.47 – 8.68 % wt). GNR-C_{12}ELP nanoassemblies (2 mL) were placed in our homemade device, and incubated at 37 °C for 6 hours; this led to the formation of GNR-C_{12}ELP nanocomposite (~2 mg, 10 mm diameter, thickness = 247 ± 65 µm) on top of a glass coverslip. In case of preparing PEG-modified gold nanorod-C_{12}ELP (PEG-GNR-C_{12}ELP) nanocomposite, PEG-GNRs were used instead of GNRs, same procedure was followed. In case of C_{12}ELP alone controls, no gold nanorods were introduced.

8.2.6 Swelling Experiments

Nanocomposite was incubated in 2 mL of 1 X PBS (pH 7.4) at room temperature for 24 hours, following which, the mass of nanocomposite plus the tube was measured. The mass of the swollen nanocomposite (M_s) was determined by subtracting the mass of the tube from the total mass. The nanocomposites were freeze-dried using lyophilizer (FreeZone, Labconco Corporation). The dry mass (M_d) was calculated by subtracting the mass of the tube from the total mass. Swelling ratio (Q) was defined as the ratio of the mass of swollen nanocomposite to the mass of dry nanocomposite.

8.2.7 Rheological Measurements

The mechanical behaviors of the GNR-C_{12}ELP nanocomposites and C_{12}ELP coacervates were assessed using AR-G2 rheometer (TA Instruments) in a parallel plate configuration (8 mm diameter). The samples (10 mm diameter, ~1 mm thickness) were loaded between the plates, the gap was closed until the sample was in good contact with both plates (normal force <0.1 N). Prior to measurement, samples were equilibrated on the temperature-controlled peltier plate for 30 minutes in order to exclude the time-dependent relaxation during the measurement. The dynamic frequency sweep was conducted over an angular frequency range of 1 – 40 rad/s, at fixed strain amplitude of 0.05, and 25 °C. Temperature sweep was performed between 25 °C and 45 °C at a temperature increment rate of 1 °C/min, the frequency and strain amplitude were controlled at 20 rad/s and 0.05, respectively. The absolute shear modulus (|G*|) and loss angle (δ), representing the stiffness and the relative measure of viscous to elastic effects of the nanocomposite under dynamic loading, respectively, were calculated and reported. The absolute magnitude of the shear modulus, |G*|, was determined based on the definition $|G^*| = (G'^2 + G''^2)^{0.5}$; where, G' is the elastic storage modulus and G" is the viscous loss modulus. For pure elastic idea solid the loss angle(δ) is 0 degree; whereas, pure viscous Newtonian fluid has a loss angle (δ)equal to 90 degree.

8.2.8 Biocompatibility of Nanocomposites

8.2.8.1 Murine Fibroblast Culture

Fibroblast cells were generous gifted from Dr. Christine Pauken at the Department of Biomedical Engineering, Arizona State University, Tempe, AZ. Cells were cultured in a 5% CO_2 incubator at 37°C using DMEM medium containing 10% heat-inactivated fetal bovine serum (FBS) and 1% antibiotics (10000 units/mL penicillin and 10000 µg/mL streptomycin). Murine fibroblast (3T3) cells were used for: (i) evaluation of the nanocomposite biocompatibility (Chapter 8.2.8.2) and (ii) nanocomposite cellularization (Chapter 8.2.8.3).

8.2.8.2 Cell Monolayer Culture

The biocompatibility of nanocomposites at various GNR (1.9-5.4 wt%) and PEG (0-19.7 wt%) weight percentages, prepared in 96-well plate, was first evaluated. Briefly, aliquots 200 µL of GNR-C_{12}ELP (or PEG-GNR-C_{12}ELP) nanoassemblies (prepared as described previously) were added into each well at 4°C. The samples were then subjected to 37°C incubation for 6 hours leading to nanocomposites formation at the bottom of the wells. After incubation, the clear supernatants were decanted; the nanocomposites were washed twice with 1 X PBS and pretreated with 200 µL of cell culture medium for 30 minutes. Fibroblast cells were seeded on top of the cell culture medium-pretreated nanocomposites with a density of 5,000 cells per well. The cell viabilities at 24, 48 and 72 hours after seeding were determined using fluorescence-based Live/dead®. Briefly, cells were treated with 4 µM ethidium homodimer-1 (EthD-1; Invitrogen) and 2 µM calcein AM (Invitrogen) for 30 minutes and imaged using Zeiss AxioObserver D1 inverted microscope (10X/0.3 numerical aperture (NA) objective; Carl Zeiss MicroImaging Inc., Germany). The nucleic acids of membrane-compromised

(dying/dead) cells were labeled red fluorescence with membrane-impermeant EthD-1; the esterases in viable/live cells cleaved membrane-permeant calcein AM to yield cytoplasmic green fluorescence. Quantitative analysis of cell viability was carried out by cell counting using the Cell Counter plug-in in ImageJ software[306] as described previously[307]. The number of live (N_L) and dead (N_D) cells were used to determine the cell viability ($N_L/(N_{L+}\ N_D)$*100%). Data reported represent the cell viability mean from more than 6 individual samples.

8.2.8.2 Cell Encapsulation

For nanocomposite cellularization, fibroblast cells were encapsulated in the nanocomposite. Briefly, PEG(4.7 wt%)-GNR(1.9 wt%)-C_{12}ELP nanoassemblies were prepared as described previously, but resuspended in cell culture media instead. A number of 250,000 cells were introduced to 2 mL PEG-GNR-C_{12}ELP nanoassembly dispersion during incubation at 37 °C and 5% CO_2 in our homemade device. After 6 hours, the cell-encapsulated nanocomposite (10 mm diameter), on top of a glass coverslip, was collected and wash thoroughly with 1X PBS three times in order to remove any loosely attached cells. The cell-encapsulated nanocomposite, covered with medium and placed in a 6-well plate, was cultured in a 5% CO_2 incubator at 37 °C. The distance of cell proliferation was monitored up to 14 days using a Zeiss AxioObserver D1 inverted microscope (10 × X/0.3 numerical aperture (NA) objective; Carl Zeiss MicroImaging Inc., Germany), where the cell culture medium was changed in every three days. The encapsulated cells were stained using fluorescence-based Live/dead® as described in previous section, and imaged using both

AxioObserver D1 inverted microscope and laser scanning Nikon C2 confocal microscope (Nikon Instruments Inc., Melville, NY). For confocal imaging, images were acquired and stacked using NIS-Elements Microscope Imaging Software (Nikon Corporation) at 60× water objective with a z-step of 0.225 µm slice and with PMT scanners at 512 × 512 pixels.

8.2.9 Laser Tissue Welding

A titanium continuous wave (CW) sapphire (Ti: S) laser (Spectra-Physics, Tsunami) pumped by a solid-state laser (Spectra-Physics, Millennia) was employed for laser tissue welding. The excitation source was tuned to overlap with the longitudinal maxima of the nanocomposites (~ 800 nm). The laser output power and the beam diameter were fixed at 20 W/cm^2 and 2 mm, respectively. Porcine small intestines were harvested, cleaned with phosphate buffered saline (1 X PBS, pH 7.4) and stored at -20°C (Animal Technologies Inc.). Prior to laser welding, tissue samples were defrosted in nanopure water for 30 minutes and kept moist using 1 X PBS at 25°C throughout the laser tissue welding and tensile testing. Rectangular intestine sections (~0.1 cm thick, 4x1 cm) were placed on a glass slide with serosa layer facing up, following which, a full thickness incision (~ 8 mm in width) was applied at the center of the tissue using serological scissors. Prior to welding, the incision edges were brought into contact with one another, and nanocomposite solder (~2 mg, 10 mm diameter, thickness= 247 ± 65 µm, GNR wt%= 1.9, 5.7 or 9.5) was applied on top of the serosa layer and across the full thickness incision with full contact. Laser light (20 W/cm^2) was applied vertically at a speed of 1 mm/second across the nanocomposite for different

durations. The temperature at the nanocomposite-tissue interface was monitored using a k-type thermocouple. Samples were remained moist during welding to prevent charring.

8.2.10Tensile Strength Characterization

Tensile strength was measured using TA XT plus Texture Analyser (Texture Technology Corp., NY) with a 5Kg load cell. Welded tissues were held with pneumatic grips to prevent slipping during testing. Testing was done in tension mode at a rate of 0.5 mm/second until failure. The maximum force (N) achieved before a sample breaks was recorded and reported in ultimate tensile strength (UTS, kPa). Intact porcine small intestine sections were subjected to mechanical testing to determine the UTS of uncut specimens. Data reported represent the mean from at least 10individual samples.

8.2.11 Bursting and Leaking Pressure

Bursting and leaking pressure tests were conducted on intact porcine intestines. A homemade pressure detection system was designed and built (Figure 61).The intact porcine intestines were cut into approximately 10cm sections. A full thickness incision(~ 5 mm) was applied to the intact intestine. The nanocomposite was placed on top of the incision and the surrounding tissue. The CW laser was then applied to the nanocomposite and tissue for various times. After LTW was complete, the intestines were tightly clamped at both ends. A 21G1 Precision Glide needle was inserted

into the tissue and dyed water was fed into the intestine sections. The pressure was monitored and recorded at the leaking and bursting points. The leaking pressure was defined as when the first drop of colored water was seen coming out of the weld site. The bursting pressure was defined as when a stream of water was seen coming out of the weld site. Control bursting and leaking pressure tests were conducted on intact and cut tissues. The bursting pressure site was always along the length of the intestine. Leaking from the needle puncture site was considered negligible.

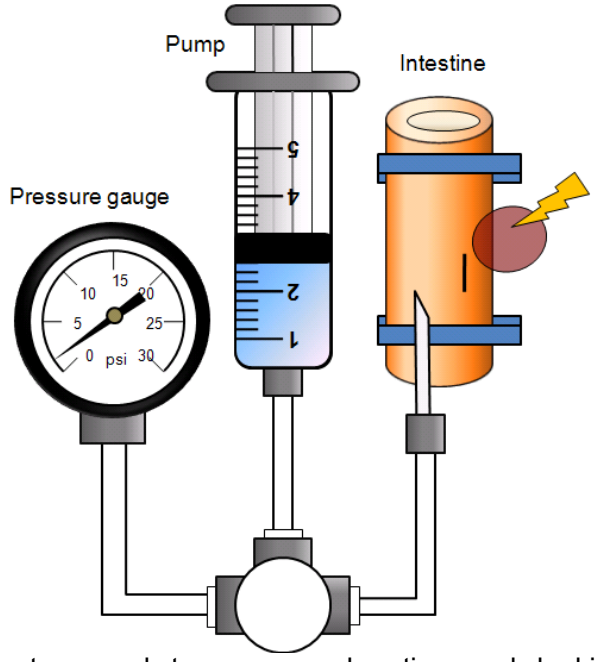

Figure 61. Apparatus used to measure bursting and leaking pressure of anastamoses.

8.2.12Statistical Analysis

Two-tailed Student's t-test and one-factor analysis of variance (ANOVA) were employedfor statistical analysis. Statistical significance was determined at a value of 0.05.

8.3 Results and Discussion

Self-assembly of C_{12}ELPs (T_t = 30.4°C, Figure 37) on GNRs (λ_{max} = 780 nm) by means of gold-thiol bonds at 4 °C resulted in the formation of well-dispersed nanoassemblies. Incubation of the nanoassemblies at 37 °C (>T_t of C_{12}ELP) for 6 hours led to temperature-triggered, entropy-dominated phase transition of C_{12}ELP[204], which, in concert with GNR-thiol and intra-and inter-molecular cysteine-cysteine cross-linking, resulted in the formation of maroon-colored plasmonic nanocomposite[238]. After nanocomposite formation, clear supernatant containing the majority of free CTAB molecules (~ 0.25 mM) was decanted. The residual CTAB molecules (0.8-32.5 nM) on the surfaces of nanorods (4.8-190 µg/ml) is minimal in the final nanocomposite [236].

As-prepared GNR-C_{12}ELP nanocomposites were 10 mm in diameter, 2.2 ± 0.2 mg in weight and 247 ± 65 µm thick (determined using digital caliper and confirmed with a light microscopy). These nanocomposites were flexible and stable at physiological environment up to at least 2 years. The absorbance spectra of the nanocomposites (Figure 40) displayed the transverse (520 nm) and red-shifted longitudinal band (~800 nm) characteristic of gold nanorods, indicating that the nanocomposites indeed demonstrated plasmonic properties

due to the uniform distribution of the gold nanorods, which was confirmed using field emission scanning electron microscopy in our previous study[238].

The swelling ratios of nanocomposites, with five gold nanorod weight percentages (GNR wt% at 0, 0.9, 1.9, 3.7 and 5.4), were determined according the protocol described in the experimental section. Swelling experiments reveal a statistically significant ($p < 0.001$) reduction of swelling ratio from 12 to 6 as GNR weight percentage increased from 0 to 5.4 wt% (Figure 62). The decrease of water uptake can be explained by the presence of gold nanorods, which facilitated nanocomposite covalent cross-linking, and resulted in the formation of rigid network to prevent swelling.

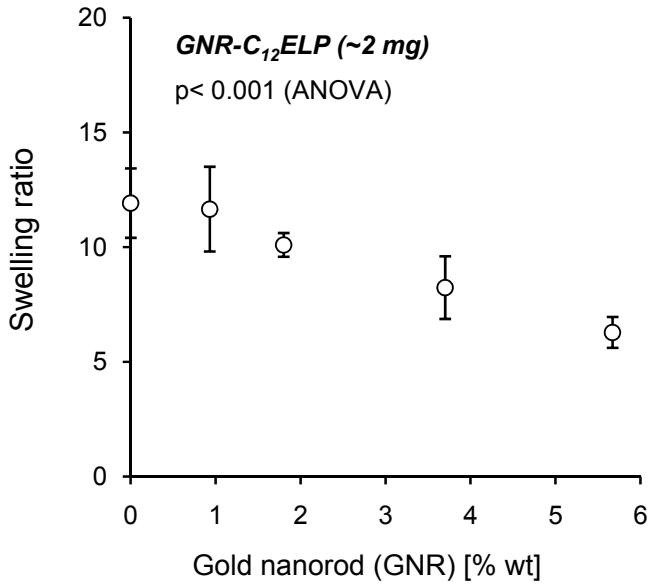

Figure 62.Swelling ratio of nanocomposites as a function of GNR weight percentage.

The rheological properties of C_{12}ELP hydrogel controls (without GNR) and GNR-C_{12}ELP nanocomposites (GNR wt% at 0.5, 0.9, 1.9 and 3.7), were measured under frequency sweep (Figure 63) and temperature sweep (Figure 64). In Figure 62A, the absolute shear modulus of C_{12}ELP hydrogels ($|G^*|$= 0.56 ± 0.1 kPa) was larger than others report on un-crosslinked ELP ($|G^*|$≈ 0.08 kPa)[308], and similar to chemically cross-linked ELP ($|G^*|$= 0.26 - 3 kPa)[305,309] under similar experimental condition. This is presumably due to the presence of intra-and inter-molecular cysteine-cysteine cross-linking in the C_{12}ELP hydrogels[238]. The mechanical integrity of C_{12}ELP was further improved upon the introduction of nanorods. The $|G^*|$ of GNR-C_{12}ELP nanocomposite increased from ~2 to ~8 kPa as a gold nanorod weight ratio rose from 0.47 to 3.7 wt%. Increase in nanocomposite stiffness (or $|G^*|$) at higher GNR wt% is due to the presence of gold nanorods, their contribution to the gold-thiol bond cross-linking in addition to intra-/inter- molecular disulfide cross-linking, and loss of water volume (decreased swelling ratio). The mean value for the loss angle (δ) of the nanocomposite was found independent of gold nanorod concentration (Figure 63B). All nanocomposite samples showed a predominantly elastic behavior, with loss angle degree less than 10.

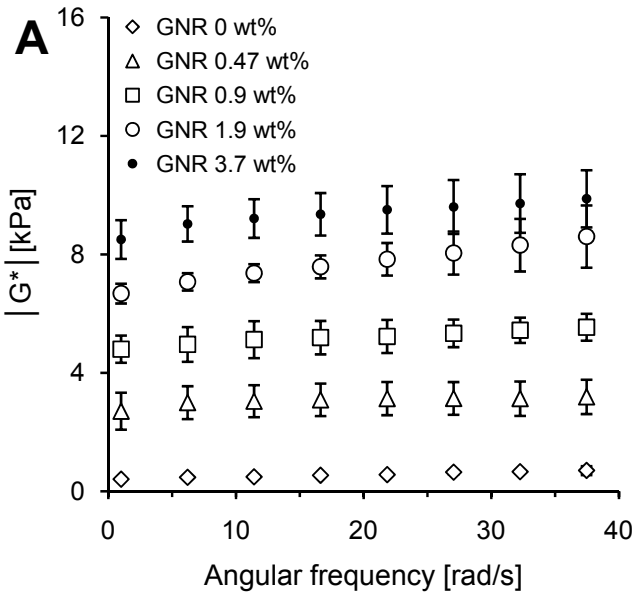
A
GNR 0 wt%
GNR 0.47 wt%
GNR 0.9 wt%
GNR 1.9 wt%
GNR 3.7 wt%
|G*| [kPa]
16
12
8
4
0
0
10
20
30
40
Angular frequency [rad/s]

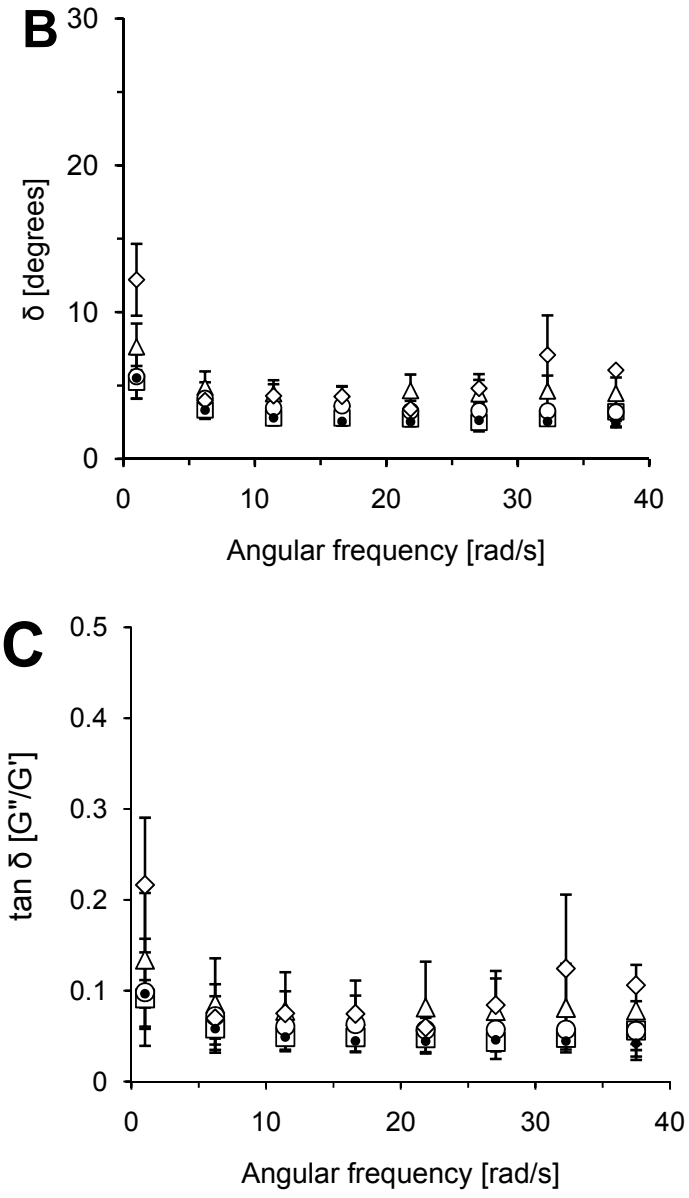

Figure 63.The rheological behavior of nanocomposites at different gold nanorod content (0-3.7 % w/w) was characterized at 25 °C.
The effect of gold nanorod concentration on the magnitude of the complex shear modules (|G*|) and phase angle (*δ*) is shown.

The effect of the temperature on the shear properties of GNR-C_{12}ELP nanocomposites is shown in Figure 64A. Increase in temperature from 25 to 45

°C did not attenuate the absolute shear moduli of nanocomposites. Furthermore, the loss angle of the nanocomposite was independent of temperature with a steady value of < 10°, again reflected the intrinsically elastic behavior of nanocomposites. Artificial elastin-like polypeptides have been repeatedly reported to be biocompatible and low immunogenicity[310]. However, low dynamic shear stiffness associated with organic crosslinker-, chemically- and enzymatically- crosslinked ELP can potentially limit their tissue engineering applications[238,305,309], specifically, in case where significant load supporting is required[305,311]. Here it was first time demonstrated crosslinking of ELPs using biocompatible inorganic gold nanorod crosslinkers can significant improve the ELP dynamic shear stiffness in a controllable manner.

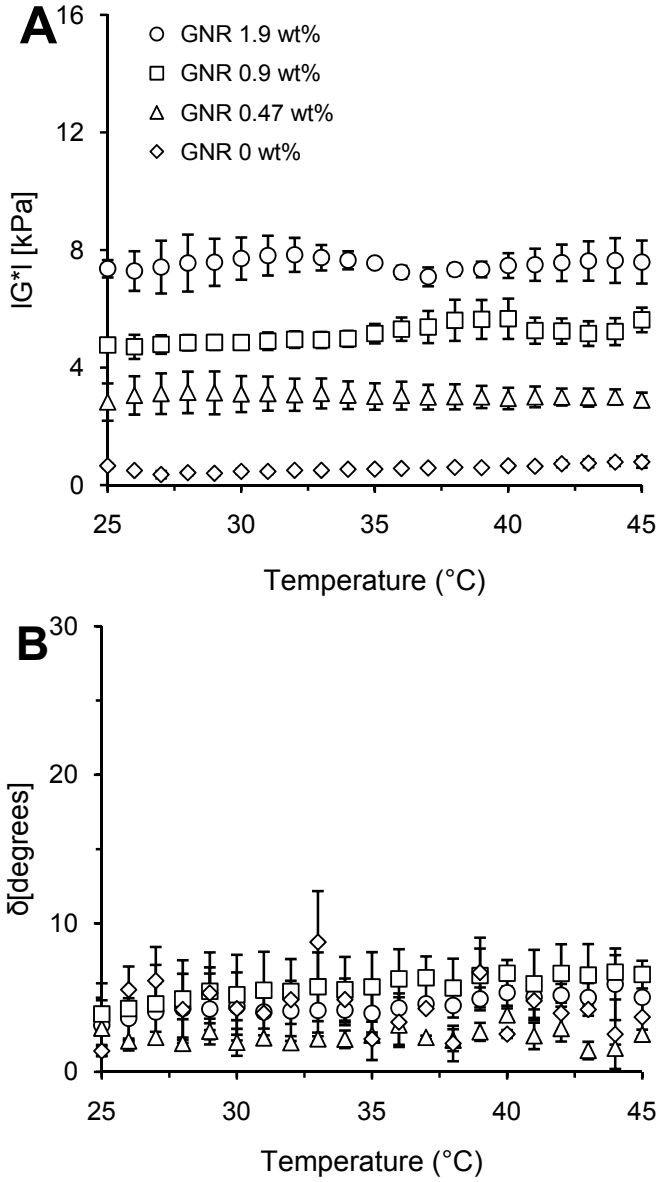
A
GNR 1.9 wt%
GNR 0.9 wt%
GNR 0.47 wt%
GNR 0 wt%
|G*| [kPa]
Temperature (°C)
B
δ[degrees]
Temperature (°C)

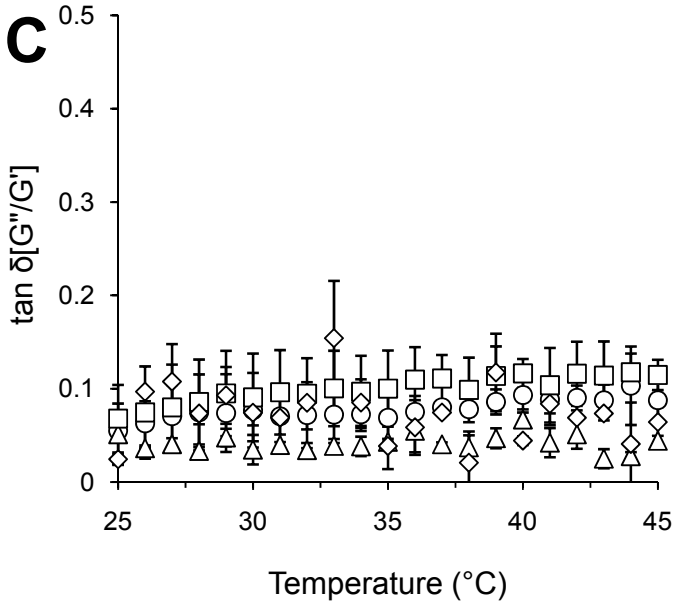

Figure 64.The effect of gold nanorod concentration and temperature on the magnitude of the complex modules (|G*|) and phase angle (*δ*) at angular frequency of 20 rad/s.

Biocompatible elastin like polypeptide-based hydrogels, aggregates, micelles and others have been repeatedly reported to support cell proliferation and/or differentiation for vascular graft, cartilage, ocular, vascular graft and liver tissue engineering[305,312-316]. In this study, the murine fibroblast cell adhesion and proliferation on top of nanocomposites (Figure 65) and cellular encapsulation inside the nanocomposite for sustained proliferation (Figure 67) were demonstrated.

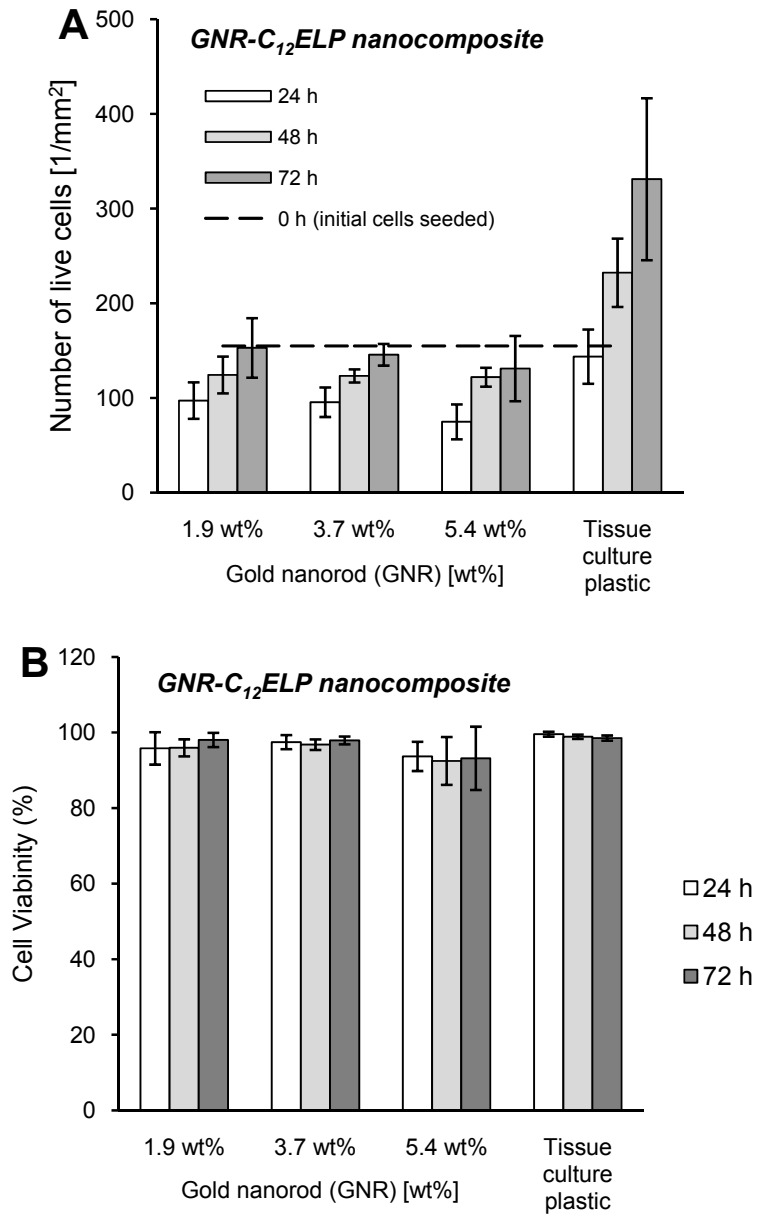

Figure 65. Fibroblast cell (A) adhesion, proliferation and (B) cell viability on top of unmodified nanocomposites at different gold nanorod weight ratios monitored up to 72 hours.

In Figure 65A, at 24 hours after cell seeding, the number of cell attached on top of nanocomposites was approximately 60% of the tissue culture plastic control. Increase in GNR weight percentage of nanocomposites from 1.9 wt% to 5.4 wt%,

resulted in an increased cell adhesion from 98 to 75 cells per mm^2. Moreover, cell proliferation, from 24 to 72 hours after cell seeding using tissue culture plastic (from 143 to 331 cells per mm^2) is significantly higher than that of nanocomposites (from ~100 to 140 cells per mm^2). A higher 3T3 cell doubling time (> 18h) was observed when using tissue culture plastic; this is presumably due to serum depletion and spatial confinement during 72 hours cell culture. Decreased cell adhesion and proliferation on nanocomposite can be explained by the presence of CTAB-capped gold nanorods. Several studies demonstrated the CTAB surfactant associated with nanorod to be cytotoxic, in which further surface modification is necessary to increase material biocompatibility and stability[241,267,317].

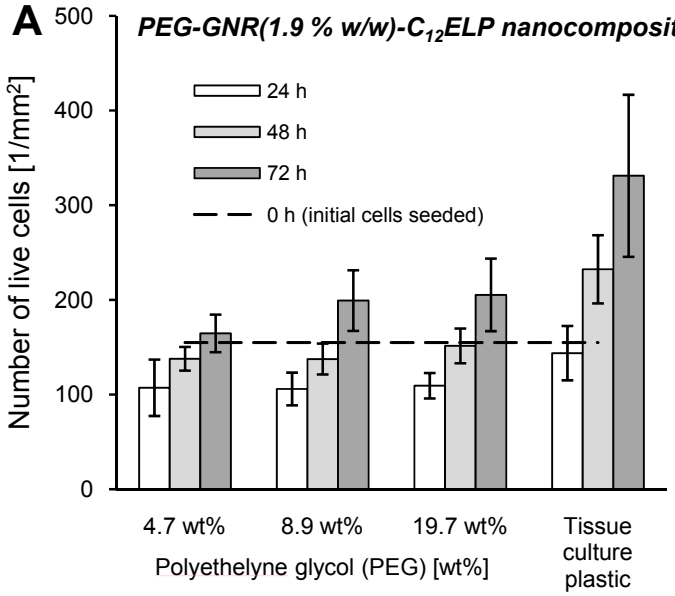

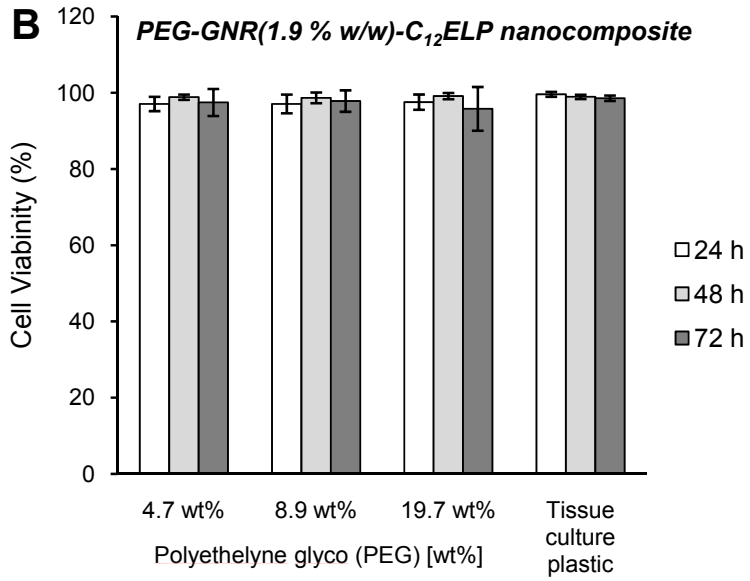

Figure 66.Fibroblast cell (A) adhesion, proliferation and (B) cell viability on top of PEG-modified nanocomposites at different gold nanorod weight ratios monitored up to 72 hours.

Here, polyethylene glycol (PEG)-modified gold nanorods was employed for crosslinking of elastin like polypeptide, leading to the formation of polyethylene glycol coated-GNR-C_{12}ELP nanocomposites, with various PEG weight percentages (4.7-19.7 wt%) and a fixed GNR concentration (1.9 wt%). In figure 66A, at 24 hours after cell seeding, a higher cell adhesion density on top of PEG-GNR-C_{12}ELP nanocomposite (~110 cells per mm^2) was observed, compared toGNR-C_{12}ELP nanocomposite (~75 cells per mm^2). Moreover fibroblast cell proliferation on top of PEG-GNR-C_{12}ELP nanocomposites is 5 to 35% higher than unmodified GNR-C_{12}ELP nanocomposite. These results suggested CTAB molecules around GNR inhibited cell adhesion and proliferation on top of gold nanorod-crosslinked C_{12}ELP nanocomposite; this can be potentially addressed by the introduction of appropriate surface modifiers. Although, the cell adhesion

and proliferation on top of the both modified and unmodified nanocomposites were less than using tissue culture plastic (Figure 65A and 66A), the viability of cells adhered on the all tested nanocomposites were found higher than 90 %, in most cases higher than 95% (Figure 65B, 66B and 67).

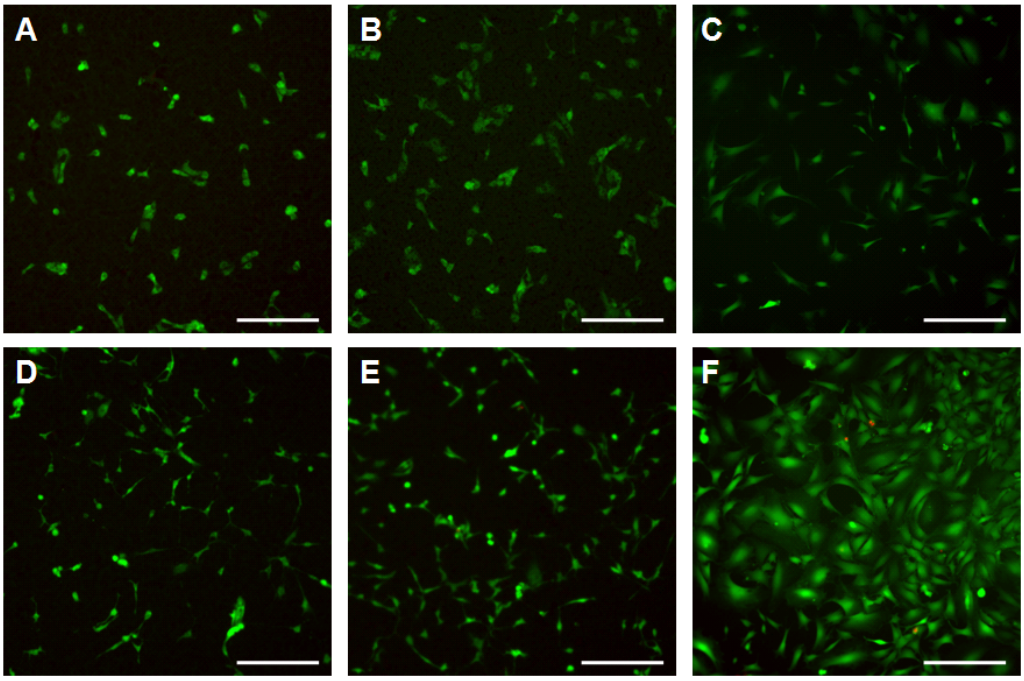

Figure 67.Florescence images of 3T3 fibroblast cells dual stained with ethidium homodimer and Calcein AM for visualization of dead/dying (colored red) and live cells (colored green). Fibroblast cells were cultured on top of (A,D) GNR (1.9 wt%)-C_{12}ELP nanocomposite, (B,E) GNR (1.9 wt%)-PEG (4.7 wt%)-C_{12}ELP nanocomposite and (C,F) tissue culture-treated well plate for 24 (upper row) and 72 (lower row) hours. Scale bar: 250 nm.

In addition to cell monolayer culture, success encapsulation of fibroblasts cell inside the PEG-GNR-C_{12}ELP nanocomposite (Figure 68) allowed sustained cell proliferation from inside the nanocomposite to its peripheral tissue culture plastic (Figure 69). Cellularized nanocomposites were less reddish in color due to the presence of cells (Figure 68A); the cell viability was analyzed using Live/dead assay followed by florescence microscopy and confocal microscopy imaging.

Florescence imaging (Figure 68B) suggested the majority of cells were viable at least three days after encapsulation (stained green) with minimum dead/dying cells (stained red). Blurriness of the florescence image is due to the presence of our-of-focused cells at different z-heights; the image quality was further improved by using confocal imaging (Figure 68C), in which, viable cells stained in green were observed inside the nanocomposite. Moreover, the proliferation of encapsulated cells was observed and monitored using light microscopy (Figure 69A). Sustained cell proliferation distance was expanding approximately 0.3 mm per day in a radial fashion up to 14 days (Figure 69 B and C).

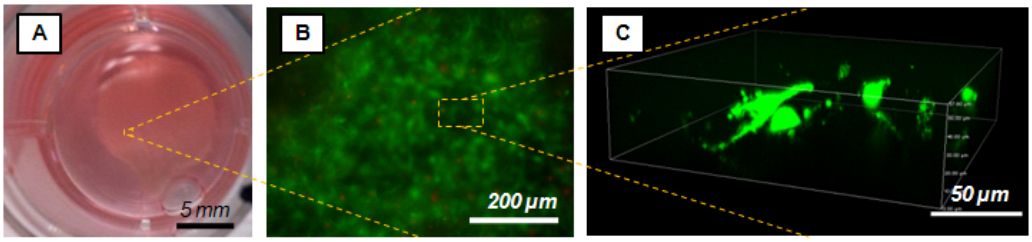

Figure 68.Cellularized nanocomposite.(A) Digital snap shot of cellularized PEG-GNR-C_{12}ELP cultured in serum containing medium. Encapsulated 3T3 fibroblast cells (at day 3) were dual stained with ethidium homodimer 1 and Calcein AM (dead/dying cells colored in red, live cells colored in green) and visualized using (C) florescence microscopy and (D) confocal microscopy. Blurriness of the florescence image (B) is due toout-of-focused cells at different focal plane (z-height).

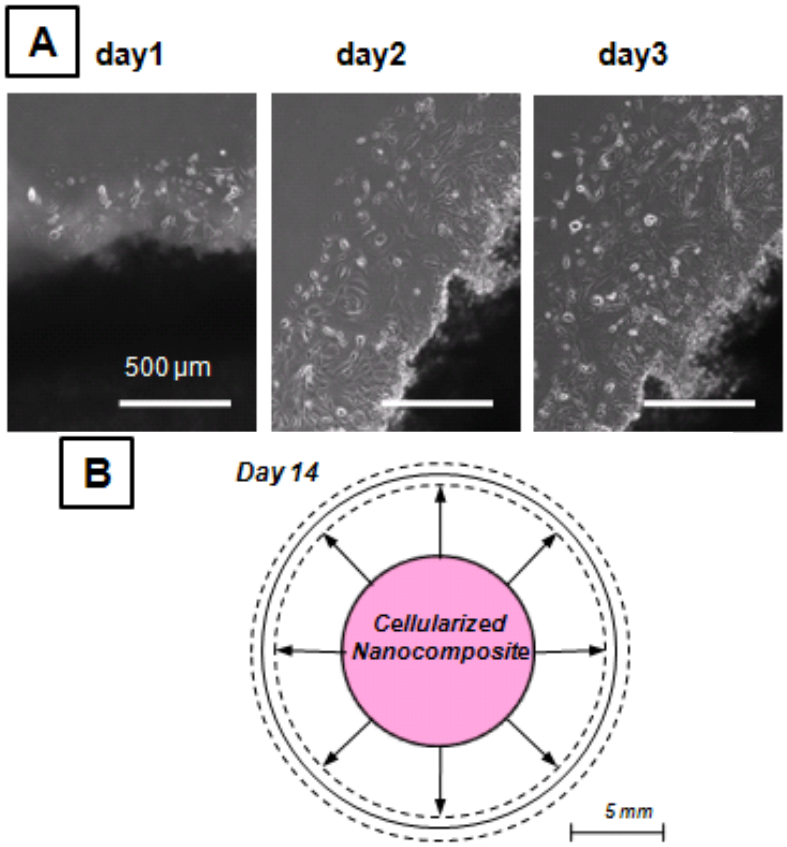
A
day1
day2
day3
500 µm
B
Day 14
Cellularized
Nanocomposite
5 mm
C
y = 0.295x
R² = 0.989
Proliferation distance (mm)
Time (Day)
0
2
4
6
8
10
12
14

Figure 69. (A) Cell proliferation from nanocomposite was confirmed using microscopy imaging. (B) Schematic depicting the cell proliferation distance (black line) at day 14, scale bar: 5 mm. (C) The proliferation of cells (distance, mm) from GNR-ELP nanocomposite is plotted as a function of time.

In this study, the GNR-C_{12}ELP nanocomposites were first time employed for laser tissue welding of porcine small intestines *ex vivo*. Tensile strength measurements were employed to evaluate the tensile strength of tissue after LWT using GNR-ELP nanocomposites. In Figure 70, small intact intestine section and incised intestine posses the highest and lowest ultimate tensile strength (UTS) at 0.45±0.02 and 0.11±0.01 MPa, respectively. Laser irradiation (20W/cm^2, 1 mm/sec and 3 min) on top of the incision did not enhance the UTS of ruptured intestine. Without laser irradiation, nanocomposite alone demonstrated minimum adhesive property, which slightly enhanced the UTS of ruptured tissue by ~0.03 MPa (p= 0.05, N=11). Upon near infra-red light irradiation (20W/cm^2) of nanocomposites (GNR wt% at 1.9, 5.4 and 8.7 wt%), heat transfer form nanocomposites resulted in temperature increase up to 46±1, 61±1.5, 64±1°C (N=9), respectively. One minute laser irradiation of ruptured tissue using nanocomposites (GNR wt% 1.9 and 5.4 wt%), resulted in UTS increase from 0.11±0.01 MPa to 0.17±0.01 MPa and 0.22±0.01 MPa (~ 50% UTS of intact intestine), respectively. Higher UST observed in using nanocomposite at GNR wt% of 5.4, can be explained by higher welding temperature 61±1.5. Increased laser power (from 1 to 3 minute) and gold nanorod weight percentage (from 5.4 to 9.5 wt %) of nanocomposite did not further enhance the UTS of rupture tissue.

It should be noted that the comparison of GNR-ELP based LTW to standard suturing has not yet be conducted. However, based on literature reports,

standard suturing techniques were able to recover ruptured tissue up to ~80 % of its original intact form will be employed as a standard threshold for comparison[318].

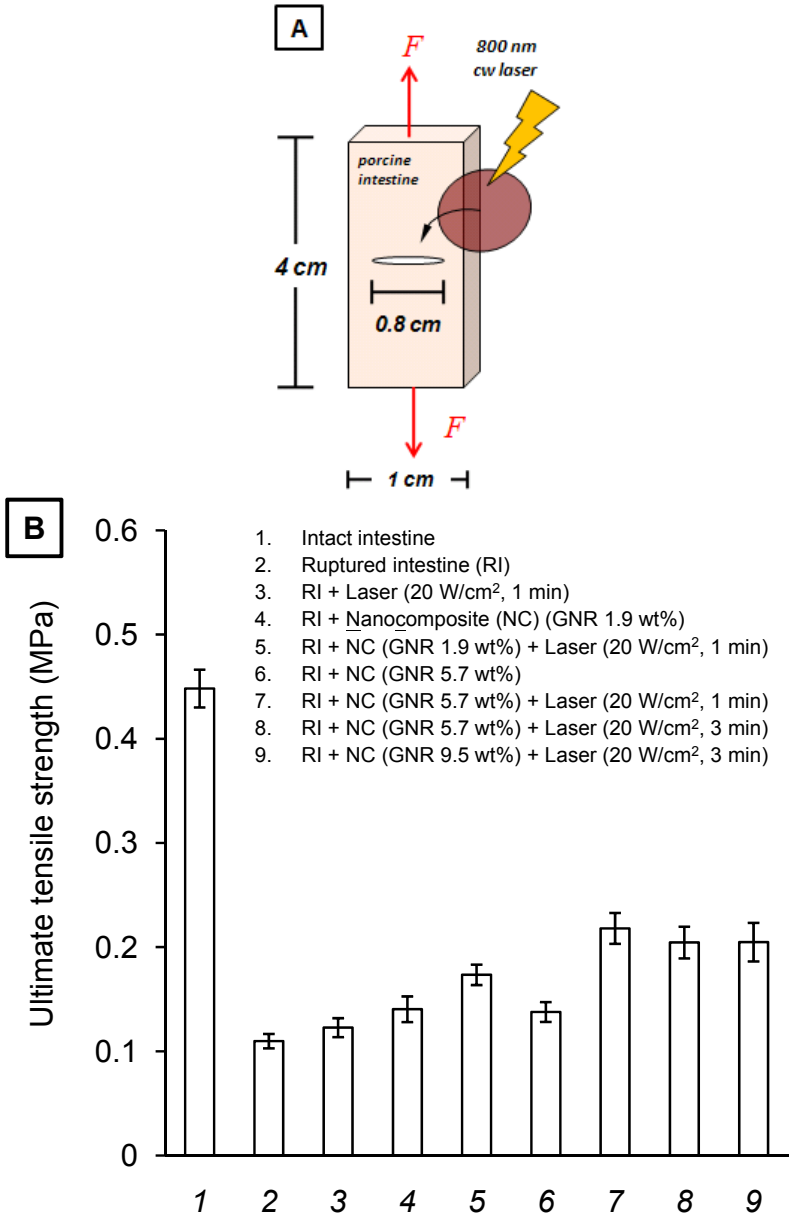

Figure 70. (A) Schematic depicting the experimental set up for laser tissue welding. (B) Ultimate tensile strength of tissues before and after laser tissue welding using nanocomposites.

Nanocomposites, at a GNR weight percentage of 5.4 wt% and providing heating up to 61±1.5°C, were further employed for leaking and bursting tests (Figure 71).

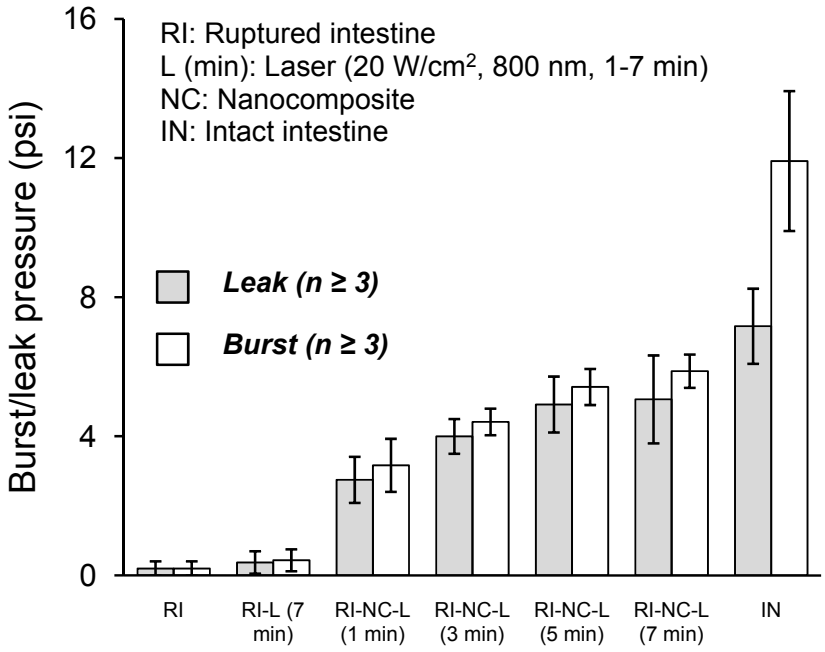

Figure 71. Bursting and leaking pressures of tissues before and after laser tissue welding using nanocomposites (GNR, 5.4 wt%).

Ruptured intestines and laser-welding rupture intestines had minimum bursting and leaking pressures. Laser irradiation of nanocomposite at the incision increased the tissue bursting and leaking pressures from ~ 2 psi up to 7 psi, where laser irradiation time increased from 1 to 7 minutes. Laser irradiation for 5 and 7 minutes resulted in similar tissue bursting and leaking pressure; whereas, obvious charring was observed after 7 minutes irradiation only. Laser irradiation of nanocomposite (GNR 5.4 wt%) for 5 minutes resulted in an optimal tissue welding, and resulted in tissue leaking and bursting pressure recovery up to 71 and 45 % of the their original intact forms .

Several reports recognized heating tissue above 60 °C is necessary to induce coagulation of photothermal-altered tissue proteins and providing robust closure [284,294]. Moreover, the photothermal damaging of tissue is irreversible; possessing the ability to precisely provide, adjust and predict laser dosage based on real-time temperature monitoring systems is critical and has been demonstrated by several groups[284,294,295,319]. This study focus on conveying the concept of laser tissue welding using biocompatible gold nanorod-crosslinked elastin-like polypeptide as a novel solder suitable for colorectal anastomosis, optimization of laser tissue welding using GNR-C_{12}ELP nanocomposites and its comparison with standard suturing and fibrin glue will be discussed in Chapter 9 (Future Directions).

8.4 Conclusions

In this chapter, it was demonstrated that the stiffness and swelling property of GNR-C_{12}ELPnanocompositescan be easily attenuated by controlling the gold nanorod concentration. This expanded the potential use of GNR-C_{12}ELPnanocomposites to a wide range of tissue engineering applications. Furthermore, the biocompatibility was evaluated by fibroblast cell monolayer culturing on top of the nanocomposite as well as encapsulating cells inside the material. Fibroblast cell can be cultured on top of nanocomposite with low toxicity; encapsulated cells enabled sustained proliferation. Last it was demonstrated the laser tissue welding using nanocomposite to successfully increase the mechanical integrity of the rupture tissue from ~ 45 % of its original intact form.

The studies supported or hypothesis, in which, laser tissue welding approach using novel GNR-C_{12}ELPnanocomposites can be employed for tissue regeneration and repair applications. Findings from this research will guide the future direct proposed in testing in larger animal models, and ultimately translation to human patients.

CHAPTER

9. Future Directions

9.1 Introduction

The field of nanotechnology has the potential to revolutionize numerous research fields. Myresearch focuses especially on the development of novel advanced nanobiomaterials towards cancer therapeutics (Chapter 3, 4 and 7), sensing (Chapter 5) and tissue engineering (Chapter 8) applications. Specifically, gold nanorods were surface modified with polyelectrolytes and polyethylene glycols for photothermal ablation of human prostate cancer cells *in vitro* (Chapter 3 and 4). Moreover, gold nanorods were interfaced with elastin-like polypeptides (ELPs) via gold-thiol covalent bonds and successfully employed, by means of optical/photothermal manipulation, for potential sensing applications (Chapter 5). Engineering of polypeptides resulted in the formation of plasmonic nanocomposites, which were employed for drug encapsulation and release. Most importantly, the nanocomposites were employed for the simultaneous administration of combination chemotherapy and hyperthermia to cancer cells *in vitro*(Chapter 7)and laser tissue welding of bowel tissue (Chapter 8) for the first time.

The inherent optical, photothermal and degradation properties made the plasmonic synergistic nanocomposites well suited for the development of verifiable unattended sensors, in which visible phase change occurs in response to photothermal changes and gamma irradiation. Moreover, the capability of cell

encapsulation and photoactivable release of small molecules made the biocompatible nanocomposite an excellent material for simultaneous laser tissue welding, drug(growth factor) delivery to facilitate wound healing with antimicrobial activity.

The chapter will discuss the use of multifunctional nanocomposites derived from nanoparticles (e.g. plasmonic nanoparticles) and biomolecules (engineered polypeptides) in two directions: ***(i) Investigation into how polypeptide-nanoparticle nanoassemblies / nanocomposites interact with gamma radiation or into the use of these advanced materials for detecting gamma radiation.(ii)Detailed investigation into cell-based, light responsive bioadhesive for laser tissue welding (LTW) of colorectal tissue, to establish a fluid-tight sealing, stimulate wound healing and minimize infection after colorectal resection.***

9.2 Engineered Polypeptide-Based Nanomatrices for Unattended Gamma Radiation Sensing

9.2.1 Background

The use of unattended sensors to detect low levels of weapons' agents is indispensible in combating mass destruction weapons. Traditional radiation detection has been performed using ionization chamber, scintillation crystals and semiconducting sensors. Ionization chamber and scintillation crystals measure instantaneous radiation dose; cumulative dose measurements requires additional electronic equipment. Semiconducting sensors can detect both instantaneous

and cumulative radiation, however, the device can be can be tampered with by thermal annealing. In medicine, radiation badges consisting of radiation sensitive film can be used to measure cumulative radiation dose, however, their temperature sensitivity and gradual decay can potentially limit their application in battle field. The goal of this proposed future direction involves the fundamental studies on polypeptide-nanoparticle nanocomposite (small molecules-encapsulated)for instantaneous and cumulative radiation dose sensing. Specifically, radiation interaction with nanoparticles and polypeptide facilitating molecules release and nanocomposite disintegration will be employed as the fundamental basis for instantaneous and cumulative dose detection. Successful delivery of this proposed research will not only play a key role in safeguarding field personnel from weapons of mass destruction, but can also translate into medicine, specifically the war of cancer for combination chemotherapeutics and radiotherapy (radiation induced controlled release of drug molecules).

9.2.2 Specific Goals

Research will focus disintegration of gold nanorod-elastin like polypeptide nanocomposite upon gamma radiation. Moreover, release of indicator molecules from nanocomposite upon radiation exposure will also be conducted.

Task1: Gamma radiation inducing nanocomposite structural damage will be investigated using different analytical methods. The role of radiation dosage, nanoparticle and polypeptide content on the structural integrity will be determined. Parameters that lead to dissolution of solid-phase matrices to liquid phase

dispersions will be identified leading to fundamental information on these materials as elements for sensing radiation.

Task2: Release of colored indictor molecules from solid-phase matrices into liquid medium above the matrices will be employed as the sensing mechanism for gamma radiation. Small molecules, as indicators, will be encapsulated inside GNR-ELP nanocomposites (Chapter 7). Different indicator (e.g. molecular weight, hydrophobicity and others) will be investigated in order to demonstrate how chemistry of the molecules affects loading and subsequent gamma radiation-induced release. As the role of radiation dose strength, ELP and nanoparticle content will again be investigated. Moreover, the integrity and state of the GNR-ELP nanocomposites (e.g. loss of color following expulsion of indicator molecules) will also be investigated.

9.3GNR-ELP nanocomposites for simultaneous laser tissue welding, drug delivery, and tissue healing in a multifunctional manner.

9.3.1 Background

Cellularized GNR-ELP nanocomposites will be used simultaneously for laser tissue welding, drug (e.g. doxycycline) delivery, tissue healing and multifunctional manner. Detailed background and motivation were presented in Chapter 8.1.

9.3.2 Specific Goals

Task1: Chapter 8 demonstrated that GNR-ELP nanocomposites support fibroblast culture and proliferation; upcoming studies include culture of colon

epithelial cells in the nanocomposites. Cellularized nanocomposites can further participate in repair and regeneration of welded tissues.

Fibroblast-cellularized hydrogels demonstrate collagen deposition[320] which increases mechanical stiffness[321] of the hydrogel compared to the acellular material. I anticipate that cellularized nanocomposites can facilitate rapid collagen deposition that can impart mechanical strength to the weld promoting tissue regeneration. The normal colon epithelial cell line, NCM460[322],availablefromINCELL Corporation, LLC, will be employed for encapsulation within PNP-ELP nanocomposites; fibroblasts and 50-50% co-cultures of the two cell types will also be used. Cell viability and proliferation of NCM46 cells from the nanocomposite towards the peripheral areas of the nanocomposites will be characterized using fluorescence microscopy.

*Task 2:*Matrix metalloproteinases (MMP) overexpression breaks down early tissue formed during anastomoses in the colon, which compromises healing[323,324]. GNR-ELP nanocomposites can be employed for diffusion-based as well as laser-triggered localized delivery of MMP inhibitors (e.g. doxycycline).

*Task 3:*Silver (Ag), including Ag nanoparticles (AgNP)[325-327], demonstrates antibacterial properties[328]. Generation of GNR, AgNP and GNR-AgNP (hybrid) nanocomposites (nanoparticle content 1-20 wt%) and investigation of their antibacterial activities against *E.coli and Staphylococcus aureus* using the agar Kirby-Bauer disk-diffusion method will be carried out.

9.3.3 Anticipated Results and Potential Pitfalls

Successful completion of this aim will set the stage for translation to pre-clinicaland clinical investigations. The study will have investigated the weld efficacies of both, cellularized and non-cellularized plasmonic nanocomposites for colorectal anastomoses. It is possible that there is cell death in the path of the laser due to high localized temperatures, but this will be restricted to a small area (laser diameter 1 mm). In addition, the viability of cells outside the laser path can promote wound healing. In case of insufficient mechanical strength with GNR-ELP nanocomposites, an investigation into GNR-collagen and GNR-collagen/ ELP blends using collagen peptides described in the literature[329] as potential weld biomaterials will be studied.

REFERENCES

1. El-Sayed MA. 'Some interesting properties of metals confined in time and nanometer space of different shapes'. 34, *Accounts of Chemical Research*, 2001, 4, 257-264.

2. Link S, El-Sayed MA. 'Spectral properties and relaxation dynamics of surface plasmon electronic oscillations in gold and silver nanodots and nanorods'. 103, *Journal of Physical Chemistry B*, 1999, 40, 8410-8426.

3. Link S, El-Sayed MA. 'Shape and size dependence of radiative, non-radiative and photothermal properties of gold nanocrystals'. 19, *International Reviews in Physical Chemistry*, 2000, 3, 409-453.

4. Weissleder R. 'A clearer vision for in vivo imaging'. 19, *Nature Biotechnology*, 2001, 4, 316-317.

5. Huang XH, El-Sayed IH, Qian W, El-Sayed MA. 'Cancer cell imaging and photothermal therapy in the near-infrared region by using gold nanorods'. 128, *Journal of the American Chemical Society*, 2006, 6, 2115-2120.

6. Chen JY, Wang DL, Xi JF, Au L, Siekkinen A, Warsen A, Li ZY, Zhang H, Xia YN, Li XD. 'Immuno gold nanocages with tailored optical properties for targeted photothermal destruction of cancer cells'. 7, *Nano Letters*, 2007, 5, 1318-1322.

7. Loo C, Lowery A, Halas N, West J, Drezek R. 'Immunotargeted nanoshells for integrated cancer imaging and therapy'. 5, *Nano Letters*, 2005, 4, 709-711.

8. Turkevich J, Stevenson PC, Hillier J. 'A Study of the Nucleation and Growth Processes in the Synthesis of Colloidal Gold'. *Discussions of the Faraday Society*, 1951, 11, 55-75.

9. Leff DV, Brandt L, Heath JR. 'Synthesis and characterization of hydrophobic, organically-soluble gold nanocrystals functionalized with primary amines'. 12, *Langmuir*, 1996, 20, 4723-4730.

10. Weare WW, Reed SM, Warner MG, Hutchison JE. 'Improved synthesis of small (d(CORE) approximate to 1.5 nm) phosphine-stabilized gold nanoparticles'. 122, *Journal of the American Chemical Society*, 2000, 51, 12890-12891.

11. Scott RWJ, Wilson OM, Crooks RM. 'Synthesis, characterization, and applications of dendrimer-encapsulated nanoparticles'. 109, *Journal of Physical Chemistry B*, 2005, 2, 692-704.

12. Shi XG, Wang SH, Meshinchi S, Van Antwerp ME, Bi XD, Lee IH, Baker JR. 'Dendrimer-entrapped gold nanoparticles as a platform for cancer-cell targeting and Imaging'. 3, *Small*, 2007, 7, 1245-1252.

13. Yuan JJ, Schmid A, Armes SP, Lewis AL. 'Facile synthesis of highly biocompatible poly(2-(methacryloyloxy)ethyl phosphorylcholine)-coated gold nanoparticles in aqueous solution'. 22, *Langmuir*, 2006, 26, 11022-11027.

14. Martin CR. 'NANOMATERIALS - A MEMBRANE-BASED SYNTHETIC APPROACH'. 266, *Science*, 1994, 5193, 1961-1966.

15. Yu YY, Chang SS, Lee CL, Wang CRC. 'Gold nanorods: Electrochemical synthesis and optical properties'. 101, *Journal of Physical Chemistry B*, 1997, 34, 6661-6664.

16. Chang SS, Shih CW, Chen CD, Lai WC, Wang CRC. 'The shape transition of gold nanorods'. 15, *Langmuir*, 1999, 3, 701-709.

17. Jana NR, Gearheart L, Murphy CJ. 'Seed-mediated growth approach for shape-controlled synthesis of spheroidal and rod-like gold nanoparticles using a surfactant template'. 13, *Advanced Materials*, 2001, 18, 1389-1393.

18. Jana NR, Gearheart L, Murphy CJ. 'Wet chemical synthesis of high aspect ratio cylindrical gold nanorods'. 105, *Journal of Physical Chemistry B*, 2001, 19, 4065-4067.

19. Jana NR, Gearheart L, Obare SO, Murphy CJ. 'Anisotropic chemical reactivity of gold spheroids and nanorods'. 18, *Langmuir*, 2002, 3, 922-927.

20. Nikoobakht B, El-Sayed MA. 'Preparation and growth mechanism of gold nanorods (NRs) using seed-mediated growth method'. 15, *Chemistry of Materials*, 2003, 10, 1957-1962.

21. Nikoobakht B, El-Sayed MA. 'Evidence for bilayer assembly of cationic surfactants on the surface of gold nanorods'. 17, *Langmuir*, 2001, 20, 6368-6374.

22. Oldenburg SJ, Averitt RD, Westcott SL, Halas NJ. 'Nanoengineering of optical resonances'. 288, *Chemical Physics Letters*, 1998, 2-4, 243-247.

23. Oldenburg SJ, Jackson JB, Westcott SL, Halas NJ. 'Infrared extinction properties of gold nanoshells'. 75, *Applied Physics Letters*, 1999, 19, 2897-2899.

24. Oldenburg SJ, Westcott SL, Averitt RD, Halas NJ. 'Surface enhanced Raman scattering in the near infrared using metal nanoshell substrates'. 111, *Journal of Chemical Physics*, 1999, 10, 4729-4735.

25. Sun YG, Mayers BT, Xia YN. 'Template-engaged replacement reaction: A one-step approach to the large-scale synthesis of metal nanostructures with hollow interiors'. 2, *Nano Letters*, 2002, 5, 481-485.

26. Chen JY, McLellan JM, Siekkinen A, Xiong YJ, Li ZY, Xia YN. 'Facile synthesis of gold-silver nanocages with controllable pores on the surface'. 128, *Journal of the American Chemical Society*, 2006, 46, 14776-14777.

27. Skrabalak SE, Au L, Li XD, Xia Y. 'Facile synthesis of Ag nanocubes and Au nanocages'. 2, *Nature Protocols*, 2007, 9, 2182-2190.

28. Elghanian R, Storhoff JJ, Mucic RC, Letsinger RL, Mirkin CA. 'Selective colorimetric detection of polynucleotides based on the distance-dependent optical properties of gold nanoparticles'. 277, *Science*, 1997, 5329, 1078-1081.

29. Li HX, Rothberg L. 'Colorimetric detection of DNA sequences based on electrostatic interactions with unmodified gold nanoparticles'. 101, *Proceedings of the National Academy of Sciences of the United States of America*, 2004, 39, 14036-14039.

30. Zhang J, Wang LH, Pan D, Song SP, Boey FYC, Zhang H, Fan CH. 'Visual cocaine detection with gold nanoparticles and rationally engineered aptamer structures'. 4, *Small*, 2008, 8, 1196-1200.

31. Pavlov V, Xiao Y, Shlyahovsky B, Willner I. 'Aptamer-functionalized Au nanoparticles for the amplified optical detection of thrombin'. 126, *Journal of the American Chemical Society*, 2004, 38, 11768-11769.

32. Lee JS, Han MS, Mirkin CA. 'Colorimetric detection of mercuric ion (Hg2+) in aqueous media using DNA-functionalized gold nanoparticles'. 46, *Angewandte Chemie-International Edition*, 2007, 22, 4093-4096.

33. Sonnichsen C, Reinhard BM, Liphardt J, Alivisatos AP. 'A molecular ruler based on plasmon coupling of single gold and silver nanoparticles'. 23, *Nature Biotechnology*, 2005, 6, 741-745.

34. Nath N, Chilkoti A. 'Interfacial phase transition of an environmentally responsive elastin biopolymer adsorbed on functionalized gold nanoparticles studied by colloidal surface plasmon resonance'. 123, *Journal of the American Chemical Society*, 2001, 34, 8197-8202.

35. Cheng SS, Yang TJ, Xue QG, Zuo HB, Gao XW, Yang WG. 'Numerical simulation for the lower shaft and the hearth bottom of blast furnace'. 10, *Journal of University of Science and Technology Beijing*, 2003, 3, 16-20.

36. Mayer KM, Lee S, Liao H, Rostro BC, Fuentes A, Scully PT, Nehl CL, Hafner JH. 'A label-free immunoassay based upon localized surface plasmon resonance of gold nanorods'. 2, *ACS Nano*, 2008, 4, 687-692.

37. Chen CD, Cheng SF, Chau LK, Wang CRC. 'Sensing capability of the localized surface plasmon resonance of gold nanorods'. 22, *Biosens Bioelectron*, 2007, 6, 926-932.

38. Dahlin AB, Tegenfeldt JO, Hook F. 'Improving the instrumental resolution of sensors based on localized surface plasmon resonance'. 78, *Anal Chem*, 2006, 13, 4416-4423.

39. Nie SM, Emery SR. 'Probing single molecules and single nanoparticles by surface-enhanced Raman scattering'. 275, *Science*, 1997, 5303, 1102-1106.

40. Yonzon CR, Zhang, X. & Van Duyne, R. P. 'Localized surface plasmon resonance immunoassay and verification using surface-enhanced Raman spectroscopy'. 5224, *Proc SPIE – Int Soc Opt Eng*, 2003, 78-85.

41. Endo T, Kerman K, Nagatani N, Hiepa HM, Kim DK, Yonezawa Y, Nakano K, Tamiya E. 'Multiple label-free detection of antigen-antibody reaction using localized surface plasmon resonance-based core-shell structured nanoparticle layer nanochip'. 78, *Anal Chem*, 2006, 18, 6465-6475.

42. Loo C, Lin A, Hirsch L, Lee MH, Barton J, Halas N, West J, Drezek R. 'Nanoshell-enabled photonics-based imaging and therapy of cancer'. 3, *Technology in Cancer Research & Treatment*, 2004, 1, 33-40.

43. El-Sayed IH, Huang XH, El-Sayed MA. 'Selective laser photo-thermal therapy of epithelial carcinoma using anti-EGFR antibody conjugated gold nanoparticles'. 239, *Cancer Letters*, 2006, 1, 129-135.

44. Kirillin M, Shirmanova M, Sirotkina M, Bugrova M, Khlebtsov B, Zagaynova E. 'Contrasting properties of gold nanoshells and titanium dioxide nanoparticles for optical coherence tomography imaging of skin: Monte Carlo simulations and in vivo study'. 14, *Journal of Biomedical Optics*, 2009, 2, 021017.

45. Zagaynova EV, Shirmanova MV, Kirillin MY, Khlebtsov BN, Orlova AG, Balalaeva IV, Sirotkina MA, Bugrova ML, Agrba PD, Kamensky VA. 'Contrasting properties of gold nanoparticles for optical coherence

tomography: phantom, in vivo studies and Monte Carlo simulation'. 53, *Physics in Medicine and Biology*, 2008, 18, 4995-5009.

46. Oldenburg AL, Hansen MN, Zweifel DA, Wei A, Boppart SA. 'Plasmon-resonant gold nanorods as low backscattering albedo contrast agents for optical coherence tomography'. 14, *Optics Express*, 2006, 15, 6724-6738.

47. Kah JCY, Olivo M, Chow TH, Song KS, Koh KZY, Mhaisalkar S, Sheppard CJR. 'Control of optical contrast using gold nanoshells for optical coherence tomography imaging of mouse xenograft tumor model in vivo'. 14, *Journal of Biomedical Optics*, 2009, 5, 054015.

48. Kim CS, Wilder-Smith P, Ahn YC, Liaw LHL, Chen ZP, Kwon YJ. 'Enhanced detection of early-stage oral cancer in vivo by optical coherence tomography using multimodal delivery of gold nanoparticles'. 14, *Journal of Biomedical Optics*, 2009, 3, 034008.

49. Durr NJ, Larson T, Smith DK, Korgel BA, Sokolov K, Ben-Yakar A. 'Two-photon luminescence imaging of cancer cells using molecularly targeted gold nanorods'. 7, *Nano Letters*, 2007, 4, 941-945.

50. Wang HF, Huff TB, Zweifel DA, He W, Low PS, Wei A, Cheng JX. 'In vitro and in vivo two-photon luminescence imaging of single gold nanorods'. 102, *Proceedings of the National Academy of Sciences of the United States of America*, 2005, 44, 15752-15756.

51. Huang HC, Barua S, Kay DB, Rege K. 'Simultaneous Enhancement of Photothermal Stability and Gene Delivery Efficacy of Gold Nanorods Using Polyelectrolytes'. 3, *ACS Nano*, 2009, 10, 2941-2952.

52. Mooradia.A. 'Photoluminescence of Metals'. 22, *Physical Review Letters*, 1969, 5, 185-197.

53. Boyd GT, Yu ZH, Shen YR. 'Photoinduced Luminescence from the Noble-metals and its enhancement on roughened surfaces'. 33, *Physical Review B*, 1986, 12, 7923-7936.

54. Wang XD, Pang YJ, Ku G, Xie XY, Stoica G, Wang LHV. 'Noninvasive laser-induced photoacoustic tomography for structural and functional in vivo imaging of the brain'. 21, *Nature Biotechnology*, 2003, 7, 803-806.

55. Ku G, Wang LHV. 'Deeply penetrating photoacoustic tomography in biological tissues enhanced with an optical contrast agent'. 30, *Optics Letters*, 2005, 5, 507-509.

56. Wang YW, Xie XY, Wang XD, Ku G, Gill KL, O'Neal DP, Stoica G, Wang LV. 'Photoacoustic tomography of a nanoshell contrast agent in the in vivo rat brain'. 4, *Nano Letters*, 2004, 9, 1689-1692.

57. Yang XM, Skrabalak SE, Li ZY, Xia YN, Wang LHV. 'Photoacoustic tomography of a rat cerebral cortex in vivo with au nanocages as an optical contrast agent'. 7, *Nano Letters*, 2007, 12, 3798-3802.

58. Song KH, Kim CH, Cobley CM, Xia YN, Wang LV. 'Near-Infrared Gold Nanocages as a New Class of Tracers for Photoacoustic Sentinel Lymph Node Mapping on a Rat Model'. 9, *Nano Letters*, 2009, 1, 183-188.

59. Zhang GD, Yang Z, Lu W, Zhang R, Huang Q, Tian M, Li L, Liang D, Li C. 'Influence of anchoring ligands and particle size on the colloidal stability and in vivo biodistribution of polyethylene glycol-coated gold nanoparticles in tumor-xenografted mice'. 30, *Biomaterials*, 2009, 10, 1928-1936.

60. Pan DPJ, Pramanik M, Senpan A, Ghosh S, Wickline SA, Wang LV, Lanza GM. 'Near infrared photoacoustic detection of sentinel lymph nodes with gold nanobeacons'. 31, *Biomaterials*, 14, 4088-4093.

61. Li PC, Wang CRC, Shieh DB, Wei CW, Liao CK, Poe C, Jhan S, Ding AA, Wu YN. 'In vivo Photoacoustic Molecular Imaging with Simultaneous Multiple Selective Targeting Using Antibody-Conjugated Gold Nanorods'. 16, *Optics Express*, 2008, 23, 18605-18615.

62. Kim JW, Galanzha EI, Shashkov EV, Moon HM, Zharov VP. 'Golden carbon nanotubes as multimodal photoacoustic and photothermal high-contrast molecular agents'. 4, *Nature Nanotechnology*, 2009, 10, 688-694.

63. Galanzha EI, Kim JW, Zharov VP. 'Nanotechnology-based molecular photoacoustic and photothermal flow cytometry platform for in-vivo detection and killing of circulating cancer stem cells'. 2, *Journal of Biophotonics*, 2009, 12, 725-735.

64. Galanzha EI, Shashkov EV, Kelly T, Kim JW, Yang LL, Zharov VP. 'In vivo magnetic enrichment and multiplex photoacoustic detection of circulating tumour cells'. 4, *Nature Nanotechnology*, 2009, 12, 855-860.

65. Zhang Q, Iwakuma N, Sharma P, Moudgil BM, Wu C, McNeill J, Jiang H, Grobmyer SR. 'Gold nanoparticles as a contrast agent for in vivo tumor imaging with photoacoustic tomography'. 20, *Nanotechnology*, 2009, 39, 395102.

66. Jackson JB, Halas NJ. 'Surface-enhanced Raman scattering on tunable plasmonic nanoparticle substrates'. 101, *Proceedings of the National Academy of Sciences of the United States of America*, 2004, 52, 17930-17935.

67. Laurent G, Felidj N, Truong SL, Aubard J, Levi G, Krenn JR, Hohenau A, Leitner A, Aussenegg FR. 'Imaging surface plasmon of gold nanoparticle arrays by far-field Raman scattering'. 5, *Nano Letters*, 2005, 2, 253-258.

68. Huang XH, El-Sayed IH, Qian W, El-Sayed MA. 'Cancer cells assemble and align gold nanorods conjugated to antibodies to produce highly enhanced, sharp, and polarized surface Raman spectra: A potential cancer diagnostic marker'. 7, *Nano Letters*, 2007, 6, 1591-1597.

69. Qian XM, Peng XH, Ansari DO, Yin-Goen Q, Chen GZ, Shin DM, Yang L, Young AN, Wang MD, Nie SM. 'In vivo tumor targeting and spectroscopic detection with surface-enhanced Raman nanoparticle tags'. 26, *Nature Biotechnology*, 2008, 1, 83-90.

70. Keren S, Zavaleta C, Cheng Z, de la Zerda A, Gheysens O, Gambhir SS. 'Noninvasive molecular imaging of small living subjects using Raman spectroscopy'. 105, *Proceedings of the National Academy of Sciences of the United States of America*, 2008, 15, 5844-5849.

71. Zaman RT, Diagaradjane P, Wang JC, Schwartz J, Rajaram N, Gill-Sharp KL, Cho SH, Rylander HG, Payne JD, Krishnan S, Tunnell JW. 'In vivo detection of gold nanoshells in tumors using diffuse optical spectroscopy'. 13, *Ieee Journal of Selected Topics in Quantum Electronics*, 2007, 6, 1715-1720.

72. Hainfeld JF, Slatkin DN, Focella TM, Smilowitz HM. 'Gold nanoparticles: a new X-ray contrast agent - Reply'. 80, *British Journal of Radiology*, 2007, 949, 65-65.

73. Kim D, Park S, Lee JH, Jeong YY, Jon S. 'Antibiofouling polymer-coated gold nanoparticles as a contrast agent for in vivo x-ray computed tomography imaging'. 129, *Journal of the American Chemical Society*, 2007, 24, 7661-7665.

74. Popovtzer R, Agrawal A, Kotov NA, Popovtzer A, Balter J, Carey TE, Kopelman R. 'Targeted Gold Nanoparticles Enable Molecular CT Imaging of Cancer'. 8, *Nano Letters*, 2008, 12, 4593-4596.

75. El-Sayed IH, Huang XH, El-Sayed MA. 'Surface plasmon resonance scattering and absorption of anti-EGFR antibody conjugated gold nanoparticles in cancer diagnostics: Applications in oral cancer'. 5, *Nano Letters*, 2005, 5, 829-834.

76. Ma LL, Feldman MD, Tam JM, Paranjape AS, Cheruku KK, Larson TA, Tam JO, Ingram DR, Paramita V, Villard JW, Jenkins JT, Wang T, Clarke GD, Asmis R, Sokolov K, Chandrasekar B, Milner TE, Johnston KP. 'Small Multifunctional Nanoclusters (Nanoroses) for Targeted Cellular Imaging and Therapy'. 3, *ACS Nano*, 2009, 9, 2686-2696.

77. Derfus AM, Chen AA, Min D-H, Ruoslahti E, Bhatia SN. 'Targeted Quantum Dot Conjugates for siRNA Delivery'. 18, *Bioconjugate Chemistry*, 2007, 5, 1391-1396.

78. Pitsillides CM, Joe EK, Wei XB, Anderson RR, Lin CP. 'Selective cell targeting with light-absorbing microparticles and nanoparticles'. 84, *Biophysical Journal*, 2003, 6, 4023-4032.

79. Zharov VP, Galitovskaya EN, Johnson C, Kelly T. 'Synergistic enhancement of selective nanophotothermolysis with gold nanoclusters: Potential for cancer therapy'. 37, *Lasers in Surgery and Medicine*, 2005, 3, 219-226.

80. Hleb EY, Hafner JH, Myers JN, Hanna EY, Rostro BC, Zhdanok SA, Lapotko DO. 'LANTCET: elimination of solid tumor cells with photothermal bubbles generated around clusters of gold nanoparticles'. 3, *Nanomedicine*, 2008, 5, 647-667.

81. Averitt RD, Westcott SL, Halas NJ. 'Linear optical properties of gold nanoshells'. 16, *Journal of the Optical Society of America B-Optical Physics*, 1999, 10, 1824-1832.

82. Hirsch LR, Stafford RJ, Bankson JA, Sershen SR, Rivera B, Price RE, Hazle JD, Halas NJ, West JL. 'Nanoshell-mediated near-infrared thermal therapy of tumors under magnetic resonance guidance'. 100, *Proceedings of the National Academy of Sciences of the United States of America*, 2003, 23, 13549-13554.

83. O'Neal DP, Hirsch LR, Halas NJ, Payne JD, West JL. 'Photo-thermal tumor ablation in mice using near infrared-absorbing nanoparticles'. 209, *Cancer Letters*, 2004, 2, 171-176.

84. Stern JM, Stanfield J, Kabbani W, Hsieh JT, Cadeddu JRA. 'Selective prostate cancer thermal ablation with laser activated gold nanoshells'. 179, *Journal of Urology*, 2008, 2, 748-753.

85. Schwartz JA, Shetty AM, Price RE, Stafford RJ, Wang JC, Uthamanthil RK, Pham K, McNichols RJ, Coleman CL, Payne JD. 'Feasibility Study of Particle-Assisted Laser Ablation of Brain Tumors in Orthotopic Canine Model'. 69, *Cancer Research*, 2009, 4, 1659-1667.

86. Chen AM, Scott MD. 'Current and future applications of immunological attenuation via pegylation of cells and tissue'. 15, *Biodrugs*, 2001, 12, 833-847.

87. Harris JM, Martin NE, Modi M. 'Pegylation - A novel process for modifying pharmacokinetics'. 40, *Clinical Pharmacokinetics*, 2001, 7, 539-551.

88. Maeda H, Wu J, Sawa T, Matsumura Y, Hori K. Tumor vascular permeability and the EPR effect in macromolecular therapeutics: a review. 2000. p 271-284.

89. Melancon MP, Lu W, Yang Z, Zhang R, Cheng Z, Elliot AM, Stafford J, Olson T, Zhang JZ, Li C. 'In vitro and in vivo targeting of hollow gold nanoshells directed at epidermal growth factor receptor for photothermal ablation therapy'. 7, *Molecular Cancer Therapeutics*, 2008, 6, 1730-1739.

90. Niidome T, Yamagata M, Okamoto Y, Akiyama Y, Takahashi H, Kawano T, Katayama Y, Niidome Y. 'PEG-modified gold nanorods with a stealth character for in vivo applications'. 114, *Journal of Controlled Release*, 2006, 3, 343-347.

91. Dickerson EB, Dreaden EC, Huang XH, El-Sayed IH, Chu HH, Pushpanketh S, McDonald JF, El-Sayed MA. 'Gold nanorod assisted near-infrared plasmonic photothermal therapy (PPTT) of squamous cell carcinoma in mice'. 269, *Cancer Letters*, 2008, 1, 57-66.

92. Kawano T, Niidome Y, Mori T, Katayama Y, Niidome T. 'PNIPAM Gel-Coated Gold Nanorods, for Targeted Delivery Responding to a Near-Infrared Laser'. 20, *Bioconjugate Chemistry*, 2009, 2, 209-212.

93. Akiyama Y, Mori T, Katayama Y, Niidome T. 'The effects of PEG grafting level and injection dose on gold nanorod biodistribution in the tumor-bearing mice'. 139, *Journal of Controlled Release*, 2009, 1, 81-84.

94. Niidome T, Akiyama Y, Yamagata M, Kawano T, Mori T, Niidome Y, Katayama Y. 'Poly(ethylene glycol)-Modified Gold Nanorods as a Photothermal Nanodevice for Hyperthermia'. 20, *Journal of Biomaterials Science-Polymer Edition*, 2009, 9, 1203-1215.

95. Goodrich GP, Bao LL, Gill-Sharp K, Sang KL, Wang J, Payne JD. 'Photothermal therapy in a murine colon cancer model using near-infrared absorbing gold nanorods'. 15, *Journal of Biomedical Optics*, 2010, 1, 018001.

96. Cheng Y, Samia AC, Li J, Kenney ME, Resnick A, Burda C. 'Delivery and Efficacy of a Cancer Drug as a Function of the Bond to the Gold Nanoparticle Surface'. 26, *Langmuir*, 2010, 4, 2248-2255.

97. Wu WT, Zhou T, Berliner A, Banerjee P, Zhou SQ. 'Smart Core-Shell Hybrid Nanogels with Ag Nanoparticle Core for Cancer Cell Imaging and Gel Shell for pH-Regulated Drug Delivery'. 22, *Chemistry of Materials*, 2010, 6, 1966-1976.

98. Jain PK, Qian W, El-Sayed MA. 'Ultrafast cooling of photoexcited electrons in gold nanoparticle-thiolated DNA conjugates involves the

dissociation of the gold-thiol bond'. 128, *Journal of the American Chemical Society*, 2006, 7, 2426-2433.

99. You J, Zhang GD, Li C. 'Exceptionally High Payload of Doxorubicin in Hollow Gold Nanospheres for Near-Infrared Light-Triggered Drug Release'. 4, *ACS Nano*, 2, 1033-1041.

100. Braun GB, Pallaoro A, Wu GH, Missirlis D, Zasadzinski JA, Tirrell M, Reich NO. 'Laser-Activated Gene Silencing via Gold Nanoshell-siRNA Conjugates'. 3, *ACS Nano*, 2009, 7, 2007-2015.

101. Bikram M, Gobin AM, Whitmire RE, West JL. 'Temperature-sensitive hydrogels with SiO2-Au nanoshells for controlled drug delivery'. 123, *Journal of Controlled Release*, 2007, 3, 219-227.

102. Guo R, Zhang LY, Qian HQ, Li RT, Jiang XQ, Liu BR. 'Multifunctional Nanocarriers for Cell Imaging, Drug Delivery, and Near-IR Photothermal Therapy'. 26, *Langmuir*, 2010, 8, 5428-5434.

103. Lu W, Zhang GD, Zhang R, Flores LG, Huang Q, Gelovani JG, Li C. 'Tumor Site-Specific Silencing of NF-kappa B p65 by Targeted Hollow Gold Nanosphere-Mediated Photothermal Transfection'. 70, *Cancer Research*, 2010, 8, 3177-3188.

104. Sershen SR, Westcott SL, Halas NJ, West JL. 'Temperature-sensitive polymer-nanoshell composites for photothermally modulated drug delivery'. 51, *Journal of Biomedical Materials Research*, 2000, 3, 293-298.

105. Paciotti GF, Myer L, Weinreich D, Goia D, Pavel N, McLaughlin RE, Tamarkin L. 'Colloidal gold: A novel nanoparticle vector for tumor directed drug delivery'. 11, *Drug Delivery*, 2004, 3, 169-183.

106. Visaria RK, Griffin RJ, Williams BW, Ebbini ES, Paciotti GF, Song CW, Bischof JC. 'Enhancement of tumor thermal therapy using gold nanoparticle-assisted tumor necrosis factor-alpha delivery'. 5, *Molecular Cancer Therapeutics*, 2006, 4, 1014-1020.

107. Visaria R, Bischof JC, Loren M, Williams B, Ebbini E, Paciotti G, Griffin R. 'Nanotherapeutics for enhancing thermal therapy of cancer'. 23, *International Journal of Hyperthermia*, 2007, 6, 501-511.

108. Chen YH, Tsai CY, Huang PY, Chang MY, Cheng PC, Chou CH, Chen DH, Wang CR, Shiau AL, Wu CL. 'Methotrexate conjugated to gold nanoparticles inhibits tumor growth in a syngeneic lung tumor model'. 4, *Molecular Pharmaceutics*, 2007, 5, 713-722.

109. Eustis S, El-Sayed MA. 'Why gold nanoparticles are more precious than pretty gold: Noble metal surface plasmon resonance and its enhancement

of the radiative and nonradiative properties of nanocrystals of different shapes'. 35, *Chem Soc Rev*, 2006, 3, 209-217.

110. Basu M, Seggerson S, Henshaw J, Jiang J, del ACR, Lefave C, Boyle PJ, Miller A, Pugia M, Basu S. 'Nano-biosensor development for bacterial detection during human kidney infection: use of glycoconjugate-specific antibody-bound gold NanoWire arrays (GNWA)'. 21, *Glycoconj J*, 2004, 8-9, 487-496.

111. Stoermer RL, Cederquist KB, McFarland SK, Sha MY, Penn SG, Keating CD. 'Coupling molecular beacons to barcoded metal nanowires for multiplexed, sealed chamber DNA bioassays'. 128, *J Am Chem Soc*, 2006, 51, 16892-16903.

112. Aravamudhan S, Kumar A, Mohapatra S, Bhansali S. 'Sensitive estimation of total cholesterol in blood using Au nanowires based micro-fluidic platform'. 22, *Biosens Bioelectron*, 2007, 9-10, 2289-2294.

113. Liu Z, Searson PC. 'Single nanoporous gold nanowire sensors'. 110, *J Phys Chem B*, 2006, 9, 4318-4322.

114. Bulbarello A, Sattayasamitsathit S, Crevillen AG, Burdick J, Mannino S, Kanatharana P, Thavarungkul P, Escarpa A, Wang J. 'Striped alloy nanowire optical reflectance barcodes prepared from a single plating solution'. 4, *Small*, 2008, 5, 597-600.

115. Sattayasamitsathit S, Burdick J, Bash R, Kanatharana P, Thavarungkul P, Wang J. 'Alloy nanowires bar codes based on nondestructive X-ray fluorescence readout'. 79, *Analytical Chemistry*, 2007, 19, 7571-7575.

116. Loaiza OA, Laocharoensuk R, Burdick J, Rodriguez MC, Pingarron JM, Pedrero M, Wang J. 'Adaptive orientation of multifunctional nanowires for magnetic control of bioelectrocatalytic processes'. 46, *Angew Chem Int Ed Engl*, 2007, 9, 1508-1511.

117. Li C, Lei B, Fan W, Zhang D, Meyyappan M, Zhou C. 'Molecular memory based on nanowire-molecular wire heterostructures'. 7, *J Nanosci Nanotechnol*, 2007, 1, 138-150.

118. Taha H, Lewis A, Sukenik C. 'Controlled deposition of gold nanowires on semiconducting and nonconducting surfaces'. 7, *Nano Lett*, 2007, 7, 1883-1887.

119. Lux KW, Rodriguez KJ. 'Template synthesis of arrays of nano fuel cells'. 6, *Nano Lett*, 2006, 2, 288-295.

120. C. W. Xu HWPKSSPJ. 'Highly Ordered Pd Nanowire Arrays as Effective Electrocatalysts for Ethanol Oxidation in Direct Alcohol Fuel Cells'. 19, *Advanced Materials*, 2007, 23, 4256-4259.

121. Hanying Bai KXYXHM. 'Fabrication of Au Nanowires of Uniform Length and Diameter Using a Monodisperse and Rigid Biomolecular Template: Collagen-like Triple Helix13'. 46, *Angewandte Chemie International Edition*, 2007, 18, 3319-3322.

122. Martin CR. 'Nanomaterials: A Membrane-Based Synthetic Approach'. 266, *Science*, 1994, 5193, 1961-1966.

123. Woo-Kyung Lee SCACSZ. 'Fabrication of Gold Nanowires by Electric-Field-Induced Scanning Probe Lithography and In Situ Chemical Development13'. 3, *Small*, 2007, 2, 249-254.

124. Sarah J. Hurst EKPLQCAM. 'Multisegmented One-Dimensional Nanorods Prepared by Hard-Template Synthetic Methods'. 45, *Angewandte Chemie International Edition*, 2006, 17, 2672-2692.

125. Wildt B, Mali P, Searson PC. 'Electrochemical template synthesis of multisegment nanowires: fabrication and protein functionalization'. 22, *Langmuir*, 2006, 25, 10528-10534.

126. Hulteen JC, Martin CR. 'A general template-based method for the preparation of nanomaterials'. 7, *Journal of Materials Chemistry*, 1997, 7, 1075-1087.

127. Kast M, Schroeder P, Hyun YJ, Pongratz P, Bruckl H. 'Synthesis of single-crystalline Zn metal nanowires utilizing cold-wall physical vapor deposition'. 7, *Nano Lett*, 2007, 8, 2540-2544.

128. Burdick J, Alonas E, Huang HC, Rege K, Wang J. 'High-throughput templated multisegment synthesis of gold nanowires and nanorods'. 20, *Nanotechnology*, 2009, 6, 065306.

129. Schwanbeck H, Schmidt U. 'Preparation and characterisation of magnetic nanostructures using filtration membranes'. 45, *Electrochimica Acta*, 2000, 27, 4389-4398.

130. Qin LD, Jang JW, Huang L, Mirkin CA. 'Sub-5-nm gaps prepared by on-wire lithography: Correlating gap size with electrical transport'. 3, *Small*, 2007, 1, 86-90.

131. Liu SH, Tok JBH, Bao ZN. 'Nanowire lithography: Fabricating controllable electrode gaps using Au-Ag-Au nanowires'. 5, *Nano Lett*, 2005, 6, 1071-1076.

132. Meenach SA, Burdick J, Kunwar A, Wang J. 'Metal/Conducting-polymer composite nanowires'. 3, *Small*, 2007, 2, 239-243.

133. Chithrani BD, Chan WCW. 'Elucidating the mechanism of cellular uptake and removal of protein-coated gold nanoparticles of different sizes and shapes'. 7, *Nano Letters*, 2007, 6, 1542-1550.

134. Choi HS, Liu W, Misra P, Tanaka E, Zimmer JP, Ipe BI, Bawendi MG, Frangioni JV. 'Renal clearance of quantum dots'. 25, *Nature Biotechnology*, 2007, 10, 1165-1170.

135. Hurst SJ, Payne EK, Qin LD, Mirkin CA. 'Multisegmented one-dimensional nanorods prepared by hard-template synthetic methods'. 45, *Angewandte Chemie-International Edition*, 2006, 17, 2672-2692.

136. Jabr-Milane L, van Vlerken L, Devalapally H, Shenoy D, Komareddy S, Bhavsar M, Amiji M. 'Multi-functional nanocarriers for targeted delivery of drugs and genes'. 130, *J Control Release*, 2008, 2, 121-128.

137. Smith AM, Duan H, Mohs AM, Nie S. 'Bioconjugated quantum dots for in vivo molecular and cellular imaging'. 60, *Adv Drug Deliv Rev*, 2008, 11, 1226-1240.

138. Cho K, Wang X, Nie S, Chen ZG, Shin DM. 'Therapeutic nanoparticles for drug delivery in cancer'. 14, *Clin Cancer Res*, 2008, 5, 1310-1316.

139. Medintz IL, Mattoussi H, Clapp AR. 'Potential clinical applications of quantum dots'. 3, *Int J Nanomedicine*, 2008, 2, 151-167.

140. Heath JR, Davis ME. 'Nanotechnology and cancer'. 59, *Annu Rev Med*, 2008, 251-265.

141. Lee KS, El-Sayed MA. 'Gold and silver nanoparticles in sensing and imaging: sensitivity of plasmon response to size, shape, and metal composition'. 110, *J Phys Chem B*, 2006, 39, 19220-19225.

142. Lee KS, El-Sayed MA. 'Dependence of the enhanced optical scattering efficiency relative to that of absorption for gold metal nanorods on aspect ratio, size, end-cap shape, and medium refractive index'. 109, *J Phys Chem B*, 2005, 43, 20331-20338.

143. El-Sayed IH, Huang X, El-Sayed MA. 'Surface plasmon resonance scattering and absorption of anti-EGFR antibody conjugated gold nanoparticles in cancer diagnostics: applications in oral cancer'. 5, *Nano Lett*, 2005, 5, 829-834.

144. Huang X, El-Sayed IH, Qian W, El-Sayed MA. 'Cancer cells assemble and align gold nanorods conjugated to antibodies to produce highly

enhanced, sharp, and polarized surface Raman spectra: a potential cancer diagnostic marker'. 7, *Nano Lett*, 2007, 6, 1591-1597.

145. Huang X, El-Sayed IH, Qian W, El-Sayed MA. 'Cancer cell imaging and photothermal therapy in the near-infrared region by using gold nanorods'. 128, *J Am Chem Soc*, 2006, 6, 2115-2120.

146. Huang YF, Chang HT, Tan W. 'Cancer cell targeting using multiple aptamers conjugated on nanorods'. 80, *Anal Chem*, 2008, 3, 567-572.

147. Skirtach AG, Dejugnat C, Braun D, Susha AS, Rogach AL, Parak WJ, Mohwald H, Sukhorukov GB. 'The role of metal nanoparticles in remote release of encapsulated materials'. 5, *Nano Lett*, 2005, 7, 1371-1377.

148. Salem AK, Searson PC, Leong KW. 'Multifunctional nanorods for gene delivery'. 2, *Nat Mater*, 2003, 10, 668-671.

149. Durr NJ, Larson T, Smith DK, Korgel BA, Sokolov K, Ben-Yakar A. 'Two-photon luminescence imaging of cancer cells using molecularly targeted gold nanorods'. 7, *Nano Lett*, 2007, 4, 941-945.

150. Sonnichsen C, Alivisatos AP. 'Gold nanorods as novel nonbleaching plasmon-based orientation sensors for polarized single-particle microscopy'. 5, *Nano Lett*, 2005, 2, 301-304.

151. Yu C, Irudayaraj J. 'Multiplex biosensor using gold nanorods'. 79, *Anal Chem*, 2007, 2, 572-579.

152. York J, Spetzler D, Xiong F, Frasch WD. 'Single-molecule detection of DNA via sequence-specific links between F1-ATPase motors and gold nanorod sensors'. 8, *Lab Chip*, 2008, 3, 415-419.

153. Huang HC, Koria P, Parker SM, Selby L, Megeed Z, Rege K. 'Optically Responsive Gold Nanorod-Polypeptide Assemblies'. 24, *Langmuir*, 2008, 24, 14139-14144.

154. Sun Z, Ni W, Yang Z, Kou X, Li L, Wang J. 'pH-Controlled reversible assembly and disassembly of gold nanorods'. 4, *Small*, 2008, 9, 1287-1292.

155. Nikoobakht B, El-Sayed MA. 'Preparation and Growth Mechanism of Gold Nanorods (NRs) Using Seed-Mediated Growth Method'. 15, *Chem Mater*, 2003, 10, 1957-1962.

156. Takahashi H, Niidome Y, Niidome T, Kaneko K, Kawasaki H, Yamada S. 'Modification of gold nanorods using phosphatidylcholine to reduce cytotoxicity'. 22, *Langmuir*, 2006, 1, 2-5.

157. Goodwin AP, Tabakman SM, Welsher K, Sherlock SP, Prencipe G, Dai H. 'Phospholipid-dextran with a single coupling point: a useful amphiphile for functionalization of nanomaterials'. 131, *J Am Chem Soc*, 2009, 1, 289-296.

158. Wijaya A, Hamad-Schifferli K. 'Ligand customization and DNA functionalization of gold nanorods via round-trip phase transfer ligand exchange'. 24, *Langmuir*, 2008, 18, 9966-9969.

159. Niidome T, Yamagata M, Okamoto Y, Akiyama Y, Takahashi H, Kawano T, Katayama Y, Niidome Y. 'PEG-modified gold nanorods with a stealth character for in vivo applications'. 114, *J Control Release*, 2006, 3, 343-347.

160. Choi BS, Iqbal M, Lee T, Kim YH, Tae G. 'Removal of cetyltrimethylammonium bromide to enhance the biocompatibility of Au nanorods synthesized by a modified seed mediated growth process'. 8, *J Nanosci Nanotechnol*, 2008, 9, 4670-4674.

161. Gole A, Murphy CJ. 'Polyelectrolyte-Coated Gold Nanorods: Synthesis, Characterization and Immobilization'. 17, *Chemistry of Materials*, 2005, 6, 1325-1330.

162. Ding H, Yong K-T, Roy I, Pudavar HE, Law WC, Bergey EJ, Prasad PN. 'Gold Nanorods Coated with Multilayer Polyelectrolyte as Contrast Agents for Multimodal Imaging'. 111, *The Journal of Physical Chemistry C*, 2007, 34, 12552-12557.

163. Connor EE, Mwamuka J, Gole A, Murphy CJ, Wyatt MD. 'Gold nanoparticles are taken up by human cells but do not cause acute cytotoxicity'. 1, *Small*, 2005, 3, 325-327.

164. Srivastava S, Kotov NA. 'Composite Layer-by-Layer (LBL) Assembly with Inorganic Nanoparticles and Nanowires'. 41, *Accounts of Chemical Research*, 2008, 12, 1831-1841.

165. Barua S, Joshi A, Banerjee A, Matthews D, Sharfstein ST, Cramer SM, Kane RS, Rege K. 'Parallel synthesis and screening of polymers for nonviral gene delivery'. 6, *Mol Pharm*, 2009, 1, 86-97.

166. Gong MC, Latouche JB, Krause A, Heston WD, Bander NH, Sadelain M. 'Cancer patient T cells genetically targeted to prostate-specific membrane antigen specifically lyse prostate cancer cells and release cytokines in response to prostate-specific membrane antigen'. 1, *Neoplasia*, 1999, 2, 123-127.

167. Chithrani BD, Ghazani AA, Chan WC. 'Determining the size and shape dependence of gold nanoparticle uptake into mammalian cells'. 6, *Nano Lett*, 2006, 4, 662-668.

168. Kaufman ED, Belyea J, Johnson MC, Nicholson ZM, Ricks JL, Shah PK, Bayless M, Pettersson T, Feldoto Z, Blomberg E, Claesson P, Franzen S. 'Probing protein adsorption onto mercaptoundecanoic acid stabilized gold nanoparticles and surfaces by quartz crystal microbalance and zeta-potential measurements'. 23, *Langmuir*, 2007, 11, 6053-6062.

169. Huff TB, Hansen MN, Zhao Y, Cheng JX, Wei A. 'Controlling the cellular uptake of gold nanorods'. 23, *Langmuir*, 2007, 4, 1596-1599.

170. Everts M, Saini V, Leddon JL, Kok RJ, Stoff-Khalili M, Preuss MA, Millican CL, Perkins G, Brown JM, Bagaria H, Nikles DE, Johnson DT, Zharov VP, Curiel DT. 'Covalently Linked Au Nanoparticles to a Viral Vector: Potential for Combined Photothermal and Gene Cancer Therapy'. 6, *Nano Letters*, 2006, 4, 587-591.

171. Fischer D, Bieber T, Li YX, Elsasser HP, Kissel T. 'A novel non-viral vector for DNA delivery based on low molecular weight, branched polyethylenimine: Effect of molecular weight on transfection efficiency and cytotoxicity'. 16, *Pharm Res*, 1999, 8, 1273-1279.

172. De Smedt SC, Demeester J, Hennink WE. 'Cationic polymer based gene delivery systems'. 17, *Pharm Res*, 2000, 2, 113-126.

173. Merdan T, Kopecek J, Kissel T. 'Prospects for cationic polymers in gene and oligonucleotide therapy against cancer'. 54, *Advanced Drug Delivery Reviews*, 2002, 5, 715-758.

174. Tang F, Hughes JA. 'Synthesis of a single-tailed cationic lipid and investigation of its transfection'. 62, *Journal of Controlled Release*, 1999, 3, 345-358.

175. Yu W, Liu C, Ye J, Zou W, Zhang N, Xu W. 'Novel cationic SLN containing a synthesized single-tailed lipid as a modifier for gene delivery'. 20, *Nanotechnology*, 2009, 21, 215102.

176. Tong L, Wei Q, Wei A, Cheng JX. 'Gold nanorods as contrast agents for biological imaging: optical properties, surface conjugation and photothermal effects'. 85, *Photochem Photobiol*, 2009, 1, 21-32.

177. Park J, Estrada A, Sharp K, Sang K, Schwartz JA, Smith DK, Coleman C, Payne JD, Korgel BA, Dunn AK, Tunnell JW. 'Two-photon-induced photoluminescence imaging of tumors using near-infrared excited gold nanoshells'. 16, *Opt Express*, 2008, 3, 1590-1599.

178. Eghtedari M, Oraevsky A, Copland JA, Kotov NA, Conjusteau A, Motamedi M. 'High sensitivity of in vivo detection of gold nanorods using a laser optoacoustic imaging system'. 7, *Nano Lett*, 2007, 7, 1914-1918.

179. Pennes HH. 'Analysis of Tissue and Arterial Blood Temperatures in the Resting Human Forearm'. 1, *Journal of Applied Physiology*, 1948, 2, 93-122.

180. Huang XH, Jain PK, El-Sayed IH, El-Sayed MA. 'Determination of the minimum temperature required for selective photothermal destruction of cancer cells with the use of immunotargeted gold nanoparticles'. 82, *Photochemistry and Photobiology*, 2006, 2, 412-417.

181. Elliott A, Schwartz J, Wang J, Shetty A, Hazle J, Stafford JR. 'Analytical Solution to Heat Equation With Magnetic Resonance Experimental Verification for Nanoshell Enhanced Thermal Therapy'. 40, *Lasers in Surgery and Medicine*, 2008, 9, 660-665.

182. Rylander MN, Feng Y, Bass J, Diller KR. 'Heat shock protein expression and injury optimization for laser therapy design'. 39, *Lasers in Surgery and Medicine*, 2007, 9, 731-746.

183. Fuentes D, Oden JT, Diller KR, Hazle JD, Elliott A, Shetty A, Stafford RJ. 'Computational Modeling and Real-Time Control of Patient-Specific Laser Treatment of Cancer'. 37, *Annals of Biomedical Engineering*, 2009, 4, 763-782.

184. Goodman TT, Chen JY, Matveev K, Pun SH. 'Spatio-temporal modeling of nanoparticle delivery to multicellular tumor spheroids'. 101, *Biotechnology and Bioengineering*, 2008, 2, 388-399.

185. He XM, Bhowmick S, Bischof JC. 'Thermal Therapy in Urologic Systems: A Comparison of Arrhenius and Thermal Isoeffective Dose Models in Predicting Hyperthermic Injury'. 131, *Journal of Biomechanical Engineering-Transactions of the Asme*, 2009, 7, 074507.

186. Diller KR, Valvano JW, Pearce JA. Bioheat Transfer. In: Kreith F, editor. CRC Handbook of Thermal Engineering. Boca Raton: CRC Press; 2000. p 4114-4187.

187. Prasher R, Bhattacharya P, Phelan PE. 'Thermal conductivity of nanoscale colloidal solutions (nanofluids)'. 94, *Physical Review Letters*, 2005, 2, 025901.

188. Henriques FC. 'Studies of Thermal Injury .5. The Predictability and the Significance of Thermally Induced Rate Processes Leading to Irreversible Epidermal Injury'. 43, *Archives of Pathology*, 1947, 5, 489-502.

189. Bhowmick P, Coad JE, Bhowmick S, Pryor JL, Larson T, De la Rosette J, Bischof JC. 'In vitro assessment of the efficacy of thermal therapy in human benign prostatic hyperplasia'. 20, *International Journal of Hyperthermia*, 2004, 4, 421-439.

190. Bhowmick S, Coad JE, Swanlund DJ, Bischof JC. 'In vitro thermal therapy of AT-1 Dunning prostate tumours'. 20, *International Journal of Hyperthermia*, 2004, 1, 73-92.

191. Incropera FP, DeWitt DP. Fundamentals of heat and mass transfer. New York: Wiley; 1996. xxiii, 886 p. p.

192. Overgaard J. 'Effect of Hyperthermia on Malignant Cells Invivo - Review and a Hypothesis'. 39, *Cancer*, 1977, 6, 2637-2646.

193. Ipe BI, Mahima S, Thomas KG. 'Light-induced modulation of self-assembly on spiropyran-capped gold nanoparticles: a potential system for the controlled release of amino acid derivatives'. 125, *J Am Chem Soc*, 2003, 24, 7174-7175.

194. Medintz IL, Trammell SA, Mattoussi H, Mauro JM. 'Reversible modulation of quantum dot photoluminescence using a protein- bound photochromic fluorescence resonance energy transfer acceptor'. 126, *J Am Chem Soc*, 2004, 1, 30-31.

195. Elghanian R, Storhoff JJ, Mucic RC, Letsinger RL, Mirkin CA. 'Selective colorimetric detection of polynucleotides based on the distance-dependent optical properties of gold nanoparticles'. 277, *Science*, 1997, 5329, 1078-1081.

196. Storhoff JJ, Marla SS, Bao P, Hagenow S, Mehta H, Lucas A, Garimella V, Patno T, Buckingham W, Cork W, Muller UR. 'Gold nanoparticle-based detection of genomic DNA targets on microarrays using a novel optical detection system'. 19, *Biosens Bioelectron*, 2004, 8, 875-883.

197. Mitsuishi M, Koishikawa Y, Tanaka H, Sato E, Mikayama T, Matsui J, Miyashita T. 'Nanoscale Actuation of Thermoreversible Polymer Brushes Coupled with Localized Surface Plasmon Resonance of Gold Nanoparticles'. 23, *Langmuir*, 2007, 14, 7472-7474.

198. Hirsch LR, Stafford RJ, Bankson JA, Sershen SR, Rivera B, Price RE, Hazle JD, Halas NJ, West JL. 'Nanoshell-mediated near-infrared thermal therapy of tumors under magnetic resonance guidance'. 100, *Proc Natl Acad Sci U S A*, 2003, 23, 13549-13554.

199. Wu C, Chen C, Lai J, Chen J, Mu X, Zheng J, Zhao Y. 'Molecule-scale controlled-release system based on light-responsive silica nanoparticles'. *Chem Commun (Camb)*, 2008, 23, 2662-2664.

200. Caruso EB, Cicciarella E, Sortino S. 'A multifunctional nanoassembly of mesogen-bearing amphiphiles and porphyrins for the simultaneous photodelivery of nitric oxide and singlet oxygen'. *Chem Commun (Camb)*, 2007, 47, 5028-5030.

201. Norman RS, Stone JW, Gole A, Murphy CJ, Sabo-Attwood TL. 'Targeted photothermal lysis of the pathogenic bacteria, Pseudomonas aeruginosa, with gold nanorods'. 8, *Nano Lett*, 2008, 1, 302-306.

202. Huang W-C, Tsai P-J, Chen Y-C. 'Functional gold nanoparticles as photothermal agents for selective-killing of pathogenic bacteria'. 2, *Nanomedicine*, 2007, 6, 777-787.

203. Lao UL, Mulchandani A, Chen W. 'Simple conjugation and purification of quantum dot-antibody complexes using a thermally responsive elastin-protein L scaffold as immunofluoresecent agents'. 128, *J Am Chem Soc*, 2006, 46, 14756-14757.

204. Urry DW. 'Physical Chemistry of Biological Free Energy Transduction As Demonstrated by Elastic Protein-Based Polymers'. 101, *J Phys Chem B*, 1997, 51, 11007-11028.

205. Zhang YJ, Trabbic-Carlson K, Albertorio F, Chilkoti A, Cremer PS. 'Aqueous two-phase system formation kinetics for elastin-like polypeptides of varying chain length'. 7, *Biomacromolecules*, 2006, 7, 2192-2199.

206. Meyer DE, Chilkoti A. 'Purification of recombinant proteins by fusion with thermally-responsive polypeptides'. 17, *Nat Biotechnol*, 1999, 11, 1112-1115.

207. Ge X, Yang DS, Trabbic-Carlson K, Kim B, Chilkoti A, Filipe CD. 'Self-cleavable stimulus responsive tags for protein purification without chromatography'. 127, *J Am Chem Soc*, 2005, 32, 11228-11229.

208. Banki MR, Feng L, Wood DW. 'Simple bioseparations using self-cleaving elastin-like polypeptide tags'. 2, *Nat Methods*, 2005, 9, 659-661.

209. Dreher MR, Liu W, Michelich CR, Dewhirst MW, Chilkoti A. 'Thermal cycling enhances the accumulation of a temperature-sensitive biopolymer in solid tumors'. 67, *Cancer Res*, 2007, 9, 4418-4424.

210. Dreher MR, Simnick AJ, Fischer K, Smith RJ, Patel A, Schmidt M, Chilkoti A. 'Temperature triggered self-assembly of polypeptides into multivalent spherical micelles'. 130, *J Am Chem Soc*, 2008, 2, 687-694.

211. Chen TH, Bae Y, Furgeson DY. 'Intelligent biosynthetic nanobiomaterials (IBNs) for hyperthermic gene delivery'. 25, *Pharm Res*, 2008, 3, 683-691.

212. Bidwell GL, 3rd, Fokt I, Priebe W, Raucher D. 'Development of elastin-like polypeptide for thermally targeted delivery of doxorubicin'. 73, *Biochem Pharmacol*, 2007, 5, 620-631.

213. Megeed Z, Haider M, Li D, O'Malley BW, Jr., Cappello J, Ghandehari H. 'In vitro and in vivo evaluation of recombinant silk-elastinlike hydrogels for cancer gene therapy'. 94, *J Control Release*, 2004, 2-3, 433-445.

214. Valiaev A, Abu-Lail NI, Lim DW, Chilkoti A, Zauscher S. 'Microcantilever sensing and actuation with end-grafted stimulus-responsive elastin-like polypeptides'. 23, *Langmuir*, 2007, 1, 339-344.

215. Fujita Y, Funabashi H, Mie M, Kobatake E. 'Design of a thermocontrollable protein complex'. 18, *Bioconjug Chem*, 2007, 5, 1619-1624.

216. Megeed Z, Winters RM, Yarmush ML. 'Modulation of single-chain antibody affinity with temperature-responsive elastin-like polypeptide linkers'. 7, *Biomacromolecules*, 2006, 4, 999-1004.

217. Janorkar AV, Rajagopalan P, Yarmush ML, Megeed Z. 'The use of elastin-like polypeptide-polyelectrolyte complexes to control hepatocyte morphology and function in vitro'. 29, *Biomaterials*, 2008, 6, 625-632.

218. Betre H, Setton LA, Meyer DE, Chilkoti A. 'Characterization of a genetically engineered elastin-like polypeptide for cartilaginous tissue repair'. 3, *Biomacromolecules*, 2002, 5, 910-916.

219. Hu M, Chen J, Li ZY, Au L, Hartland GV, Li X, Marquez M, Xia Y. 'Gold nanostructures: engineering their plasmonic properties for biomedical applications'. 35, *Chem Soc Rev*, 2006, 11, 1084-1094.

220. El-Sayed MA. 'Some interesting properties of metals confined in time and nanometer space of different shapes'. 34, *Acc Chem Res*, 2001, 4, 257-264.

221. Meyer DE, Chilkoti A. 'Genetically encoded synthesis of protein-based polymers with precisely specified molecular weight and sequence by recursive directional ligation: examples from the elastin-like polypeptide system'. 3, *Biomacromolecules*, 2002, 2, 357-367.

222. Banta S, Megeed Z, Casali M, Rege K, Yarmush ML. 'Engineering protein and peptide building blocks for nanotechnology'. 7, *J Nanosci Nanotechnol*, 2007, 2, 387-401.

223. Lowery AR, Gobin AM, Day ES, Halas NJ, West JL. 'Immunonanoshells for targeted photothermal ablation of tumor cells'. 1, *Int J Nanomedicine*, 2006, 2, 149-154.

224. Miao X, Wilson B, Lin LY. 'Low power laser induced microfluidic mixing through localized surface plasmon'. 2007, *Conf Proc IEEE Eng Med Biol Soc*, 2007, 6307-6310.

225. Cheng X, Wang Y, Hanein Y, Bohringer KF, Ratner BD. 'Novel cell patterning using microheater-controlled thermoresponsive plasma films'. 70, *J Biomed Mater Res A*, 2004, 2, 159-168.

226. Tom RT, Samal AK, Sreeprasad TS, Pradeep T. 'Hemoprotein bioconjugates of gold and silver nanoparticles and gold nanorods: structure-function correlations'. 23, *Langmuir*, 2007, 3, 1320-1325.

227. Das M, Sanson N, Fava D, Kumacheva E. 'Microgels loaded with gold nanorods: photothermally triggered volume transitions under physiological conditions'. 23, *Langmuir*, 2007, 1, 196-201.

228. Reismann M, Bretschneider JC, von Plessen G, Simon U. 'Reversible photothermal melting of DNA in DNA-gold-nanoparticle networks'. 4, *Small*, 2008, 5, 607-610.

229. Shiotani A, Mori T, Niidome T, Niidome Y, Katayama Y. 'Stable incorporation of gold nanorods into N-isopropylacrylamide hydrogels and their rapid shrinkage induced by near-infrared laser irradiation'. 23, *Langmuir*, 2007, 7, 4012-4018.

230. Jones CD, Lyon LA. 'Photothermal patterning of microgel/gold nanoparticle composite colloidal crystals'. 125, *J Am Chem Soc*, 2003, 2, 460-465.

231. Moon HK, Lee SH, Choi HC. 'In Vivo Near-Infrared Mediated Tumor Destruction by Photothermal Effect of Carbon Nanotubes'. 3, *ACS Nano*, 2009, 11, 3707-3713.

232. Torti SV, Byrne F, Whelan O, Levi N, Ucer B, Schmid M, Torti FM, Akman S, Liu J, Ajayan PM, Nalamasu O, Carroll DL. 'Thermal ablation therapeutics based on CNx multi-walled nanotubes'. 2, *Int J Nanomedicine*, 2007, 4, 707-714.

233. Dennis CL, Jackson AJ, Borchers JA, Ivkov R, Foreman AR, Hoopes PJ, Strawbridge R, Pierce Z, Goerntiz E, Lau JW, Gruettner C. 'The influence of magnetic and physiological behaviour on the effectiveness of iron oxide nanoparticles for hyperthermia'. 41, *Journal of Physics D-Applied Physics*, 2008, 13, 134020.

234. Cherukuri P, Glazer ES, Curleya SA. 'Targeted hyperthermia using metal nanoparticles'. 62, *Advanced Drug Delivery Reviews*, 2010, 3, 339-345.

235. Johannsen M, Gneueckow U, Thiesen B, Taymoorian K, Cho CH, Waldofner N, Scholz R, Jordan A, Loening SA, Wust P. 'Thermotherapy of prostate cancer using magnetic nanoparticles: Feasibility, imaging, and three-dimensional temperature distribution'. 52, *European Urology*, 2007, 6, 1653-1662.

236. Rostro-Kohanloo BC, Bickford LR, Payne CM, Day ES, Anderson LJE, Zhong M, Lee S, Mayer KM, Zal T, Adam L, Dinney CPN, Drezek RA, West JL, Hafner JH. 'The stabilization and targeting of surfactant-synthesized gold nanorods'. 20, *Nanotechnology*, 2009, 43, 1-10.

237. Huang H-C, Koria P, Parker SM, Selby L, Megeed Z, Rege K. 'Optically Responsive Gold Nanorod,àíPolypeptide Assemblies'. 24, *Langmuir*, 2008, 24, 14139-14144.

238. Huang H-C, Yang Y, Nanda A, Koria P, Rege K. 'Synergistic administration of photothermal therapy and chemotherapy to cancer cells using polypeptide-based degradable plasmonic matrices'. 6, *Nanomedicine*, 2011, 3, 459-473.

239. Cirulis JT, Bellingham CM, Davis EC, Hubmacher D, Reinhardt DP, Mecham RP, Keeley FW. 'Fibrillins, Fibulins, and Matrix-Associated Glycoprotein Modulate the Kinetics and Morphology of in Vitro Self-Assembly of a Recombinant Elastin-like Polypeptide'. 47, *Biochemistry*, 2008, 47, 12601-12613.

240. Goodwin AP, Tabakman SM, Welsher K, Sherlock SP, Prencipe G, Dai HJ. 'Phospholipid-Dextran with a Single Coupling Point: A Useful Amphiphile for Functionalization of Nanomaterials'. 131, *Journal of the American Chemical Society*, 2009, 1, 289-296.

241. Takahashi H, Niidome Y, Niidome T, Kaneko K, Kawasaki H, Yamada S. 'Modification of gold nanorods using phospatidylcholine to reduce cytotoxicity'. 22, *Langmuir*, 2006, 1, 2-5.

242. SwansonVethamuthu M, Almgren M, Hansson P, Zhao J. 'Surface tension studies of cetyltrimethylammonium bromide-bile salt association'. 12, *Langmuir*, 1996, 9, 2186-2189.

243. Modaressi A, Sifaoui H, Grzesiak B, Solimando R, Domanska U, Rogalski M. 'CTAB aggregation in aqueous solutions of ammonium based ionic liquids; conductimetric studies'. 296, *Colloids and Surfaces a-Physicochemical and Engineering Aspects*, 2007, 1-3, 104-108.

244. Zhao JP, Zhang GZ, Pispas S. 'Thermo-Induced Aggregation Behavior of Poly(ethylene oxide)-b-poly(N-isopropylacrylamide) Block Copolymers in the Presence of Cationic Surfactants'. 113, *Journal of Physical Chemistry B*, 2009, 31, 10600-10606.

245. Tom RT, Samal AK, Sreeprasad TS, Pradeep T. 'Hemoprotein bioconjugates of gold and silver nanoparticles and gold nanorods: Structure-function correlations'. 23, *Langmuir*, 2007, 3, 1320-1325.

246. Bellingham CM, Lillie MA, Gosline JM, Wright GM, Starcher BC, Bailey AJ, Woodhouse KA, Keeley FW. 'Recombinant human elastin polypeptides self-assemble into biomaterials with elastin-like properties'. 70, *Biopolymers*, 2003, 4, 445-455.

247. Cox BA, Starcher BC, Urry DW. 'Coacervation of Tropoelastin Results in Fiber Formation'. 249, *Journal of Biological Chemistry*, 1974, 3, 997-998.

248. Overgaard J. 'The Current and Potential Role of Hyperthermia in Radiotherapy'. 16, *International Journal of Radiation Oncology Biology Physics*, 1989, 3, 535-549.

249. He XM, Wolkers WF, Crowe JH, Swanlund DJ, Bischof JC. 'In situ thermal denaturation of proteins in dunning AT-1 prostate cancer cells: Implication for hyperthermic cell injury'. 32, *Annals of Biomedical Engineering*, 2004, 10, 1384-1398.

250. Lepock JR. 'Cellular effects of hyperthermia: relevance to the minimum dose for thermal damage'. 19, *International Journal of Hyperthermia*, 2003, 3, 252-266.

251. Seki T, Wakabayashi M, Nakagawa T, Imamura M, Tamai T, Nishimura A, Yamashiki N, Inoue K. 'Percutaneous microwave coagulation therapy for solitary metastatic liver tumors from colorectal cancer: A pilot clinical study'. 94, *American Journal of Gastroenterology*, 1999, 2, 322-327.

252. Gazelle GS, Goldberg SN, Solbiati L, Livraghi T. 'Tumor ablation with radio-frequency energy'. 217, *Radiology*, 2000, 3, 633-646.

253. Hilger I, Andra W, Bahring R, Daum A, Hergt R, Kaiser WA. 'Evaluation of temperature increase with different amounts of magnetite in liver tissue samples'. 32, *Investigative Radiology*, 1997, 11, 705-712.

254. Jolesz FA, Hynynen K. 'Magnetic resonance image-guided focused ultrasound surgery'. 8, *Cancer Journal*, 2002, 1, 100-112.

255. Dickerson EB, Dreaden EC, Huang X, El-Sayed IH, Chu H, Pushpanketh S, McDonald JF, El-Sayed MA. 'Gold nanorod assisted near-infrared plasmonic photothermal therapy (PPTT) of squamous cell carcinoma in mice'. 269, *Cancer Lett*, 2008, 1, 57-66.

256. Gobin AM, Lee MH, Halas NJ, James WD, Drezek RA, West JL. 'Near-Infrared Resonant Nanoshells for Combined Optical Imaging and Photothermal Cancer Therapy'. 7, *Nano Letters*, 2007, 7, 1929-1934.

257. Skrabalak SE, Chen J, Sun Y, Lu X, Au L, Cobley CM, Xia Y. 'Gold Nanocages: Synthesis, Properties, and Applications'. 41, *Accounts of Chemical Research*, 2008, 12, 1587-1595.

258. Huang X, Jain PK, El-Sayed IH, El-Sayed MA. 'Plasmonic photothermal therapy (PPTT) using gold nanoparticles'. 23, *Lasers Med Sci*, 2008, 3, 217-228.

259. von Maltzahn G, Park JH, Agrawal A, Bandaru NK, Das SK, Sailor MJ, Bhatia SN. 'Computationally guided photothermal tumor therapy using long-circulating gold nanorod antennas'. 69, *Cancer Res*, 2009, 9, 3892-3900.

260. Ma LL, Feldman MD, Tam JM, Paranjape AS, Cheruku KK, Larson TA, Tam JO, Ingram DR, Paramita V, Villard JW, Jenkins JT, Wang T, Clarke GD, Asmis R, Sokolov K, Chandrasekar B, Milner TE, Johnston KP. 'Small multifunctional nanoclusters (nanoroses) for targeted cellular imaging and therapy'. 3, *ACS Nano*, 2009, 9, 2686-2696.

261. Lepock JR. 'Cellular effects of hyperthermia: relevance to the minimum dose for thermal damage'. 19, *Int J Hyperthermia*, 2003, 3, 252-266.

262. Gibbons NB, Watson RW, Coffey RN, Brady HP, Fitzpatrick JM. 'Heat-shock proteins inhibit induction of prostate cancer cell apoptosis'. 45, *Prostate*, 2000, 1, 58-65.

263. Rylander MN, Feng Y, Bass J, Diller KR. 'Thermally induced injury and heat-shock protein expression in cells and tissues'. 1066, *Ann N Y Acad Sci*, 2005, 222-242.

264. Heath EI, Hillman DW, Vaishampayan U, Sheng SJ, Sarkar F, Harper F, Gaskins M, Pitot HC, Tan W, Ivy SP, Pili R, Carducci MA, Erlichman C, Liu G. 'A Phase II Trial of 17-Allylamino-17-Demethoxygeldanamycin in Patients with Hormone-Refractory Metastatic Prostate Cancer'. 14, *Clinical Cancer Research*, 2008, 23, 7940-7946.

265. Solit DB, Osman I, Polsky D, Panageas KS, Daud A, Goydos JS, Teitcher J, Wolchok JD, Germino FJ, Krown SE, Coit D, Rosen N, Chapman PB. 'Phase II Trial of 17-Allylamino-17-Demethoxygeldanamycin in Patients with Metastatic Melanoma'. 14, *Clinical Cancer Research*, 2008, 24, 8302-8307.

266. Huang HC, Rege K, Heys JJ. 'Spatiotemporal temperature distribution and cancer cell death in response to extracellular hyperthermia induced by gold nanorods'. 4, *ACS Nano*, 2010, 5, 2892-2900.

267. Huang H-C, Barua S, Kay DB, Rege K. 'Simultaneous Enhancement of Photothermal Stability and Gene Delivery Efficacy of Gold Nanorods Using Polyelectrolytes'. 3, *ACS Nano*, 2009, 10, 2941-2952.

268. Huang X, El-Sayed IH, Qian W, El-Sayed MA. 'Cancer Cell Imaging and Photothermal Therapy in the Near-Infrared Region by Using Gold Nanorods'. 128, *Journal of the American Chemical Society*, 2006, 6, 2115-2120.

269. Karanjia ND, Corder AP, Bearn P, Heald RJ. 'Leakage from Stapled Low Anastomosis after Total Mesorectal Excision for Carcinoma of the Rectum'. 81, *British Journal of Surgery*, 1994, 8, 1224-1226.

270. Isbister WH. 'Anastomotic leak in colorectal surgery: A single surgeon's experience'. 71, *Anz Journal of Surgery*, 2001, 9, 516-520.

271. Park IJ. 'Influence of Anastomotic Leakage on Oncological Outcome in Patients with Rectal Cancer'. 14, *Journal of Gastrointestinal Surgery*, 7, 1190-1196.

272. Thomson GA. 'An investigation of leakage tracts along stressed suture lines in phantom tissue'. 29, *Medical Engineering & Physics*, 2007, 9, 1030-1034.

273. Park IJ. 'Influence of Anastomotic Leakage on Oncological Outcome in Patients with Rectal Cancer'. 14, *Journal of Gastrointestinal Surgery*, 2010, 7, 1190-1196.

274. Anderson RH. 'Endoscopic laser surgery handbook (Science and practice of surgery series, vol. 10)'. 20, *International journal of cardiology*, 1988, 1, 157.

275. Zuger BJ, Ott B, Mainil-Varlet P, Schaffner T, Clemence JF, Weber HP, Frenz M. 'Laser solder welding of articular cartilage: Tensile strength and chondrocyte viability'. 28, *Lasers in Surgery and Medicine*, 2001, 5, 427-434.

276. Wolf -de Jonge ICD, Beek JF, Balm R. '25 years of laser assisted vascular anastomosis (LAVA): What have we learned?' 27, *European Journal of Vascular and Endovascular Surgery*, 2004, 5, 466-476.

277. Spector D, Rabi Y, Vasserman I, Hardy A, Klausner J, Rabau M, Katzir A. 'In Vitro Large Diameter Bowel Anastomosis Using a Temperature Controlled Laser Tissue Soldering System and Albumin Stent'. 41, *Lasers in Surgery and Medicine*, 2009, 7, 504-508.

278. Asencioarana F, Garciafons V, Torresgil V, Molinaandreu E, Vidalmartinez J, Perezsarrio R, Martinezsoriano F. 'Effects of a Low-

Power He-Ne-Laser on the Healing of Experimental Colon Anastomoses - Our Experience'. 31, *Optical Engineering*, 1992, 7, 1452-1457.

279. Matteini P, Rossi F, Menabuoni L, Pini R. 'Microscopic characterization of collagen modifications induced by low-temperature diode-laser welding of corneal tissue'. 39, *Lasers in Surgery and Medicine*, 2007, 7, 597-604.

280. Wadia Y, Xie H, Kajitani M. 'Liver repair and hemorrhage control by using laser soldering of liquid albumin in a porcine model'. 27, *Lasers in Surgery and Medicine*, 2000, 4, 319-328.

281. Kirsch AJ, Miller MI, Hensle TW, Chang DT, Shabsigh R, Olsson CA, Connor JP. 'Laser-Tissue Soldering in Urinary-Tract Reconstruction - First Human-Experience'. 46, *Urology*, 1995, 2, 261-266.

282. Schober R, Ulrich F, Sander T, Durselen H, Hessel S. 'Laser-Induced Alteration of Collagen Substructure Allows Microsurgical Tissue Welding'. 232, *Science*, 1986, 4756, 1421-1422.

283. Gobin AM, O'Neal DP, Watkins DM, Halas NJ, Drezek RA, West JL. 'Near infrared laser-tissue welding using nanoshells as an exogenous absorber'. 37, *Lasers in Surgery and Medicine*, 2005, 2, 123-129.

284. Cilesiz I, Springer T, Thomsen S, Welch AJ. 'Controlled temperature tissue fusion: Argon laser welding of canine intestine in vitro'. 18, *Lasers in Surgery and Medicine*, 1996, 4, 325-334.

285. Chikamatsu E, Sakurai T, Nishikimi N, Yano T, Nimura Y. 'Comparison of Laser Vascular Welding, Interrupted Sutures, and Continuous Sutures in Growing Vascular Anastomoses'. 16, *Lasers in Surgery and Medicine*, 1995, 1, 34-40.

286. Gennaro M, Ascer E, Mohan C, Wang S. 'A Comparison of Co-2 Laser-Assisted Venous Anastomoses and Conventional Suture Techniques - Patency, Aneurysm Formation, and Histologic Differences'. 14, *Journal of Vascular Surgery*, 1991, 5, 605-613.

287. Grubbs PE, Wang S, Marini C, Basu S, Rose DM, Cunningham JN. 'Enhancement of Co2-Laser Microvascular Anastomoses by Fibrin Glue'. 45, *Journal of Surgical Research*, 1988, 1, 112-119.

288. Capon A, Iarmarcovai G, Gonnelli D, Degardin N, Magalon G, Mordon S. 'Scar Prevention Using Laser-Assisted Skin Healing (LASH) in Plastic Surgery'. 34, *Aesthetic Plastic Surgery*, 2010, 4, 438-446.

289. Matteini P, Ratto F, Rossi F, Cicchi R, Stringari C, Kapsokalyvas D, Pavone FS, Pini R. 'Photothermally-induced disordered patterns of

corneal collagen revealed by SHG imaging'. 17, *Optics Express*, 2009, 6, 4868-4878.

290. Bass LS, Moazami N, Pocsidio J, Oz MC, Logerfo P, Treat MR. 'Changes in Type-I Collagen Following Laser-Welding'. 12, *Lasers in Surgery and Medicine*, 1992, 5, 500-505.

291. Murray LW, Su L, Kopchok GE, White RA. 'Crosslinking of Extracellular-Matrix Proteins - a Preliminary-Report on a Possible Mechanism of Argon-Laser Welding'. 9, *Lasers in Surgery and Medicine*, 1989, 5, 490-496.

292. Lauto A, Foster LJR, Ferris L, Avolio A, Zwaneveld N, Poole-Warren LA. 'Albumin-genipin solder for laser tissue repair'. 35, *Lasers in Surgery and Medicine*, 2004, 2, 140-145.

293. Cilesiz I, Thomsen S, Welch AJ, Chan EK. 'Controlled temperature tissue fusion: Ho:YAG laser welding of rat intestine in vivo .2'. 21, *Lasers in Surgery and Medicine*, 1997, 3, 278-286.

294. Poppas DP, Stewart RB, Massicotte M, Wolga AE, Kung RTV, Retik AB, Freeman MR. 'Temperature-controlled laser photocoagulation of soft tissue: In vivo evaluation using a tissue welding model'. 18, *Lasers in Surgery and Medicine*, 1996, 4, 335-344.

295. Klioze SD, Poppas DP, Rooke CT, Choma TJ, Schlossberg SM. 'Development and Initial Application of a Real-Time Thermal Control-System for Laser-Tissue Welding'. 152, *Journal of Urology*, 1994, 2, 744-748.

296. Matteini P, Ratto F, Rossi F, Rossi G, Esposito G, Puca A, Albanese A, Maira G, Pini R. 'In vivo carotid artery closure by laser activation of hyaluronan-embedded gold nanorods'. 15, *Journal of Biomedical Optics*, 2010, 4, 0415081-0415086.

297. Matteini P, Ratto F, Rossi F, Centi S, Dei L, Pini R. 'Chitosan Films Doped with Gold Nanorods as Laser-Activatable Hybrid Bioadhesives'. 22, *Advanced Materials*, 2010, 38, 4313-4316.

298. LaJoie EN, Barofsky AD, Gregory KW, Prahl SA. 'Patch welding with a pulsed diode laser and indocyanine green'. 12, *Lasers in Medical Science*, 1997, 1, 49-54.

299. Poppas D, Sutaria P, Sosa RE, Mininberg D, Schlossberg S. 'Chromophore Enhanced Laser-Welding of Canine Ureters in-Vitro Using a Human Protein Solder - a Preliminary Step for Laparoscopic Tissue Welding'. 150, *Journal of Urology*, 1993, 3, 1052-1055.

300. Poppas DP, Massicotte JM, Stewart RB, Roberts AB, Atala A, Retik AB, Freeman MR. 'Human albumin solder supplemented with TGF-beta(1) accelerates healing following laser welded wound closure'. 19, *Lasers in Surgery and Medicine*, 1996, 3, 360-368.

301. Huang XH, Jain PK, El-Sayed IH, El-Sayed MA. 'Plasmonic photothermal therapy (PPTT) using gold nanoparticles'. 23, *Lasers in Medical Science*, 2008, 3, 217-228.

302. Hu M, Chen JY, Li ZY, Au L, Hartland GV, Li XD, Marquez M, Xia YN. 'Gold nanostructures: engineering their plasmonic properties for biomedical applications'. 35, *Chemical Society Reviews*, 2006, 11, 1084-1094.

303. Mackay JA, Chilkoti A. 'Temperature sensitive peptides: Engineering hyperthermia-directed therapeutics'. 24, *International Journal of Hyperthermia*, 2008, 6, 483-495.

304. Koria P, Yagi H, Kitagawa Y, Megeed Z, Nahmias Y, Sheridan R, Yarmush ML. 'Self-assembling elastin-like peptides growth factor chimeric nanoparticles for the treatment of chronic wounds'. 108, *Proceedings of the National Academy of Sciences of the United States of America*, 2010, 3, 1034-1039.

305. McHale MK, Setton LA, Chilkoti A. 'Synthesis and in vitro evaluation of enzymatically cross-linked elastin-like polypeptide gels for cartilaginous tissue repair'. 11, *Tissue Engineering*, 2005, 11-12, 1768-1779.

306. Abramoff MD MP, Ram SJ. 'Image processing with ImageJ'. 11, *Biophotonics International*, 2004, 7, 36-42.

307. Taylor DJ, Parsons CE, Han HY, Jayaraman A, Rege K. 'Parallel screening of FDA-approved antineoplastic drugs for identifying sensitizers of TRAIL-induced apoptosis in cancer cells'. 11, *Bmc Cancer*, 2011, 470, 1-18.

308. Betre H, Setton LA, Meyer DE, Chilkoti A. 'Characterization of a genetically engineered elastin-like polypeptide for cartilaginous tissue repair'. 3, *Biomacromolecules*, 2002, 5, 910-916.

309. Trabbic-Carlson K, Setton LA, Chilkoti A. 'Swelling and mechanical behaviors of chemically cross-linked hydrogels of elastin-like polypeptides'. 4, *Biomacromolecules*, 2003, 3, 572-580.

310. Koria P, Yagi H, Kitagawa Y, Megeed Z, Nahmias Y, Sheridan R, Yarmush ML. 'Self-assembling elastin-like peptides growth factor chimeric nanoparticles for the treatment of chronic wounds'. 108, *Proceedings of*

the National Academy of Sciences of the United States of America, 3, 1034-1039.

311. Nettles DL, Chilkoti A, Setton LA. 'Applications of elastin-like polypeptides in tissue engineering'. 62, *Advanced Drug Delivery Reviews*, 15, 1479-1485.

312. Nettles DL, Chilkoti A, Setton LA. 'Applications of elastin-like polypeptides in tissue engineering'. 62, *Advanced Drug Delivery Reviews*, 2010, 15, 1479-1485.

313. Minato A, Ise H, Goto M, Akaike T. 'Cardiac differentiation of embryonic stem cells by substrate immobilization of insulin-like growth factor binding protein 4 with elastin-like polypeptides'. 33, *Biomaterials*, 2012, 2, 515-523.

314. Mie M, Mizushima Y, Kobatake E. 'Novel extracellular matrix for cell sheet recovery using genetically engineered elastin-like protein'. 86B, *Journal of Biomedical Materials Research Part B-Applied Biomaterials*, 2008, 1, 283-290.

315. Bhattarai N, Edmondson D, Veiseh O, Matsen FA, Zhang MQ. 'Electrospun chitosan-based nanofibers and their cellular compatibility'. 26, *Biomaterials*, 2005, 31, 6176-6184.

316. Betre H, Ong SR, Guilak F, Chilkoti A, Fermor B, Setton LA. 'Chondrocytic differentiation of human adipose-derived adult stem cells in elastin-like polypeptide'. 27, *Biomaterials*, 2006, 1, 91-99.

317. Alkilany AM, Nagaria PK, Hexel CR, Shaw TJ, Murphy CJ, Wyatt MD. 'Cellular Uptake and Cytotoxicity of Gold Nanorods: Molecular Origin of Cytotoxicity and Surface Effects'. 5, *Small*, 2009, 6, 701-708.

318. Kilkelly FX, Choma TJ, Popovic N, Miller DW, Sweet DE. 'Tendon repair by laser welding: A histologic and biomechanical comparison and suture repair with CO2 and Argon lasers'. 19, *Lasers in Surgery and Medicine*, 1996, 4, 487-491.

319. Cilesiz I. 'Controlled temperature phototheramal issue welding'. 4, *Journal of Biomedical Optics*, 1999, 3, 327-336.

320. Skardal A, Zhang J, McCoard L, Oottamasathien S, Prestwich GD. 'Dynamically Crosslinked Gold Nanoparticle – Hyaluronan Hydrogels'. 22, *Advanced Materials*, 2010, 42, 4736-4740.

321. Raub CB, Putnam AJ, Tromberg BJ, George SC. 'Predicting bulk mechanical properties of cellularized collagen gels using multiphoton microscopy'. 6, *Acta Biomaterialia*, 2010, 12, 4657-4665.

322. Moyer MP, Manzano LA, Merriman RL, Stauffer JS, Tanzer LR. 'NCM460, a normal human colon mucosal epithelial cell line'. 32, *In Vitro Cellular & Developmental Biology-Animal*, 1996, 6, 315-317.

323. Pasternak B, Matthiessen P, Jansson K, Andersson M, Aspenberg P. 'Elevated intraperitoneal matrix metalloproteinases-8 and -9 in patients who develop anastomotic leakage after rectal cancer surgery: a pilot study'. 12, *Colorectal Disease*, 2010, 7, 93-98.

324. Pasternak B, Rehn M, Andersen L, Ågren M, Heegaard A-M, Tengvall P, Aspenberg P. 'Doxycycline-coated sutures improve mechanical strength of intestinal anastomoses'. 23, *International Journal of Colorectal Disease*, 2008, 3, 271-276.

325. Galya T, Sedlarik V, Kuritka I, Novotny R, Sedlarikova J, Saha P. 'Antibacterial Poly(vinyl Alcohol) Film Containing Silver Nanoparticles: Preparation and Characterization'. 110, *Journal of Applied Polymer Science*, 2008, 5, 3178-3185.

326. Wei DW, Sun WY, Qian WP, Ye YZ, Ma XY. 'The synthesis of chitosan-based silver nanoparticles and their antibacterial activity'. 344, *Carbohydrate Research*, 2009, 17, 2375-2382.

327. Vimala K, Mohan YM, Sivudu KS, Varaprasad K, Ravindra S, Reddy NN, Padma Y, Sreedhar B, MohanaRaju K. 'Fabrication of porous chitosan films impregnated with silver nanoparticles: A facile approach for superior antibacterial application'. 76, *Colloids and Surfaces B-Biointerfaces*, 2010, 1, 248-258.

328. Rai M, Yadav A, Gade A. 'Silver nanoparticles as a new generation of antimicrobials'. 27, *Biotechnology Advances*, 2009, 1, 76-83.

329. Rubert Pérez CM, Panitch A, Chmielewski J. 'A Collagen Peptide-Based Physical Hydrogel for Cell Encapsulation'. 11, *Macromolecular Bioscience*, 2011, 10, 1426-1431.

APPENDIX

DATA COLLECTED MAY-AUGUST 2012

List of Publications

1. **Huang, H-C.**, Nanda, A., Rege, K. *Investigation of Phase Separation of Polypeptide-Gold Nanorod Nanoassemblies and Formation of Plasmonic Nanocomposites,* ***Langmuir*** ***Accepted, 2012.***

2. **INVITED PROTOCOL** Ramos, J., **Huang, H-C.**, Rege, K. *Delivery of Plasmid DNA to Mammalian Cells using Polymer-Gold Nanorod Assemblies.* ***Meth. Mol. Biol****. Accepted, 2012.*

3. Sanyal, S., **Huang, H-C.**, Rege, K., Dai, L. *Thermo-Responsive Core-Shell Composite Nanoparticles Synthesized via One-Step Pickering Emulsion Polymerization for Controlled Drug Delivery,* ***Journal of Nanomedicine & Nanotechnology*** ***2012; 2(7):1000126***

4. **Huang, H-C.**, Ramos, J., Potta, T., Grandhi, T. Rege, K. *Gold Nanoparticles in Nanomedical Cancer Research. Accepted for Publication,* ***Nano LIFE*** ***2011; 1(3-4): 289-307***

5. **Huang, H-C.**, Barua, S., Sharma, G., Dey, S.K., Rege, K. *Inorganic Nanoparticles for Cancer Imaging and Therapy.* ***J. Control. Release*** ***2011; 155(3): 344-357.***

6. **Huang, H-C.**, Yang, Y., Nanda, A., Koria, P., Rege, K. *Synergistic administration of Photothermal Therapy and Chemotherapy to Cancer Cells using Polypeptide-based Degradable Plasmonic Nanomatrices.* ***Nanomedicine*** ***2011; 6(3): 449-458.***

7. **INVITED REVIEW** Barua, S., Ramos, J., Potta, T., Taylor, D., **Huang, H-C.**, Montaneza, G., Rege, K. *Discovery of Cationic Polymers for Non-viral Gene Delivery using Combinatorial Approaches.* ***Comb. Chem. High T. Scr.*** ***2011; 14(10): 908-924.***

8. **Huang, H-C.**, Rege, K. and Heys, J.J., *Spatiotemporal Analysis of Temperature Response and Cancer Cell Injury following Extracellular Hyperthermia induced by Gold Nanorods.****ACS Nano*** ***2010; 4(5): 2892-2900.***

9. **Huang, H-C.**, Barua, S., Kay, D.B., and Rege, K. *Simultaneous Enhancement of Photothermal Stability and Gene Delivery Efficacy of Gold Nanorods Using Polyelectrolytes.* ***ACS Nano*** ***2009; 3(10): 2941-2952.***

10. Burdick, J., Alonas, E. **Huang, H-C.**, Rege, K., and Wang, J. *High-throughput templated multisegment synthesis of gold nanowires and nanorods.* ***Nanotechnology****2009; 20(6): 065306.*

11. **Huang, H-C.**, Koria, P., Parker, S. M., Selby, L., Mewed, Z., and Rege, K. *Optically Responsive Gold Nanorod-Polypeptide Assemblies.* ***Langmuir*** ***2008; 24(24): 14139-14144.***

Manuscript/Book Chapters in Preparation

12. **Huang, H-C.**, Nanda, A., Christensen, M., Sutiyoso, C., Rege, K. *In vitro Laser Tissue Welding using Polypeptide-Gold Nanorod Nanocomposite Solders.* ***In preparation, 2012.***

13. **INVITED BOOK CHAPTER** Ramos, J., **Huang, H-C.**, Rege, K. Chapter 64 "Laser targeting to nanoparticles", ***Handbook of Photomedicine***, editors: Michael Hamblin and Sulbha Sharma editors, Taylor and Francis Publishers. ***To be published 2012.***

14. **INVITED BOOK CHAPTER** Ramos, J., **Huang, H-C.**, Rege, K. Chapter "Inorganic Nanopreparations for Medical Use", ***Frontiers of Nanobiomedical Research***, editor: Vladimir Torchilin.

INDEX

Magnetic resonance (MR)

Mass spectrometry (MS)

Maturation constant (k_m)

Maturation velocity (V_m)

Methotrexate (MTX)

Nanoparticles (NP)

Near infrared (NIR)

Numerical aperture (NA)

Optical coherence tomography (OCT)

Optical Density (OD)

Optical density (OD)

PEG-conjugated (PEGylated)

Phosphate buffered saline (PBS)

Photoacoustic tomography (PAT)

Poly (N-isopropylacrylamide) (PNIPAM)

Polyethylene glycol (PEG)

Polyethyleneimine (pEI25)

Polystyrene sulfonate PSS)

Polyvinylpyrrolidone PVP

Scanning electron microscopy (SEM)

Serum-containing media (SCM)

Serum-free media (SFM)

Surface enhanced Raman scattering (SERS)

Surface plasmon resonance (SPR)

Thiolated poly(ethylene glycol) (mPEG-SH)

Titanium sapphire (Ti:S)

Transition temperature (T_t)

Tumor necrosis factor alpha (TNF-α)

Twelve cysteines-containing elastin-like polypeptide (C_{12}ELP)

Two cysteines-containing elastin-like polypeptide (C_2ELP)

Two photon luminescence (TPL)

Viscous loss modulus (G")